Improved estimation of surface biophysical parameters through inversion of linear BRDF models

Mathias Inguar Disney

Remote Sensing Unit

Department of Geography, University College London

26 Bedford Way

London

WC1H 0AP

mdisney@geog.ucl.ac.uk

Submitted for the fulfilment of degree of Doctorate of Philosophy

Supervised by Dr. P. Lewis

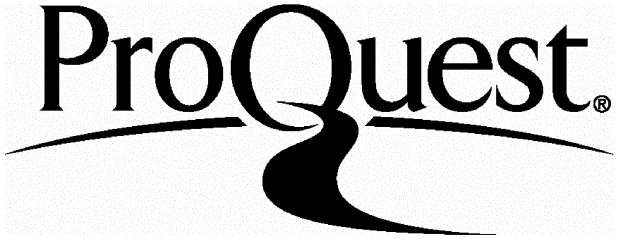

Artist's impression of the NASA Terra platform, launched in December 1999 as part of long term efforts to monitor and understand global climatic and circulation processes (courtesy of NASA).

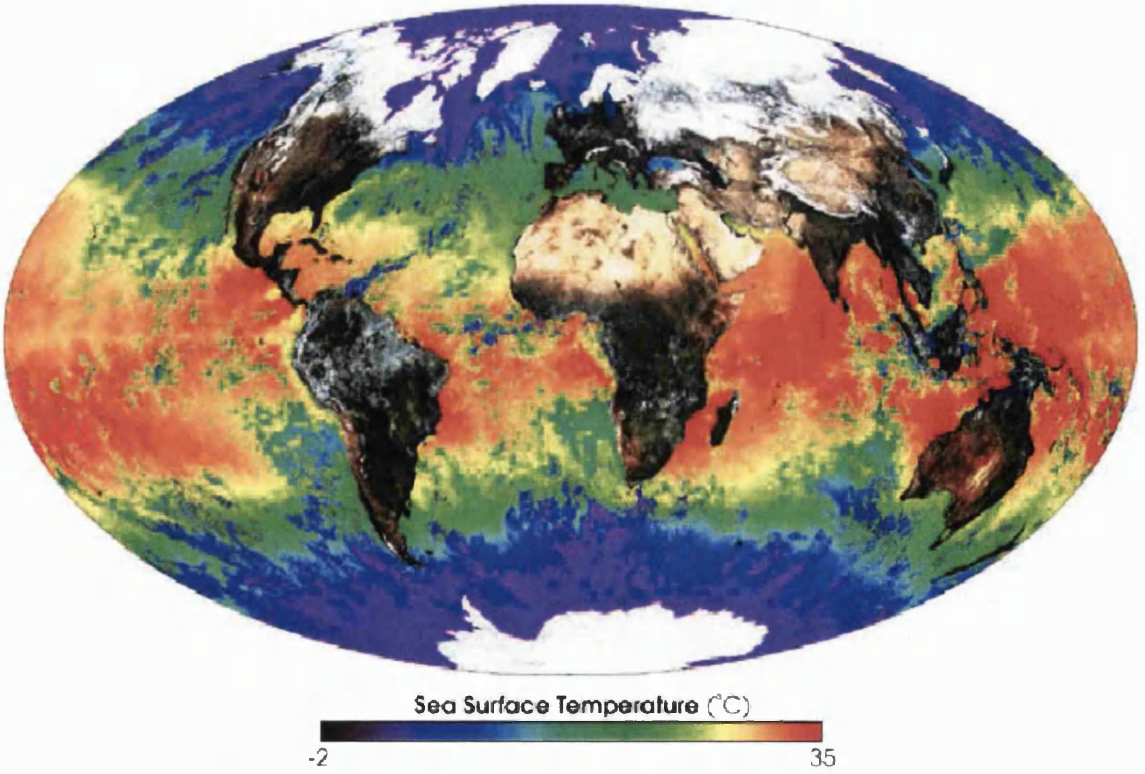

False colour representation of global land surface reflectance and sea surface temperature derived from instruments aboard the Terra platform (courtesy of NASA).

Abstract

An investigation is presented into the ability of linear kernel-driven models to adequately describe the surface bidirectional reflectance distribution function (BRDF) of vegetation. Such models were developed primarily for deriving albedo from limited angular samples of reflectance at moderate resolution (100s of m to km) and are based on semi-empirical approximations to more complex physically-based models. They assume that BRDF can be described by a linear combination of separate scattering 'shapes' (kernels), each of which is a function of purely geometric terms (viewing and illumination angles) only.

The assumptions underlying the linear kernel-driven models were tested using 3D geometric canopy structural models allied to a description of the radiometric scattering behaviour within the 3D canopy. This is the first time the properties of the models have been explicitly tested in this manner. The assumption that canopy reflectance can be represented as a linear combination of volumetric and geometric-optic (GO) scattering terms appears to be well founded. The kernels perform less well when the canopy departs too far (structurally or radiometrically) from the assumptions made in the model formulation. It is shown that the volumetric and GO kernels are not always capable of separating the components of canopy reflectance and that there can be coupling between the kernels. It is also demonstrated that the model parameters are not purely geometric as intended and that they contain biophysical information (related to leaf area and leaf reflectance). However, this information may require ancillary data if it is to be extracted from the model parameters.

A linear kernel-driven model of spectral reflectance is proposed which would allow interpolation (and extrapolation) of narrowband spectral samples of reflectance across the solar spectrum. Results suggest that this approach is very effective and can complement the angular kernels, allowing a full spectral, directional kernel-driven description of canopy reflectance. This is likely to prove extremely useful for deriving broadband albedo and for separating the spectral components of soil and vegetation scattering for studies of canopy-atmosphere transfer and productivity.

Acknowledgements

Firstly, I want to thank my supervisor, Lewis. He has provided far more inspiration and help than I probably deserve. He taught me that it can actually be fascinating watching (and understanding) grass grow. I owe my interest and continued development in plant modelling (and much else) to him. I would also like to thank colleagues such as Crystal Schaaf and the BU MODIS team, Jean-Louis Roujean, Charlie Walthall and in particular Mike Barnsley, for influence and guidance over the last few years. Thanks also go to colleagues within the Department of Geography at UCL for stimulating conversation over the years. I owe a debt of gratitude I can never repay to my Mum and Dad for always supporting me and making me realise what an incredible place the world is. Finally, above all else, I must thank Helen. For supporting me (financially and emotionally), for getting me through the bad and for sharing the good. Without you, it wouldn't be worth it. Helen, this is for you (maybe one day you'll read it!).

This work was carried out under NERC studentship GT19/96/14/EO, with CASE sponsorship from NRSC (now Infoterra) and Matra Marconi Space. Computing resources were provided in part by the University of London Intercollegiate Research Services (ULIRS). All help is gratefully acknowledged.

Table of contents

Page

Chapter 1 Introduction 1

1.1 Change and uncertainty in global climate..... 1

1.2 Developments in Earth Observation..... 3

1.3 Land Surface Processes..... 5

1.3.1 Biophysical parameters and vegetation..... 6

1.3.2 Shortwave energy budget and albedo..... 9

1.3.3 Albedo and surface scattering..... 12

1.3.4 Surface scattering and vegetation..... 13

1.4 Surface reflectance anisotropy..... 15

1.5 Thesis outline..... 18

Chapter 2 Review of canopy reflectance modelling 21

2.1 Factors affecting surface reflectance anisotropy..... 23

2.1.1 Bidirectional reflectance distribution function (BRDF)..... 25

2.1.2 Removal of reflectance anisotropy effects from observed reflectance..... 30

2.1.3 Reflectance anisotropy as a source of information..... 32

2.2 Atmospheric effects on measured surface reflectance..... 32

2.3 Canopy reflectance: the forward and inverse problems..... 37

2.4 Mathematical approaches to model inversion..... 39

2.4.1 Linear inversion..... 40

2.4.2 Numerical inversion..... 41

2.4.3 Multidimensional minimisation..... 43

2.4.4 Summary..... 45

2.5 Canopy reflectance modelling..... 47

2.5.1 Empirical models..... 48

2.5.2 Physically based models 51

2.5.2.1 Canopy reflectance, the turbid medium and radiative transfer (RT)..... 52

2.5.2.2 Approximations made possible by the turbid medium approach..... 55

2.5.2.3 Limitations of the turbid medium approach..... 58

2.5.2.4 Geometric-optic models..... 61

2.5.3 Computer simulation models..... 63

2.5.3.1 Ray Tracing..... 64

2.5.3.2 Radiosity..... 65
2.5.3.3 Other numerical CR modelling methods..... 66
2.5.3.4 BPMS/*ararat* model..... 67
2.5.4 Semi-empirical models..... 69
2.5.4.1 Linear (kernel-driven) semi-empirical kernels..... 70
2.5.4.1.1 Volumetric kernels..... 72
2.5.4.1.2 GO kernels..... 73
2.5.4.2 Non-linear semiempirical models..... 77
2.6 Conclusion..... 78

Chapter 3 Description of field-measured data 79

3.1 Summary of data, collection methods and validation..... 81
3.1.1 Plant structural measurements..... 83
3.1.2 Ground spectro-radiometric data..... 86
3.1.3 Canopy coverage estimates..... 89
3.1.4 LAI measurements..... 91
3.1.5 Airborne data..... 93
3.2 Summary..... 94

Chapter 4 Examination of volumetric and GO scattering behaviour 96

4.1 Experimental method..... 98
4.2 Exploring the hypotheses behind the linear models..... 101
4.2.1 ρ_{canopy} as a linear combination of volumetric and GO scattering..... 101
4.2.2 Volumetric and GO components of ρ_{canopy}..... 106
4.2.3 Discussion of directional shapes and magnitudes of α and β..... 113
4.2.3.1 Volumetric component of ρ_{canopy}, α..... 113
4.2.3.2 GO component of ρ_{canopy}, β..... 123
4.3 Conclusion..... 125

Chapter 5 Canopy scattering and the linear model parameters 127

5.1 Relationships between α and k_{vol}, and β and k_{GO}..... 127
5.2 Variation of volumetric component, α against k_{vol}..... 138
5.2.1 Results..... 138

5.2.2 Analysis of regression relationships..... 142
5.2.3 Slopes and intercepts a_{vol}, b_{vol} of α against k_{vol}..... 143
5.2.4 Summary..... 144
5.3 Variation of GO component, β against k_{GO} 145
5.3.1 Results..... 145
5.3.2 Analysis of regression relationships 152
5.3.3 Slopes and intercepts a_{GO}, b_{GO} of β against k_{GO} 155
5.3.4 Summary 156
5.4 Conclusion..... 157

Chapter 6 Separability of canopy scattering components and information content 160

6.1 Introduction..... 160
6.2 Method..... 162
6.3 Results..... 164
6.4 Discussion..... 172
6.4.1 Barley - 18th April..... 172
6.4.2 Barley – 13th May..... 174
6.4.3 Barley – 4th June..... 175
6.4.4 Barley – 24th June..... 175
6.4.5 Wheat – 23rd March..... 176
6.4.6 Wheat – 23rd April..... 176
6.4.7 Summary..... 177
6.5 Implications of coupling between model parameters..... 178
6.6 Implications of negative model parameters..... 187
6.6.1 Discussion of two parameter inversion..... 191
6.7 Conclusion..... 192

Chapter 7 Development and application of spectral kernels 196

7.1 Introduction..... 196
7.2 Concept of spectral kernels..... 199
7.3 Derivation of spectral kernels 202
7.3.1 Reflectance features of vegetation..... 204
7.3.2 Soil kernels: the soil component of $\rho_{canopy}(\lambda)$..... 206

7.3.3 Vegetation kernels: the vegetation component of $\rho_{canopy}(\lambda)$ **210**
7.4 Testing the spectral kernels **211**
7.4.1 Demonstration of vegetation spectral kernels against measured spectra ... **217**
7.5 A spectral directional kernel-driven model of ρ_{canopy} **221**
7.5.1 Performance of spectral kernels against simulated ρ_{canopy} **224**
7.5.2 Separation of soil and vegetation components **228**
7.5.3 Reconstruction from limited wavebands **232**
7.5.4 Directional component **234**
7.5.5 Demonstration of spectral kernels against airborne reflectance data **236**
7.6 Conclusion **239**

Chapter 8 Conclusions and directions for further work **241**
8.1 Exploring the concept of linear kernel-driven models **241**
8.2 Extension of the kernel-driven modelling concept **244**
8.3 Directions for future research **245**
8.3.1 Application of full spectral, directional kernel-driven model **245**
8.3.2 Other canopy types **246**
8.3.3 Multiple scattering **248**
8.3.4 Improved fieldwork measurements **249**
8.3.5 Optical and microwave scattering **250**

Appendix 1 Constraint of linear model parameters for inversion **251**
Appendix 2 Sunlit and shaded scene components for barley and wheat **255**

References **259**
WWW links **281**

Figures

Page

Chapter 1

1.1 MODIS 16-day reflectance image..... 5
1.2 Albedo and positive and negative feedback loops of surface fluxes..... 7
1.3 Solar irradiance curve at top and bottom of atmosphere..... 8
1.4 The fate of incoming solar radiation at the Earth's surface..... 9
1.5 Interactions between incoming radiation, the surface and the atmosphere..... 11
1.6 Schematic representation of radiation transport processes within a vegetation canopy..... 15

Chapter 2

2.1 Four examples of surface reflectance..... 24
2.2 Configuration of viewing and illumination vectors in the viewing hemisphere... 26
2.3 Angular effects caused by satellite repeat pattern..... 31
2.4 Four sources of atmospheric perturbation to the measured surface reflectance signal..... 33
2.5 Schematic representation of forward and inverse modes of ρ_{canopy} model operation..... 38
2.6 Three extreme types of error surface that may be encountered in function optimisation..... 45
2.7 Canopy geometry contributing to BRDF..... 50
2.8 Schematic representation of the turbid medium approximation..... 53
2.9 Geometry of an illuminated cone and its shadow..... 61
2.10 Geometry of spheroid-on-a-stick with shape controlling parameters..... 62
2.11 Angular variation of the Ross and Li kernels..... 75
2.12 Family of LiSparse GO kernels..... 75
2.13 Family of LiDense GO kernels..... 76

Chapter 3

3.1 AVHRR image, SPOT image and aerial photograph of field site..... 80
3.2 Wireframe representation of barley plant..... 83
3.3 Simulated wheat canopy in early growth stage..... 85

3.4 Simulated barley canopy (shortly prior to harvest)..... **85**
3.5 Geometry of ground radiometer measurements..... **86**
3.6 Measured and simulated canopy reflectance at four bands..... **87**
3.7 Scatter of BPMS against measured ρ_{canopy}, barley 13th May 1997..... **89**
3.8 Canopy cover photographs for barley canopy..... **90**
3.9 %cover estimated from photography and BPMS simulations..... **91**
3.10 Measured and modelled LAI for barley and wheat..... **92**
3.11 NERC ATM image over Barton Bendish, 2/8/97..... **94**

Chapter 4

4.1 Reflectance from vegetation and soil demonstrated..... **100**
4.2 Simulated images of measured barley and wheat canopies..... **103**
4.3 Viewing and illumination geometry and canopy extent for simulations..... **104**
4.4 Simulated barley reflectance, θ_v from -50^o to 0^o..... **105**
4.5 Variation with view zenith angle of BPMS-derived volumetric component of barley and wheat canopy reflectance for six dates..... **107-109**
4.6 Variation with view zenith angle of BPMS-derived GO component of barley and wheat canopy reflectance for six dates..... **110-112**
4.7 Proportional contribution of sunlit scene components to scene reflectance, for barley (four dates) and wheat (two dates)..... **114-116**
4.8 Cumulative LAD for four barley and two wheat canopies..... **117**
4.9 Examples of Bunnik's LAD function..... **119**
4.10 Correlation of measured LAD against Bunnik distributions..... **119**
4.11 Leaf projection function $G(\Omega)$ in viewing direction $\Omega(\theta_v, \phi_v)$..... **120**
4.12 Phase function, for $\theta_i = 0^o$..... **121**

Chapter 5

5.1 BPMS-derived volumetric parameter (α) against k_{vol}..... **129-131**
5.2 BPMS-derived GO parameter (β) against k_{GO} (LiDense)..... **132-134**
5.3 BPMS-derived GO parameter (β) against k_{GO} (LiSparse)..... **135-137**
5.4 Perspective view of barley plants from above..... **152**
5.5 Simulated 'spheroids on sticks' canopy..... **154**
5.6 Variation in sunlit leaf and soil, 24th June barley canopy, $\theta_i = 60^o$..... **159**

Chapter 6

6.1 Estimating model parameters f_{iso}, f_{vol} and f_{GO} from two directions..... **163**

6.2 ρ_{leaf} and ρ_{soil} spectra used in BPMS ρ_{canopy} simulations..... **164**

6.3 Comparison of f_{iso}, f_{vol} (RossThick) and f_{GO} (LiSparse) parameters derived from BPMS simulations and inversion of a full linear model..... **166-168**

6.4 Comparison of f_{iso}, f_{vol} (RossThin) and f_{GO} (LiDense) parameters derived from BPMS simulations and inversion of a full linear model..... **169-171**

6.5 Principal component analysis of the separate α and β components of ρ_{canopy} for barley (four dates) and wheat (two dates)..... **182-184**

6.6 Model parameters from 2 and 3 kernel inversions, 24th June barley..... **189**

6.7 Model parameters from 2 and 3 kernel inversions, 23rd April barley..... **190**

Chapter 7

7.1 Direct and diffuse scattering contributions to simulated ρ_{canopy} as a function of scattering order..... **200**

7.2 Examples of fresh, laboratory-measured vegetation reflectance spectra..... **203**

7.3 Examples of field-measured soil and vegetation reflectance spectra..... **203**

7.4 Price's first four basis functions of observed soil reflectance spectra..... **205**

7.5 First five vegetation spectral kernels derived from fresh and dry single scattered albedo..... **208**

7.6 Cumulative relative error of inversion of vegetation spectral kernels derived from fresh and dry reflectance and transmittance spectra, against all EPFS spectra. **211**

7.7 Cumulative relative error of inversion of vegetation spectral kernels derived from fresh single scattering albedo only, against all EPFS spectra..... **212**

7.8 Cumulative relative error of inversion of vegetation spectral kernels derived from fresh and dry single scattering albedo, against all EPFS spectra..... **212**

7.9 Relative error of inversion against EPFS reflectance spectra, 1 and 4 kernels.... **214**

7.10 Original and modelled lush and dry grass spectra, 1 and 4 kernels, NIR..... **216**

7.11 Measured against modelled grass reflectance, 1 - 5 vegetation kernels..... **217-218**

7.12 Residual error between measured and modelled lush and dry grass reflectance, one and four kernel cases..... **219**

7.13 Simulated ρ_{canopy}, LAI = 0.1..... **221**

7.14 Simulated ρ_{canopy}, LAI = 4..... **222**

7.15 Demonstration of spectral kernels' ability to reconstruct spectral reflectance

for two LAI cases, for two separate kernel combinations..... 224
7.16 Original against modelled reflectance, LAI = 0.1..... 226
7.17 Original against modelled reflectance, LAI = 4..... 226
7.18 Scatter plot of all view zenith angles and kernels combinations..... 227
7.19 Residuals from fitting spectral kernels to reflectance data..... 228
7.20 Soil and vegetation model parameters, LAI = 0.1..... 229
7.21 Soil and vegetation model parameters, LAI = 4..... 229
7.22 Scatter plot of soil components of ρ_{canopy}, two LAI cases..... 231
7.23 Scatter plot of vegetation components of ρ_{canopy}, two LAI cases..... 232
7.24 Reflectance generated from samples at selected MODIS wavebands..... 233
7.25 Scatter of reflectance generated at selected MODIS wavebands..... 234
7.26 Angular variation of inverted spectral kernel parameter values (s1v1 case)..... 235
7.27 Inversion of spectral kernels against airborne (ATM) data..... 237
7.28 Scatter of original against modelled radiance values (using spectral kernels) for random points within ATM image of figure **7.27**..... 238

Chapter 8

8.1 Simulated vegetation canopy..... 247

Appendix 2

A2.1 Proportional contribution of sunlit and shaded scene components to total scene reflectance, for barley (four dates) and wheat (two dates)..... 255-257

Tables

2.1 Values of r^2 for comparison of measured to modelled reflectances..... 68
3.1 Values of r^2 for comparison of measured to modelled reflectances..... 88
3.2 Values of LAI derived from BPMS canopies..... 93
4.1 Details of the canopies used in simulations..... 102
5.1 Slopes, intercepts and regression coefficients for volumetric kernels as a function of θ_i and ϕ_{row} (barley and wheat, six dates)..... 139-141
5.2 Slopes, intercepts and regression coefficients for the LiDense and LiSparse GO kernels as a function of θ_i and ϕ_{row}(barley and wheat, six dates)..... 146-148
5.3 Slopes, intercepts and regression coefficients for GC variants of GO kernels as a function of θ_i and ϕ_{row} (barley and wheat, six dates)..... 149-151

6.1 r^2 values for BPMS-derived against inverted values of f_{iso}, f_{vol} and f_{GO}..... **178**
7.1 First five eigenvalues of PCA of LOPEX fresh and dry single scattering albedo, and the corresponding percent variance..... **209**
7.2 RMSE of inversion of various kernel combinations against measured spectra... **213**
7.3 Comparison of RMSE to alternative estimates of model fit (k is kernels)..... **220**
7.4 RMSE of inversion of spectral kernels against reflectance data..... **225**

List of principal symbols

Each symbol is explained in the text when it is first introduced.

Symbol	Description
$A_{G,C,Z,T}$	Areal proportions of illuminated ground and crown, and shadowed ground and crown
α	Albedo
α	Volumetric component of canopy scattering
β	GO component of canopy scattering
C	Canopy clumping factor
E	Irradiance arriving at the surface
$F^{\downarrow}$	Downwelling (total) flux
$F^{\uparrow}$	Upwelling (total) flux
f_{iso}, f_{vol}, f_{GO}	Isotropic, volumetric and GO linear model parameters
$G(\Omega)$	Leaf projection function in viewing (or illumination) direction
$g_l(\Omega_l)$	Angular distribution of leaf normals
$\Gamma(\Omega' \rightarrow \Omega)$	Leaf scattering phase function
H	Sensible heat flux
$I^{\downarrow}$	Downwelling diffuse flux
$I^{\uparrow}$	Upwelling diffuse flux
k_{iso}, k_{vol}, k_{GO}	Isotropic, volumetric and GO linear model kernels
LE	Latent heat flux
L_c	Radiance exitant from the surface
$L\downarrow$	Downwelling radiance
$L\uparrow$	Upwelling radiance
λ	Wavelength
μ, μ'	Cosine of view, illumination zenith angles

$Q(\Omega' \rightarrow \Omega, z)$	Joint gap probability
$\Omega(\theta_v, \phi_v)$ or Ω	Viewing vector (solid angle)
$\Omega(\theta_i, \phi_i)$ or Ω'	Illumination vector (solid angle)
R_n	Net radiation
ρ	Reflectance
$\bar{\rho}(\lambda, \mathbf{\Omega}, \mathbf{\Omega}')$	Spectral directional hemispherical reflectance
$\bar{\bar{\rho}}(\lambda)$	Spectral bihemispherical reflectance
σ_c	Extinction coefficient of the canopy medium
σ_s	Differential scattering coefficient of canopy medium
τ	Transmittance (in canopy) or optical depth (in atmosphere)
θ_i, ϕ_i	Illumination zenith and azimuth angles
θ_v, ϕ_v	View zenith and azimuth angles
w	Weighting value
ω	Single scattering albedo
ξ	Phase angle of scattering
Z_o	Surface roughness length
z	Depth/height within canopy

Acronyms/abbreviations

Each acronym/abbreviation is explained in the text when it is first introduced.

Acronym	Definition
ADEOS	Advanced Earth Observing System
AERONET	Aerosol Robotic Network
AIC	Akaike information criteria
AMBRALS	Algorithm for MODIS bidirectional reflectance and albedo
ANN	Artificial neural network
ARARAT	Advanced Radiometric Ray Tracer
ARS	Airborne Research System
ASAS	Advanced Solid state Array Spectrometer
ASTER	Advanced Spaceborne and Thermal Emission and Reflection Radiometer
ATM	Airborne Thematic Mapper

ATSR	Along Track Scanning Radiometer
AVHRR	Advanced Very High Resolution Radiometer
BPMS	Botanical Plant Modelling System
BRDF	Bidirectional reflectance distribution function
CASI	Compact Airborne Spectrographic Imager
CERES	Clouds and Earth's Radiant Energy System
CHRIS	Compact High Resolution Imaging Spectrometer
CR	Canopy reflectance
CSAR	Coupled Surface-Atmosphere Reflectance
DART	Discrete Anisotropic Radiative Transfer
DEM	Digital elevation model
EGO	European Goniometric Observatory
ENVISAT	Environmental Satellite
EO	Earth observation
EOS	Earth Observing System
EPFS	Equipment Pool for Field Spectroscopy
ERS	European Remote Sensing Satellite
fAPAR	Fraction of absorbed photosynthetic radiation
FCC	False colour composite
GA	Genetic algorithm
GARP	Global Atmospheric Research Program
GCM	General/global circulation model
GO	Geometric optic
IFB	International Forum on BRDF
IFOV	Instantaneous field of view
IGBP	International Geosphere Biosphere Program
IPCC	International Panel on Climate Change
IWMMM	International Workshop on Multiangle Modelling Methods
IR (NIR)	Infrared (near IR)
ISLSCP	International Satellite Land Surface Climatology Project
JRC	Joint Research Centre
KBS	Knowledge-based system
LAI	Leaf area index
LAD	Leaf angle distribution
LiDAR	Light detection and ranging

LOPEX	Leaf Optical Properties Experiment
LSP	Land surface process
LUT	Look-up table
MISR	Multi-angle Imaging Spectro-Radiometer
MODIS	Moderate Resolution Imaging Spectroradiometer
MOPITT	Measurement of Pollution in The Troposphere
MSG	METEOSAT Second Generation
MTPE	Mission To Planet Earth
MVA	Multiple view angle
MVC	Maximum value composite
NASA	National Aeronautical and Space Agency
NDVI	Normalised difference vegetation index
NERC	Natural Environment Research Council
NOAA	National Oceanic and Atmospheric Administration
NPOESS	National Polar Orbiting Environmental Satellite System
NPP	Net primary productivity
PCA	Principal component analysis
POLDER	Polarisation and Directionality of the Earth's Surface
PROBA	Project for On Board Autonomy
PSN	(daily) net photosynthesis
RADAR	Radio detection and ranging
RAMI	Radiative Transfer Model Intercomparison
RMSE	Root mean square error
RPV	Rahman-Pinty-Verstraete
RT	Radiative transfer
SAIL	Scattering by arbitrarily inclined leaves
SOSA	Successive orders of scattering approximation
SPOT	Systeme Probatoire d'Observation de la Terra
SVAT	Soil-vegetation-atmosphere transfer
SW	Shortwave
TOA	Top-of-atmosphere
TIR	Thermal infrared
TM	Thematic mapper
UNFCC	United Nations Framework Convention on Climate Change

1 Introduction

1.1 Change and uncertainty in global climate

The development of remote sensing as a tool for better understanding the dynamics of biogeochemical processes controlling the Earth's climate has been driven by a growing recognition of the need to determine human impact on the global environment (Global Atmospheric Research Program (GARP) report, 1975; Henderson-Sellers and Wilson, 1983; Sellers, 1994; Trenberth, 1995; Hall *et al.*, 1995). This need has been exacerbated by the apparent increase in extreme climatic events of recent years such as the unusually long-lived and severe El Niño event of 1997-8, the subsequent droughts and fires in South East Asia and flooding in Central America in the latter part of 1998 (Webster and Curry, 1998). Such potentially catastrophic climate events have impacted virtually all aspects of human life around the globe: from minor regional climatic and ecosystem variability to life-threatening fires; the threat of sea-level rise inundating low-lying coastal regions (Schneider, 1999), to more indirect manifestations such as the instability of global economic and political conditions.

It is widely accepted that the increase in frequency of extreme climate events is related to changes in the overall global climate, and in particular, a gradual increase in global mean temperature over the past century (Intergovernmental Panel on Climate Change (IPCC), 1995a,b, 2001a,b, www[1.1]; International Geosphere Biosphere Program (IGBP), 1998). It is mooted that such changes may be the result of (or be exacerbated by) anthropogenic activities such as the burning of fossil fuels, intensified agriculture and urban development, amongst other activities (IPCC, 2001b; www[1.2]). Scientific uncertainty over the projected impact of anthropogenic impacts on global climate has also led to international political conflict, most notably over the US government's refusal to ratify the United Nations Framework Convention on Climate Change (UNFCCC) 'Kyoto protocol' on planned reductions in CO_2 (www[1.3]). Uncertainty over cause and effect has polarised the scientific community in some respects (Musser, 2001) and a great deal of effort is now being expended to quantify this uncertainty (Visser *et al.*, 2000; Wigley and Raper, 2001). Long term climate monitoring of global climate processes has been identified as key to this task. Other aspects of global change and the impact of human activity have raised more general issues, such as how best to sustainably exploit natural resources, how to monitor and/or prevent reductions in biodiversity and how to predict and adapt to potential changes in climate (www[1.4]). As

a result, many governments recognise the necessity of investing heavily in research aimed at developing a better understanding of both the underlying mechanisms and the actions of global climatic processes (Sellers, 1992).

The drive towards a better understanding of climate processes is exemplified by recent efforts such as NASA's Earth Observing System (EOS) (formerly the Mission To Planet Earth (MTPE)). EOS is an ongoing series of experiments, instruments and projects, the stated aim of which is *"...is to develop understanding of the total Earth system, and the effects of natural and human-induced changes on the global environment"* (EOS press release, January 1998). As an indication of the seriousness with which such aims are being pursued, EOS was allocated a budget of $1.42 billion in the 1998 Congressional spending projections (*ibid.*). Other projects with similar aims are the Japanese Advanced Earth Observing System (ADEOS), with instruments such as POLDER (Polarisation and Directionality of the Earth's Surface) on board, designed to measure land surface reflectance, polarisation, and atmospheric aerosol distributions (Deschamps *et al.*, 1994; Leroy *et al.*, 1996), and the next generation meteorological observation programme NPOESS (National Polar Orbiting Environmental Satellite System, www[1.5]).

In conjunction with developments in climate modelling such as rapid advances in computing speed and efficiency and sophistication of algorithms (Hack, 1995), Earth Observation (EO) has emerged as one of the most powerful tools for improving our understanding of the surface processes controlling global climate. Such processes operate over a huge range of spatial and temporal scales – from local and regional weather variations, to long-term warming and cooling trends of global climate. In order to detect perturbations in the global climate system (such as might be caused by anthropogenic increases in greenhouse gases like CO_2) methods of monitoring large (even global) areas over long time-scales are required (Charlson *et al.*, 1992). The spatial coverage afforded by EO makes it particularly suited to such a task. Long-term temporal coverage will require successive generations of EO programmes. This has led to the inception of major international interdisciplinary projects such as the International Satellite Land Surface Climatology Project (ISLSCP) (Sellers, 1994), which aim to exploit the potential for timely, large-scale coverage offered by remotely sensed data (Sellers, 1992; IPCC 2001a,b).

1.2 Developments in Earth Observation

"[To] expand the observational foundation for climate studies to provide accurate, long-term data with expanded temporal and spatial coverage.... there is a need for long-term consistent data to support climate and environmental change investigations and projections."

Part of conclusion of IPCC Working Group I, 2001 (IPCC, 2001a).

A great deal of progress has been made in EO over the last thirty years. This has been driven largely by the realisation that the observation of global climate processes requires the type of spatial and temporal coverage only afforded by remote sensing. The current sophisticated, versatile and multi-purpose payloads exemplified by the NASA EOS programme (Running *et al.*, 1994; Kaufman *et al.*, 1998) represent a significant advance from the days of Landsat 1, a crude multispectral radiometer launched in 1972. A great deal of money and effort has been invested in developing remote sensing instruments to probe all aspects of global climate. This encompasses a wide range of processes including: the role of atmospheric aerosols and clouds in climate change (Charlson *et al.*, 1992; Arking, 1991); ocean circulation and exchanges of latent and sensible heat with the atmosphere (Hsiung, 1985; Randall *et al.*, 1992); carbon budget calculations (Schimel, 1995; IGBP, 1998; Wessman and Asner, 1998); biosphere-atmosphere transfer (Sellers *et al.*, 1995); the influence of the cryosphere (Nolin and Stroeve, 1997); and absorption (and reflection/re-radiation) of incoming solar radiation at the Earth's surface (Henderson-Sellers and Wilson, 1983; Dickinson, 1983, 1995).

The major obstacle to achieving more complete understanding of global climate processes has been identifying very gradual underlying long-term trends in global climate indicators beneath the highly variable short-term fluctuations of day-to-day weather patterns. The need for long-term, global data sets has led to an increased interest in the design and development of remote sensing platforms and methods specifically targeted at observing the Earth's climatic processes. The NASA EOS program, with a number of planned missions, each carrying several complementary instruments, exemplifies the move towards a more comprehensive understanding of global climate processes through long-term integrated monitoring[1].

The EOS program is designed to monitor the interchanges of energy, moisture and carbon, land use, and ocean and atmospheric circulation for at least eighteen years. The EOS era began with the launch of the EOS-AM1 (*Terra*) platform in December 1999 (Kaufman *et al.*, 1998. www[1.6]). The follow-up platform, EOS-PM1 (*Aqua*), designed to monitor hydrosphere and cryosphere processes, is due to be launched in 2002. To illustrate the comprehensive nature of EOS, the various instruments aboard the *Terra* platform are listed below:

- ASTER (Advanced Spaceborne and Thermal Emission and Reflection Radiometer) for monitoring local and regional processes such as surface temperature, energy balance and mapping of soils, geology and land cover change (Yamaguchi *et al.*, 1998);

- CERES (Clouds and Earth's Radiant Energy System) to determine the radiative forcing effect of Earth's cloud cover and quantify the radiative budget (Wielicki *et al.*, 1998);

- MISR (Multi-angle Imaging Spectro-Radiometer) a pointable instrument with nine look angles designed to observe the angular variations of scattering from the surface, atmospheric aerosols and clouds (Diner *et al.*, 1998);

- MODIS (Moderate resolution Imaging Spectrometer) to provide comprehensive monitoring of land, ocean and atmosphere at moderate resolution, with high temporal coverage and capabilities to provide global estimates of land cover characteristics such as albedo (Justice *et al.*, 1998).

- MOPITT (Measurement of Pollution in The Troposphere) for mapping atmospheric CO and CH_4 (Gilles *et al.*, 1996).

Early results from Terra have already provided a remarkable look at the Earth's climate processes and scientists are beginning to apply the data to some of the unanswered questions. Figure **1.1** is an example of reflectance data now being delivered by MODIS. This is one of 44 separate products delivered by MODIS now in their

[1] NASA is currently shifting the emphasis of future EO missions toward the 'smaller, faster, cheaper' model in order to reduce mission lead-in times and potential losses from failed missions.

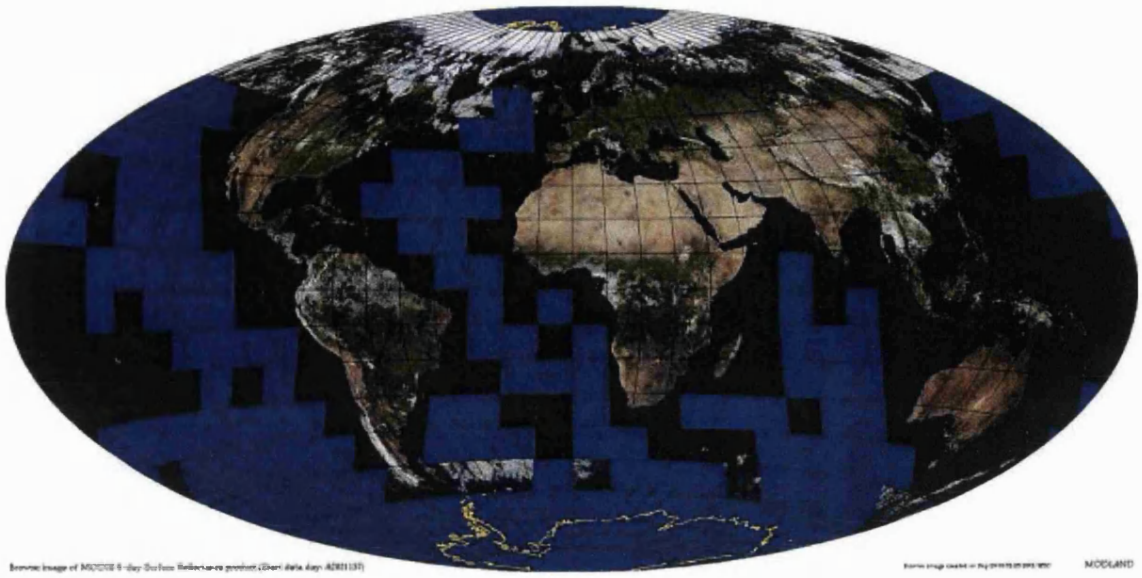

Figure 1.1 MODIS 16 day reflectance image (period ending 17th May, 2001). Bands 1, 4 and 3 (620-640nm, 545-565nm, 459-479nm).

advanced quality assurance phase before dissemination to the scientific community. These products represent a great improvement over data from sensors such as the National Oceanic and Atmospheric Administration (NOAA) Advanced Very High Resolution Radiometer (AVHRR). Greatly improved sensor technology and calibration combined with sophisticated processing have resulted in products usable by the wider community rather than just raw radiance data or simple empirical indices. The variety of long-term data from EOS, in conjunction with the Japanese Advanced Earth Observing System mission (www[1.7]) and European missions such as the Environmental Satellite (ENVISAT) (www[1.8]) and the European Remote Sensing satellites ERS-1 and 2 (www[1.9]), will enable a clearer understanding of the complex processes controlling Earth's climate to be established. Data from a variety of such remote sensing platforms can also be combined to provide a synergistic view of the Earth's climate processes.

1.3 Land surface processes

Land surfaces are particularly important in considering climate variability as they provide a lower boundary layer to the climate system (Dickinson, 1983; Graetz, 1991; Sellers, 1992; Dickinson, 1995). Ocean surfaces are generally more important in terms of the magnitude and mobility of stored heat energy but land surfaces tend to be far more spatially variable. As a result, land surface processes such as exchanges of moisture from the surface to the atmosphere, and reflection, absorption and re-radiation of incoming

solar radiation are far less spatially and temporally predictable than their ocean surface equivalents. Another major consideration is that human existence is almost exclusively dependent on the state of the land surface.

Earth observation has been deployed in many ways to improve understanding of land surface processes either by directly observing processes where possible or, in most cases, utilising observations made of surrogate (dependent) variables. One area where this is extremely important and of direct relevance to this thesis is the observation of surface biophysical parameters. Parameters such as total biomass, the fraction of absorbed photosynthetic radiation (fAPAR), transpiration rates, surface roughness (Z_o), and albedo provide linkages between biogeochemical processes such as nutrient availability, soil composition and the transfer of carbon and climatic drivers such as the fluxes of moisture and energy at the surface. These linkages take the form of near-surface atmospheric forcing, which in turn results in exchanges of water, radiation, and momentum between the surface and atmosphere (Sellers, 1995a). Consequently, much effort has been devoted to measuring and modelling land surface processes and their controlling biophysical parameters (Hall *et al.*, 1995; Sellers, 1995b; Sellers *et al.*, 1997).

1.3.1 Biophysical parameters and vegetation

In considering biophysical processes for inclusion into climate models, models of land surface processes (LSPs) have been developed (Dickinson, 1984; Sellers *et. al*, 1986; Henderson-Sellers *et al.*, 1993). A wide range of surface types (vegetation, ice/snow, desert) are considered when modelling land surface processes, each having their own regions of influence and importance. Vegetation is recognised as one of the most important cover types, both in terms of the linkage between biogeochemical processes and atmospheric circulation but also in terms of impact on human beings (Aber, 1995). For obvious reasons humans tend to favour vegetated areas over desert or snow and ice covered ones. In addition, processes controlling vegetation growth and development tend to have time-scales allowing them to strongly influence the atmospheric climate processes to which they link. For example, leaf-scale chemical processes such as photosynthesis have time-scales of a few seconds or less; evapotranspiration, CO_2, N_2 and nutrient fluxes vary over time-scales of days to weeks. These scales are similar to those over which

atmospheric energy transport processes such as turbulence, convection and radiation may act (Sellers, 1995a).

Vegetation is also an important factor in mediating interactions between the biogeophysical system and atmospheric circulation processes through the biophysical parameters mentioned above, such as fAPAR, Z_o and albedo[2]. An example of the influence of vegetation and the potential feedback on these surface-atmosphere interactions is illustrated in figure **1.2**. This is the feedback cycle for surface roughness under hypothetical conditions of deforestation and/or desertification. Figure **1.2** emphasises that the energy exchanges between the surface and the atmosphere are heavily influenced by the quantity and activity of surface vegetation.

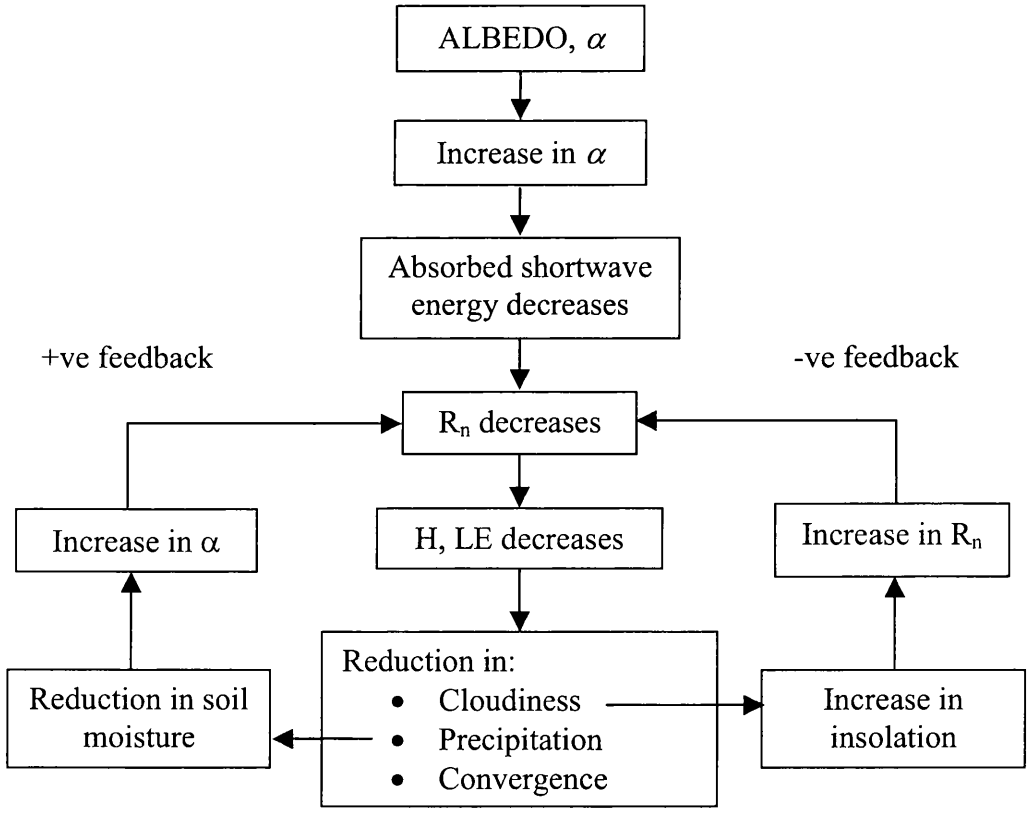

Figure 1.2 Potential positive and negative feedback loops resulting from large-scale change of surface albedo, α. R_n = net radiation, Wm^{-2}; H = sensible heat flux (conduction to the air) Wm^{-2}; LE = latent heat flux (through evaporation of moisture to the air) Wm^{-2} (after Sellers, 1995).

[2] Albedo is not an intrinsic surface parameter due to its relationship with atmospheric state (see later).

The driver of all climate processes is incoming solar radiation. Consequently, understanding the fate of solar radiation arriving at the Earth's surface (through reflectance, absorption and/or re-radiation) is the key to understanding many of the major global climate processes. This thesis will concentrate on developments in measurement and modelling of incoming shortwave solar radiation interacting with vegetation. The emphasis is on shortwave radiation i.e. wavelengths from around 350nm up to 2500nm, as the vast majority of the radiant energy emitted from the sun lies in this wavelength range. Figure **1.3** shows the variation of incoming solar radiation with wavelength, in addition to the theoretical blackbody curve for a body at 5900° K (solar surface temperature). The energy distribution is sharply peaked around 0.55μm, which has driven the evolution of chlorophyll pigments in green vegetation which efficiently facilitate the conversion of incoming solar radiation into carbohydrates used in plant growth.

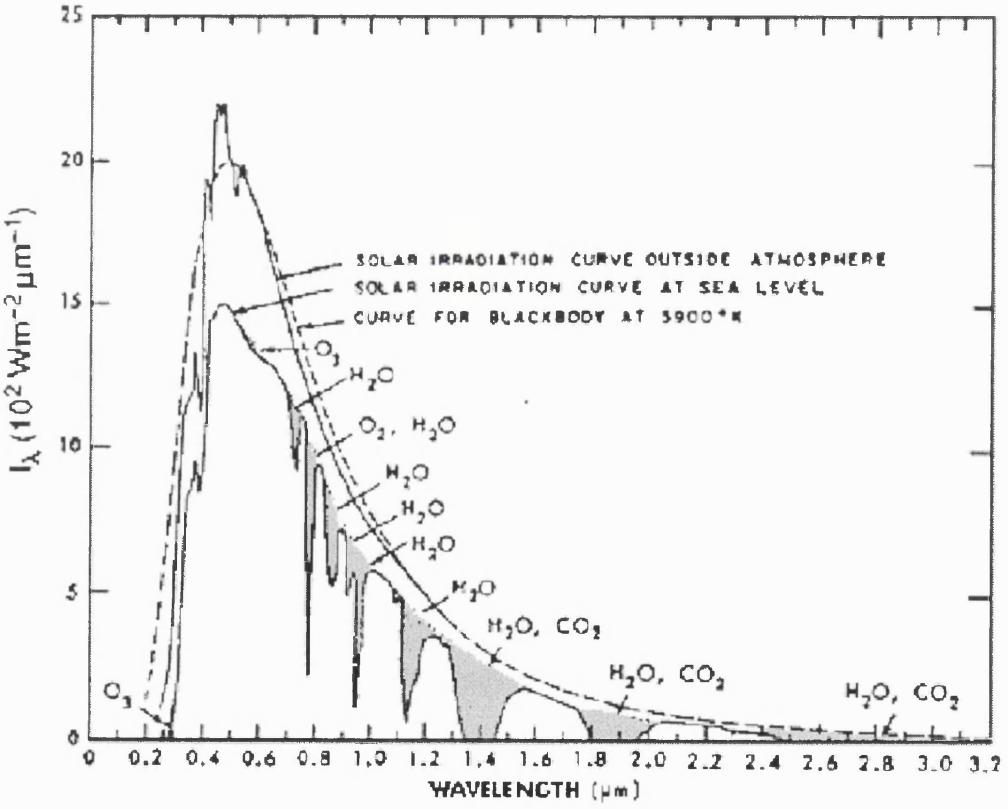

Figure 1.3 Solar irradiance at the top and bottom of the earth's atmosphere. Shaded areas indicate absorption by atmospheric gases (after Slater, 1980).

1.3.2 Shortwave energy budget and albedo

Remote sensing techniques have been applied in a number of areas in an effort to understand the processes affecting the Earth's climate. One of the most important of these applications is that of shortwave energy budget studies: the study of the reflection and absorption of incoming shortwave (SW) i.e. visible and near-infrared (near IR, or NIR) solar radiation at the Earth's surface, and its subsequent re-radiation into the atmosphere as thermal IR radiation. The role of surface reflectance in the Earth's radiation budget is illustrated schematically in figure **1.4**. This demonstrates general mechanisms of solar interaction with the atmosphere and land surface.

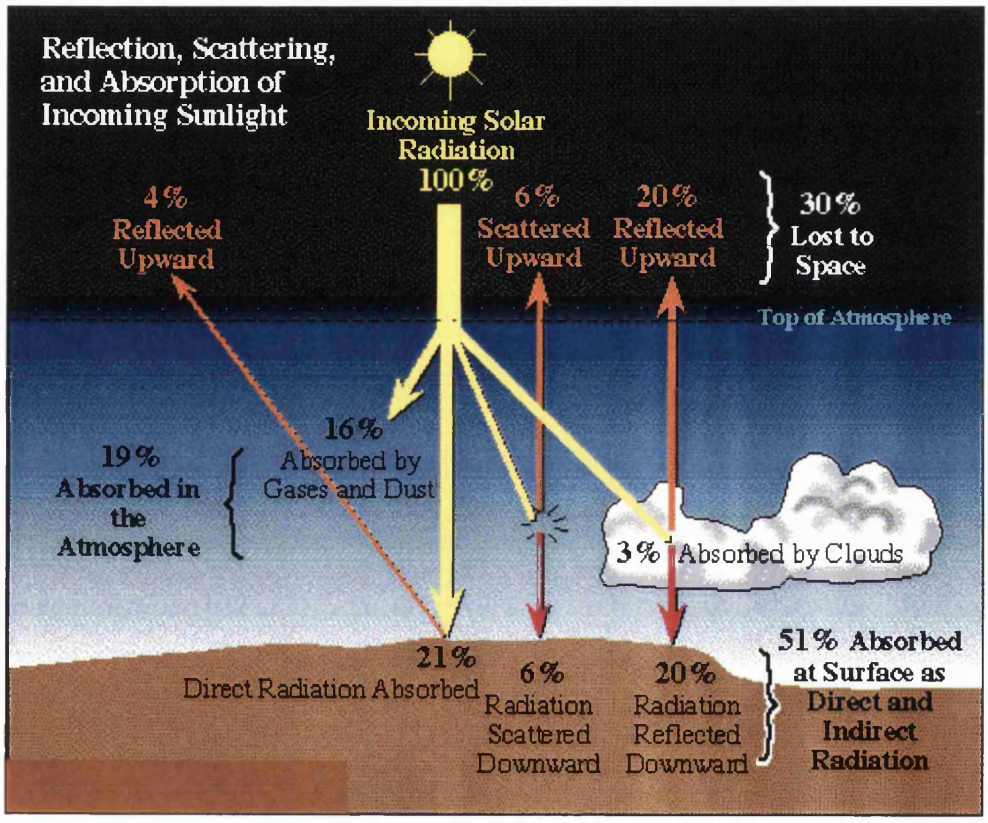

Figure 1.4 The fate of incoming solar radiation at the Earth's surface (from www[1.10]).

The absorption of solar energy at the Earth's surface is the primary driving force behind all climatic processes (Dickinson, 1983). The amount of energy absorbed at the surface is determined by the surface **albedo**. Albedo (α) is defined as the ratio between the hemispherical upwelling and downwelling fluxes ($F^{\uparrow}$ and $F^{\downarrow}$) at a point (Wanner *et al.*, 1997) i.e.

$$\alpha = \frac{F^{\uparrow}}{F^{\downarrow}} \qquad \textbf{1.1}$$

Albedo is a unitless quantity lying between 0 (all incoming energy absorbed) and 1 (all incoming energy reflected), and is often expressed as a percentage. Albedo is a measure of how much of the radiation incident on a surface is reflected back into the atmosphere, and consequently, how much is absorbed by the surface. If incoming solar radiation is the energy source driving all climate processes, to understand the mechanics of global climate more accurately it is vital to be able to determine the albedo of the Earth's surface as precisely as possible (Henderson-Sellers and Wilson, 1983; Mintz, 1984; Dickinson *et al.*, 1990). Figure **1.5** is a schematic representation of the relationships driven by incoming solar radiation, which illustrates the difficulty of this task. The presence or absence of surface vegetation and cloud cover, along with atmospheric composition, are some of the critical factors affecting the rate of incoming solar radiation and emitted longwave radiation.

A wide variety of sophisticated numerical models have been developed to represent the circulation and transport processes occurring within the global climate system. Due to the importance of albedo in determining the amount of energy absorbed at the lower boundary of the atmosphere it is desirable that it should be represented as accurately as possible within any general/global circulation model (GCM) (Hall *et al.*, 1995). Henderson-Sellers and Wilson (1983) provide a detailed review of the major GCMs in operation at the time and list the variety of different representations of albedo that are used within these models. Their conclusion is that subsequent differences between model climatologies (predicted climate outcomes based on a fixed set of starting parameters) are quite likely due to the differences in albedo. In order to remove these uncertainties, studies to obtain global albedo estimates with an accuracy of $\pm$ 5% should be initiated immediately. Henderson-Sellers and Wilson (1983) also point out that the requirement for accurate estimates of surface albedo is not a new phenomenon even in 1983, citing the GARP Joint Organizing Committee report (1975) which concludes that "there is an increasing need for reliable data concerning surface albedo". More recently, Dickinson (1995) and Bengtsson (1995) have highlighted the continuing requirement for accurate estimates of albedo for climate models.

If there have been such demands for estimates of albedo, why have they not been met? Henderson-Sellers and Wilson (1983) list a number of the difficulties involved in generating coherent global albedo data sets:

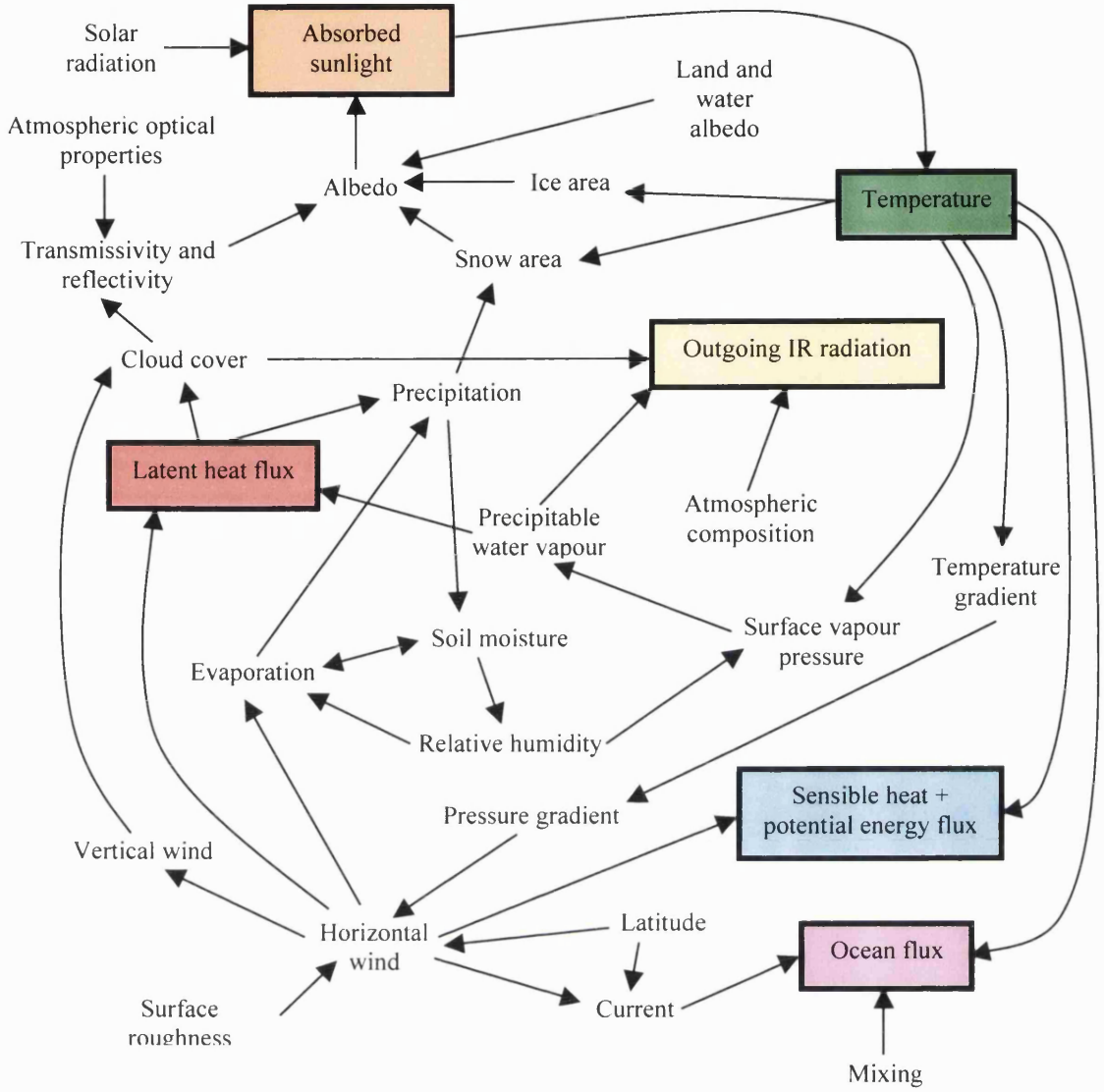

Figure 1.5 An illustration of some of the complex interactions between incoming electromagnetic radiation, the surface and the atmosphere (after Smith, 1985).

- Spectral variation of albedo (depending on the physical structure and chemical composition of the surface).
- Angular variations of albedo leading to differences in direct and diffuse albedo. Measured albedo is assumed to lie between the two extreme cases, i) purely directional illumination conditions i.e. assuming no diffuse component of illumination (clear- or black-sky albedo), and ii) purely diffuse illumination (white-sky albedo). Consequently albedo is estimated as a function of the proportions of direct and diffuse illumination.
- Increased estimates of clear- or black-sky albedo due to a scattering atmosphere.

- Heterogeneity of the surface at various scales.
- Non-linearity of surface albedo in terms of spatial scale, necessitating generation of albedo at the correct scale for the application required (spatial interpolation and averaging are not generally appropriate).

These factors (and a number of others) combine to make albedo a very difficult parameter to determine accurately. It is still the case, however, as has been widely recognised, that satellite observations provide perhaps the best opportunity to compile global estimates of surface albedo (Henderson-Sellers and Wilson, 1983; Kimes and Sellers, 1985; Brest and Goward, 1987, Wanner *et al.*, 1997).

1.3.3 Albedo and surface scattering

Albedo describes the ratio of upwelling to downwelling fluxes, $F^{\uparrow}$ and $F^{\downarrow}$, as expressed in equation **1.1**. More exactly, albedo is defined as follows:

$$\alpha(\lambda) = \frac{\int_0^{2\pi}\int_0^{\pi/2} L_{\uparrow}(\theta_v, \phi_v, \lambda)\sin\theta_v \cos\theta_v d\theta_v d\phi_v}{\int_0^{2\pi}\int_0^{\pi/2} L_{\downarrow}(\theta_i, \phi_i, \lambda)\sin\theta_i \cos\theta_i d\theta_i d\phi_i} \qquad \textbf{1.2}$$

$L\downarrow(\theta_i, \phi_i, \lambda)$ is the downwelling radiance in the illumination (solar) direction (solar zenith angle θ_i and azimuth angle ϕ_i), at wavelength λ. $L\uparrow(\theta_v, \phi_v, \lambda)$ is the upwelling radiance from the surface in the viewing direction (view zenith angle θ_v and azimuth angle ϕ_v) at wavelength λ. $L\uparrow$ is of course also dependent on surface reflectance. Because $L\uparrow$ is a function of the angular distribution of downwelling irradiance, $\alpha(\lambda)$ is a function of atmospheric state and will be affected by things such as water vapour concentration and aerosol loading. Albedo should therefore not be considered an intrinsic surface property and cannot be measured directly via remote sensing. What is required for climate modelling purpose is some average, integrated hemispherical value of albedo that is independent of the atmospheric state, and is an intrinsic surface property (Wanner *et al.*, 1997).

In order to produce such a parameter from remotely sensed data, a detailed understanding of the mechanisms determining the radiance (total incident energy) measured at the instrument is needed. This in turn requires knowledge of how the radiation incident on a surface is absorbed and scattered by that surface (ignoring for the

moment any intervening atmosphere between the surface and the sensor). More specifically, some kind of mathematical model of the surface scattering behaviour is required. If such a model can be formulated it may be possible to use the model to interpret remotely sensed observations of the surface radiance. The increasing variety and availability of remotely sensed data has driven a corresponding increase in the development of models of surface reflectance for a wide variety of applications (Goel, 1988; Asrar, 1989; Myneni *et al.*, 1989; Hall *et al.*, 1995; Arking *et al.*, 1998; Knyazikhin *et al.*, 1998a,b; Martonchik *et al.*, 1998a,b). This thesis is concerned with one specific type of surface scattering model, developed primarily for examining predominantly vegetated land surface types.

1.3.4 Surface scattering and vegetation

One of the most important absorbing/scattering land surface types is that covered by vegetation (Dickinson, 1983; Mintz, 1984; Goel, 1988). Vegetated areas of one sort or another, from arable grazing land to tropical rainforest, cover between 50% and 70% of the Earth's land surface (Dickinson, 1983). Moreover, vegetation plays an extremely important role in global climate (Otterman, 1985; Sellers, 1989; Graetz, 1991). It provides a primary mechanism for the exchange of oxygen and carbon dioxide in the atmosphere (Schimel, 1995), regulates the transport of moisture (Shukla and Mintz, 1982) and absorbs large amounts of solar radiation for use in photosynthetic activity which may then be re-radiated into the atmosphere at a range of wavelengths. It has been shown that the time integral of photosynthetically active radiation (PAR) absorbed by vegetation canopies can be related to net primary productivity (NPP), an indicator of vegetation health, age and biomass (Steven *et al.*, 1983; Asrar *et al.*, 1984). NPP is primarily a measure of carbon uptake: it is the quantity of carbon fixed within vegetation (per unit area per unit time, $gCm^{-2}yr^{-1}$) as a net result of the transpiration minus respiration (carbon released) and photosynthesis (carbon absorbed) (Running *et al.*, 1996). NPP has implications for global climate in terms of atmospheric CO_2 variations (IGBP, 1998). In addition to understanding the biophysical impacts of vegetation cover on the Earth's climate, the need to monitor and develop global agriculture has provided massive economic impetus to the development of remote sensing techniques for studying vegetation. For these reasons much emphasis has been placed on attempting to understand how vegetation can be identified and monitored from remote sensing measurements. One

of the primary ways in which this has been achieved has been the development and refinement of techniques for modelling canopy reflectance (ρ_{canopy}) (Goel, 1989; Privette *et al.*, 1997).

If it is possible to compute the radiant energy distribution within a vegetation canopy using a model of ρ_{canopy} behaviour then a number of aims may be achieved. It may be possible to compute canopy photosynthetic rates from leaf surface projected irradiances. Hence ρ_{canopy} (the exitant, measurable response of the canopy to an incident irradiance) may be calculated. This then describes the signal available for measurement from a remote sensing instrument. Models of ρ_{canopy} may also be inverted against remotely measured ρ_{canopy} data to enable the estimation of canopy phytometric attributes and the computation of absorbed energy (Goel and Strebel, 1983; Goel, 1989; Kustas, 1989; Sellers, 1989; Hall *et al.*, 1995). Research into remote sensing of vegetation has long aimed to derive accurate spatial estimates of important vegetation canopy parameters such as leaf area index (LAI)[3], leaf angle distribution (LAD)[4] and fAPAR from observed ρ_{canopy} data.

Figure **1.6** illustrates some of the main processes governing radiation transport within a vegetation canopy. These processes must be described accurately in order to model ρ_{canopy} behaviour. Expressions relating $I^{\uparrow}$ and $I^{\downarrow}$ in figure **1.6** (upward and downward diffuse radiative fluxes, normalised by incident flux) to observed reflectance can be derived (Ross, 1975). These expressions are based on approximations and assumptions regarding canopy structural properties (3D arrangement of scattering elements within the canopy), LAI, LAD and cumulative leaf area, as well as radiometric properties (leaf reflectance, ρ_{leaf}, and transmittance, τ_{leaf}). Canopy reflectance modelling methods are discussed in more detail in chapter **2**.

[3] LAI is defined as the single sided leaf area of canopy per unit ground area (m^2 per m^2).

[4] LAD is a function describing the distribution of leaf zenith angles within the canopy.

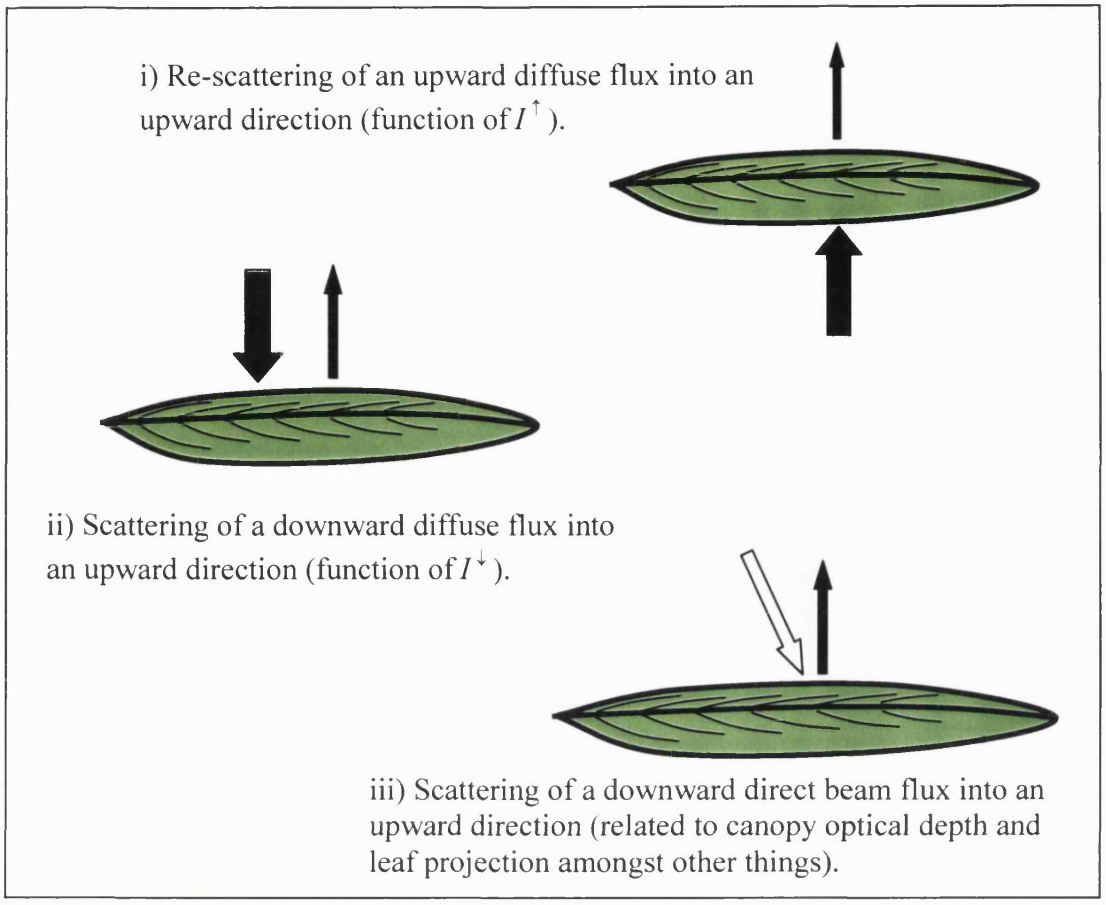

Figure 1.6 Schematic representation of radiation transport processes within a vegetation canopy (after Sellers, 1989) relating up- and downward diffuse fluxes within the canopy, $I^{\uparrow}$ and $I^{\downarrow}$.

1.4 Surface reflectance anisotropy

"Research over the past 15 years has conclusively established that the Earth's surface is non-Lambertian, and any future analyses, excepting perhaps the most simple and crude of approximations, cannot legitimately assume Lambertian properties. Reflectance anisotropy is significant."

Conclusion drawn by Diane E. Wickland (Manager, NASA Terrestrial Ecology Programme) following NASA workshop on multiangular remote sensing for environmental applications, Jan. 29-31 1997, Univ. Maryland, (in Privette *et al.*, 1997).

It has long been known that natural surfaces do not in general reflect incident radiation equally in all directions but instead tend to display varying degrees of anisotropy (Minnaert, 1941; Nicodemus *et al.*, 1977; Hapke, 1981). As mentioned previously, surface reflectance is not only a function of the spectral and spatial properties of the incident radiation and target respectively, but also of the direction from which the surface is illuminated and viewed (Ross, 1981; Goel, 1988; Privette *et al.*, 1997). The reflectance anisotropy of a surface is determined by two principal factors. Firstly, the intrinsic directionality of the spectral reflectance, transmittance and absorptance of the scattering material. Secondly, anisotropy is a function of surface roughness, or structure. The latter property is determined by the density and arrangement of objects on a surface and hence the nature of the shadowing caused by these objects as a function of illumination and observation angles (Torrance and Sparrow, 1966; Otterman and Weiss, 1982; Li and Strahler, 1986, 1992; Roujean *et al.*, 1992). Surface structure will tend to cause incident radiation to be reflected more strongly in some directions than others. This dependence of surface reflectance on viewing and illumination geometry is described by the Bidirectional Reflectance Distribution Function (BRDF). Knowledge of the surface BRDF can therefore potentially be exploited to provide information regarding the structure of the scattering surface. Clearly, knowledge of surface reflectance is also vital in order to calculate albedo, which is intimately related to BRDF. This thesis investigates models of surface reflectance which have been developed recently in response to the need for accurate characterisation of surface reflectance at global scales.

It is clear that the anisotropic nature of the Earth's surface will have an effect on the reflectance observed from a remote sensing platform and such effects can derive from a variety of sources. Sensors possessing wide viewing swaths, such as AVHRR and MODIS, have large variations in view angle across recorded scenes (Cihlar *et al.*, 1994; Leroy and Roujean, 1994). The same is true of sensors with along-track scanning or off-nadir pointing capabilities such as MISR, and the Along Track Scanning Radiometer instruments (ATSR and ATSR-2). Variations in the solar zenith (illumination) angle over a point on the Earth's surface will also tend to have the same effect as varying the viewing zenith angle. This occurs if a particular point is imaged at different times of day or at the same time of day throughout the year. The anisotropy of surface reflectance makes direct comparisons between such data impossible. Apparent observed changes in the nature of the surface may in fact be caused purely by variations in viewing and illumination conditions from one image to another. As the availability of time-series of

reflectance data has increased, variations caused by inconsistent viewing and illumination angles has come to be recognised as a serious problem (Leroy and Roujean, 1994; Cihlar *et al.*, 1994).

Problems may also arise within individual scenes. Land surface process and climate modelling requirements have directed many new sensors towards global coverage at lower spatial resolution (of the order of km per pixel), and away from the high resolution observations of limited spatial coverage that have been the norm (10s of m per pixel). This is necessary in order to keep the quantities of data produced manageable. The wide swaths of such sensors such as AVHRR, MODIS and POLDER mean that there may be large variations in view angle across any single swath. MODIS for example has a swath width of approximately 2330km, with a consequent variation in view zenith of around 110° from one side to the other. So there are likely to be directional effects in observed reflectance within MODIS data simply because the viewing zenith angle varies from 0° at nadir to nearly 55° at either edge of the image. The orbital characteristics of the sensor also mean that on repeated orbits a particular point on the surface will be observed at a wide range of viewing (and illumination) angles.

Directional effects in EO data were typically ignored until relatively recently. This is exemplified by the widespread use of AVHRR maximum-value composite (MVC) products (Holben, 1985). It is now recognised that in order to make comparisons of measured surface reflectance across or between scenes, then directional effects must be accounted for (Roujean *et al.*, 1992; Wu *et al.* 1994; Privette *et al.*, 1997). In examining changes in cover type for example, comparisons must be made between data that may be separated in time by many months, and which may have been measured at significantly different viewing and illumination angles (Cihlar *et al.*, 1994). In addition to the effects mentioned above, which are often considered as obstacles to be overcome (e.g. Roujean *et al.*, 1992; Leroy and Roujean, 1994), the directional nature of surface reflectance can also be exploited. The directional dependence of the surface reflectance on its structural properties implies that observations of the directional component of reflectance will contain information relating to these properties (Goel and Strebel, 1983; Goel, 1988; Goel and Reynolds, 1989; Myneni *et al.*, 1989). It may be possible to relate variations in observations at different viewing and illumination angles to the surface features causing these variations (Asrar, 1989; Pinty and Verstraete, 1991; Myneni *et al.*, 1995).

Analogous to the manner in which spectral variations in reflectance are exploited via multi-band data, the directional component can be exploited using multi-angle data.

The fact that the directional signature of remotely sensed surfaces will contain structural information has led to the development of new missions designed specifically to explore and exploit the directional signal. This signal is not available to sensors that have no directional sampling capability, either through a wide field of view, a pointing capability or orbital characteristics. Airborne instruments such as the NASA Advanced Solid state Array Spectrometer (ASAS) (Irons *et al.*, 1991) have been in use for some time (Barnsley *et al.*, 1997b; Lewis *et al.*, 1999). On a much larger scale, the MODIS and MISR instruments on-board the *Terra* platform are both specifically designed to exploit directional variations in surface reflectance (Wanner *et al.*, 1997; Knyazikhin *et al.*, 1998a,b; Martonchik *et al.*, 1998a,b). MODIS data exploit the instrument's wide swath and rapid repeat coverage to provide viewing and illumination variation, whilst MISR is has nine fixed cameras, giving four look angles in the along-track direction fore and aft as well as a nadir view. An intermediate instrument is CHRIS (Compact High Resolution Imaging Spectrometer) aboard the PROBA (Project for On Board Autonomy) platform launched in autumn 2001 (Barnsley *et al.*, 2000; www[1.11]). CHRIS is a high-resolution (25 to 50m) optical instrument which (uniquely) combines (19) selectable radiometric bands with a pointable multi-angle capability. This variety of instruments highlights the well-established (and growing) interest in multi-angle remote sensing.

1.5 Thesis outline

Much of the impetus for the work in this thesis derives from developments made in the design and algorithm development for a new generation of spaceborne instruments. Models of BRDF have been developed to allow both the correction of directional effects in measured reflectance data and also, more interestingly, the exploration of the directional signal. The range of approaches to modelling the reflectance of vegetation canopies has been extremely wide, with attendant variations in complexity. With MODIS already launched and entering its operational phase (and with other similar missions planned), it is becoming increasingly important to understand exactly what information can be practically and usefully extracted from the data, and how this process might be improved. This thesis presents work which is part of ongoing validation for sensor

programmes such as MODIS and CHRIS, as well as contributing to the understanding of existing algorithms and the development of new ones.

Chapter 2 contains a theoretical discussion of BRDF as well as a review of important concepts and developments in surface reflectance modelling. In particular, simple semi-empirical kernel-driven models of BRDF developed specifically for use with the MODIS sensor are introduced. These models are an important development for near real-time production of the type of global, moderate resolution products required for the study of global climate processes. The kernel-driven models are just starting to be used operationally to produce estimates of albedo and burn scar area from surface reflectance. This thesis explores how these relatively simple models can apparently describe the complex scattering behaviour of vegetation canopies at a range of scales. In addition, the nature of biophysical information contained in the model parameters is explored and potential improvements and extensions of the modelling concept are proposed.

Chapter 3 is a description of fieldwork carried out to obtain a variety of plant canopy data. Detailed 3D models of canopy structural and radiometric properties are generated from structural measurements and subsequently used to simulate values of canopy reflectance, ρ_{canopy}. The simulations of ρ_{canopy} are the basis for exploration and understanding of the assumptions underlying certain canopy reflectance modelling techniques. Contemporaneous measurements of a variety of canopy parameters made during the field campaign are used to validate simulated values of ρ_{canopy}.

Chapter 4 describes a set of experiments intended to establish the validity of the semi-empirical kernel-driven approach to modelling BRDF. Values of ρ_{canopy} are simulated under the assumptions made in the formulation of the linear kernel-driven models and the results are used to explore these assumptions. The assertion that ρ_{canopy} can be separated into its constituent scattering components is examined. Results show that the separate components of simulated ρ_{canopy} do in general describe what they are purported to in the model formulation.

Chapter 5 explores the relationship between the linear kernel-driven model parameters and the corresponding scattering components derived from the 3D canopy simulations. The assumptions underlying the linear kernel-driven models are tested and situations where these assumptions may break down are highlighted. This is the first time

that these assumptions have been tested explicitly, rather than being inferred from the ability of the kernel-driven models to fit observed reflectance data.

Chapter 6 contains an analysis of the information content of the model parameters. Results show that model parameters may contain biophysical information that can be exploited but it may be coupled with other information. This indicates that the model parameters should be interpreted with great care, particularly in the absence of other ancillary information. Model parameters may have an indirect use for analysis such as land cover classification or change detection.

Chapter 7 presents a new extension of the linear kernel-driven modelling approach into the spectral domain. Such an approach appears to offer significant improvements over current kernel-driven models, which are limited to the angular domain. This is particularly true for the derivation of products such as broadband (across visible and NIR wavelengths) albedo from narrowband spectral samples. So-called 'spectral kernels' are derived and tested against simulated (and measured) reflectance data.

Chapter 8 contains conclusions drawn from the experimental results presented in the thesis and discusses directions for further research. In particular, further developments of the spectral kernels are proposed and plans are outlined for the application of a full spectral directional kernel-driven model of the type developed in chapter **7** to airborne and spaceborne data.

2 Review of BRDF and canopy reflectance modelling

Liang *et al.* (2000a) review the current state of multi-angle remote sensing following the International Forum on BRDF (IFB), San Francisco, December 1998. They conclude that multi-angle remote sensing, at the threshold of the EOS era, is now yielding data which are set to provide unique insight into surface biogeophysical processes.

Radiation reflected from the Earth's surface is characterised by a small number of key signatures (or domains of information) (Gerstl, 1990; Liang and Strahler, 1994):

1. **Spectral (λ)**: reflectance, transmittance and absorptance response of canopy elements to radiation of different wavelengths (Jacquemoud and Baret, 1990; Curran *et al.*, 1992).

2. **Spatial (x, y):** e.g. spatial structure at the macroscopic level (objects are much larger than the wavelength of incident radiation), arrangement of scattering objects on a surface, appearance of target at different scales, adjacency, mixed pixels (Woodcock *et al.*, 1988).

3. **Temporal (t):** e.g. seasonal change of vegetation growth profiles; inter-annual variability of vegetation quantity (Myneni *et al.*, 1997).

4. **Angular $\Omega(\theta_v, \phi_v)$, $\Omega'(\theta_i, \phi_i)$:** reflectance anisotropy caused by surface structure e.g. hotspot – the peak of reflectance in retro-reflection direction (viewing and illumination vectors, Ω and Ω', are near coincident) (Ross, 1981; Kuusk, 1985).

5. **Polarization $p(\phi)$:** e.g. polarization information contained in surface reflectance signal (Vanderbilt *et al.*, 1985; Deschamps *et al.*, 1994).

6. **Time-resolved (∂T):** time-resolved returns from active instruments, such as optical (laser) LiDAR (Light Detection And Ranging), and phase information from microwave RADAR (Radio Detection and Ranging) instruments (λ of the order of cm).

The intrinsic surface reflectance is a function of all of these signatures, but differs from the signal measured at the sensor due to the effects of atmosphere, sensor response etc. Exploration of the first three signatures above has formed the basis of conventional remote sensing (Goel, 1988; Gerstl, 1990). The fifth component has only been deliberately exploited recently with the advent of the (now-defunct) POLDER, and forthcoming POLDER II instruments (Deschamps *et al.*, 1994; Leroy *et al.*, 1996). The sixth component has also been exploited only relatively recently: LiDAR is currently being explored as a new method of obtaining information on surface properties, particularly vegetation canopy structure (www[2.1]). Phase information from RADAR instruments can be used to determine information regarding the structure and scattering behaviour of the surface (Sun and Ranson, 1995; Saich *et al.*, 2001).

The directional signal (4) has historically been one of the least exploited of these signatures (Goel, 1992; Liang and Strahler, 1994; Myneni *et al.*, 1995; Privette *et al.*, 1997) and was until relatively recently mostly ignored. Barnsley et *al.* (1997a) have shown that multiple view angle (MVA) data contain information entirely separate from the spectral component of measured reflectance. This indicates that the directional signal can be used to distinguish between cover types purely on the basis of surface structural detail, even where spectral responses are identical (Asner, 2000). This thesis is primarily concerned with the information content of the directional signature, but also examines the possibility of extending and including spectral information into simple directional modelling methods.

Considering the reflectance signal from a vegetation canopy, Goel (1992) extends the description by Gerstl (1990) given above to propose the following functional description of the relationship, R, between the measured spectral directional reflectance ρ of a vegetation canopy, and the parameters controlling that signature:

$$\rho = R(\lambda, t, (x, y), (\mathbf{\Omega}, \mathbf{\Omega'}), P, \partial T; C) \qquad \textbf{2.1}$$

In addition to the five signatures described above, R is also dependent on a set of canopy parameters, C, representing the characteristics of the canopy and its underlying surface (soil, snow etc.) contributing to the form of ρ. In order to derive information regarding vegetation from measurement of reflectance, models of vegetation canopy reflectance (CR) are constructed (Goel, 1988). A model of CR is an attempt to i) formulate an accurate *forward* relationship to predict ρ for given R and ii) determine C from measured

ρ (at given values of λ, t, (x,y), (Ω, Ω'), ∂T, P) i.e. to *invert* (or understand) the canopy parameters from the relationship in equation **2.1**.

The development of EO as a powerful tool for monitoring and mapping the global environment has been introduced in chapter **1**. This chapter discusses the implications of the anisotropic nature of surface reflectance under variable viewing and illumination conditions. The potential for exploitation of the directional nature of surface reflectance through the application of canopy reflectance models is explored. Mathematical techniques for the inversion of such models against measured reflectance data are introduced. Following this a review of some of the many available canopy reflectance modelling (CR) techniques is undertaken. The conclusion of this is the introduction of a particular class of canopy reflectance models, developed for their simplicity and effectiveness, which are to be used to derive products from forthcoming sensors such as MODIS and MISR. Experimentation in subsequent chapters explores the potential for these models to extract information regarding vegetation canopies from reflectance data in practice.

2.1 Factors affecting surface reflectance anisotropy

The size, shape and distribution of objects on a surface have a direct impact on the nature of the radiation scattered from the surface (Hapke, 1981, 1993). The measured reflectance signal is therefore a function of surface structure. Vegetation is one of the most important absorbing/scattering land surfaces that can impact a remote sensing signal (Asrar, 1989; Myneni and Ross, 1990; Sellers, 1992; Asner, 1998). Examples of important biophysical parameters such as LAI, fAPAR and albedo, which are used by ecologists, climatologists and remote sensing scientists to describe the quantity and influence of vegetation, were introduced in the previous section.

Vegetation plays an extremely important role in the global climate (Dickinson, 1983, 1995; Otterman, 1985), providing a primary mechanism for the exchange of O_2 and CO_2 in the atmosphere (Schulz *et al.*, 2001; Zhan and Kustas, 2001), as well as energy fluxes through photosynthetic activity (Ross, 1981; Verstraete, 1987), moisture fluxes (Shukla and Mintz, 1982) and transfers of momentum (Sellers, 1995). Indeed, Asner (2000) notes "MVA remote sensing measurements are uniquely sensitive

to variation in key structural characteristics of vegetation, soils and atmospheric constituents". For these reasons, much emphasis has been placed on attempting to understand how vegetation can be detected and monitored from remote sensing measurements. One of the primary ways in which this has been achieved has been the development and refinement of CR modelling techniques (Allen *et al.*, 1970; Ross, 1981; Goel, 1988; Asrar, 1989; Privette *et al.*, 1997; Strahler, 1996).

It is well-known that natural surfaces are generally not Lambertian reflectors (i.e. reflecting incident radiation equally in all directions), but will tend to display varying degrees of anisotropy (Minnaert, 1941; Nicodemus *et al.*, 1977; Hapke, 1981). Surface reflectance is therefore not only a function of the spectral, spatial and polarising properties of the target, but also of the direction from which the surface is illuminated and viewed (Ross, 1981; Goel, 1988). Measured reflectance (as opposed to the intrinsic surface reflectance) will also be dependent on the spectral and directional nature of the irradiance. The directional nature of surface reflectance is illustrated in figure **2.1**.

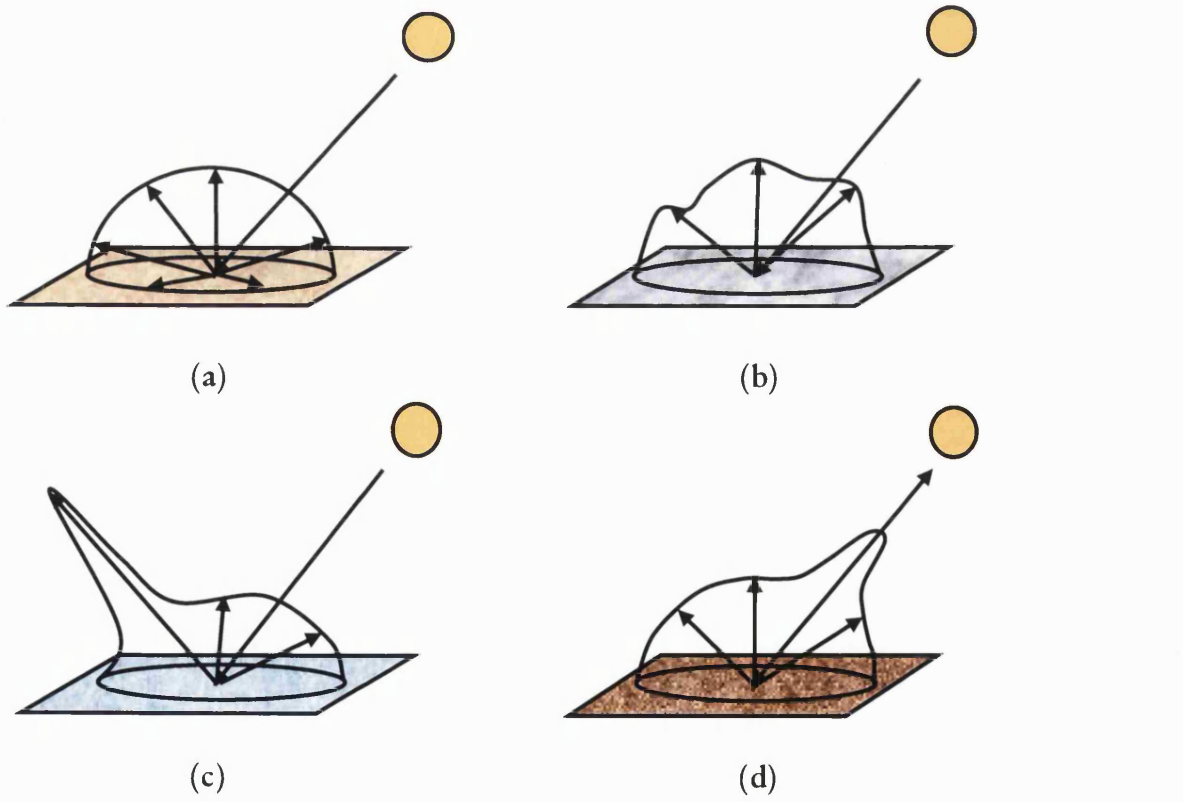

Figure 2.1 Four examples of surface reflectance: (a) Lambertian reflectance (b) non-Lambertian (directional) reflectance (c) specular (mirror-like) reflectance (d) retro-reflection peak (hotspot).

The degree to which incident radiation from a surface is reflected anisotropically is determined by factors such as the density and arrangement of objects on the surface, and hence the nature of the shadowing caused by these objects as a function of viewing and illumination zenith and azimuth angles, $\theta_{i,v}$, and $\phi_{i,v}$ respectively (Otterman and Weiss, 1982; Li and Strahler, 1986, 1992; Roujean *et al.*, 1992), as well as the intrinsic directionality of the reflectance, transmittance and absorptance properties of the scattering materials (Asrar, 1989). Reflectance anisotropy can also be a function of the aggregated scattering properties of objects. The existence of surface structure tends to cause the surface to depart from Lambertian and, as a result, incident radiation is reflected more strongly in some directions than others. This directionality of surface reflectance can potentially be exploited to provide information regarding the surface structure. This is illustrated by the specular and hotspot peaks shown in figure **2.1c** and **d**. The hotspot peak arises because a minimum of shadowed surface is viewed when the viewing and illumination vectors are collinear (Hapke, 1984). This is a characteristic feature of vegetation canopy reflectance and is related to the size and distribution of scattering objects within the canopy (Kuusk, 1985; Pinty and Verstraete, 1992). The next step is to introduce a formal description of surface reflectance anisotropy.

2.1.1 Bidirectional reflectance distribution function (BRDF)

Figure **2.1** illustrates the tendency of natural surfaces tend to reflect incident radiation anisotropically. This behaviour is formally described by the (spectral) bidirectional reflectance distribution function (BRDF) (Nicodemus, 1970; Nicodemus *et al.*, 1997; Hapke, 1981). The BRDF of a small surface area δA (at a particular wavelength of (non-polarised) illuminating radiance) is defined as the ratio of the incremental radiance leaving the surface through an infinitesimal solid angle in the direction defined by the viewing vector, $\Omega(\theta_v, \phi_v)$ (where θ_v, ϕ_v are the viewing zenith and azimuth angles) to the incremental irradiance from direction defined by the illumination vector, $\Omega'(\theta_i, \phi_i)$ (where θ_i, ϕ_i are the illumination zenith and azimuth angles). This is expressed in equation **2.2** (ignoring any dependence of BRDF on wavelength, λ)

$$BRDF\ (\boldsymbol{\Omega}, \boldsymbol{\Omega}') = \frac{dL_e(\boldsymbol{\Omega}, \boldsymbol{\Omega}')}{dE_i(\boldsymbol{\Omega}')}\left[sr^{-1}\right] \qquad \textbf{2.2}$$

Where dL_e is the incremental radiance reflected from the surface into the differential solid angle in the viewing direction Ω ($Wm^{-2}sr^{-1}$) (Nicodemus *et al.*, 1977; Martonchik *et al.*,

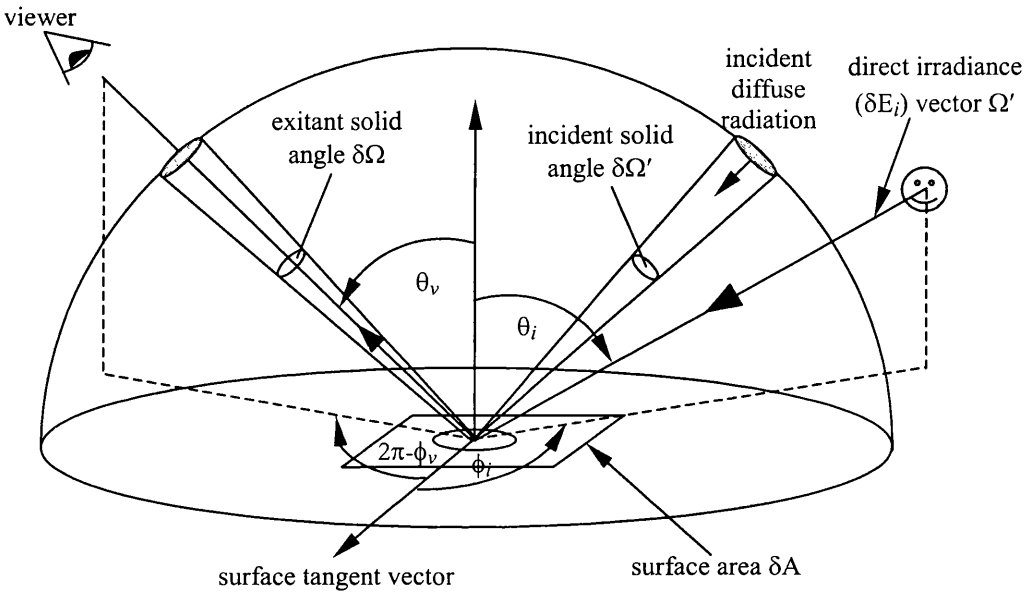

Figure 2.2 Configuration of viewing and illumination vectors in the viewing hemisphere, with respect to an element of surface area, δA.

2000); dE_i is the incremental irradiance ($Wm^{-2}sr^{-1}$) arriving from the illumination direction, Ω' i.e. $dE_i = L_i(\mathbf{\Omega}')\cos\theta_i \sin\phi_i d\theta_i d\phi_i$. Figure **2.2** shows the configuration.

Equation **2.2** only deals with two of the domains of information described in the expression for measured reflectance given in equation **2.1,** but for exploring spectral directional reflectance these are the important ones. BRDF as defined in equation **2.2** is a fundamental property of the surface, describing the intrinsic surface reflectance. However, it is defined only for infinitesimal viewing and illumination solid angles and an infinitesimal wavelength interval. Consequently it cannot be directly measured. In EO applications, illumination is typically over a hemisphere with both direct and diffuse sources (solar illumination, and sky radiance respectively). Viewing is typically over some finite sensor instantaneous field-of-view (IFOV), defined by the sensor optics and geometry, with a spectral response over some finite wavelength interval rather than at some discrete value of λ.

In practice, it is assumed that the BRDF can be retrieved with some level of uncertainty, from radiance measurements over the IFOV using a collimated beam light source (e.g. laser or direct sunlight). In this case, BRDF is the limit case of biconical reflectance measurement. To overcome the problem that the BRDF is a non-measurable property, we define a bidirectional reflectance factor (BRF) ρ(λΩ, Ω'), which is the ratio of radiance leaving the surface in a finite solid angle in the viewing direction Ω to the

radiance from a perfect Lambertian reflector under the same illumination conditions as the target, into the same finite solid angle i.e.

$$\rho(\mathbf{\Omega},\mathbf{\Omega}',L_{sky,sun}(\mathbf{\Omega},\mathbf{\Omega}'))=\frac{L_e(\mathbf{\Omega},\mathbf{\Omega}',L_{sky,sun}(\mathbf{\Omega},\mathbf{\Omega}'))}{L_{Lambertian}(\mathbf{\Omega},\mathbf{\Omega}',L_{sky,sun}(\mathbf{\Omega},\mathbf{\Omega}'))} \quad \textbf{2.3}$$

where L_e is the radiance exitant from the surface ($Wm^{-2}sr^{-1}$); $L_{Lambertian}$ is the radiance from a perfect Lambertian reflector ($Wm^{-2}sr^{-1}$); $L_{sky,sun}$ are the sky and sun radiance distributions ($Wm^{-2}sr^{-1}$). It can be seen that the BRF is dimensionless.

As a result of the incident irradiance and exitant radiance being defined over infinitesimal solid angles $\delta\Omega$ and $\delta\Omega$', BRF can be calculated as an integrated property i.e. the numerator in equation **2.2** becomes:

$$L_e(\mathbf{\Omega},\mathbf{\Omega}',E_i(\mathbf{\Omega},\mathbf{\Omega}'),L_{sky,sun}(\mathbf{\Omega},\mathbf{\Omega}'))=\int_0^{2\pi}\int_0^{\pi/2}\rho_s(\mathbf{\Omega},\mathbf{\Omega}')d\mathbf{\Omega}d\mathbf{\Omega}' \quad \textbf{2.4}$$

where ρ_s is the surface reflectance function (BRDF); $d\mathbf{\Omega}=\iint\cos\theta\sin\theta d\theta d\phi$ (and similarly for $d\Omega'$. It can be seen from equation **2.3** that in order to derive the exitant radiance, the viewing and illumination vectors are integrated over the respective viewing

$$L_{Lambertian}(\mathbf{\Omega},\mathbf{\Omega}',L_{sky,sun}(\mathbf{\Omega},\mathbf{\Omega}'))=\frac{1}{\pi}\int_0^{2\pi}L_{sky,sun}(\mathbf{\Omega},\mathbf{\Omega}')d\mathbf{\Omega}' \quad \textbf{2.5}$$

and illumination hemispheres. In the same way, the radiance from the Lambertian surface is defined as

The integral is purely over the illumination direction as the observed reflectance, by definition, is the same regardless of the viewing direction. In practice, the BRF is often defined as the radiation exiting the scene in a given direction (an infinitesimal angle), rather than as an integrated property. If a point illumination source is considered i.e. no sky irradiance, then, for this case

$$BRF\ (\mathbf{\Omega},\mathbf{\Omega}')=\pi BRDF\ (\mathbf{\Omega},\mathbf{\Omega}') \quad \textbf{2.6}$$

The expression in equation **2.6** utilises the fact that the BRDF of perfect Lambertian reflector is $1/\pi$. This is due to the fact that a perfectly diffuse surface reflects the same radiance, $E_i(\theta_i)/\pi$ in all directions. As a result, the BRF of any surface is equal to its BRDF multiplied by π.

Practically, measured surface reflectance is a function of the direct and diffuse component of incident irradiance (rather than being an intrinsic surface property).

Consequently, integrals of the BRDF over the viewing and illumination hemispheres are defined. The directional hemispherical reflectance (or DHR), $\bar{\rho}(\boldsymbol{\Omega},\boldsymbol{\Omega}')$, is the integral of BRF over the viewing (or illumination) hemisphere. It is the hemispherical reflectance assuming a directional (collimated beam) illumination source (or alternatively, the directional reflectance for a diffuse illumination). This can be expressed as:

$$\bar{\rho}(\boldsymbol{\Omega}';2\pi)=\frac{1}{\pi}\int^{2\pi} BRDF(\boldsymbol{\Omega},\boldsymbol{\Omega}')d\boldsymbol{\Omega} \qquad \textbf{2.7}$$

This expression defines the so-called black-sky albedo (Wanner *et al.*, 1995) i.e. it defines the hemispherical reflectance under conditions of purely directional illumination (no sky radiance). $\bar{\rho}(\boldsymbol{\Omega}')$ can be integrated over all illumination directions to yield $\bar{\bar{\rho}}$ the bi-hemispherical (or hemispherical-to-hemispherical) reflectance (or BHR). This is the reflectance of a surface over all viewing angles due to a diffuse illumination source i.e.

$$\bar{\bar{\rho}}(2\pi;2\pi)=\int^{2\pi}\bar{\rho}(\boldsymbol{\Omega}')d\boldsymbol{\Omega}'=\frac{1}{\pi}\int^{2\pi}\int^{2\pi} BRDF(\boldsymbol{\Omega},\boldsymbol{\Omega}')d\boldsymbol{\Omega}d\boldsymbol{\Omega}' \qquad \textbf{2.8}$$

which is the so-called white-sky albedo i.e. the hemispherical reflectance under perfectly diffuse illumination conditions.

It is important in the context of remote sensing applications to note that BRDF cannot be directly measured because:

i) (from equations **2.2** and **2.3**) BRDF is defined as the ratio of two partial derivatives and BRF is defined as reflectance relative to that of a perfect Lambertian reflector.

ii) No sensor has a perfectly discrete spectral response, and so measurement of BRDF is inevitably a convolution of the signal with the sensor spectral response function over a range of wavelengths. Additionally, the projected instantaneous IFOV of the sensor must be accounted for i.e. measurement is not over an infinitesimal angle.

iii) In practice, observations are made through some depth of atmosphere so that the measured signal is also a function of atmospheric absorption and scattering (reflectance and transmittance). To retrieve measures of surface reflectance through the atmosphere, the scattering behaviour of the

atmosphere (and in particular the scattering phase function) must be characterised accurately.

Using the relationships in equations **2.2-2.8** it is now possible to relate BRDF to albedo. The BRDF explicitly describes the directional nature of exitant radiation from a surface. As a result, albedo, the total irradiant energy (both direct and diffuse) reflected in all directions from the surface, is an integrated measure of the directional reflectance over the viewing/illumination hemisphere. Albedo is thus a function of the quantities of diffuse and direct illumination arriving at the surface. In the discussion above, dependence of BRDF on λ has not been considered. In practice, BRDF is also a function of λ. Typically reflectance data are either reported as a function of λ, or the finite wavelength interval over which the parameters have been integrated during observation is specified. In such instances, parameters such as BRF, DHR and BHR are should be prefaces by "spectral" or "narrowband".

Further approximations are required in practice in order to relate estimates of albedo made at narrow wavelength bands (narrowband) to total albedo over the visible and NIR regions of the spectrum (broadband). This has been discussed by a number of researchers, in a variety of ways (Stephens *et al.*, 1981; Stum *et al.*, 1985; Kimes and Sellers, 1985; Cess and Potter, 1986; Brest and Goward, 1987; Koepke and Kriebel, 1987; Dickinson *et al.*, 1990; Liang *et al.*, 1999). Spectral albedo $\alpha(\lambda)$ can be approximated as a combination of the two components of black-sky and white-sky albedo (Wanner *et al.*, 1997; Strugnell and Lucht, 1999), weighted by D, the proportion of diffuse illumination from the atmosphere i.e.

$$\alpha(\lambda) = (1 - D(\lambda, \boldsymbol{\Omega}', \tau))\overline{\rho}(\lambda, \boldsymbol{\Omega}') + D(\lambda, \boldsymbol{\Omega}', \tau)\overline{\overline{\rho}}(\lambda) \qquad \textbf{2.9}$$

where $D(\lambda, \Omega', \tau)$ is function of the illumination conditions and the atmospheric state, characterised by the atmospheric optical depth, τ. Equation **2.9** is a reasonable approximation to spectral albedo except at high solar zenith angles (Lewis and Barnsley, 1994). The total surface albedo, α i.e. the ratio of the total incident shortwave radiation to the reflected radiation can then be approximated as an integral over all shortwave (SW) radiation (ignoring anisotropy of incident diffuse radiation) i.e.

$$\alpha = \int_{SW} p(\lambda)\alpha(\lambda)d\lambda \qquad \textbf{2.10}$$

where $p(\lambda)$ is the proportion of illumination in the solar spectrum, dependent on the atmospheric state. $1-\alpha$ is then the proportion of incident shortwave radiation absorbed at the surface (stored as heat energy and chemical energy through photosynthesis). Application of the method to EO data requires the integral over all SW to be approximated with a weighted sum of the available wavebands (Lewis *et al.*, 1999), or through the use of other modelling techniques (Liang, 2000; Lucht and Roujean, 2000). This limitation will be discussed in later chapters.

The properties defined above can be measured in practice. To characterise up- and downwelling radiation fluxes from the surface a description of the surface scattering behaviour is required. Indeed, surface properties cannot be related to measured radiance without such a model. Many models describing the scattering of radiation by vegetation have been developed; some to correct angular dependencies (Roujean *et al.*, 1992; Cihlar *et al.*, 1994 Liang *et al.*, 2000b), some to relate canopy scattering behaviour to remote measurements of reflectance (e.g. Goel and Strebel, 1983; Goel 1988, 1992; Nilson and Kuusk, 1989; Pinty and Verstraete, 1991). An overview of these methods is given in section **2.5**.

2.1.2 Removal of reflectance anisotropy effects from observed reflectance

Reflectance anisotropy arises in a variety of ways. Sensors possessing wide viewing swaths such as AVHRR, with a swath width of 2500km, have variations in view angle across scenes (70° in the case of AVHRR) (Leroy and Roujean, 1994; Cihlar *et al.*, 1994; Li *et al.*, 1996). In addition, a point on the surface may be located in different parts of the viewing swath on subsequent orbits, and will therefore be viewed from different angles. This is also true for sensors with along-track scanning or off-nadir pointing capabilities such as ATSR-2 (North *et al.*, 1999) POLDER (Deschamps *et al.*, 1994), and the forthcoming CHRIS instrument (Barnsley *et al.*, 2000). This is schematically illustrated in figure **2.3**. Surface reflectance is also dependent on the solar zenith angle. This is manifested if a point on the Earth's surface is viewed at different times of day, for example from a geostationary viewing platform such as METEOSAT, or is viewed on different days from a polar orbiting platform such as AVHRR. Sun-synchronous observations will also tend to be affected by the annual cycles of variation in solar zenith

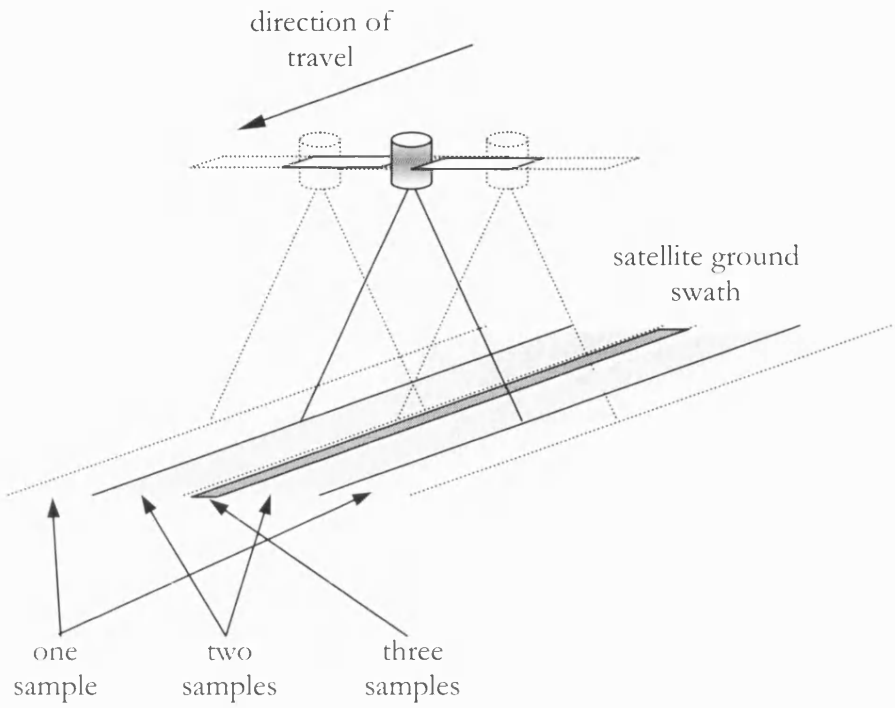

Figure 2.3 Angular effects caused by satellite repeat pattern (differently shaded areas represent different numbers of samples).

angle. Liang *et al.* (2000b) review recent developments in the angular correction of BRDF data, in particular for modelling surface energy fluxes, and in particular, albedo.

With the increase in availability of large satellite data sets, the reflectance variations caused by inconsistent viewing and illumination angles has come to be recognised as a serious problem (Kimes *et al.*, 1980; Royer *et al.*, 1985; Leroy and Roujean, 1994; Cihlar *et al.*, 1994). Assuming that the Earth's surface is Lambertian and ignoring directional effects will introduce significant errors in estimates of surface reflectance from EO data. In order that observations separated in time by many months and measured at significantly different viewing and illumination angles may be compared, directional effects must be accounted for (Lee and Kaufman, 1986; Roujean *et al.*, 1992; Wu *et al.* 1994; Privette *et al.*, 1997a). This may be achieved by normalising reflectance measurements to a standard viewing and illumination equivalent reflectance which permits intercomparison of data obtained at varying sun and view zenith angles (Gutman, 1994). It is now recognised that viewing and illumination angle effects should be considered significant: reflectance observations made at different viewing and illumination angles are not directly comparable, even if all other things are considered equal (Privette *et al.*, 1997; Roy *et al.*, 2001).

2.1.3 Reflectance anisotropy as a source of information

In contrast to the undesirable effects described above, the directional nature of surface reflectance can also be exploited as a source of information. The directional dependence of surface reflectance on structural properties implies that observations of the directional signal will contain information relating to these properties (Goel and Strebel, 1983; Goel, 1988; Myneni *et al.*, 1989; Pinty and Verstraete, 1991). If it is possible to relate radiant energy from a vegetation canopy to observed reflectance using a model of some kind, then it may also be possible to use such a model to relate variations in observed reflectance to surface properties causing these variations (Asrar, 1989; Pinty and Verstraete, 1991; Myneni *et al.*, 1995; Asner, 2000). Such a relationship can be used to normalise directional effects in directional data sets, as discussed above (Roujean *et al.*, 1992; Cihlar *et al.*, 1994; Liang *et al.*, 2000b). More usefully for the study of vegetation characteristics however, such a model may be inverted against measured reflectance data to provide estimates of model parameters (Goel and Strebel, 1983; Pinty and Verstraete, 1990, 1992; Hall *et al.*, 1995; Liang *et al.*, 2000a). If the model parameters describe surface properties, such as the size and distribution of scattering objects say, then estimates of these surface properties may be obtained. This thesis is concerned with recent developments in modelling surface scattering from vegetation, which are now being used to produce land-cover products from recent and forthcoming instruments. Before describing methods of CR modelling however, attention must be paid to the effect of the atmosphere on remotely sensed measurements.

2.2 Atmospheric effects on measured surface reflectance

Reflected solar radiation measured at a remote sensing platform must travel through the Earth's atmosphere both on the way down from the direction of the sun, and on the way back up to the measuring platform. The intervening atmosphere contains various gases and aerosols, which absorb and/or scatter upwelling and downwelling radiation. The most abundant atmospheric gas in terms of absorption of incoming radiation is water vapour (contributing approximately 75% of the global greenhouse effect), which absorbs radiation strongly in the NIR and mid-IR regions (Salby, 1995). In addition, the atmosphere contains aerosol particles such as sulphates, mineral dust, soot and sea salt, originating from sources such as volcanic eruption, industrial and urban

emissions or oceanic evaporation. These aerosols can have significant scattering effects (Rayleigh and Mie, depending on particle diameter) and cause the signal received at the sensor to be attenuated (Kaufman, 1989; Vermote *et al.*, 1997a,b). This can be particularly important when investigating surface properties such as albedo (Lyapustin, 1999). Atmospheric gases and aerosols can also be highly temporally and spatially variable and are therefore difficult to characterise accurately (Martonchik *et al.*, 1998a). This behaviour is generally characterised by the aerosol optical depth, τ (Zibordi and Voss, 1989).

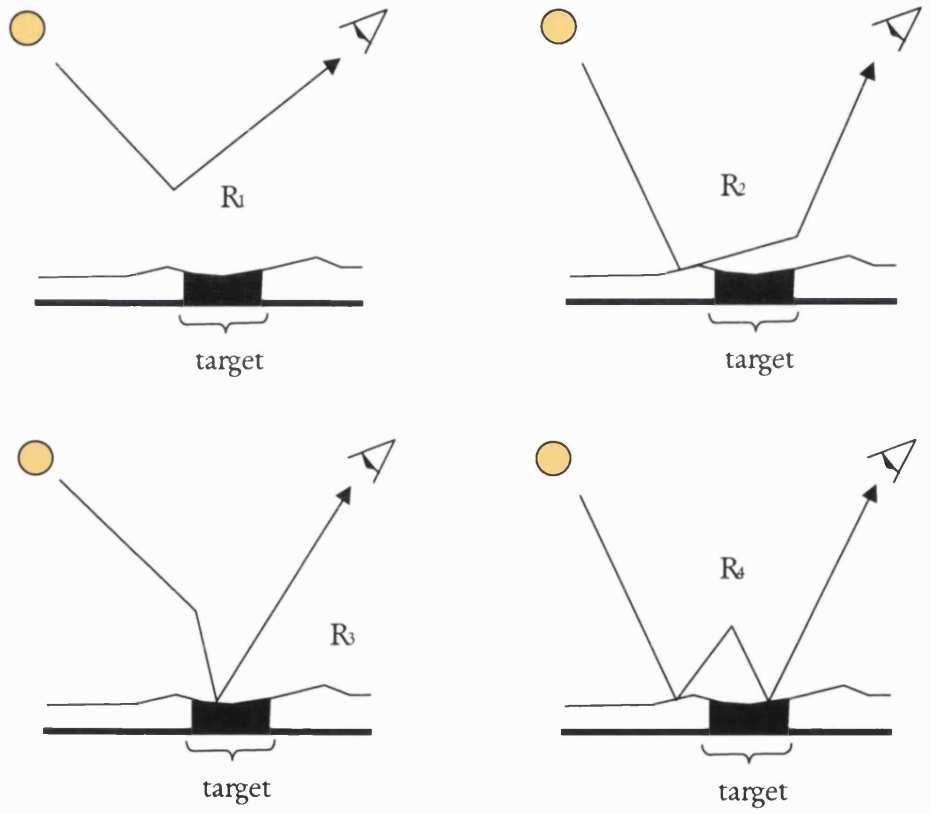

Figure 2.4 Four sources of atmospheric perturbation to the measured surface reflectance signal.

Figure **2.4** illustrates four sources of atmospheric scattering that cause perturbation of the surface reflectance signature. R_1 is incoming radiation reflected towards the sensor by a single scattering interaction in the atmosphere. R_2 is incoming radiation scattered first from the surface outside the target area then by the atmosphere into the path of the sensor. R_3 is incoming radiation scattered by the atmosphere onto the target and then to the sensor. R_4 is incoming radiation scattered from the surface outside the target, then by the atmosphere above the target back on to the target, then to the

sensor. Note in R4 that a component of the signal reaching the sensor will contain radiation reflected from the area surrounding the target in addition to the desired signal (Kaufman, 1989). There are obviously more complex interactions if higher orders of scattering between the surface and atmosphere are considered. These will tend to be successively smaller in magnitude than the single scattered interactions due to attenuation by absorption, scattering and transmission at each successive interaction, and will also tend to be isotropic (Vermote *et al.*, 1997a,b). If information regarding the scattering behaviour of the target is sought, this extraneous atmospheric signal which acts to 'blur out' the surface reflectance signal, must be accounted for. It is clear that the atmosphere adds significantly to the path radiance at red wavelengths (and even more so at shorter wavelengths), whilst attenuating the surface reflectance at IR wavelengths (Kaufman, 1989; Myneni *et al,* 1993).

In order to isolate the desired surface signal, the contribution of the intervening atmosphere must either be removed (as far as possible) or modelled as part of the signal through the application of a coupled model of surface-atmosphere scattering. Removing the atmospheric perturbation of measured surface reflectance is typically performed using a model of the scattering behaviour of the atmosphere (coupled with some assumption of surface reflectance behaviour). The Second Simulation of the Satellite Signal in the Solar Spectrum (6S) code of Vermote *et al.* (1996) for example, uses available ozone and water vapour concentrations, aerosol optical depth at 550nm, knowledge of sensor response and atmospheric pressure and a model of surface reflectance properties to generate parameters which allow surface reflectance to be calculated from at-sensor top-of-atmosphere (TOA) radiance values. There are a number of other models for the atmospheric correction of measured radiance data such as those of Rahman and Dedieu (1994) and Berk *et al.* (1992). Kaufmann (1989) gives a comprehensive review of methods that have been developed in order to account for the atmospheric component of remote measurements of the Earth's surface.

The second approach to accounting for atmospheric effects is based on the observation that the measured directional reflectance signal is a function of both the surface and the atmosphere and the coupling between them (Myneni and Asrar, 1993). A number of combined surface-atmosphere models have been developed in order to characterise this coupling. Liang and Strahler (1993) described the coupled atmosphere-canopy system as two plane-parallel layers with a non-Lambertian soil boundary. The

total radiation field in this case is calculated by treating the unscattered, single scattered and multiple scattered radiation separately. A similar approach is taken by Rahman *et al.* (1993a, b) in their coupled surface-atmosphere reflectance (CSAR) model. Their results show that the BRDF signal undergoes smoothing as a result of atmospheric effects, thus emphasising the importance of considering the coupling between surface and atmosphere. Lewis *et al.* (1999) demonstrate that both the magnitude and (more importantly) the shape of the surface BRDF can be completely mis-estimated if atmospheric correction is not performed accurately. In particular, the correct choice of scattering phase function is shown as crucial in maintaining the surface reflectance shape. Lyapustin (1999), and Lyapustin and Privette (1999), have shown the importance of the accurate characterisation of atmospheric absorption and scattering in the derivation of albedo from multi-angular measurements. Interestingly, Lyapustin (1999) has recently shown that there appears to be a small, well-defined range of solar zenith angles between approximately 52° and 57° where surface albedo is almost insensitive to atmospheric opacity.

Atmospheric correction of remotely sensed data has generally been performed on a 'per scene' basis, ignoring spatial variability within scenes and assuming a uniform Lambertian surface (Tanré *et al.*, 1986; Fraser *et al.*, 1992). Typically, the total radiation flux from the top of the atmosphere (TOA) to the surface is described as the sum of direct and diffuse components – the latter caused by absorption and transmission of atmospheric gases such as water vapour and scattering by atmospheric aerosols. The assumption of Lambertian surface reflectance is made in order to simplify the calculation of radiation scattered multiply between the surface and atmosphere. Lee and Kaufmann (1986) demonstrate that this assumption can cause significant errors in the retrieval of surface reflectance, particularly in the backscattering direction and for large illumination angles (60° and above) due to coupling between surface reflectance and the atmosphere. Hu *et al.* (1999) state that such errors can be from 2-7% up to 15% in the worst case. As a result, when investigating directional reflectance variations, a more spatially accurate approach requiring per-sample (per pixel, depending on pixel resolution) corrections is required (Vermote *et al.*, 1997a). The additional computational effort required to achieve this is a major limitation on the rapid processing of large data sets. Recent instruments designed to measure surface reflectance variations (e.g. MODIS and POLDER) have been developed to use a variety of data regarding the state of the atmosphere and the surface surrounding the target in order to produce improved atmospheric corrections.

Atmospheric correction developed for the MODIS surface reflectance product for example, assumes that the signal at the sensor is a distance-weighted sum of the contributions from the pixels surrounding the target (Vermote *et al.*, 1997a,b). Measurements of ozone, water vapour and pressure are also used in calculating atmospheric attenuation of the measured signal. Simultaneous multi-angle measurements of the surface during a single overpass from sensors such as MISR (Martonchik *et al.*, 1998) and CHRIS (Barnsley *et al.*, 2000) provide another possibility. The (now defunct) POLDER instrument was designed to measure the polarisation of incoming radiation in order to characterise the atmospheric aerosol scattering phase function. This information can be used to further improve the atmospheric correction process by identifying the various types and concentrations of scattering particles (Leroy *et al.*, 1996).

It has been shown that the atmosphere between target and sensor contributes significantly to the difficulty of measuring surface BRDF remotely. As such, it is desirable to account for the scattering behavior of the atmosphere in some way. However, it should also be noted that the scattering caused by atmospheric aerosols is a valuable source of information in its own right. Clearly, if radiation reflected from surface to sensor is attenuated due to atmospheric scattering, the same must also be true for incoming solar radiation. In fact, atmospheric aerosols play a major role in the Earth's radiation budget (Charlson *et al.*, 1992; Kiehl and Briegleb, 1993). Tropospheric aerosols (and associated indirect effects) are thought to contribute of the order of $1 Wm^{-2}$ to atmospheric radiative forcing (IPCC report, 1995). The effects are not well understood, however, owing to the inherent spatial and temporal variability of atmospheric aerosols, combined with uncertainty regarding tropospheric composition of aerosols and their single scattering albedo and phase function. This is a severe barrier to understanding the impact of atmospheric aerosols on global climate.

As a consequence of the poor quality of available knowledge of atmospheric aerosol distribution and scattering behaviour, instruments such as MISR are now generating information regarding atmospheric aerosol concentration and type (Martonchik *et al.*, 1998a). Rather than attempt to compensate for the scattering behaviour of the atmosphere, the nine cameras of the MISR instrument (four spectral bands) characterise atmospheric scattering at the various path lengths experienced by each camera. Pre-determined aerosol mixture models have been used in conjunction with radiative transfer models of scattering behaviour to pre-calculate TOA radiance values.

These are compared with measured radiance values in order to invert the actual aerosol scattering properties on a global scale. It is hoped that the creation of a detailed aerosol climatology will enable a far more accurate characterisation of the impact of aerosol forcing on global climate than has so far been possible. Further, it is notable that the use of multi-angle imaging (e.g. MISR, ATSR etc.) can be used to overcome the difficulty of separating the components of surface and atmospheric reflectance inherent in the measured signal.

2.3 Canopy reflectance: The forward and inverse problems

Monitoring vegetation using remotely measured data is a problem of the sort occurring in the observation of almost any complex physical system (Twomey, 1977; Gershenfeld, 1999). The solution in general is to construct a model of the system. If the model describes the interactions of the system sufficiently well (i.e. to some desired level of accuracy), then the model can be used to describe the outcome of the system based on chosen inputs. This is described as running the model in 'forward' mode or 'forward modelling' (Goel, 1992). If the model predictions are in agreement with the observed behaviour of the system, we can have some degree of faith in the ability of the model to predict the behaviour of the system under arbitrary input conditions. An important caveat is that no matter how good the agreement between the modelled and measured state of the system, the model can never truly be 'validated'. It is always prone to the twin problems that natural systems are never closed and that model results are always non-unique (Oreskes *et al.*, 1994). The primary cause of non-closedness in a natural system is 'noise': unwanted perturbations of the desired signal by factors outside immediate consideration. For example, the intervention of the atmosphere between the surface and a remote sensing instrument causes perturbation of the observed reflectance, as does the imperfect spectral response of the sensor. As a result, a single point on the Earth's surface may appear to have quite different reflectance if observed on different days, at different times of day or from different sensors. These effects can be modelled (Lucht and Lewis, 1999) but other factors such as the difficulty of accurately characterising generalised parameters and the sensitivity of the model inversion process to sampling (spectral and directional) conspire to make model validation difficult. This is an ever-present problem that must always be addressed carefully in modelling natural systems (Justice *et al.*, 2000).

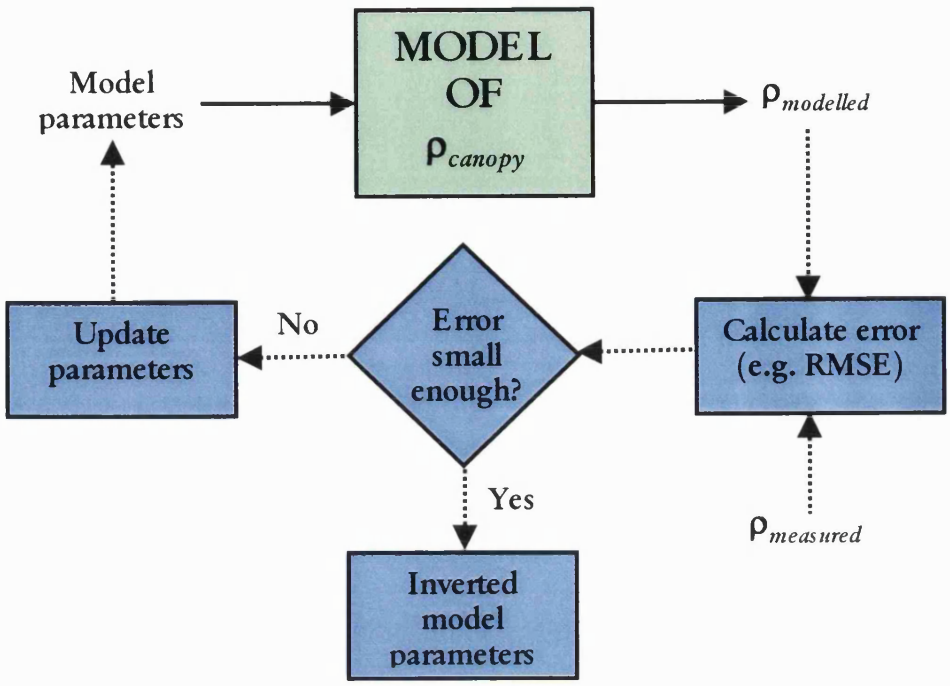

Figure 2.5 Schematic representation of forward and inverse modes of ρ_{canopy} model operation (solid lines represent the model in forward mode; dashed lines and blue boxes represent path taken during model inversion).

Having a forward model that adequately describes the state of a system is useful in that it may allow predictions on the future state of the system to be made. However, what is often of most interest is the set of parameters governing the system. How can information regarding these parameters be derived from the model? The solution is to 'invert' the model (or run the model in 'inverse' mode). This implies making observations of the system and then manipulating the model parameters so that the outputs of the model match the observations as closely as possible. It can then be postulated that the resulting parameter values are the values that cause the system to be in the measured state. This explanation relies on the fact that for any particular model state there exists a unique set of driving parameters (which in practice is never the case due to noise). However, model inversion against reflectance data provides a very powerful method of deriving information about canopy parameters from remote measurements. The generic forward and inverse process is illustrated schematically in figure **2.5**. The solid arrows in figure **2.5** represent the modelling process for linear systems, which can be inverted analytically. The dashed lines represent the iterative inversion process that is typically required to invert a non-linear model of ρ_{canopy}. The experimental work presented in this thesis aims to investigate the possibilities for vegetation canopy parameter retrieval from measured reflectance data, primarily using linear models developed for the MODIS sensor (Wanner *et al.*, 1995, 1997). To fully understand the way in which such models

can be applied, and the type of information it may be possible to retrieve, a good understanding of the various methods of model inversion, both linear and non-linear, is required.

2.4 Mathematical approaches to model inversion

There are many ways of inverting mathematical models. In simple linear systems an analytical solution may be found to the problem of inversion (ignoring for the moment any uncertainty due to noise in the observations) as long as the system is determinate. This implies the system is neither underdetermined (N unknowns, less than N equations), or overdetermined (more than N equations in N unknowns, none of which are a linear combinations of any others). Such a system can be inverted against observations using standard linear algebraic techniques, such as the method of linear least squares. This method is extremely widely used because of its simplicity and effectiveness.

The problem of inversion is relatively easy to state (if not always to carry out). It simply requires minimising some error function expressing the difference between modelled and observed reflectance values. Consequently, the first task in inverting a model of any sort, linear or non-linear, is to define a suitable error measure describing the difference between model values and measurements, which in practice contain noise of some sort. In least squares estimation, the assumption is made that random measurements of ρ_n are described by a Gaussian (normal) distribution. This assumption is supported by the Central Limit Theorem, which states that in the limit as N approaches infinity, the distribution of the means of N (independent) samples taken from any distribution approaches a Gaussian irrespective of the shape of the original distribution. This assumes that errors are equally distributed between positive and negative. In the absence of any other evidence a Gaussian is the most reasonable choice of probability distribution for a random variable. If no assumption is made about model variance, inverting a CR model is then a question of minimising the sum of the squared errors minimising e^2 (familiar least squares) i.e.

$$e^2 = \sum_{i=1}^{N} w_i \left[\rho_{i,observed} - \rho_{i,modelled}\right]^2 \qquad \textbf{2.11}$$

i = 1, 2 ... N is the number of observations and w_i the associated weights attributed to each observation The aim is therefore, to find values for which e^2 is a minimum, potentially by finding partial derivatives of e^2 with respect to parameter weights.

2.4.1 Linear inversion

The least squares method is often used in cases where the data are not necessarily normally distributed, but may not differ too far from the Gaussian assumption because of its simplicity and ease of implementation. It is not infallible however. Application of least squares to a bimodal distribution, for example, will result in a solution located between the two modes, where in reality there is only a very small probability of occurrence. Gershenfeld (1999) notes that the square of the difference between the modelled and measured values is not the only power that can be used: if the errors are distributed exponentially, the first power (the magnitude) is the maximum likelihood estimate; higher powers place more emphasis on outliers.

The next stage of model inversion is to obtain estimates of the parameters for the distribution that minimises equation **2.11**. In the case of linear models, standard linear algebraic techniques can be applied. In this case, it is assumed the data can be described by a linear summation of M model parameters, k_j i.e.

$$\rho = \sum_{j=1}^{M} f_j k_j \qquad \textbf{2.12}$$

f_j are the associated weights of each term. The task is then to find the f_i that minimise the sum of the squared errors between the model values, and a set of N observations ρ_n. This problem can be expressed in the form

$$\begin{bmatrix} k_1 & k_2 & \cdots & k_M \\ k_1 & k_2 & \cdots & k_M \\ \vdots & \vdots & \vdots & \vdots \\ k_1 & k_2 & \cdots & k_M \end{bmatrix} \begin{bmatrix} f_1 \\ f_2 \\ \vdots \\ f_N \end{bmatrix} = \begin{bmatrix} \rho_{obs,1} \\ \rho_{obs,2} \\ \vdots \\ \rho_{obs,N} \end{bmatrix} \qquad \textbf{2.13}$$

or, more concisely **Gm** = **d** (Twomey, 1977). In order to invert a generic linear model of this sort against observed values of reflectance and determine values of f_j that minimise **2.11**, a covariance-variance matrix of the model parameters, $k_{M,N}$, is formed by multiplying **G** by its transverse, **G'**. The variance-covariance matrix is then inverted, to give $[\mathbf{G'G}]^{-1}$. Multiplying $[\mathbf{G'G}]^{-1}$ by **d** then yields **m**, the vector of f_j values.

If the number of model parameters, M, is two or three, the variance-covariance matrix is trivial (and very quick) to invert. This is one reason why linear models have been favoured for many applications, as will be seen in later chapters. For larger order matrices however, inversion is not so simple. However, a variety of methods for performing this task exist, including various elimination and decomposition methods. Press *et al.* (1994) provide a readable and practical summary of some of these methods, as well as potential pitfalls of implementation and application. One such pitfall is deciding whether a particular system is over- or underdetermined. This is trivial for small systems (only a few model parameters and/or observations), but is not for systems where M and/or N are large. Further, very small changes in the numerical values of some coefficients can rapidly disturb the system from a determined to an underdetermined or indeterminate (contradictory) state. This can cause problems in real systems where measurements always contain noise and the model itself is a series of approximations. The power of linear methods is such that inversion of non-linear systems involving integral transforms is often reduced to linear systems for ease of handling via techniques such as numerical quadrature (Twomey, 1977).

2.4.2 Numerical inversion

If the model under consideration is non-linear, and an analytical solution is not generally available (as is most often the case), then further numerical techniques are available to allow inversion of the model (Press *et al.*, 1994; Gershenfeld, 1999). Such techniques can be complex, require a great deal of computational time and may prove to be a limiting factor on the effective application of a particular model. However there are enough techniques that are sufficiently robust and efficient for them to be in common use for inverting non-linear CR models. The following section briefly introduces some of these techniques. The reader is directed to Press *et al.* (1994) and Gershenfeld (1999) for detailed and extremely readable texts on linear and non-linear model fitting methods.

The basis of numerical inversion of a CR model is the same as that described previously for linear inversion i.e. the formulation of an error metric describing the 'goodness-of-fit' of modelled reflectances compared with observed reflectances (Goel, 1988; Pinty and Verstraete, 1990; Kimes *et al.*, 2000). The problem is then to find the minimum of the error function, which is an optimisation problem (minimisation in this

case). Optimisation problems are common in many fields, and as a consequence many tried and tested methods exist for their solution. Root mean square error (RMSE) is typically used as the error measure because of the assumption of normally distributed errors (equal probability of positive and negative errors), as in the linear least squares approach (Pinty and Verstraete, 1991). This is an optimal choice if no prior information regarding the form of the error distribution is available. However, it should be noted that this is not the only option (Tarantola, 1987). Numerical inversion is an iterative procedure and generally proceeds in the manner shown in figure **2.5**.

Inversion of a CR model against reflectance data is a constrained minimisation problem where some variables lie between fixed limits and cannot take on arbitrary (physically impossible) values. A solution resulting in physically unrealisable parameter values is not valid (or useful). In practice, parameter values should be constrained to lie within physically realisable limits during inversion (this is discussed in greater detail in appendix **1**). This is not simply a case of clamping parameters to boundary values when the boundaries are reached, as this equates to arbitrarily moving the location of the current solution on the N-dimensional error surface. Rather, the parameters should remain free but the penalty function (RMSE) should be heavily increased in some way (e.g. exponentially) as the solution heads out of bounds. In this way, subsequent iterations are 'encouraged' to move back in bounds by virtue of preferential (lower) RMSE (Press *et al.*, 1994).

All methods of optimisation are prone to the twin difficulties of avoiding local minima and knowing when to stop. Many optimisation methods, gradient methods in particular, tend to 'fall' straight down (local) minimum closest to where they started, rather than finding the global error minimum. Unless the characteristic length scale of the problem is known, this is likely to be the outcome. Knowing when to stop can also be difficult, and will depend on the accuracy required: better solutions require a great deal more work for successively smaller improvements. It is also important not to continue past the point where such 'improvements' are smaller than the floating-point precision of the machine on which the calculations are being performed (Press *et al.*, 1994).

2.4.3 Multidimensional minimisation

A range of multidimensional minimsation methods have been developed for solving optimisation problems of all types (Press *et al.*, 1994) and many of these have been applied to CR model inversion (Kimes *et al.*, 2000). Although they have mostly been developed for non-linear inversion problems, the distinction is now becoming blurred. As will be seen later, complex non-linear problems can often be well represented by much simpler linear approximations. Hence inversion becomes a hybrid process of linear and non-linear forward and inverse methods, depending on the speed and accuracy required for a particular application.

Some methods are based in the mathematical and computational theory of optimisation, including gradient (Acton, 1990) and simplex methods (Nelder and Mead, 1965; Press *et al.*, 1994). Algorithms requiring well-behaved, continuously differentiable error surfaces have generally been avoided as the error surfaces were not well-understood. Recent work however shows that such surfaces may actually be rather predictable (O'Dwyer, 1999; Barnsley *et al.*, 2001) and this knowledge may be used to restrict parameter space during model inversion.

Other optimisation methods exist which are based on observation of natural systems, which can solve immensely complex optimisation problems in simple and elegant ways. Simulated annealing mimics the thermodynamic properties of cooling crystalline solids (Press *et al.*, 1994), and is particularly suited to problems with error surfaces having many small local minima. Genetic Algorithms (GAs) seek to emulate the slow, incremental improvements of evolution via natural selection (Goldberg, 1998). Artificial Neural Networks (ANNs) approximate the ability of biological neural networks (i.e. brains) to solve complex optimisation problems (Pierce *et al.*, 1994). This is achieved by "training" an ANN to respond according to previously experienced situations, and adapting these responses to new situations. There are a number of examples of the application of ANNs to the problem of inverting biophysical parameters from optical and microwave data of vegetation canopies (Chuah, 1993; Jin and Liu, 1997; Abuelgasim *et al.*, 1996, 1998; Kimes *et al.*, 1997, 2000; Bicheron *et al.*, 1999; Gong *et al.*, 1999). ANNs have also proved very promising for the classification of EO data, where supervised methods (requiring training data) are already the norm (Foody, 1997).

Knowledge-based systems (KBS) comprise a variety of methods which use ancillary data to constrain the parameter space of the optimisation problem (Kimes *et al.*, 2000). An example is the work of Kimes and Harrison (1990) and Kimes *et al.* (1991) who developed a KBS incorporating spectral (directional) data with *a priori* information derived from literature, field data etc., into a system for inferring physical and biological surface properties from reflectance data. More recently, Strugnell and Lucht (2000) have demonstrated the use of BRDF 'archetypes' (broad classes of BRDF shape) to constrain inversion of BRDF models in the derivation of albedo. The justification is that within classes, the BRDF shapes of different canopies are likely to differ much more in terms of magnitude than shape. Between classes, shape is likely to be more important. This idea of "magnitude inversion" is currently being used in the production of MODIS land surface albedo product for pixels where unconstrained inversion is not possible e.g. through lack of samples of directional reflectance.

Look-up tables (LUTs) are potentially a more promising approach for CR model inversion than either ANNs (limited by training data) or KBS (potentially limited by the ability to describe ancillary data) (Kimes *et al.*, 2000). The LUT approach is to separate the calculation of CR from the problem of finding the optimum solution (model parameter set) to a specific model inversion. An arbitrarily detailed set of discrete CR scenarios can be pre-computed with an arbitrarily complex model and the corresponding parameter values are then stored in the LUT. The optimisation task is then to find the required parameter values in the LUT as quickly as possible, given a set of measured reflectance data (Kimes *et al.*, 2000). Knowledge of external parameters e.g. biome and cover type, viewing/illumination geometry etc. are used to limit the search space as far as possible. Closest matching parameters are then pulled out of the LUT yielding the inverted model parameter set. An important advantage of the LUT approach is that the majority of the computational load i.e. the repeated running of the forward model, is done prior to parameter retrieval and is therefore not a run-time operation. (Running *et al.*, 1996; Kimes *et al.*, 2000). In addition, as developments and improvements are made to the underlying CR model, the LUT can be recomputed and updated accordingly. Knyazikhin *et al.* (1998a, b) have developed a LUT algorithm for the retrieval of canopy parameters such as LAI and fAPAR from MISR data. O'Dwyer (1999) and Barnsley *et al.* (2000) examined the use of a LUT in the inversion of the widely-used CR model of Kuusk (1991). Simple grids of CR values of varying densities (two, three or four model parameters) were generated using the Kuusk model (Nilson and Kuusk, 1989) in forward

mode. They showed that in the region of the grid closest to the required solution, the error surfaces are likely to be smooth and well-behaved. As a result, the best solution can be found very rapidly by piecewise linear interpolation between the closest values in the grid. Barnsley *et al.* (2000) showed that in many cases the error surfaces are simple enough for coarse LUT grids of the order of 4 or 5 steps on a side to be employed, in conjunction with localized linearisation, with no significant loss of accuracy in inversion. Weiss *et al.* (2000) have also shown the effectiveness of LUT-based parameter retrieval, using (thresholded) average parameter values to interpolate between LUT grid points. In a further development, Combal *et al.* (2001) have shown that the use of prior information (e.g. ancillary biophysical and architectural measurements) can significantly improve the accuracy of biophysical parameter retrieval through LUT inversion of CR models.

2.4.4 Summary

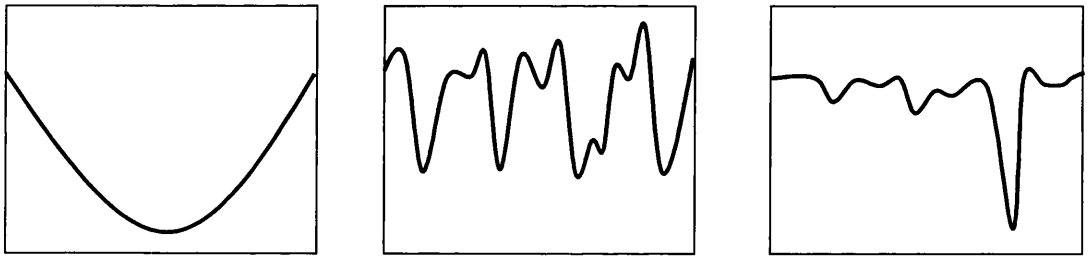

Figure 2.6 Three extreme types of error surface that may be encountered in function optimisation (after Gershenfeld, 1999).

The preceding section gives a brief overview of some of the numerical methods available for optimisation in CR model inversion. Gershenfeld (1999) illustrates the difficulty of selecting between these methods by subdividing all minimsation problems into three extreme categories (figure **2.6**). Each category lends itself to a different type of search. Smooth functions with a single well-defined global minimum are well-suited to gradient searches. Functions with many equally good nearby minima, but no global one, are suited to search by stochastic methods such as simulated annealing and GAs. The third case is characterised by many small local minim, and one clearly defined global minima, requiring some kind of global search method such as ANNs or LUTs. Paradoxically, large minimsation problems are often relatively simple to solve by virtue of having many possible solutions of nearly equal merit: finding one of these from any given starting point is not hard. Small problems are not hard either, as their size permits exhaustive search of the available solutions. Approaching the mid-point of these two size

extremes from either direction however the system becomes too large to search exhaustively, yet not large enough for many good solutions to be obvious. This emphasises the importance of considering the nature of the model, the starting parameter values, and, most importantly, the error function being searched. Information regarding any of these may dramatically improve the search regardless of which algorithm is used.

Of all the methods discussed in the preceding section, LUT-based inversion using localised linearisation appears to be the most promising recent development for improved retrieval of biophysical variables from measured reflectance. This is a result of their highly attractive properties: separation of the major computational load from the operational stage; independence from specific models of CR; rapidity of inversion due to the possibilities for coarse parameterisation; easy incorporation of ancillary data. Much of the experimental work in this thesis is concerned with the application and inversion of linear models of BRDF. However, the distinction between linear and non-linear methods is becoming blurred with the increasing use of LUT methods. Arbitrarily complex non-linear models can be used for populating the search space of canopy reflectance values. However, the search through parameter space during inversion can often be reduced to a linear problem, particularly if the parameter space can be constrained and/or something is known of the error surface itself.

2.5 Canopy reflectance modelling

Canopy reflectance, ρ_{canopy}, is known to be sensitive to a number of factors. These can be broadly divided into two categories:

i. **structural** i.e. the number, angular and spatial distribution of scattering elements.
ii. **radiometric** i.e. the scattering properties of individual canopy elements.

Vegetation components such as leaves and stems are radiometrically characterised by their reflectance (ρ) and transmittance (τ) (Jacquemoud and Baret, 1990). A complete canopy, on the other hand, is an aggregation of individual scattering objects. The total ρ_{canopy} depends on the nature of this aggregation, described by structural properties such as the area density, as well as the angular and spatial distribution (clumping) of scattering elements within the canopy (Ross, 1981; Qin and Liang, 2000). In addition to being a function of canopy (and atmospheric) parameters ρ_{canopy} will also be a function of the lower boundary beneath the canopy e.g. soil, snow, leaf litter etc. This boundary has its own radiometric and structural properties (microscopic and macroscopic roughness) which may contribute to the measured reflectance signal (Price, 1990; Hapke, 1993). Cierniewski (1987, 1999) and Cierniewski and Verbrugghe (1997) discuss impact of soil roughness on surface BRDF, particularly in relation to large aggregated scattering objects and their resultant shadowing. Nolin and Liang (2000) review recent developments in modelling the BRDF of particulate media, such as soil and snow.

Mathematical models of numerous forms have been developed in order to describe the scattering of radiation from vegetation canopies (Ross, 1981; Goel, 1988; Myneni *et al.*, 1989; Pinty and Verstraete, 1992; Strahler, 1994; Goel and Thompson, 2000). Models have been derived from sources including radiative transfer theory (Ross, 1975), planetary astronomy (Hapke, 1981) and many other areas of mathematics and engineering (Asrar, 1989). The diversity of influences on CR modelling may be regarded as one of the strengths of the field – the ability to adapt methods that have been developed and tested for a whole range of other applications. Approaches to CR modelling can be broadly divided into four categories described in sections **2.5.1** to **2.5.4** (Goel and Reynolds, 1989; Goel, 1992; Strahler, 1994). The following sections briefly describe some of the many modelling approaches, in particular their usefulness for derivation of biophysical parameter information from reflectance data.

2.5.1 Empirical models

Empirical models attempt to describe surface scattering by fitting some (usually simple polynomial) function to observed reflectance data i.e.

$$\rho = F(p) \qquad \textbf{2.14}$$

where F(p) is some arbitrary function not related to physical properties of the system under observation (Minnaert, 1941; Walthall *et al.*, 1985). The advantages of this approach are firstly that no assumptions are made regarding the type of canopy under observation i.e. whether it is largely homogeneous (e.g. grassland) or more spatially discrete (e.g. tree crowns in a forest canopy). Secondly, the chosen function can be arbitrarily complex in order to describe the surface reflectance behaviour to a desired degree of accuracy. In practice, functions are selected that remain simple enough to invert rapidly. The huge disadvantage of the empirical approach is that there is no physical basis linking the physical scattering behaviour of the canopy and the model coefficients. As a result, purely empirical models tend to be useful for correction/normalisation of directional effects in multi-angular reflectance data, but are of little use for deriving biophysical information (Roujean *et al.*, 1992; Cihlar *et al.*, 1994).

The simplest description of scattering from a surface is that credited to Lambert (Wolff *et al.*, 1992). All radiation incident on a Lambertian surface is reflected equally in all directions. In this case, the Lambert reflectance ρ_L (recall figure **2.1**) can be defined as (Hapke, 1981):

$$\rho_L = E_i \frac{\cos \theta_i}{\pi} \qquad \textbf{2.15}$$

E_i is the incident irradiance. The $\cos\theta_i$ term accounts for the reduced component of illumination incident on the surface with increasing illumination zenith angle θ_i, a consequence of the reduced surface area projected in the illumination direction. Reflectance from a Lambertian surface is therefore perfectly diffuse. Minnaert (1941) proposed a simple two parameter empirical model to describe observed brightness variations across the lunar surface. Reflectance is expressed as a function of θ_v and θ_i

$$\rho = \frac{c(\cos \theta_v \cos \theta_i)^k}{\cos \theta_i} = c(\cos \theta_v)^k (\cos \theta_i)^{k-1} \qquad \textbf{2.16}$$

where c and k are empirical constants. The model thus relates observed reflectance to purely photometric principles, and not to the nature of the observed surface. Hapke (1981) demonstrated that Minnaert's model appears to describe some surfaces well at a limited range of angles, but also points out that both c and k themselves are empirical functions of the scattering phase angle and are thus not strictly constants at all. The Helmholz (H) reciprocity condition is also satisfied by Minnaert's model i.e. the system appears the same if the viewing and illumination vectors are exchanged (Clarke and Parry, 1985). It should be noted that source/detector (S/D) reciprocity (which should not be confused with true H reciprocity) is violated in certain practical cases, particularly when considering reflectance at varying scales. This does not necessarily invalidate model assumptions or conservation of energy arguments (Li and Wan, 1998; Snyder, 1998; Chen *et al.*, 2000).

Walthall *et al.* (1985) proposed an empirical model more directly suited to describing ρ_{canopy}, and outlined applications such as describing directional soil reflectance as the boundary condition in a more complex CR model, or as a tool for studying directional effects in multi-angle reflectance data. BRDF is expressed as

$$\rho = a\theta_v^2 + b\theta_v \cos(\phi_v - \phi_s) + c \qquad \textbf{2.17}$$

ϕ_v and ϕ_s are the view and solar azimuth angles respectively; a, b and c are constants to be determined empirically. Walthall *et al.* (1985) justify the model form by noting that the θ_v^2 term describes the general upward 'bowl' shape of observed reflectance. ρ_{canopy} generally increases with $\theta_{v,i}$ due to the reduced amount of shadowed canopy viewed at these angles (Ross, 1981; Goel, 1988). Figure **2.7** illustrates this. The $\theta_v\cos(\phi_v-\phi_s)$ term provides a linear dependence of ρ on θ_v, which can account for observed anisotropy in surface reflectance i.e. increased reflectance in the back-scattering direction. The final constant c can be thought of as a 'brightness magnitude' term. Walthall *et al.* (1985) demonstrated the ability of their model to accurately fit a variety of measured BRDFs. Due to its simplicity and robustness the Walthall model has been applied in many cases (Barnsley *et al.*, 1997; Privette *et al.*, 1997; Lewis *et al.*, 1999a). As a linear model of three parameters it can also be simply and rapidly inverted. Walthall *et al.* (1985) updated their model with a fourth term to take account of θ_i, the sun position, although the model was not reciprocitous. Nilson and Kuusk (1989) modified the Walthall model to satisfy reciprocity, although this is not strictly necessary in BRDF applications (Chen *et al.*, 2000; Leroy 2001). The updated expression is as follows

$$\rho = a + b\theta_v\theta_i\cos(\phi_v - \phi_s) + c\theta_v^2\theta_i^2 + d(\theta_v^2 + \theta_i^2) \qquad \textbf{2.18}$$

This expression has been used extensively for both the correction of angular effects (Barnsley *et al.*, 1997b; Wanner *et al.*, 1997) and to represent directional soil reflectance as a lower boundary for more sophisticated CR models (Nilson and Kuusk, 1989). Huete (1989) reviews methods of modelling the soil contribution to remote sensing measurements of soil-canopy spectra.

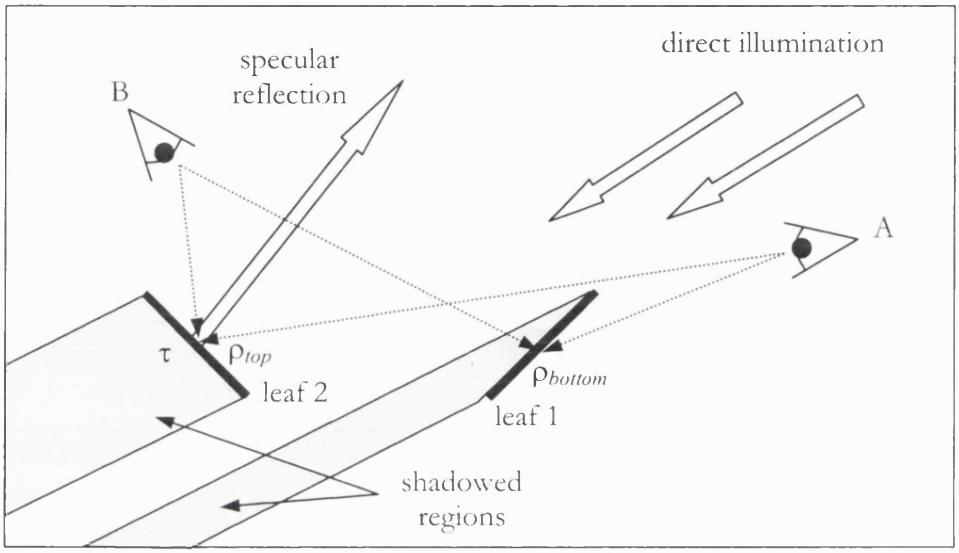

Figure 2.7 Canopy geometry contributing to BRDF (after Norman *et al.*, 1985). **A** sees the brightly lit top of leaf 2 and bottom of leaf 1, and very little of the shadowed regions. **B** sees much more of the shadowed top of leaf 1 and much less of brightly lit leaf 2. As a consequence, the scene appears much brighter to viewer A than viewer B due only to the canopy geometry

Empirical CR models may represent ρ_{canopy} well simply by their generic nature, but their domain of applicability is bounded by the limits of the measurements from which they were derived. A BRDF model may be required to extrapolate to angles beyond those from which the observations are taken (Wanner *et al.*, 1995), or to describe reflectance of canopy types not used in the model derivation. Empirical models are not strictly valid in this case. The largest drawback of empirical models for use in remote sensing of vegetation however is the lack of physical meaning in the model parameters. If biophysical information is required, then physically meaningful relationships between ρ_{canopy} and model parameters must be found (Asrar *et al.*, 1989).

2.5.2 Physically-based models

A great deal of effort has been devoted to development of physically-based models of surface scattering (e.g. Suits, 1972; Ross, 1981; Hapke, 1981, 1993; Goel, 1988; Myneni *et al.*, 1988a, 1989). A primary advantage of using physical models is that they are based on physical processes and so their parameters will have some physical meaning. It is also often possible to make reasonable *a priori* estimations of the model parameters, and to constrain them to physically realistic values during inversion. The following section presents a brief overview of various approaches to physically-based CR modelling. Concepts that will reoccur in later chapters are introduced, particularly in regard to simplifications of radiative transfer (RT) and geometric optic (GO) models of reflectance. Goel (1988, 1992) provides a comprehensive review of the theoretical basis of many of these methods (updated by Goel and Thompson, 2000). Qin and Liang (2000) review recent developments in RT modelling techniques, while Chen *et al.* (2000) do the same for GO modelling.

Strahler (1994) proposes that BRDF is a function of three distinct scattering processes:

1. Coherent superposition of scattered incident radiation. This can cause a retro-reflectance peak (hotspot), but is dependent on the mean free path between scattering events within the canopy being of the order of the wavelength of the incident radiation. Coherence is generally ignored for vegetation, but is important for soils (Hapke, 1984, 1993).
2. Scattering effects resulting from the arrangement of objects on the surface i.e. specular reflectance, and reflectance variations caused GO shadowing assuming parallel rays of incident radiation (Otterman and Weiss (1984), Li and Strahler (1985, 1986) for vegetation; Ranson and Daughtry (1987) for shrubs and snow; Cierniewski (1987) for soil). The scale of these effects ranges from microscopic roughness, to shadowing due to topography (Liang *et al.*, 2000a).
3. Volume (diffuse) scattering behaviour of aggregated canopy elements. This is particularly important for dense vegetation and is modelled using RT methods, based on the work of Chandrasekhar (1960). As higher orders of photon scattering are considered, the interactions become increasingly random in direction, and the volume scattering component tends to become isotropic.

In a complex physical system such as that of photon interaction with vegetation, often the only effective way to achieve a manageable[1] and tractable representation of the system is to make approximations. Typical requirements of a physical CR model are:

- To represent (selected/all) scattering features of the canopy in the spatial, spectral and angular domains.
- Agreement with ρ_{canopy} measurements of a real canopy of the same type to a specified accuracy (according to some criterion such as RMSE).
- To relate observed reflectance behaviour to the controlling biophysical parameters sufficiently well such that these parameters may be derived from measured reflectances through model inversion.
- To allow generalisations of theoretical treatments of canopy scattering based on observed scattering behaviour.

The following section describes some of the approaches that have been taken to simplify the physical approach to CR modelling, and highlights the diversity of models which have been developed for a huge variety of cases.

2.5.2.1 Canopy reflectance, the turbid medium and radiative transfer (RT)

One of the most powerful tools used in modelling canopy scattering behaviour is that of radiative transfer. RT theory was developed by Chandrasekhar (1960) as a method describing radiation transport in the gaseous clouds formed during stellar evolution. Chandrasekhar's idea has since been modified and applied in many fields, including canopy reflectance modelling. In this approach the canopy is approximated as a layer (or layers) of infinitely extended, plane-parallel homogenous scattering medium consisting of randomly oriented infinitesimal scattering phytoelements ('leaves'). This so-called 'turbid medium' approach is illustrated in figure **2.8**. The assumption of the canopy as a turbid medium allows a number of approximations and simplifications to be made regarding canopy scattering behaviour (Goel, 1988; Myneni *et al.*, 1989; Pinty and Verstraete, 1998).

[1] Manageable implies the problem can be represented to an acceptable accuracy, and is not prohibitively computationally expensive.

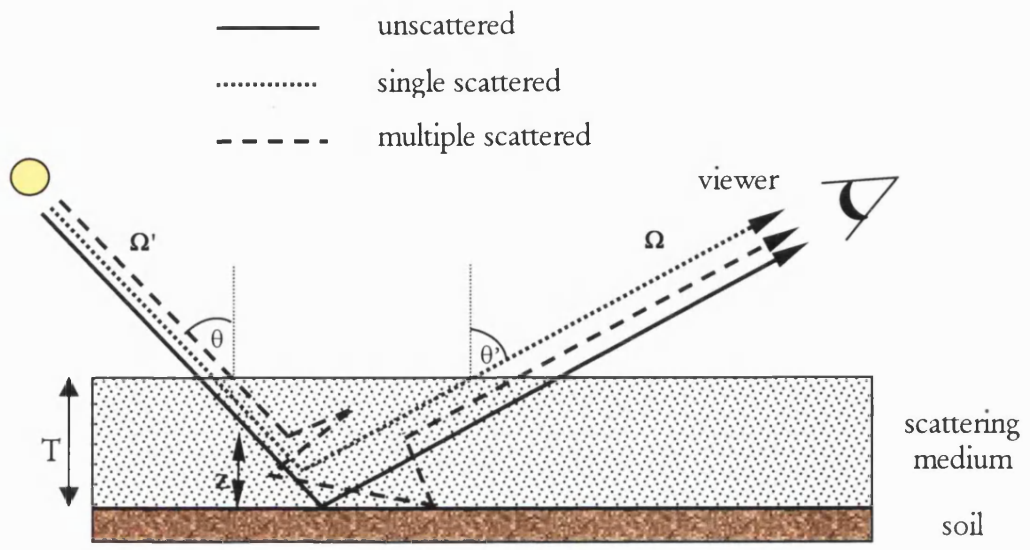

Figure 2.8 Schematic representation of the turbid medium approximation, showing the various scattered components of exitant radiation.

The turbid medium approach has proved a powerful technique modelling photon transport in vegetation canopies and has been applied widely to the problem (Ross, 1981; Goel and Strebel, 1984; Myneni *et al.*, 1988a,b; Myneni *et al.*, 1989; Qin and Liang, 2000). The radiance field resulting from single and multiple scattered photon interactions (see figure **2.8**) can be described by considering the conservation of energy within each canopy layer, and specifying the sources of radiation external to that layer (boundary conditions). The result is an integro-differential equation describing the change in intensity along a viewing direction **Ω** due to i) scattering interactions causing radiation to be scattered out of the illumination direction **Ω'** (sink term), and ii) interactions causing radiation to be scattered from other directions into the direction **Ω** (source term). If the so-called far-field approximation is made (Myneni *et al.*, 1990), whereby scattering elements are assumed to be infinitesimal and there is no mutual shadowing (and polarization, frequency shifting interactions and emission are disregarded) the problem of upward and downward energy fluxes within the canopy can then be represented as a solution of the well-known radiative transfer equation (Chandrasekhar, 1953) i.e.

$$-\mu\frac{\partial I(z,\mathbf{\Omega})}{\partial z}+\sigma_e(z,\mathbf{\Omega})I(z,\mathbf{\Omega})-\int_{4\pi}\sigma_s(z,\mathbf{\Omega}'\rightarrow\mathbf{\Omega})I(z,\mathbf{\Omega}')d\mathbf{\Omega}'=0 \qquad \textbf{2.19}$$

I(z, **Ω**) is the specific energy intensity at a height z within a horizontal plane-parallel canopy of total height T (0 < z < T) (so $\partial I(z,\Omega)/\partial z$ is the steady-state radiance

distribution function); σ_e is the extinction coefficient of the canopy medium; σ_s is the differential scattering coefficient for photon scattering from direction the illumination direction Ω' into a unit solid angle about the viewing direction Ω.

This problem has been studied extensively in astrophysics, planetary astronomy, particle physics and neutron transport among other fields, and many methods are available for its solution under certain conditions (Chandrasekhar, 1960). To solve equation **2.19** for a vegetation canopy, approximations regarding σ_c and σ_s are often made (Shultis and Myneni, 1988; Goel, 1988; Ross and Marshak, 1989; Myneni *et al.*, 1989, 1990, 1995b). Other approaches attempt to include modifications for observed features such as the hotspot (Nilson and Kuusk, 1989; Gerstl and Borel, 1992). Perhaps the most difficult problem in solving equation **2.19** is that of modelling the source term, as this requires keeping a 'scattering history' of each photon from one interaction to the next (Myneni *et al.*, 1991). This problem is to all intents and purposes insoluble analytically (Knyazikhin *et al.*, 1992), but approximations can be made (Myneni and Ganapol, 1991) or a computer simulation model can be used (see section **2.5.3**). It is also necessary to define the boundary conditions in the case of a canopy illuminated from above. At the top of the canopy the incident radiation can be considered to consist of diffuse and direct components of solar irradiation. In addition, some radiation arriving at the base of the canopy re-radiates isotropically back up through the canopy effectively creating a source function at the lower canopy boundary (Knyazikhin and Marshak, 2000).

Modified forms of equation **2.19** have been the basis for many detailed investigations into ρ_{canopy} (Gerstl and Zardecki, 1985; Goel and Grier, 1988; Shultis and Myneni, 1988; Ahmad and Deering, 1992; Rahman *et al.*, 1993a,b; Iaquinta and Pinty, 1994; Liang and Strahler, 1993b, 1994; Knyazikhin and Marshak, 2000). Further approximations and simplifications have been applied for specific types of canopy (e.g. Goel and Grier, 1988 for row crops). A variety of numerical techniques have been applied to solving RT in a vegetation canopy, including Successive Orders of Scattering Approximation (SOSA) (Myneni *et al.*, 1987a), Gauss-Seidel methods and discrete ordinates (Shultis and Myneni, 1988; Myneni *et al.*, 1988a). Perhaps the most widely-used simplification however, has been to treat single and multiple scattering interactions separately. A brief outline of these methods is given below.

2.5.2.2 Approximations made possible by the turbid medium approach

One of the most powerful approximations used in modelling reflectance behaviour is to concentrate on single scattering interactions within the canopy. Single scattering interactions are in most cases the dominant component of ρ_{canopy} (Myneni *et al.*, 1989; Myneni and Ross, 1990), particularly at visible wavelengths. Considering single scattering interactions within a turbid medium, the radiation intensity in the incident direction, Ω', at a depth z within the canopy can be described using Beer's law (Beer-Lambert law) (Monsi and Saeki, 1953):

$$I(\Omega',z)=I(\Omega',0)\exp\left(-\frac{L(z)G(\Omega')}{\mu'}\right) \qquad \textbf{2.20}$$

$I(\Omega',0)$ is the direct irradiance incident on the top of the canopy; L(z) is the downward cumulative LAI in the canopy at depth z (m^2m^{-2}). This is actually $u_l(z)$, the leaf area density (one-sided leaf area per unit volume of canopy at depth z in the canopy in m^2m^{-3}) integrated over all z. $G(\Omega')$ is the leaf projection function i.e. the fraction of leaf area projected in the illumination direction Ω'; μ' is the cosine of the illumination zenith angle, θ_i. $G(\Omega)$, the leaf projection function (in the viewing direction), is defined as

$$G(\Omega)=\frac{1}{\pi}\int_{2\pi+} g_l(\Omega_l)\left|\Omega_l \bullet \Omega'\right| d\Omega_l \qquad \textbf{2.21}$$

$g_l(\Omega_l)$ is the angular distribution of the leaf normals, Ω_l i.e. LAD. $g_l(\Omega_l)$ is typically assumed to be spherical for simplicity i.e. all leaf orientations are equally probable (Myneni *et al.*, 1988a, 1990). Although this is a widely used assumption, it can cause inaccuracies (Kimes, 1984; Goel and Strebel, 1984; Verstraete, 1987).

Beer's law as stated is for a perfectly homogeneous canopy, and the LAI parameter takes no account of the possibility of vegetation being clumped. This is highly unlikely in practice (Ross, 1981). If LAI is redefined as effective LAI, L_e, then a true LAI can be defined as $L = L_e/C$, where C is a clumping index (Ross, 1981; Nilson and Kuusk, 1989). If $C > 1$ then leaves are regularly dispersed within the canopy e.g. row crops; if $C = 1$ then leaves are dispersed randomly; if $C < 1$ then the canopy is clumped dense patches of vegetation interspersed with voids (gaps between the clumps). As clumping increases, L_e decreases, and the probability of gaps in the canopy increases leading to a higher soil reflectance for given LAI.

The assumption of the turbid medium, along with the approximations required to derive Beer's law, permits a description of the single scattering radiance field within a vegetation canopy as a function of a small number of simple structural parameters. A normalised leaf scattering phase function, $\Gamma(\Omega' \rightarrow \Omega)$, describing the angular distribution of scattering (from the illumination direction Ω' into the viewing direction, Ω) at each photon interaction (c.f. σ_s in equation **2.19**) and a joint gap probability, $Q(\Omega' \rightarrow \Omega, z)$, can be derived (Ross, 1981). Q describes the probability of existence of free lines of sight to the top of the canopy for a photon travelling from Ω' to Ω at a depth z within the canopy. Clearly, if a photon is unable to make it both down and back up to the top of the canopy, it will not emerge to be available for measurement (without further scattering). If the far-field approximation is made, then $Q(\Omega' \rightarrow \Omega, z)$ is simply the probability of photons travelling a distance z/μ' in direction Ω', multiplied by the probability of travelling z/μ in the direction Ω. The individual gap probabilities in the downward and upward paths can be calculated according to Beer's law (equation **2.20**).

The far-field approximation applies when scattering elements are small enough not to interfere with the joint gap probability, such as in neutron transport or cloud physics (Chandrasekhar, 1960; Dickinson, 1983). However this is not the case in a vegetation canopy where scattering elements have a finite size (Myneni *et al.*, 1989; Myneni and Asrar, 1993). Further approximations are required to circumvent this problem (Myneni and Ganapol, 1991; Myneni *et al.*, 1991; Knyazikhin *et al.*, 1992; Pinty and Verstraete, 1998). Single scattered ρ_{canopy} can then be expressed as a sum of the single scattered contributions from vegetation and soil, ρ^1_{soil} and $\rho^1_{vegetation}$. ρ^1_{soil} is simply the probability of a photon penetrating to the base of the canopy (z = 0) and escaping again, multiplied by the soil reflectance. Using Beer's law

$$\rho^1_{soil}(\Omega', \Omega) = Q(\Omega' \rightarrow \Omega, z)\rho_s(\Omega', \Omega) \qquad \textbf{2.22}$$

$\rho^1_{vegetation}$ can be shown to be (Ross, 1981)

$$\rho^1_{vegetation}(\Omega', \Omega) = \frac{\Gamma(\Omega' \rightarrow \Omega)}{G(\Omega')\mu + G(\Omega)\mu'}\left[1 - \exp\left(-L\frac{G(\Omega')\mu + G(\Omega)\mu'}{\mu\mu'}\right)\right] \qquad \textbf{2.23}$$

Thus single scattering ρ_{canopy} is a function of both structural (LAI, $g_l(\Omega_l)$) and radiometric parameters (leaf and soil reflectance, leaf transmittance, τ_{leaf}). $G(\Omega_l)$ requires the evaluation of an integral (equation **2.21**) so any attempt to find an analytical solution

for equation **2.23** requires approximations regarding $g_l(\Omega_l)$ to be made. Many models simply assume a spherical LAD (Goel, 1988) i.e. all leaf angles are equally likely, in which case $g_l(\Omega_l)$ is 1 and $G(\Omega_l)$ is 0.5 (Asrar *et al.*, 1989; Myneni *et al.*, 1989). Other approaches include the discrete geometrical distribution of Bunnik (1978) based on observed data; the continuous two-parameter beta distribution of Goel and Strebel (1984); the elliptical distribution of Nilson and Kuusk (1989), controlled by mean leaf angle and eccentricity parameters.

Equation **2.19** can be further simplified if the assumption is made that ρ_{leaf} and τ_{leaf} can be considered Lambertian (bi-Lambertian) and equal (i.e. $\rho_{leaf} = \tau_{leaf}$) (Ross, 1981). In this case, single scattered canopy reflectance, ρ^1_{canopy} can be described as

$$\rho^1_{canopy} = \frac{4\rho_{leaf}}{3\pi} \frac{\left[\sin\gamma + \cos\gamma\left(\frac{\pi}{2} - \gamma\right)\right]}{\mu + \mu'} \left[1 - \exp\left(\frac{-L}{2}\frac{\mu + \mu'}{\mu\mu'}\right)\right] + \rho_{soil}\exp\left(\frac{-L}{2}\frac{\mu + \mu'}{\mu\mu'}\right) \qquad \textbf{2.24}$$

where γ is the phase angle between θ_i and θ_v. This relatively simple analytical expression has been widely used in practice (Wanner *et al.*, 1995, 1997) and forms the basis of some of the semi-empirical models described in section **2.5.4**, which are the basis of much of this thesis.

Many models have been based on the approach outlined above (Goel, 1988), originating from the work of Monsi and Saeki (1953). The major assumption underpinning Beer's law is that the number of scattering objects in a volume of canopy (leaves, stems etc.) is proportional to its volume. However, Knyazikhin *et al.* (1998c) show that the structure of vegetation canopies may in some cases be fractal in nature, resulting in non-linear relationships between canopy volume and the density of scattering elements. They suggest that modifications may need to be made to extend the applicability of Beer's law in such cases. However, it has been shown that the basic formulation of Beer's law can be a useful tool in describing single scattering interactions within the canopy (Monsi and Saeki, 1953).

Approximations based on the turbid medium approach have been widely applied to describing ρ_{canopy}. Although single scattering interactions dominate ρ_{canopy} at visible wavelengths (typically 95% of total reflectance), the multiple scattered component of ρ_{canopy} becomes important if scattering in the near-IR region is considered (up to 50% of

total reflectance). As a result, approximations to the multiple scattering component of ρ_{canopy} have also been developed (although the multiple scattered component may be important in magnitude, it is less so in terms of BRDF as a result of the tendency of multiple scattered radiation to be scattered in all directions). Descriptions of multiple scattering are typically based on simplifications of and approximations to the RT equation (equation **2.19**), some of which are described briefly below. The remainder of this thesis concentrates on consideration of the single scatterering component of ρ_{canopy} so a detailed description of the many formulations for canopy multiple scattering approximations is not given here. Myneni *et al.* (1989) and Qin and Liang (2000) review these methods in detail.

2.5.2.3 Limitations of the turbid medium approach

A major drawback of the turbid medium approach is that the size of the scattering objects within the canopy is not considered. By definition, the canopy is assumed to be a homogeneous medium of infinitesimal scatterers (to satisfy the far-field approximation) with mutual shadowing not permitted. Consequently, expressions describing the reflected radiation from such a canopy do not contain information regarding the size of scattering objects (Qin and Liang, 2000). However, certain properties of observed ρ_{canopy}, particularly the hotspot, are directly controlled by the size and orientation of scattering objects (Kuusk, 1985; Hapke, 1986; Marshak, 1989; Jupp and Strahler, 1991; Pinty and Verstraete, 1998). Turbid medium approximations will not capture such features, and if the size of scattering objects is to be considered a different approach is needed. Myneni *et al.* (1991) considered voids between finite dimensional canopy elements in order to model the dimensions of scattering elements explicitly. Their model represents the hotspot feature quite accurately and gives far better agreement of scattered reflectance in the hotspot direction than treatments than those which ignore scatterer size.

In a series of excellent papers discussing the theory of diffuse scattering from particulate media, Hapke (1981, [and Wells] 1981, 1984, 1986) developed a comprehensive model of bidirectional reflectance from the RT theory of Chandrasekhar (1960) for use in planetary astronomy. Hapke constructed an analytic expression describing the bidirectional reflectance from a particulate surface, formulating analytic expressions for (amongst other things) single scattering albedo, integral phase function

and bihemispherical radiance. The importance of Hapke's approach is the analytical nature of his model, and the inclusion of a hotspot term. Hapke's approach has been successfully applied, with modifications, to modelling ρ_{canopy} (Verstraete *et al.*, 1990; Pinty and Verstraete, 1991; Iaquinta and Pinty, 1994). Single and multiple scattering are treated separately with the single scattered radiation being characterised exactly and the multiple scattered radiation being approximated using a two-stream approach. This can cause errors however, because of the greatly increased multiple scattering occurring in the near-IR wavelength region (Liang and Strahler, 1994) as described above. Others have proposed a more exact four-stream approximation for the solution of multiple scattered radiation (e.g. Liang and Strahler, 1995). Some of the earliest developments in CR modelling used the two-stream approximation in order to describe the radiation field in a canopy. Suits (1972) used a four-stream approximation to calculate radiation intensity from the projected horizontal and vertical canopy scattering elements. This approach was extended by Verhoef (1984) to handle arbitrary leaf angles in the widely-used Scattering by Arbitrarily Inclined Leaves (SAIL) model.

Separation of canopy fluxes into uncollided and collided intensities of various orders (Kubelka and Munk, 1931; Suits, 1972; Hapke, 1981) has often been employed in order to simplify the RT approach (Myneni *et al.*, 1990; Verstraete *et al.*, 1990; Iaquinta and Pinty, 1994; Gobron *et al.*, 1997). The discrete properties of the canopy (those related to the size and distribution of scatterers) tend to impact only the first few orders of scattering. As the scattering order increases, these features tend to become 'smeared out' by the multiple scattering interactions (Marshak, 1989; Liang and Strahler, 1993a; Iaquinta and Pinty, 1994). Dividing the radiation field into collided and uncollided intensities as opposed to following a standard RT treatment may preserve these features. Hapke's original theory has been extended, notably Verstraete *et al.* (1990), Dickinson *et al.* (1990) and Iaquinta and Pinty (1994), to overcome the inability to account for finite sized scattering elements. Ahmad and Deering (1992) added a specular reflection term to Hapke's empirical hotspot term, resulting in a relatively straightforward analytical model which agreed well with various measured reflectance data. But the number of model parameters (8) and the coupling between them limits the use of the model for inversion of biophysical information.

The above discussion illustrates how the behaviour of a real vegetation canopy is likely to diverge rapidly from classical RT theory as a result of finite leaf size (Myneni

and Ganapol, 1991). As the canopy becomes denser, mutual shadowing cannot be ignored (Myneni *et al.*, 1991; Myneni and Asrar, 1993). It also becomes increasingly difficult to justify using convenient values of scattering phase function, leaf normal distribution and leaf projection function based on the assumption that leaf normals are randomly oriented and azimuthally invariant. This is clearly partially or wholly violated for a number of canopies, particularly row-oriented agricultural crops. Verstraete *et al.* (1990) proposed replacing the components of the full RT treatment explicitly dependent on leaf size and orientation (e.g. σ_s and σ_c, which are impossible to characterise exactly for a large canopy of many leaves) with a parameterised average description. However, accounting for the discrete nature of vegetation within a RT (continuous) description of the canopy radiation regime leads to an apparent paradox (Knyazikhin *et al.*, 1998c): the more accurate the representation of canopy geometry, the less accurate the description of radiation transport and photosynthesis in the canopy is likely to be. Knyazikhin *et al.* (1998c) use a fractal description of a plant stand at scales at which the assumptions underlying the RT approach break down (i.e. at leaf level) to demonstrate the difficulty of scaling the RT approach from leaf to canopy scale.

Once the size of scattering elements in the canopy is considered, gaps between the scatterers must also be considered. Myneni and co-workers have developed a model based on considering the canopy as a binary medium of convoluted voids (gaps between leaves) only broken by the leaves themselves (Myneni *et al.*, 1991). Further problems are caused by the fact that the diffuse component of illumination impinging on the canopy will itself contain a component of radiation reflected back from the top of the canopy (Knyazikhin and Marshak, 2000). A number of authors have considered this problem, and various coupled surface-atmosphere scattering models have been developed (Rahman *et al.*, 1993a,b; Liang and Strahler, 1994). These models can significantly improve agreement between measured and modelled reflectances, at the expense of model complexity. Solution of the RT equation in a vegetation canopy is still a complex problem, however, despite all approximations. As a result, inversion of such models must also be performed numerically, or using LUTs. Additionally, the approximations made in order to formulate equation **2.29** result in the driving parameters of such models being relatively far-removed from parameters directly representative of physical canopy properties.

2.5.2.4 Geometric-optic (GO) models

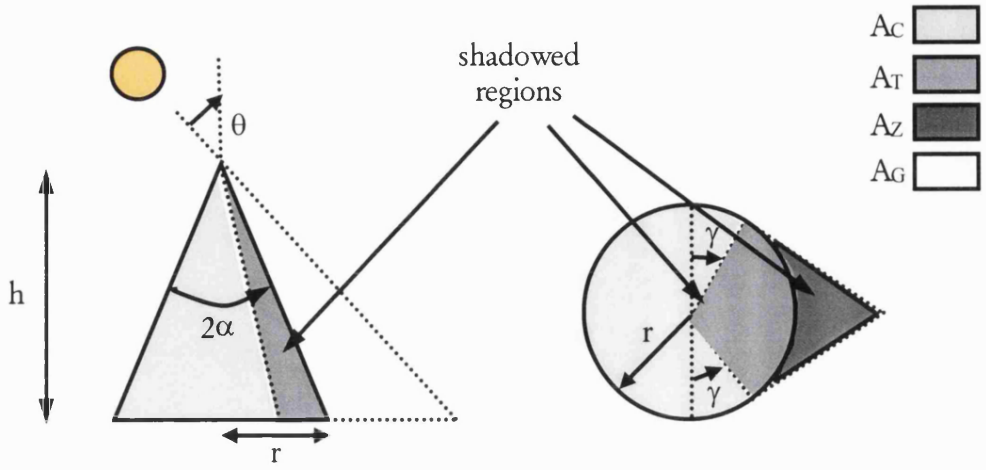

Figure 2.9 Geometry of an illuminated cone and its shadow. $A_{C/T}$ = sunlit/shaded crown, $A_{G/Z}$ = sunlit/shaded ground (after Li and Strahler, 1985).

In direct contrast to the turbid medium approach, GO models of ρ_{canopy} describe surface scattering due to discrete objects (spheroids, blocks, cylinders etc.) arranged on a surface under the assumption of parallel-ray geometry. This approach is exemplified by the work of Li and Strahler (1985, 1986, 1988, 1992) in a series of papers investigating the use of cones and spheroids to model the scene variance of forest canopies. Their work extended that of Egbert (1976), and Otterman and Weiss (1984) who were able to explain a significant proportion of the measured reflectance of soybean using a model composed of thin, vertical cylindrical protrusions. Significantly, they concluded that while retrieving the reflectance of the cylinders through inversion of the model might be possible, retrieval of the projected shadow (effectively the cylinder size) would not.

Li and Strahler postulated that a typical forest canopy comprises large, discrete crowns of a variety of shapes, separated by relatively large intervening spaces. They considered simple geometric objects (cones) with a lognormal height distribution and known number density located randomly on a Lambertian plane. The resulting areal proportions of sunlit and shadowed canopy and soil components were then calculated using GO theory. This is illustrated in figure **2.9**. The scene geometry is controlled by r, the cone base radius; α - half the crown apex angle; h, the crown height; γ is the angle identifying the portion of the cone illuminated beyond the cone half ($\sin^{-1}(\tan\alpha/\tan\theta)$). Scene reflectance is divided into four components: sunlit crown, sunlit ground, shadowed crown and shadowed ground. The geometry of a particular scene is calculated according

the size and density distribution of objects, and the average reflectance of a scene pixel is then a linear sum of the various areal proportions i.e.

$$S = \frac{(A_G G + A_C C + A_Z Z + A_T T)}{A} \qquad \textbf{2.25}$$

$A_{G,C,Z,T}$ are the areas of illuminated background and crown, and shadowed background and crown respectively; G, C, Z, T are the multispectral reflectance vectors for unit areas of illuminated background and crown, and shadowed background and crown respectively. Variations in S are caused by variations in crown density and size in each pixel. Initially the model was formulated for non-overlapping cones, but a general case based on the theory of the moments of overlapping areas has been developed (Li and Strahler, 1992). Cierniewski (1987, 1999) followed a similar approach in formulating a model of soil reflectance by calculating the shadowing of a square grid of equally sized spheres on an arbitrarily inclined plane.

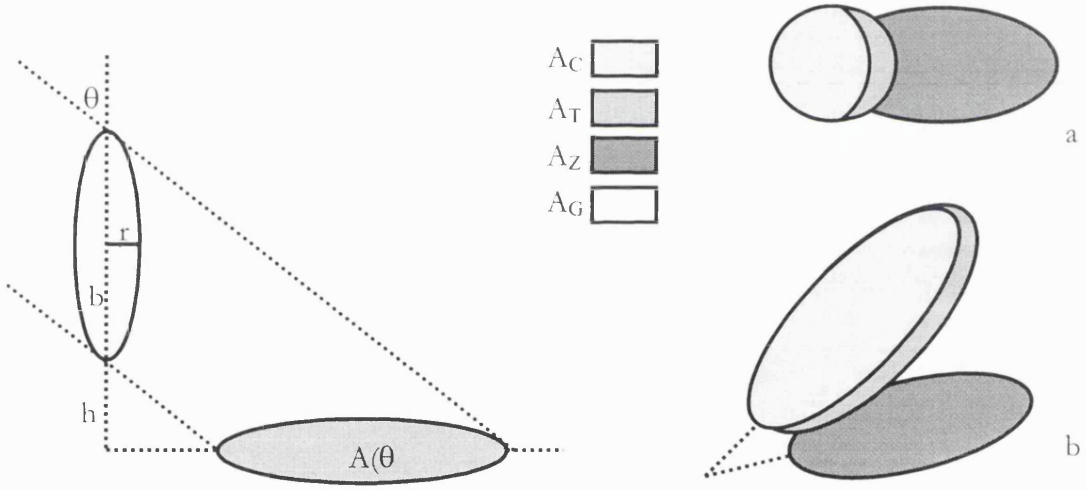

Figure 2.10 (left) Geometry of spheroid-on-a-stick with shape controlling parameters and shadowed area A(θ) (right) nadir (a) and off-nadir (b) areas of illuminated shadow ($A_{C,T,Z,G}$ = as in figure **2.9**) (after Strahler and Jupp, 1990).

Strahler and Jupp (1990) extended the GO approach, using Boolean models of random set overlap to model the BRDF of forest and woodland as a collection of randomly located 'spheroids on sticks'. This is illustrated in figure **2.10**. The spheroids, with major and minor axes b and r respectively, are located a height h above the surface (the concept of the stick is merely to indicate height above the surface). The nadir and off-nadir illumination and shadow components of the scene are also shown. The model treats the areal proportions of sunlit and shadowed components at both the scene level and the leaf level, resulting in a two-stage model. Chen and Leblanc (1997) have examined

the application of GO modelling at scales larger and smaller than tree crowns, and in particular the impact of the departure from the Lambertian assumption with varying scale.

The GO approach has been further developed by consideration of a vegetation canopy as a collection of scattering elements located within a GO "envelope". Scattering within the envelope can be handled using some model of attenuation (e.g. Beer's law, or a full RT approach), whilst shadowing at canopy stand-level is modelled using the standard GO theory discussed above. This hybrid GO-RT approach (Li *et al.*, 1994, 1995) relies on the calculation of gap probabilities between crowns and the path lengths within crowns (Li and Strahler, 1988). Roujean *et al.* (1992) follow a similar line to that of Li *et al.* (1994) by combining non-overlapping opaque blocks randomly located on a Lambertian surface modelled using GO theory, with an RT description of the attenuation within the blocks. Goel and Grier (1988) modelled reflectance of inhomogeneous canopies by combining the GO and RT approaches with some success. In a similar way, Bégué (1992) models the directional reflectance of regular-clumped canopies by considering (radiometrically) porous cylinders located on a hexagonal grid. This hybrid approach combines the benefits of the GO approach i.e. the inherent ability to describe the discrete nature of a discontinuous canopy (shadowing, hotspot, crown size etc.), with the RT approach to scattering within the crown envelopes (accurate description of radiation interception and multiple scattering). For this reason both GO and RT models are considered in the semi-empirical approach described in section **2.5.4**.

2.5.3 Computer simulation models

To solve the RT problem of photon scattering in a homogeneous medium, approximations regarding the size, orientation and spatial distribution of scatterers within the canopy are required. An ideal solution would specify these properties in 3D for every scattering element in the canopy in order that the behaviour of every photon could be modelled physically. This implies an enormous number of parameters controlling ρ_{canopy} making it impossible to invert such a model directly. However, with increases in computing power and memory it is possible to construct physically detailed 3D models which can be run in the forward mode. The results of these models can then be used to test the assumptions and approximations that are made in the physically based models described above (Govaerts, 1996; Kuusk *et al.*, 1997; Disney and Lewis, 1998), or to

populate LUTs for indirect inversion algorithms (Kimes *et al.*, 2000). There are two primary methods for implementing "scene simulation" models, ray tracing (based on a Markov chains) and radiosity (originating from thermal engineering). Both these methods have benefited (particularly in terms of practical implementation) from developments in computer graphics (CG) (Goel, 1988; Goel and Thompson, 2000).

2.5.3.1 Ray Tracing

Ray tracing is a method of rendering realistic images of 3D scene representations through detailed modelling of scene illumination and shading (Foley *et al.*, 1992). Ray tracing essentially involves calculating the intersections of rays (photons) "fired" into a 3D scene with the objects in the scene, and determining the behaviour of the photons at each intersection. The subsequent direction and energy of a scattered photon following an intersection is governed by the radiometric properties of absorption, transmission and reflection of the surface at the point of intersection in addition to the geometric scattering properties (phase function) of the object. Objects are not limited to representation by simple polygons. Volumetric objects (treating scattering through radiative transfer) can be used, in conjunction with a description of the (volumetric) scattering properties of the materials contained within (North, 1996). Shadows can be simulated by the casting of 'shadow' rays from objects to the light source and diffuse sampling can also be used to simulate diffuse light sources (Govaerts, 1996; Lewis, 1999). Realistic depiction of the bidirectional reflectance of any scene (represented as a collection of 3D objects) can be simulated by repeating the sampling process for every sample (pixel) in the viewing plane (Disney *et al.*, 2000).

Ray tracing is computationally expensive compared to ρ_{canopy} models based on RT or GO approaches. Every object within a scene must be represented accurately in 3D along with associated radiometric properties, and this information must be stored in memory. Intersection tests are carried out for each fired ray to see where (if at all) they intersect the scene, and for each subsequent interaction (and for shadowing). In addition, to achieve a convergent solution (representing the scattering behaviour of the scene to within some accuracy threshold) some form of numerical integration, typically Monte Carlo sampling (Press *et al.*, 1994; Veach, 1997) is used. Clearly, the more detailed the scene, the more calculations are required for each photon. Objects within the scene are

composed of polygonal or volumetric primitives, and the primitives can be chosen to be of arbitrary size – larger for coarser representation but quicker calculation and lower storage requirements; smaller for finer detail, but requiring more processing and storage. A range of variance reduction techniques and CG methods, such as the use of bounding-boxes, can be used to further speed up the ray tracing process (Disney *et al.*, 2000).

A variety of implementations of ray tracing have been developed for remote sensing scene simulation. Ross and Marshak (1988) developed a simple model for radiometric scene simulation. Goel *et al.* (1991) demonstrated ray tracing for simulating reflectance of corn plants. The model of Govaerts (1996) has been used for comparison with a variety of RT modelling techniques (Govaerts *et al.*, 1995; Gobron *et al.*, 1997) and target BRDFs. Govaerts (1996) and Lewis (1999) have used ray tracing to simulate the timed-return signal of LiDAR (Light Detection and Ranging) instruments, which are an interesting new development for probing vegetation canopy structure (Dubayah *et al.*, 1997). Chelle and Andrieu (1999) have used ray tracing to validate a physically-based CR model (Kuusk *et al.* 1997). North (1996) developed a ray tracing model to simulate GO ρ_{canopy} in forest stands (Gerard and North, 1997), as well as for simulation of synthetic Along-Track Scanning Radiometer (ATSR-2) data. The BRDF modelling community has recently initiated an ongoing model intercomparison exercise, RAMI (RAdiation Transfer Model Intercomparison, Pinty *et al.*, 2001 and www[2.2]). The aim of the exercise is to establish the strengths and weaknesses of BRDF models of all types, in a carefully controlled model "bake off". The ongoing RAMI exercise has shown that ray tracing models are the most flexible, if slower than other types of model. The trade off is that they can simulate almost any conceivable canopy configuration and hence can be used to benchmark more approximate models.

2.5.3.2 Radiosity

Radiosity methods originated in thermal engineering and have been adapted for realistic scene simulation techniques in computer graphics (Goral *et al.*, 1984). In contrast to the view/illumination oriented approach of ray tracing (all calculations based on a particular viewing/illumination configuration), radiosity is based solely on the scene geometry. All energy emitted or reflected by every surface in a scene is accounted for by its reflection and absorption by other surfaces (Foley *et al.*, 1992). The rate at which

energy leaves a surface (the radiosity) is then simply the sum of the rates at which the surface emits energy and reflects or transmits it from other surfaces. To calculate BRDF, all light interactions in an environment are calculated independent of view (the so-called 'view' or 'form factors' of each surface). Scene radiosity can be calculated very simply for an arbitrary view. Radiosity is even more computationally expensive than ray tracing when the view factors are being calculated, but this need only be carried out once for any particular scene/illumination scenario (the two methods reduce to essentially the same solution calculated in different ways under certain conditions). Borel *et al.* (1991) show that radiosity methods can be used to simulate scenes for use in analysis of remotely sensed data. They apply the radiosity method to modelling a layered plant canopy, and draw parallels between the radiosity and RT solutions. Qin and Gerstl (2000) have coupled 3D plant models (derived from L-systems) with radiosity to simulate reflectance of semi-arid scrubland. Their results agree well with field, and provide further proof that explicit 3D plant modelling in combination with radiosity or ray tracing methods can be extremely useful in scene simulation at a range of scales.

2.5.3.3 Other numerical CR modelling methods

Another interesting numerical approach is that adopted by Gastellu-Etchegorry *et al.* (1996) in their DART (Discrete Anisotropic Radiative Transfer) model, which is some way between ray tracing and radiosity. Based on the 3D canopy transport model of Kimes and Kirchner (1982) DART simulates RT in heterogeneous 3D scenes that may contain many elements. A scene is simulated as a 3D matrix of parallelipipedic cells (voxels), and the phase functions of each cell are calculated from the scattering behaviour of the elements contained within the cell. DART significantly extends the Kimes and Kirchner model as it can cope with non-uniform, unequally spaced cells, and multiple scattering processes within cells. The microwave model of Sun and Ranson (1995) is functionally similar to that of Gastellu-Etchegorry *et al.* (1996) in that a solution is formed over 3D gridded (voxel) space. This raises the prospect of coupled microwave and optical models of canopy response based on 3D structural canopy representations. This appears to be a realistic and sensible goal in that in both cases, the models are designed to describe the physical interaction of light with matter; the difference is only one of wavelength of the incident radiation. This approach might also be extended to a third domain: thermal wavelengths.

The major advantage of the explicit 3D representation of geometry required for ray tracing and radiosity is that every object within a canopy can be represented to whatever level of detail is required or is convenient. Ray tracing is ideally suited for precisely modelling the scattering processes used in RT techniques as leaves and voids in the canopy are modelled explicitly. Assumptions that are made in such models regarding the size and orientation distribution of scattering elements within a canopy can also be modelled explicitly. Clearly this type of complex numerical model cannot be inverted directly but such models can be very useful for testing the approximations made in other (invertible) scattering models designed. Further, the development of LUT methods make it increasingly feasible to invert biophysical information from such models, albeit indirectly.

2.5.3.4 BPMS/ararat model

Simulation of ρ_{canopy} used in chapters 4-7 of this thesis is undertaken using the 3D model of Lewis (1999). This forms part of the Botanical Plant Modelling System (BPMS) (Lewis and Muller, 1990; Lewis, 1996, 1999) which has been used for simulating canopy radiation for a wide range of purposes (Lewis, 1996; Lewis and Disney, 1997, 1998; Disney *et al.*, 2000). The BPMS essentially consists of software tools and protocols and for capturing, representing and processing 3D data representing the canopy-soil system; Ararat (the Advanced Radiometric Ray Tracer) is a Monte Carlo ray tracing tool for simulating the radiation regime within the 3D canopy.

3D canopy architecture can be specified within the model in a number of ways e.g. from photogrammetric measurements, or through the use of growth rules, such as a modified L-systems approach (Prusinkiewicz and Lindenmayer, 1990; Prusinkiewicz, 1999). L-systems have proved eminently suitable for the development of 3D plant and canopy models (de Reffye *et al.*, 1988; de Reffye and Houllier, 1997; Prusinkiewicz, 1999). 3D representations of individual plants can be constructed within the BPMS from manual measurements of a few key structural parameters, such as leaf and stem lengths and widths, leaf base and tip zenith and azimuth angles etc. These properties are extrapolated (using specified functional relationships) to a full 3D representation of individual plants (surfaces are tessellated with polygons, triangles by default, during ray

tracing). Individual plants can then be 'cloned' (duplicated with arbitrary rotation and translation) and then 'planted' on a surface according to some predefined pattern to build up a full canopy.

The ray tracing part of the BPMS (ARARAT, the Advanced RAdiometric RAy Tracer) is also very flexible, having been designed specifically for investigating scattering in plant canopies. Information can be stored as a function of scattering order within a simulated scene, permitting analysis of multiple scattering (Lewis and Disney, 1998). Arbitrary camera models can be used (e.g. allowing integration over the entire viewing hemisphere in order to directly simulate albedo), as can texture mapping, material mapping and diffuse sampling. Associated information such as the proportions of sunlit and shadowed canopy components can also be calculated (Lewis, 1999). The BPMS can incorporate ancillary data in addition to measured plant parameter data, such as row and plant spacing, seed depth, digital elevation models (DEMs) of the underlying soil surface etc. This flexibility make the BPMS an extremely useful tool for examining BRDF model operation (Lewis and Disney, 1997, 1998; Disney and Lewis, 1998) as well as more general properties such as spatial variation of ρ_{canopy} (Lewis *et al.*, 1999b).

The experiments described in chapters **4-6** use values of ρ_{canopy} simulated from 3D plant data measured in the field, processed via the BPMS plant modelling software, and rendered by the ray tracing component, *ararat*. The BPMS/Ararat model was chosen because of its flexibility as well as the capability for analysing canopy radiation as a function of canopy parameters. Several other models are used in the experimental chapters of this thesis, and these are listed below with an explanation of where and why they are used, as well as indications as to where more detailed descriptions of each model can be found.

Table 2.1 Canopy reflectance models used in this thesis.

Model	Used	Reason	Details
BPMS/ararat	Chapters 4-6	Flexibility: can represent full 3D structure at arbitrary scale, and simulate radiation under arbitrary viewing and illumination conditions.	Canopy simulation carried out using Monte Carlo ray tracing, in reverse mode (rays traced from viewer back to illumination source), with importance sampling at each ray intersection. More details in Lewis (1996, 1999).
Linear kernel-drive	Referred to and/or used in chapters 4-7.	Basis of thesis: models are currently in use generating MODIS albedo product. Assumptions underlying these models are tested using BPMS/Ararat model.	Simple semi-empirical, kernel-driven models, based on more complex physical models of BRDF. Described in detail in section **2.5.4**
Kuusk	Chapter 7	Used for simplicity & rapidity to simulate spectral directional reflectance samples for testing of with spectral kernels.	Physical model of canopy reflectance (Nilson and Kuusk, 1989). Variant of 1D RT solution in homogeneous medium. Considers unscattered, single scattered and multiple-scattered radiation separately.

2.5.4 Semi-empirical models

The final class of CR models to be mentioned are semi-empirical (so-called kernel-driven) models. These have been developed in response to the requirement for dynamic (near real-time) estimates of global albedo (Wanner *et al.*, 1995; Lucht *et al.*, 1999; Lucht and Roujean, 2000). Generation of albedo in near real-time from the large quantities of moderate resolution (hundreds of m to km scale) data from instruments such as MODIS and MISR requires rapidly invertible models capable of describing reflectance from spatially heterogeneous scenes at sub-km resolution (Roujean and Leroy, 1992; Wanner *et al.*, 1997).

Semiempirical models attempt to bridge the gap between the physical and empirical modelling approaches (Wanner *et al.*, 1995). The aim is to maintain some physical basis, while still allowing rapid analytical inversion against moderate resolution

data. The assumption is made that at moderate resolution, scattering from heterogeneous surfaces will be composed of separable scattering components (kernels). Each kernel represents a particular component of canopy scattering behaviour, and contributes to the overall reflectance 'shape'. Approaches using either linear additive or multiplicative combinations of kernels have been developed (Lucht and Roujean, 2000). Linear kernel-driven models assume reflectance is composed of volumetric and GO scattering components. Multiplicative models are based on magnitude, anisotropy and hot-spot terms. Both approaches are less flexible for describing BRDF than purely empirical models. This is because they are constrained to the basic shapes represented by individual kernels. A benefit of this constraint however, is that it permits extrapolation as well as interpolation, which is not the case for purely empirical models.

2.5.4.1 Linear (kernel-driven) semi-empirical models

Linear semi-empirical models assume that scattering from homogeneous surfaces can be described using a weighted linear superposition of a small number of kernels based on approximations to physical solutions for volumetric and GO scattering. The general form of the linear kernel-driven models is (Wanner *et al.*, 1995)

$$BRDF(\theta_i,\theta_v,\phi;\lambda)=\sum_n f_n(\lambda)k_n(\theta_i,\theta_v,\phi;\{P_n\}) \qquad \textbf{2.26}$$

Where the k_n kernels are purely geometrical expressions of fundamental scattering behaviour of radiation within the canopy; f_n are the model parameters, and P_n are potential preset terms that may modify the kernels behaviour. More specifically, BRDF is typically considered as

$$BRDF(\theta_i,\theta_v,\phi;\lambda)=f_{iso}(\lambda)+f_{vol}(\lambda)k_{vol}(\theta_i,\theta_v,\phi)+f_{GO}(\lambda)k_{GO}(\theta_i,\theta_v,\phi) \qquad \textbf{2.27}$$

$k_{vol,GO}$ are the kernels representing volumetric and GO scattering components of BRDF (k_{iso} is assumed to be unity); $f_{iso,vol,GO}$ are the spectrally dependent model parameters (weights associated with each kernel). Importantly, the kernels depend only on (θ_i, θ_v, ϕ) and hence can be pre-calculated for angular integration. Although approximate in nature, the physical basis of the various kernels can be used to provide meaningful constraint of the model inversion process (see appendix **1**), as well as (potentially) providing

biophysical information, as will be seen in later chapters. Semiempirical models require more samples than purely physical models, but far less than purely empirical ones.

Describing BRDF as a linear superposition of volumetric and GO BRDF 'shapes' is justified by considering that any moderate resolution pixel will contain surfaces contributing both volumetric and GO scattering to the total pixel reflectance. This is modulated by the respective sub-pixel areas (weights) of each cover type (Wanner *et al.*, 1995). Even for scenes likely to be dominated by a single type of scattering there will probably be some contribution from the other component. Wanner *et al.* (1995) use the example of a forest canopy, where reflectance from the discrete crowns is likely to be characterised largely by GO scattering. However, the dense vegetation within the crowns is likely to contribute some component of volumetric scattering to the total BRDF. This does assume that there is no multiple scattering between the separate components. The kernels are based on the assumption of single-scattering interactions only and to compensate for this multiple scattering is included in the isotropic term. Scattered radiation from a directional source tends to become increasingly isotropic with successively higher order scattering interactions. Hence it seems reasonable to include multiple scattering (as a first approximation) as an additive (scaling) "brightness" term, rather than as a function of viewing or illumination angle. In the linear kernel-driven models the isotropic term is defined as the nadir reflectance at nadir illumination.

There are several major advantages of the linear kernel-driven approach to modelling BRDF.

1. Being linear, the models lend themselves to rapid, analytical inversion using methods described previously (Lewis, 1995).
2. As the forms of the kernels are known in advance, angular integrals of BRDF directional-hemispherical and bihemispherical reflectance ($\overline{\rho}$ and $\overline{\overline{\rho}}$) can be pre-calculated in a LUT. Total albedo can then be calculated as a weighted sum of the kernel albedos, avoiding computationally expensive numerical integration (Wanner *et al.*, 1997).
3. Most importantly, if adjacency effects over heterogeneous regions are neglected (Wanner *et al.*, 1997), the linear models can be assumed to scale linearly with area. They can therefore be arbitrarily scaled for application to any required resolution, making them ideal for production of albedo at a range

of scales. The linear scaling property also means that such models can be applied to surfaces with arbitrary combinations of volumetric and GO scattering with no requirement for *a priori* assumptions of cover type.

4. Finally, as the model parameters have some physical basis there is the hope that parameter estimates might be inverted to provide biophysical information.

Due to the approximate nature of the kernels it is not straightforward to determine what information is contained within the inverted model parameters, or how this might be exploited (Disney and Lewis, 1998). The remainder of this thesis is concerned with examining what type of biophysical information may be derived from reflectance data using kernel-driven models, and how such models might be improved. The derivation of the kernels is presented below.

2.5.4.1.1 Volumetric kernels

A number of kernels approximating volumetric and GO scattering have been developed. The volumetric kernels are based on Ross' (1981) solution for RT in a turbid medium. Two separate versions of the so-called Ross kernel for canopies with LAI >> 1 (RossThick) and LAI << 1 (RossThin) are described below. The RossThick kernel was developed by Roujean *et al.* (1992), from Ross's formulation for BRDF given in equation **2.24**, assuming: a horizontally homogeneous canopy (randomly oriented leaves) over a flat Lambertian surface of reflectance ρ_o; single scattering only; leaf reflectance (ρ_{leaf}) = leaf transmittance (τ_{leaf}). The assumption is then made that LAI >>1, in which case LAI dominates the $\exp\left(-LAI\sqrt{\sec\theta_i + \sec\theta_v}\right)$terms. The $\sqrt{\sec\theta_i + \sec\theta_v}$ terms (denoted B) are replaced with a typical value over the angle range θ_i, θ_v = 0°, 30°, 60° of 1.5. In this case, $R_{thick} = c_1 k_{vol} + c_2$ and the RossThick kernel is

$$k_{vol(thick)}(RossThick) = \frac{\left(\frac{\pi}{2} - \xi\right)\cos\xi + \sin\xi}{\cos\theta_i + \cos\theta_v} - \frac{\pi}{4} \qquad \textbf{2.28}$$

ξ is the phase angle of scattering, and $\cos\xi = \cos\theta_i\cos\theta_v + \sin\theta_i\sin\theta_v\cos\phi$. The $\pi/4$ term arises from a convention introduced by Roujean *et al.* (1992) that the kernels should satisfy the condition that $k_{vol} = 0$ when θ_i, $\theta_v = 0$. The constants c_1 and c_2 are $c_1 = \frac{4\rho_{leaf}}{3\pi}\left(1 - e^{\{-LAIB\}}\right)$ and $c_2 = \frac{s}{3} + e^{(-LAIB)}\left(\rho_o - \frac{\rho_{leaf}}{3}\right)$ respectively. c_1 is the weight of

the kernel in the full kernel-driven model (equation **2.27**) and c_2 is included in the isotropic term.

The adaptation of the Ross volumetric kernel for LAI << 1 has been proposed by Wanner *et al.* (1995). In this case the approximation that $e^x \approx 1+x$ if x is small is made. If $R_{thin} = c_1 k_{thin} + c_2$, the RossThin kernel for volumetric scattering (from equation **2.24**) is

$$k_{vol}(RossThin) = \frac{\left(\frac{\pi}{2} - \xi\right)\cos\xi + \sin\xi}{\cos\theta_i \cos\theta_v} - \frac{\pi}{2} \qquad \textbf{2.29}$$

where this time, the constants $c_1 = \frac{2\rho_{leaf} LAI}{3\pi}$ and $c_2 = \frac{\rho_{leaf} LAI}{3} + \rho_l$. In the same way as for the RossThick kernel, c_1 is the weighting of the kernel in the full linear model, and c_2 is included in the isotropic brightness term. Both kernels are functions of θ_i and θ_v only, as desired.

2.5.4.1.2 GO kernels

The GO kernels are based on the work of Li and Strahler (1986), described above and Roujean *et al.* (1992). Shadowed regions are assumed perfectly black (no contribution to scene reflectance) and sunlit crown and ground components are assumed equally bright. Wanner *et al.* (1995) consider the proportions of sunlit crown and ground resulting from spheroidal protrusions of length 2b and width 2r, number density λ, randomly located at height h above a flat Lambertian surface (c.f. fig. **2.10**). To calculate the area of projected shadow, the spheroids are transformed to the 'equivalent' sphere that would result in the same shadowed area at given θ_i, θ_v. The resulting (transformed) zenith angles are denoted $\theta'_{i,v} = \tan^{-1}(b/r \tan\theta_{i,v})$. Two GO kernels are presented; one for scenes in which mutual shadowing of spheroids is not permitted (LiSparse), and one for the mutual shadowing case (LiDense). In the same manner as for the volumetric kernels, reflectance is expressed as $R_{GO} = c_1 k_{sparse} + c_2$, and the LiSparse kernel is

$$k_{GO}(LiSparse) = O(\theta'_i, \theta'_v) - \sec\theta'_i - \sec\theta'_v + \tfrac{1}{2}(1 + \cos\xi')\sec\theta'_v \qquad \textbf{2.30}$$

$\cos\xi' = \cos\theta'_i\cos\theta'_v + \sin\theta'_i\sin\theta'_v\cos\phi'$. $O(\theta'_i, \theta'_v, \phi')$ describes the overlap between the areas of viewing and illumination shadow dependent on the transformed zenith angles, height h, and ratio of b to r. The constants c_1 and c_2 in this case are $C\lambda\pi r^2$ and C

respectively, where C is the reflectance of the sunlit crown and ground (assumed equal). This dependence on the size distribution of the spheroids results in a family of kernels for different b/r and h/b. In practice these are reduced to four cases for oblate/prolate spheroids, and high/low crowns.

The LiDense kernel describes ρ_{canopy} including mutual shadowing by considering the spheroids on the surface as tree crowns with lognormal height distribution. In this case, $R_{GO} = c_1 k_{dense} + c_2$ and the LiDense kernel is:

$$k_{GO}(LiDense) = \frac{(1+\cos\xi')\sec\theta_v'}{\sec\theta_v' + \sec\theta_i' - O(\theta_i', \theta_v')} - 2 \qquad \textbf{2.31}$$

The factor of 2 is subtracted to ensure the kernel is zero for θ_i, $\theta_v = 0^o$. All other terms are as above, except $c_1 = C/2$ and $c_2 = C$. The dependence on the ratios b/r and h/b remain. Figure **2.11** shows the directional variation of the full complement of Ross and Li kernels. Included are GC (Ground-Crown) versions of the LiSparse and LiDense kernels. The GC versions treat the ground and crown as having different brightnesses. The asymmetric bowl shape is apparent in both the Ross and Li kernels. The peak in the backscatter direction is present only in the Li kernels as it is a manifestation of the finite size of scattering elements, and hence is not described by the RT approximation. This peak is more prominent in the LiDense kernel (mutual shadowing of spheroids permitted).

Figure **2.12** shows the family of LiSparse kernels with various values of h/b and b/r, including:

- high oblate (HO) h/b = 2.5, b/r = 0.75;
- high prolate (HP) h/b = 2.5, b/r = 2.5;
- low oblate (LO) h/b = 1.5, b/r = 0.75;
- low prolate (LP) h/b = 2.5, b/r = 2.5.

Figure **2.13** shows the corresponding family of LiDense kernels. In practice (i.e. in production of the MODIS nadir reflectance and albedo product) the RossThick LiSparse kernel combination is used, in preference to RossThin and/or LiSparse. The RossThick LiSparse combination fits as well or better than any other in most circumstances, and so has become the de facto choice of linear kernels (Schaaf *et al.*, 2000a).

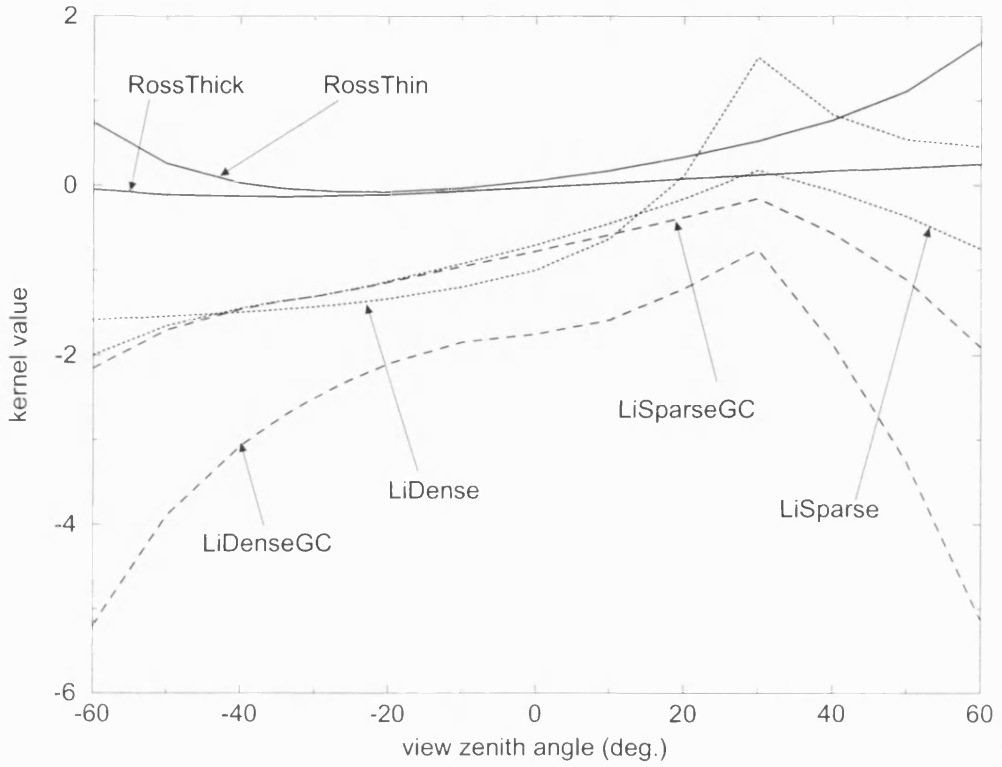

Figure 2.11 Angular variation of the Ross and Li kernels.

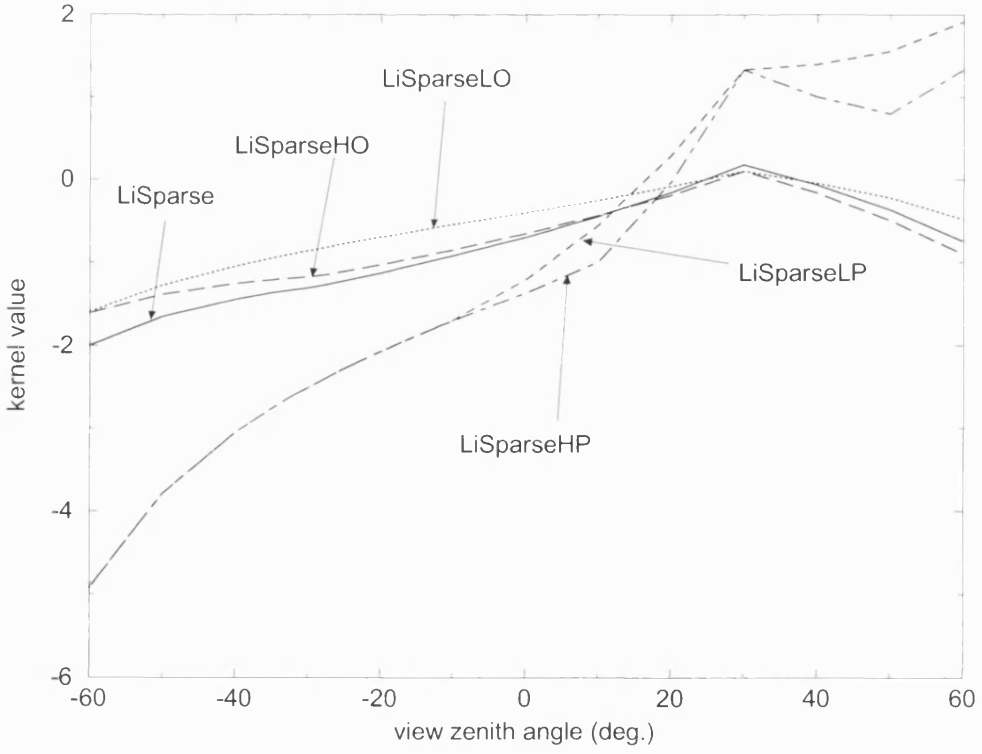

Figure 2.12 Family of LiSparse GO kernels.

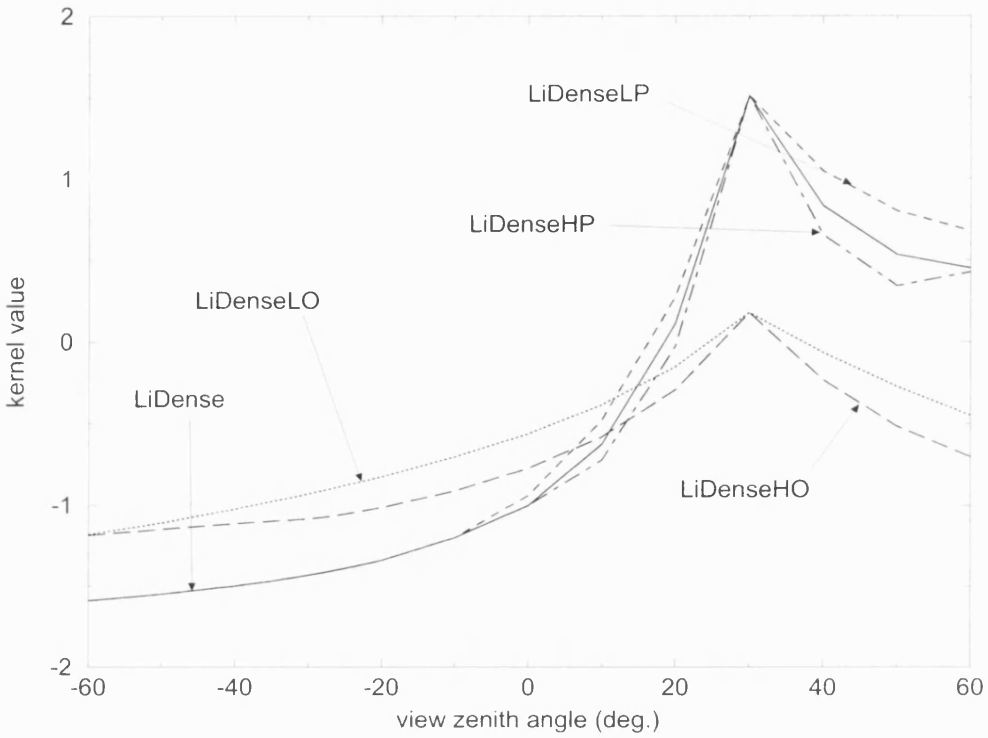

Figure 2.13 Family of LiDense GO kernels.

Two other kernels should be mentioned. Firstly, a GO kernel developed by Roujean *et al.* (1992) based on the sunlit and shadowed scene components due to randomly oriented rectangular Lambertian blocks of height h, length *l* and width b arranged on a surface. Shadows are assumed perfectly black and all sunlit areas are considered equally bright, with reflectance ρ_o. Mutual shadowing is ignored, restricting the validity of the model to situations where shadows do not fall outside the basal area of the block casting them (i.e. θ_i, θ_v < 60°). Additionally *l* is assumed >> h, and *l* >> b in order that the shadowing by the sides of the blocks (area bh) may be disregarded. The reflectance of blocks on a surface is expressed as $R_{Roujean} = c_1 k_{Roujean} + c_2$ where $k_{Roujean}$ is

$$k_{Roujean} = \frac{1}{2\pi}\left[(\pi - \phi)\cos\phi + \sin\phi\right]\tan\theta_i \tan\theta_v - \frac{1}{\pi}\left(\tan\theta_i + \tan\theta_v + \sqrt{\tan^2\theta_i + \tan^2\theta_v + 2\tan\theta_i \tan\theta_v \cos\phi}\right) \quad \textbf{2.32}$$

and c1 and c2 are $\rho_o h/b$ and ρ_o respectively. This has recently been extended to the LiTransit kernel (Gao *et al.*, 2001).

The other kernel included is that of Walthall *et al.* (1985) described in equation **2.17**, and in its modified form in equation **2.18**. This expression is also dependent only on

viewing and illumination. In practice, the modified Walthall model often provides a better fit to observed data (in terms of RMSE) than the volumetric or GO kernels (Lucht *et al.*, 1999). However, it suffers from the drawback of all empirical models, namely that inverted model parameters have no physical meaning. Whilst the linear models were developed in order to facilitate production of integrated products such as albedo, there is naturally an interest in their capability for producing biophysical parameter information. However it is not clear to what extent the kernels contain (uncoupled) biophysical information, or how this information might be interpreted. The remainder of this thesis seeks to explore this problem.

Goel and Thompson (2000) note that a limitation of the kernel-driven approach to modelling BRDF is that the assumption that there is little cross coupling between volumetric and GO scattering within a scene may be hard to justify in some cases. They conclude that the sensitivity of the kernels to angular sampling makes it difficult to determine the weightings for different sensor sampling regimes. However Lucht and Lewis (2000) have shown that it is possible to determine in advance the dependence of the kernels on sampling. Knowledge of the sampling characteristics of new sensors (Barnsley *et al.*, 1994) can be used to overcome this dependence (Lucht, 1998).

2.5.4.2 Non-linear semiempirical models

There has been parallel development of non-linear (or semi-linear) semiempirical models (Rahman *et al.*, 1993). In contrast to equation **2.26**, non-linear models typically follow the form

$$BRDF(\theta_i, \theta_v \phi; \lambda) = \prod_n t_n(\theta_i, \theta_v \phi; \{f(\lambda)_n\}) \qquad \textbf{2.33}$$

where t_n are the terms controlling basic scattering shape, and f_n are the model parameters. Multiplicative kernel-driven models of this sort tend to have complementary benefits and disadvantages over the linear models, and are currently being used to model surface reflectance from MISR data (Martonchik *et al.*, 1998b). The RPV model (Rahman *et al.*, 1993a) is based on Minnaert's empirical function given in equation **2.18**, modified to include a Henyey-Greenstein phase function term describing the asymmetry of the BRDF between forward- and backscattering, and a hotspot term. The advantages of this approach are that despite its empirical core, the RPV model has physically meaningful

parameters. In addition, the multiplicative nature of the model means a larger number of BRDF shapes can be represented than with a purely additive model. However, non-linearity implies numerical (or iterative) inversion, which is a major drawback. In practice, a semi-linear modified version of the RPV model (MRPV) (Martonchik *et al.*, 1998b) is used which may be inverted using an iterative LUT-based approach. This forms the basis of surface reflectance retrieval for MISR (Martonchik *et al.*, 1998b). Intercomparison between the best-performing linear and non-linear semiempirical models (RossThick LiSparse and MRPV) has shown their performance to be comparable in most cases, with only marginal differences between them (Lucht, 1998; Lucht *et al.*, 1999).

2.6 Conclusion

The preceding discussion illustrates the huge variety and ingenuity of approaches to CR modelling, as well as some of the benefits and drawbacks in each case. Empirical models are simple, generally fit observed BRDF well and may be useful as directional interpolants. However they require many directional samples to constrain their fit, and are not valid for extrapolation. Physical models require many less samples and have physically meaningful parameters, but are generally complex and require numerical inversion. Computer simulation models can represent canopy scattering at in almost arbitrary detail but are often computationally intensive, and are not invertible directly due to the potentially very large number of controlling parameters. Semiempirical kernel-driven models bridge the gap between simple empirical and complex physical descriptions of BRDF. Kernels describing various scattering properties can be linearly or multiplicatively combined to describe BRDF. Kernel-driven models can be used to interpolate or extrapolate from limited samples of BRDF, and can be rapidly inverted against measured reflectance at arbitrary scales.

The remainder of this thesis is concerned with the ability of the linear semiempirical models to describe BRDF. They are the models of choice for production of global BRDF and albedo products from the MODIS instrument. The ability of the linear models to describe BRDF, even in unfavourable circumstances, is examined, along with novel methods for extracting biophysical information from their parameters.

3 Description of field-measured data

The data used in the experimental chapters of this thesis were collected during the growing season of 1997 from a study site based around Barton Bendish Farm, Norfolk (52" 37.2' N 0" 32.0' E). The farm covers some 9 km^2 and produces winter wheat, several varieties of spring barley, peas and sugar beet. Due to the initial work done here (Disney *et al.*, 1997) and subsequent field experiments, this site and the surrounding area has been taken on as a MODIS core validation site.

Three barley fields, and one wheat field were selected at the start of the fieldwork campaign. These fields are identified as follows (and will be referred to as such throughout):

barley 24th April	Fields ba_104, ba_112 and ba_119.
barley 13th May	Combines measurements made from the 13th - 15th May 1997 (due to bad weather) in fields ba_112 and ba_119.
barley 4th June	Fields ba_104, ba_112 and ba_119
barley 24th June	Fields ba_112 and ba_119
wheat 23rd March	Field ww_109
wheat 23rd April	Field ww_109

Figure 3.1 AVHRR image of UK (top left); SPOT FCC image of East Anglia (top right); aerial photograph of Barton Bendish farm (bottom) showing selected fields used in fieldwork study, August 1997 (courtesy of NERC).

Figure **3.1** shows the fieldwork site at three different scales: an AVHRR image of the UK (9/8/95) showing the East Anglia region; a false-colour composite SPOT image (4/4/97) of the NIR, visible red and green bands highlighting vegetation as red. Also shown is a scanned aerial photograph of the Barton Bendish farm and surrounding area (6/8/97), obtained by the Natural Environmental Research Council (NERC) Airborne Research System (ARS) Facility aircraft. The Barton Bendish farm area and the fields selected for this study are marked on the image. RAF Marham air-base, clearly visible in the SPOT image, is just visible at the top of the aerial photograph. The cereal crops have been harvested at this stage, and the remaining green areas are fields of sugar beet.

It can be seen that there are quite large variations in the soil brightness throughout the site, caused by differences in soil composition and drainage efficiency. To compensate as far as possible for any effect this variability may have on crop density and/or structure, as many samples as possible were taken from within each field. Data were also collected from several fields during each visit to minimise the possibility of selecting an atypical field of any particular crop. The planned temporal sampling (a full set of complementary measurements every two weeks) was not achieved due to the inclemency of the weather during the growing season of 1997. This resulted in a lack of sampling between early May and early June.

3.1 Summary of data, collection methods and validation

The field data, collected on eight visits to the Barton Bendish field site between 24th April and 6th August 1997, consist of measurements of a number of properties including:

- Ground spectro-radiometric measurements.
- Canopy coverage estimates.
- LAI measurements.
- Canopy height, and plant and row spacing.
- 3D plant structure, for BPMS modelling, characterisation of LAD.
- Airborne data (NERC ARS ATM, CASI data and aerial photography).

Data collection methods are described in detail below, in addition to validation studies performed in order to provide confidence in the measured data. This is primarily a comparison of 3D barley and wheat canopies reconstructed from measured plant parameter data using the BPMS, with properties measured in the field such as LAI, LAD and BRDF. The ability to characterise the primary structural properties (and the consequent radiometric behaviour) of the measured canopies within the BPMS is fundamental to this thesis. Much of the following work deals with analysis of BPMS-simulated canopy reflectance. Establishing agreement between reflectance behaviour simulated using measured plant parameters within the BPMS, and the reflectance behaviour of the real canopies, permits conclusions drawn from analysis of BPMS results to be applied to real data. The canopy structural data collected through manual measurement are first described, followed by various other measurements collected for validation of the BPMS data and for subsequent comparison with information derived from airborne data.

How the various sources of data described above are subsequently used within this thesis:

- *3D structural measurements*: described in section **3.1.1**, these measurements were used within BPMS/Ararat generate 3D scene representations of barley and wheat canopies. Values of ρ_{canopy} was simulated under realistic conditions (multiple scattering, direct and diffuse illumination) in order to compare with field-measured reflectance data. This provides independent validation of the 3D modelling approach (described in section **3.1.2**). Subsequent simulations of ρ_{canopy} are performed under the assumptions made in the formulation of the linear kernel-driven models (single scattering only, $\rho_{leaf} = \tau_{leaf} = 0.5$, Lambertian soil) in order to investigate these assumptions (chapters **4**, **5**, and **6**).
- *Canopy structural measures:* described in sections **3.1.2** and **3.1.3**, properties such as LAI, %cover and canopy directional reflectance were measured directly in order to compare with values derived from canopies generated using the 3D structural measurements within the BPMS.
- *Airborne Thematic Mapper Data:* described briefly in section **3.1.5**, these data are used in chapter **7** to test the kernel-driven approach to modelling spectral, directional reflectance (in particular, image of June 6th 1997 is used).

3.1.1 Plant structural measurements

Plant and row spacing for each field were recorded along with the planting densities of the various crops i.e. the number of plants per meter[1]. In addition, detailed descriptions of the topology and structure of individual plants were made for use within the BPMS. These measurement techniques are discussed in detail by Lewis and Muller (1990), Lewis and Disney (1997) and Lewis (1999). Typically five or six plants per field per date were measured. A set of ten measurements were made of each plant, with the 'leaf' subset of these measurements being made for every leaf of a plant. Brief details of the measurements are as follows:

For each tiller:

- *tiller azimuth angle*
- *tiller zenith angle*

For each stem section (emergent from ground, and between leaf nodes):

- *stem length*
- *stem width*

For each leaf:

- *leaf base zenith angle*
- *leaf tip zenith angle*
- *leaf length*
- *% leaf length to maximum width*
- *(maximum) leaf width*

[1] This does not take account of some areas in the barley and wheat fields where the seed drilling vehicle has crossed back on itself leading to patches of doubly drilled crop. These areas are noticeably denser than the main body of the fields and were avoided for all measurements.

Individual leaf angles (base, tip) and stem section angles were measured with a protractor to an estimated precision of 5°. Leaf length, maximum width and stem lengths were measured to an estimated precision of 1 mm. Figure **3.2** shows a measured barley plant. Sensitivity analysis was carried out to test whether simulated BRDF is sensitive to any particular BPMS measurement. The measured parameters were perturbed randomly according to a Gaussian distribution of specified mean and standard deviation and BRDF was simulated for each 'perturbed' canopy. Simulated BRDF was found to be more sensitive in shape to row and plant spacing than any of the individual structural measurements, and more sensitive in magnitude to the specified leaf and soil reflectance values. Figures **3.3** and **3.4** show simulated canopies using BPMS measurements.

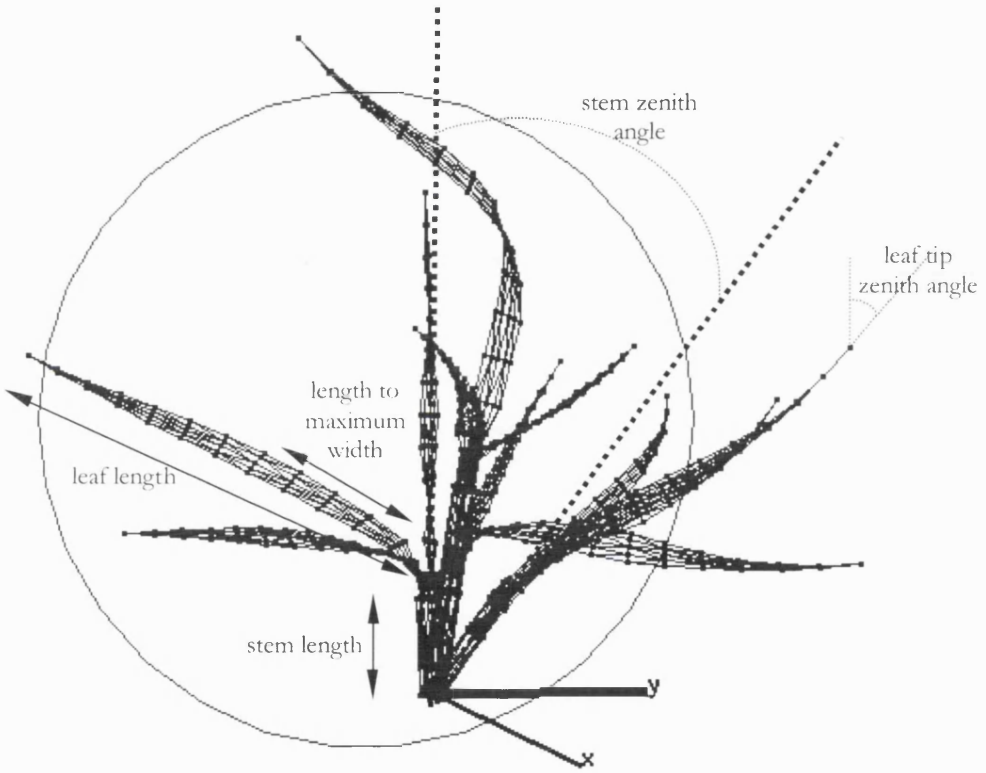

Figure 3.2 Wireframe representation of manually measured barley plant (13/5/97) showing measured parameters.

Figure 3.3 Simulated wheat canopy in early growth stage, Lambertian soil.

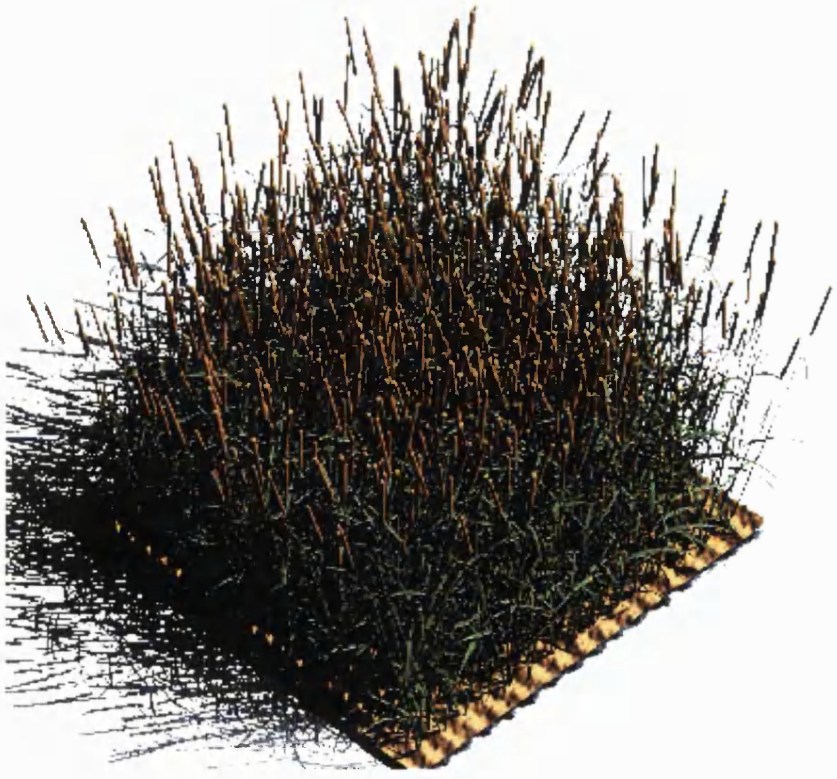

Figure 3.4 Simulated barley canopy (shortly prior to harvest) with Lambertian seed heads and soil properties modelled on observed soil spatial statistics.

3.1.2 Ground spectro-radiometric measurements

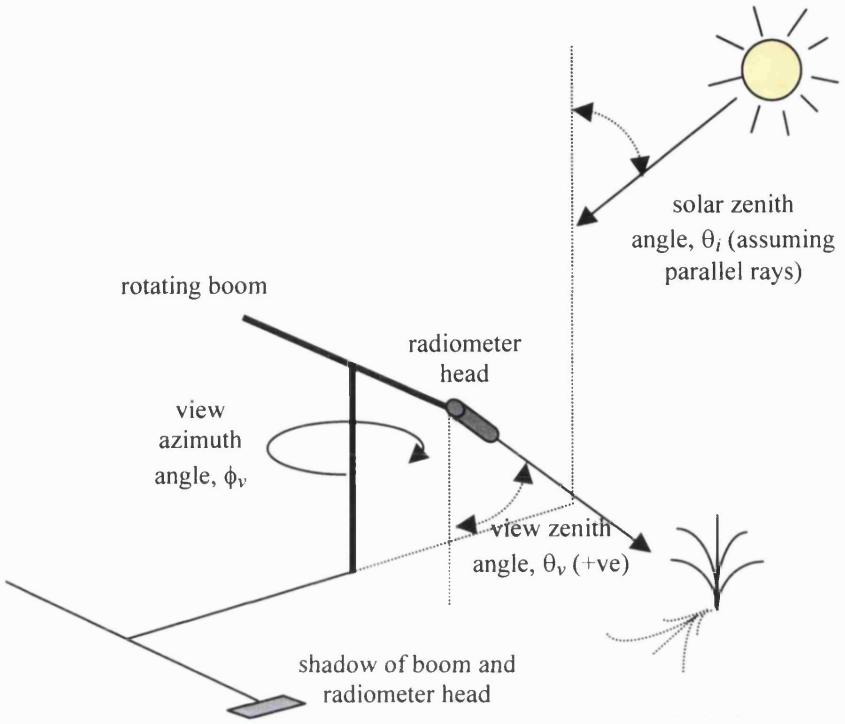

Figure 3.5 Viewing and illumination geometry of PS-II radiometer measurements.

Measuring BRDF in the field is not trivial, largely because of variable atmospheric conditions and hence varying quantities of diffuse and direct illumination (Sandmeier and Itten, 1999). Other uncertainties are caused by the difficulty of determining precisely what the instrument IFOV is seeing, movement of crops due to wind, lack of a stable instrument base etc. Although no atmospheric scattering data were available during this field campaign (sun photometer measurements are now made at Barton Bendish to augment field measurements), measurements were recorded rapidly and repeated often to try and minimise the effects of changing atmospheric conditions. In addition, BRDF measurements were restricted to 'blue sky' days. However, these can be few and far between in a typical UK summer and 1997 transpired to be particularly wet. However, samples of directional reflectance were made with a boom-mounted ASD PS-II radiometer (www[3.1]) in the visible to NIR wavelength range (due to limitations in the instrument, effectively, 450-900 nm). Measurements were made at 10^o intervals in view zenith (θ_v) from -70^o to $+70^o$ in both the principal and cross-principal solar planes[2]. The relative azimuth angle, ϕ, between θ_v and the illumination zenith, θ_i, is then 0^o or 90^o for

[2] Negative angles in this case imply measurements in the backscatter direction, and positive ones the specular direction.

viewing in or across the principal plane. This viewing and illumination geometry is illustrated in figure **3.5**. In addition to the target radiance measurements, near-simultaneous radiance measurements of a polythene (assumed) Lambertian reference panel were made. Reflectance is then calculated as the ratio of the target radiance to that of the reference panel (see equation **2.2**). For each reference panel measurement, the so-called dark current response of the instrument was also recorded. This is a measurement of the signal recorded when no light is incident on the radiometer, caused by background (thermal) noise in the silicon detector. The dark current is subtracted from the measured radiance to provide an accurate measurement of target radiance. An example of measured barley BRDF is given in figure **3.6**, along with reflectance simulated using the manually measured canopy structural parameters within the BPMS.

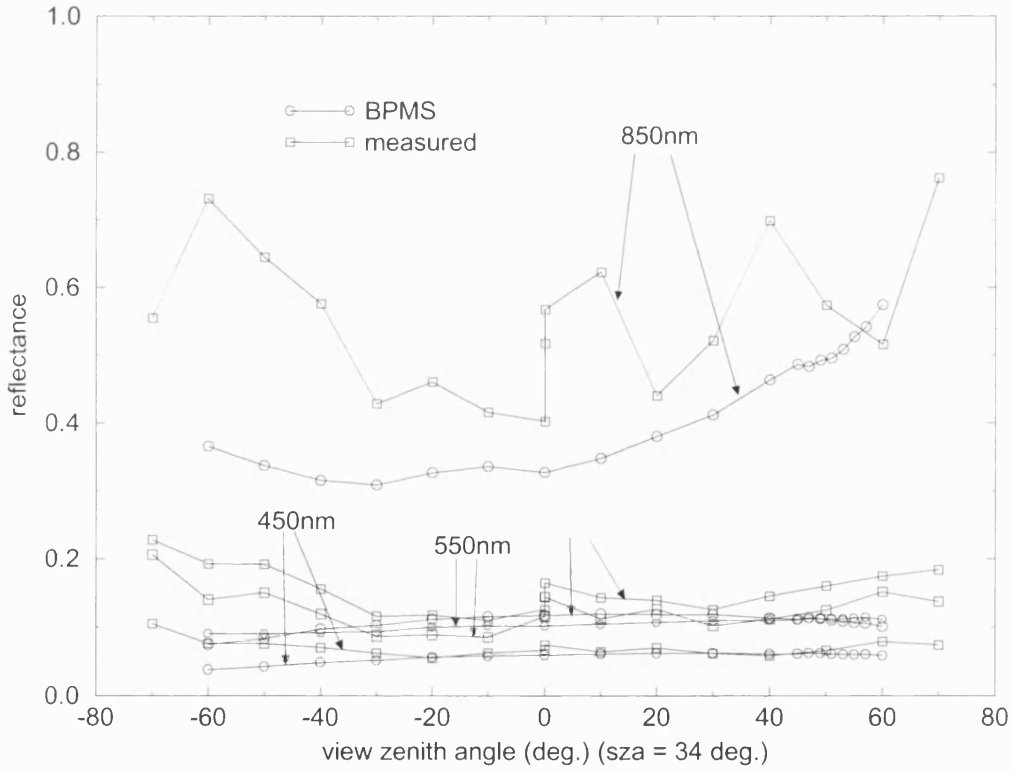

Figure 3.6 Measured and simulated canopy reflectance at four bands (barley field ba_119, 13/5/97, LAI = 3.89; ρ_{leaf} and τ_{leaf} from laboratory measurements, ρ_{soil} from field measurements[3]).

Agreement between the modelled and measured reflectance data is reasonable at visible wavelengths ($r^2 > 0.7$), but not so in the NIR (850nm) ($r^2 < 0.5$). Whilst the

[3] Laboratory measurements provided by B. Hosgood from LOPEX data set (Hosgood *et al.*, 1994); field measurements provided by E. J. Milton at NERC EPFS facility, Southampton, UK.

directional variation of simulated reflectance may be reasonable, the magnitude is generally too low. This is a result of reflectance being simulated without multiple scattering (as discussed in section **2**, the multiple scattered component of canopy reflectance tends to be isotropic, and will therefore increase the magnitude of simulated canopy reflectance without significantly changing the shape). In addition, the level of noise in the measurements can be seen. This is particularly obvious at nadir where three measurements were made, one at the start of the string of measurements, one in the middle and one at the end. The variability of these measurements (up to 10% reflectance) is caused largely by changes in atmospheric conditions during the measurement period, even on a 'blue sky' day with little or no cloud. This is a typical problem when performing field radiometric measurements and is discussed at the end of this chapter, as well as in chapter **8**. Values of r^2 for linear regression of the measured against modelled reflectances are given in table **3.1**.

Table 3.1 Values of r^2 for comparison of measured to modelled reflectances.

	r^2 values			
canopy	***450nm***	***550nm***	***650nm***	***850nm***
ba_112 18/04	0.82	0.84	0.87	0.68
ba_119 13/05	0.94	0.95	0.89	0.74
ba_112 04/06	0.90	0.96	0.95	0.80
ba_119 24/06	0.79	0.84	0.80	0.71
ww_109 23/03	0.78	0.80	0.78	0.64
ww_109 23/04	0.92	0.95	0.89	0.83

The figures in table **3.1** demonstrate reasonable between the measured and modelled canopy reflectance values, however there is significant disagreement in a number of cases. The cases where agreement is not so good are likely to be due to the canopy being very sparse (LAI <<1). The agreement between the angular variation is higher than the spectral variation. Overall agreement between the BPMS and measured reflectance values is generally good in the visible but the variance of the NIR reflectance values is clear. The signal-to-noise ratio (SNR) of the detector in the region beyond 900nm (SNR ≈5:1) is very much lower than in the visible part of the spectrum (SNR better than 20:1).

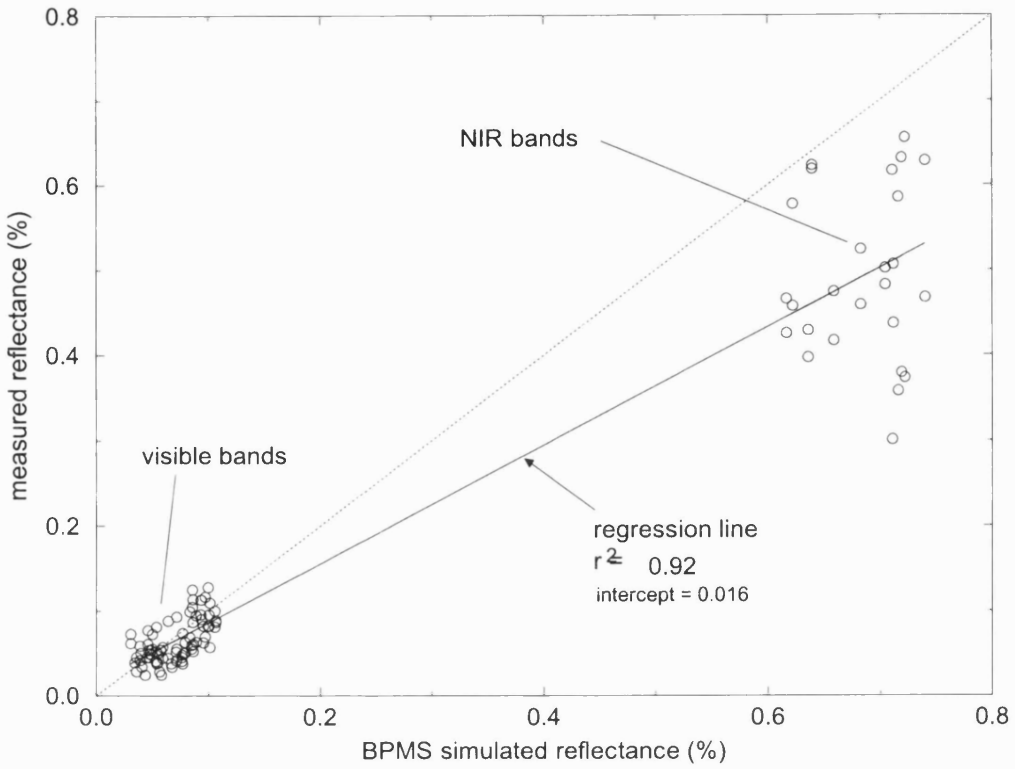

Figure 3.7 Scatter of BPMS against measured ρ_{canopy}, barley 13th May 1997.

3.1.3 Canopy coverage estimates

Nadir-pointing photographs were taken (from a height of 1m above the ground) of the various canopies throughout their development. No photographs were taken during the later stages when the canopy heights exceed 1m as there was total coverage in these cases. A series of canopy cover photographs showing the progression of cover in barley field 119 are shown in figure **3.8**. The variability of local planting density (even in such a small region) is clear in the 13th May image. The camera tripod is visible at the lower extent of the first two images.

Figure 3.8 Canopy cover photographs for barley canopy 119 (from l to r) on 18th April, 15th May and 24th June 1997.

Canopy cover was derived from the photographic data by estimating the proportion of visible soil per unit ground area (Disney *et al.*, 1998). Only the central portion of each image was used to avoid image plane distortions caused by the relatively wide field of view (115°). RGB to HSI transformations were performed on the scanned images, which were then thresholded manually on hue. The mid-range hue values corresponded closely to soil, while the higher values corresponded to vegetation. This allows percent cover to be simply estimated. Values of % cover as estimated from the photography are presented in figure **3.9** in the form of a scatter plot with corresponding BPMS derived values. The error bars in figure **3.9** represent the variability of % cover estimates made from photography (one SD). For the barley, twenty eight separate %cover images were used from four dates; for wheat, ten images from two dates were used. The regression of all samples together shows reasonably high correlation, with a slight offset (overestimation) of around 10% in the values derived from photography. This is due to inaccuracy in the thresholding of the HSI-transformed photography. Relatively small changes in the value of the selected threshold cause significant changes in % cover. Conservative threshold values were chosen deliberately to make sure all vegetation was included.

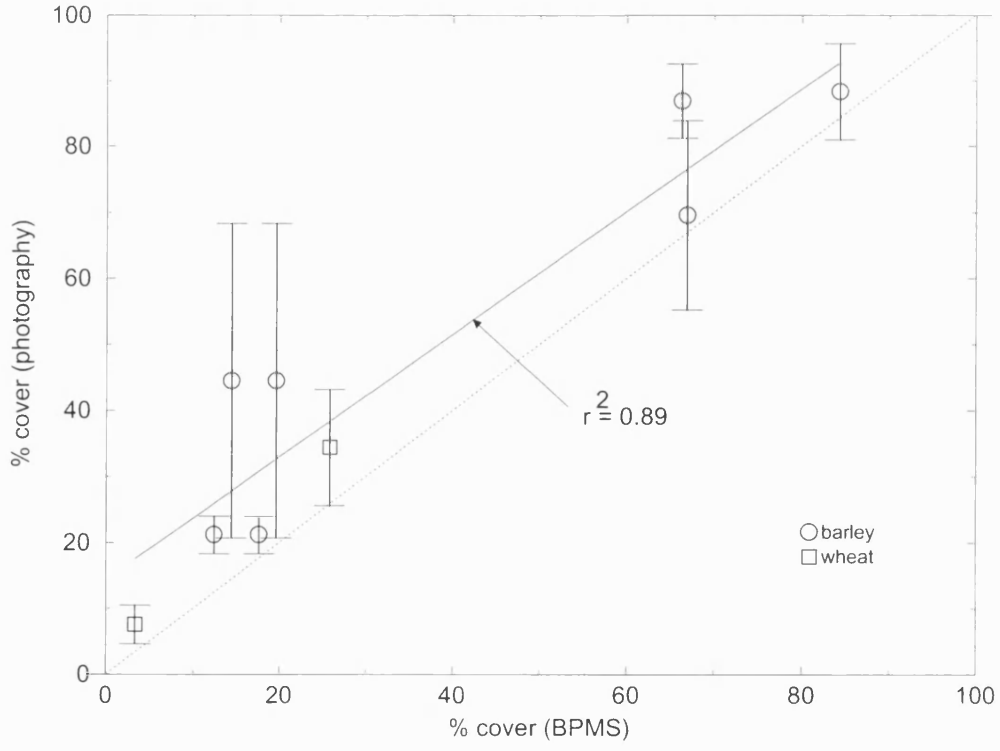

Figure 3.9 %cover estimated from photography and BPMS simulations.

3.1.4 LAI measurements

LAI measurements were made with a LI-COR LAI 2000 instrument, which works by comparing the intensity of (diffuse) incident illumination measured at the bottom of the canopy with that arriving at the top (LI-COR technical report; Welles and Norman, 1990). Incident light is recorded over five concentric angular rings, each of approximately 15° in width (giving a nearly hemispherical field of view). LAI is estimated by calculating the probability of a photon penetrating to a depth z in the canopy (under various assumptions regarding the arrangement and radiometric properties of scattering elements in the canopy), and comparing this with the measured radiance at the bottom of the canopy. The probability of non-interceptance at depth z within the canopy is described by Beer's law (equation **2.20**). The angular integral of this property (over all zenith angles) is approximated as a weighted summation over the five concentric angular rings of the instrument.

The manufacturer's recommendations were followed in deciding a measurement plan. One measurement was made at the top of the canopy followed by ten measurements at different locations below the canopy. This pattern was repeated three times per field, and the resulting thirty-three samples comprise one full set of measurements. Measurements were made following transects at an angle of between 30° and 45° to the row direction, and at intervals suitably spaced to avoid over or under-estimation of LAI caused by measuring at integer numbers of rows or inter-row gaps. Care was also taken with regard to the illumination conditions under which measurements were made. The instrument operates under the assumption that the canopy is illuminated by a diffuse source, and therefore should be shadowed from any direct sunlight. Due to the weather during the fieldwork campaign it was possible to make the majority of the measurements under diffuse conditions. On days with significant direct sunlight a 270° view cap was used to mask out both the operator and sun from the viewing hemisphere. Measurements were also made as late or early as possible in the day when penetration of the canopy by direct sunlight is minimised. Measured values of LAI for the barley and wheat canopies are plotted as a function of day of year (doy) in figure **3.10**. Also shown are estimates of LAI derived from BPMS canopies generated from the manually measured canopy structural data. These values are presented explicitly in table **3.2**.

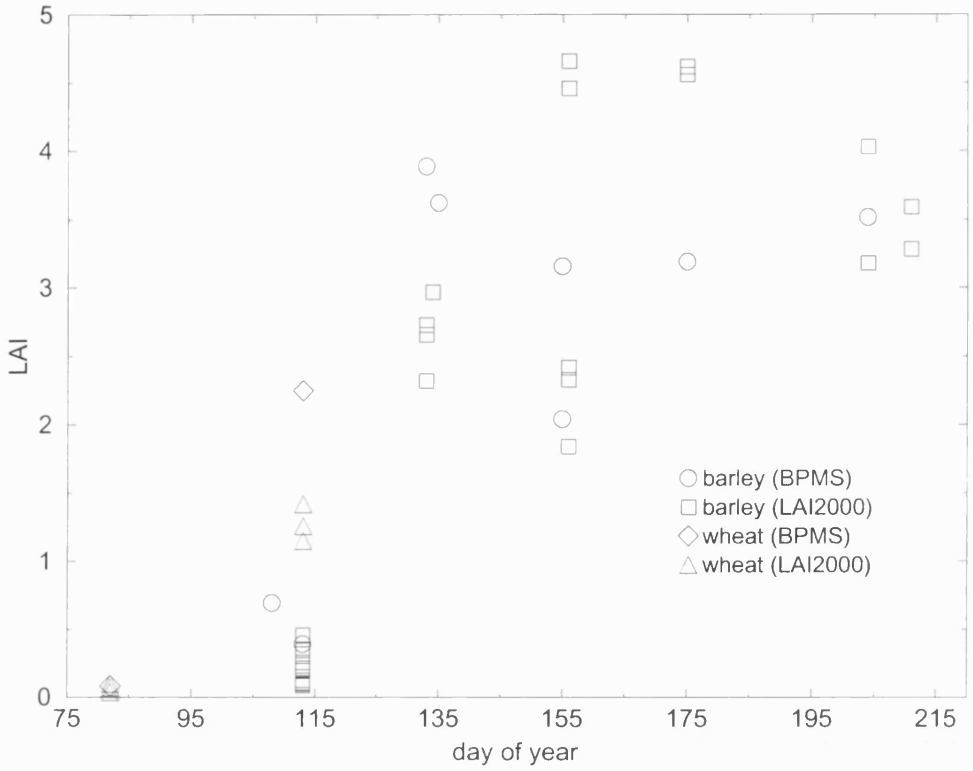

Figure 3.10 Measured and modelled LAI for barley and wheat.

It can be seen that there is a wide spread of measured LAI values for some canopies during development, resulting in a relatively poor agreement between the measured and modelled values in some cases. The likeliest cause of this divergence is the intra-field variability of measured LAI: the coverage of the barley canopy of 13th May (ba_119) varied from 10% to 70% across the field.

Table 3.2 Values of LAI derived from BPMS canopies.

canopy	*LAI*
ba_112 18/04	0.70
ba_119 13/05	3.89
ba_119 04/06	3.16
ba_119 24/06	3.19
ww_23/03	0.09
ww_23/04	2.25

3.1.5 Airborne data

A variety of airborne data were collected by the NERC ARS aircraft over the Barton Bendish field site during the 1997 field campaign. Due to the weather, the dates on which data could be collected were not ideally spaced through the growing season (see below). In addition, atmospheric conditions were not ideal when airborne data could be obtained (clouds and/or haze). However, contemporaneous ground measurements of LAI and BRDF described above were made. The nature of the data collected by the NERC aircraft is as follows:

- *Daedalus 1268 Airborne Thematic Mapper (ATM) data* – radiometer measurements in 11 broadband channels in the visible/NIR, SWIR, and TIR. Parallel flight lines were flown over the scene to provide overlap which gives BRDF sampling in the central region of overlap due to the wide (70°) FOV of the sensor (Barnsley *et al.*, 1997a). The data were recorded at an altitude of 3000m giving a spatial resolution of around 5m. Forty three flight lines were flown in total, on three dates: 5/6/97, 2/8/97 and 6/8/97, each of which was accompanied by contemporaneous ground measurements of the properties described above. An ATM image of the field site is shown in figure **3.11**.

- *Compact Airborne Spectrographic Imager (CASI) data* - hyperspectral radiometer data, consisting of 288 channels in the visible/NIR, obtained concurrently with the ATM data. Forty two flight lines were flown in total, on the dates given above, with a spatial resolution of approximately 3 m.

- *Colour aerial photography* - obtained concurrently with the ATM and CASI data. The resolution of the photography is approximately 2m (see figure **3.1**).

Figure 3.11 NERC ATM image over Barton Bendish, 2/8/97.

3.2 Summary of field measurements and validation

The fieldwork described above was designed to provide information permitting validation of simulations of ρ_{canopy}. In particular, measurements of structural and radiometric canopy properties were designed for comparison with modelled properties derived from a full 3D (BPMS) structural model of the canopy. A number of general difficulties of conducting such fieldwork were encountered, in addition to specific problems caused largely by the weather conditions of summer 1997, which was an unusually wet summer.

In general, the BPMS estimates of canopy structural parameters agreed relatively well with the measured parameters. Given the inter- and intra-field variability of the crops agreement between measured and modelled values of %cover and LAI were generally good. Agreement of the measured and modelled values of canopy were not always so good but this is largely a function of the changing atmospheric conditions and the

uncertainty of what is being viewed through the radiometer IFOV (to better characterise this variability, simulations should be performed using an equivalent size IFOV). Even a small wind can move the canopy enough to change this dramatically, particularly at low canopy LAI when soil can be very visible. Given these constraints, it was concluded that the BPMS characterisation of canopy structure was more than sufficient for the experimental work described in succeeding chapters.

4 Examination of volumetric and GO scattering behaviour

The basis of the linear kernel-driven BRDF models described in chapter **2** is the assumption that ρ_{canopy} can be described by a sum of one or two representative BRDF 'shapes', each approximating the behaviour of a separate component of canopy reflectance. Studies have shown that certain (angular) features of canopy reflectance are common to many types of vegetation (Kimes, 1984; Walthall *et al.*, 1985; Goel, 1988; Barnsley *et al.*, 1997b). Such features include the hotspot, increasing reflectance with view zenith angle (bowl shape) and the asymmetry of the bowl-shape caused by increased reflectance in the backscatter direction. In practice these features are modelled using a weighted sum of isotropic, volumetric and GO scattering components, each of which is a function of viewing and illumination geometry only (Wanner *et al.*, 1995). This was introduced in equation **2.27**.

As described in section **2.5.4**, the volumetric kernels are approximations to the solution of radiative transfer in a plane parallel homogenous medium (Ross, 1981; Wanner *et al.*, 1995). The GO kernels are derived from considering the proportions of sunlit and shadowed ground and canopy components from the illumination of spheroids randomly distributed on a Lambertian surface (Li and Strahler, 1986, 1990, 1992; Wanner *et al.*, 1995). In both cases a variety of approximations are made to the physically complete solutions to allow the kernels to be formulated as linear functions of viewing and illumination angles only. They can then be summed to describe the BRDF of arbitrary surfaces. Most importantly, they can be linearly scaled (spatially) and applied to heterogeneous surfaces at arbitrary resolution (ignoring adjacency effects), typically 100s of m to km-scale (Lucht *et al.*, 1999).

Linear kernel-driven BRDF models have been practically applied to airborne, spaceborne and field-measured multi-angular reflectance data and have been shown to fit observed data well (Roujean *et al.*, 1992; Privette and Vermote, 1995; Hobson *et al.*, 1999; Lewis *et al.*, 1999). In addition, such models have been inverted against reflectance data to produce model parameters estimates, which in turn have been used to derive integrated quantities such as surface albedo (Barnsley *et al.*, 1997b; Disney *et al.*, 1997; Lewis *et al.*, 1999; Strugnell and Lucht, 1999; Schaaf *et al.*, 1999). There is ample evidence to suggest that the linear models are sufficiently flexible to describe the shapes of a variety of directional reflectance features. More recently, linear kernel-driven BRDF

models are being used to produce the first global spatial albedo products from MODIS directional reflectance measurements have (Schaaf *et al.*, 1999, 2000a,b).

Given the approximations underlying the kernels it is perhaps surprising that the linear models are able to represent the form of surface reflectance so well. The kernels are severe simplifications of the physical solutions for volumetric and GO scattering from anisotropic surfaces, which are approximations in themselves. Further simplifications are needed in both cases to make the kernels linear functions of θ_i and θ_v only. Considering these various degrees of approximation, two questions regarding the modelling of scattered radiation by the linear kernel-driven BRDF models can be asked:

- **How are kernel-driven models able to adequately describe complex scattering from such a wide variety of surfaces, given their approximate nature and the simplifications they contain?**

- **What biophysical information (if any) is contained within the linear model parameters, and is it possible to extract and exploit such information from model inversion against measured reflectance data?**

These two questions form the basis of the work presented in this thesis. Linear models have been designed for use in processing global moderate resolution data sets because of their simplicity, linear scaling and rapid inversion properties. The application of linear models to process global MODIS data means it is now vitally important to understand both the limits of operation of the kernel-driven models and the information that may be accessible through their inversion.

This chapter presents results of experiments exploring the validity of modelling BRDF as a linear combination of volumetric and GO components. Chapter **5** presents further analysis of the information contained in the model parameters, and explores to what extent the kernels act independently. In chapter **6** knowledge gained from these experiments is applied to the development of a new linear kernel-driven model of BRDF with a spectral component. Chapter **7** proposes how improved kernel-driven models of BRDF might be applied to air- and space-borne data.

4.1 Experimental method

In order to investigate how linear models are able to describe scattering from vegetation canopies, a method of examining the underlying scattering behaviour occurring within the canopy has been developed. Measured 3D plant parameter data (described in section **3.1.5**) have been used within the BPMS to simulate the scattered radiation field of developing barley and winter wheat canopies. The BPMS permits scattered radiation to be analysed purely in terms of the controlling geometric factors such as the proportions of sunlit and shaded canopy and soil. Scattering behaviour can also be analysed **independently of wavelength**, which is essential if conclusions are to be drawn regarding the operation of the kernel-driven models: they are formulated purely as functions of viewing and illumination angle and not wavelength. Using the measured 3D plant data within the BPMS, an investigation of the scattering behaviour of the canopy under arbitrary viewing and illumination conditions can be carried out. Any assumptions made in the BRDF models under consideration can also be replicated, making it the ideal tool for benchmarking BRDF modelling techniques (Lewis, 1999).

The barley and wheat canopies were chosen because their properties differ sufficiently from those postulated in the formulation of the kernels so that they should provide a difficult test case for the linear models:

- They are row crops (azimuthal variability).
- They are not horizontally homogenous (clumping, and variable density).
- They do not have a uniform, spherical LAD.
- They do not exist over a Lambertian surface (non-Lambertian soil).

In addition to these factors, there are a number of other departures from the assumptions made in the linear models common to all canopies. Radiometric properties may differ from those assumed (e.g. $\rho_{leaf} \neq \tau_{leaf}$); shadows within the canopy are not perfectly black (diffuse illumination will always be present); illuminated crown and ground regions are not likely to be equally bright. These canopies will provide a sterner test of the kernels' ability to describe BRDF than canopies which closely conform to the assumptions of the models. If the models can adequately describe the BRDF of the chosen canopy, then they are likely to work in less demanding cases, where less of the assumptions made in the linear models are violated. Information regarding (non canopy-

specific) scattering behaviour derived from these canopies will be generally applicable. A secondary reason for selecting these crops is that agricultural canopies are of commercial and scientific interest to end-users attempting to derive biophysical parameter information from moderate resolution EO data (Lucht and Roujean, 2000).

Canopy reflectance generated using the ray tracing component of the BPMS software provides a full numerical solution for scattering within a simulated canopy (referred to subsequently as BPMS, or BPMS-generated) (Lewis, 1999). It is used here as a 'baseline case' i.e. it is assumed to be the single scattered bidirectional reflectance of the measured canopy under given viewing and illumination conditions, with the specified reflectance and transmittance behaviour of the canopy components. Results in chapter **3** support this assumption, demonstrating that the BPMS simulations using measured plant data are capable of accurately representing the observed features of the field-measured canopy reflectance, at the correct (angular) magnitudes. Derived structural parameters such as LAI, % cover and joint gap probability also agree within experimental limits (given the variability of measured values), although there is significant variability.

Recalling section **2.5.4**, the assumption underpinning the linear kernel-driven BRDF models is that canopy reflectance may in general be considered as a linear superposition of volumetric and GO scattering components (Roujean *et al.*, 1992; Wanner *et al.*, 1995). The assumptions are made that $\rho_\lambda = k\tau_\lambda$ for canopy elements (k is constant, unity in this case), and that only single scattering interactions are considered. It follows that canopy reflectance, ρ_{canopy}, can be expressed simply as a linear sum of the scattering from the canopy and soil respectively i.e.

$$\rho_{canopy} = \rho_{leaf}\alpha + \rho_{soil}\beta \qquad \textbf{4.1}$$

If equation **4.1** is compared with equation **2.27** (ignoring the isotropic term for the present) then, as a result of the single scattering assumption (i.e. soil→leaf and leaf→soil scattering events are precluded) the $\rho_{leaf}\alpha$ term must represent the volume scattering component of ρ_{canopy}, and the $\rho_{soil}\beta$ term must represent the GO component. The volume scattering component, α, **must originate purely from the vegetation elements within the canopy** (and is therefore related to LAI) as there can be no leaf→soil interaction; similarly. the GO component must originate purely from the soil. If this is the case, then β

is simply **the proportion of sunlit soil visible to the viewer**, and is hence a function of θ_i and θ_v (as well as the inherent LAI and LAD of the canopy). These two components of ρ_{canopy} are illustrated in figure **4.1** which shows two nadir simulated images of a barley canopy in early stages of growth. In the left image $\rho_{leaf} = 1$, $\tau_{leaf} = 0$ and $\rho_{soil} = 0$ i.e. white areas correspond to sunlit vegetation and black areas to sunlit soil. In the right image $\rho_{leaf} = 0$ and $\rho_{soil} = 1$ i.e. black areas correspond to vegetation and white to soil.

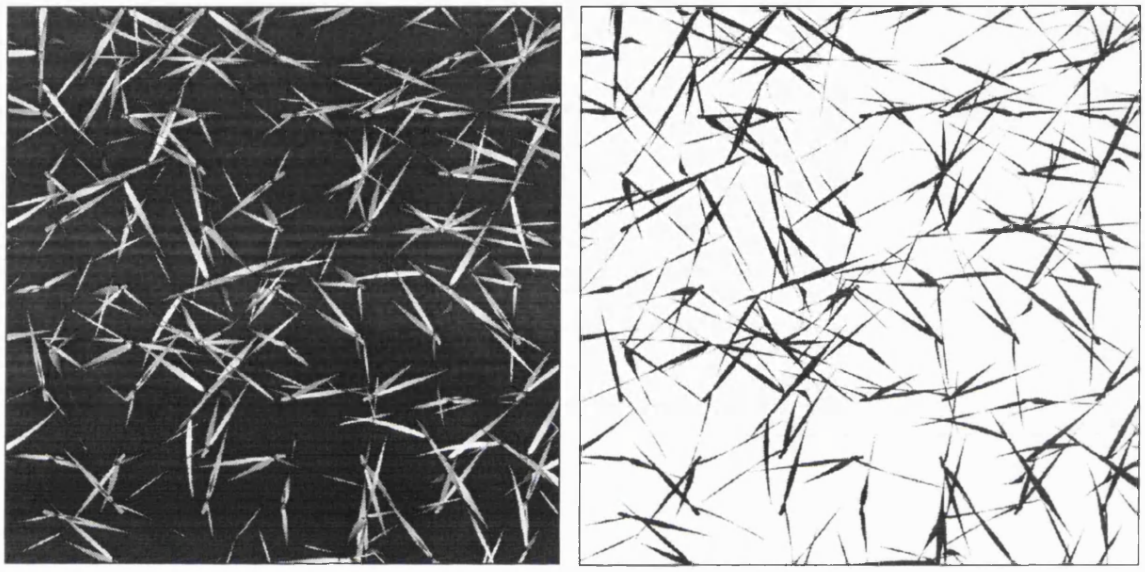

Figure 4.1 Components of ρ_{canopy}: left image $\rho_{leaf} = 1$, $\tau_{leaf} = \rho_{soil} = 0$ (volume scattering); right image $\rho_{leaf} = \tau_{leaf} = 0$, $\rho_{soil} = 1$ (GO scattering).

Recalling the form of the volume scattering kernels (**2.5.4.1.1**) the volume scattering component of canopy reflectance is given as (c.f. equation **2.23**):

$$\alpha = \frac{P(\theta_i, \theta_v, \phi)}{4G\mu\mu'}\left\{1 - e^{-LAI\left(\frac{G'\mu + G\mu'}{\mu\mu'}\right)}\right\} \qquad \textbf{4.2}$$

$P(\theta_i, \theta_v, \phi)$ is the single scattering phase function, LAI is the leaf area index, G' and G are the leaf projection functions in the viewing and illumination directions, and μ and μ' are the cosines of θ_i and θ_v respectively. Note that both α and β are functions purely of viewing and illumination angle (and row azimuth in the case of row crops). As a result, any investigation of these parameters will be independent of wavelength. This is highly desirable for examining the operation of the linear kernel-driven (angular) models due to their reliance on purely geometric terms. Any conclusions that can be drawn will be solely concerned with geometric dependencies and not spectral ones.

4.2 Exploring the hypotheses behind the linear models

The linear kernel-driven approach to modelling BRDF is based on two fundamental and linked hypotheses, the first of which shall be examined in detail in the subsequent sections of this chapter, and the second in chapter **5**:

1. **Canopy reflectance can be modelled as a linear combination of volumetric and GO scattering components.**

2. **The volumetric component of ρ_{canopy} is adequately modelled by the volume scattering kernel alone and similarly, the GO component is adequately modelled by the GO kernel.**

All other properties of the linear models are reliant on the validity of these two hypotheses. If either proves unreliable then it can be concluded that the linear kernel-driven approach to modelling ρ_{canopy} may need to be reconsidered. By testing them it is possible to demonstrate whether (and how) the linear models are capable of modelling a variety of different canopy types and surfaces. In addition it is hoped that the limits of their operation can be explored and extended. As noted previously, the kernels are designed to operate on heterogeneous surfaces at moderate resolution. In order to explore the scattering processes within canopies in detail however, we consider homogeneous surfaces at high resolution (cm).

4.2.1 ρ_{canopy} as a linear combination of volumetric and GO scattering

The initial part of this experiment is designed to test hypothesis 1 above – namely that ρ_{canopy} can be satisfactorily modelled as a linear combination of volumetric and GO scattered components. That is, can the two components be linearly related to the (purely geometric) terms governing the scattering from the vegetation and soil i.e. α and β in equation **4.1**? If the assumption of linearity is valid, it is vital to know under what conditions this assumption will hold and where it is likely to break down.

In order to test the hypothesis, BRFs were generated using measured plant parameter data characterising the 3D structure of barley (four dates) and winter wheat

(two dates). The structural data measurements described in detail in chapter **3**. Values of LAI and % cover are given for the various canopies in table **4.1** and simulated views of each canopy are shown in figures **4.2a-f**.

Table 4.1 Details of the canopies used in simulations

Canopy	Date	LAI	% cover
barley	18th April	0.56	15.1
barley	13th May	3.44	66.3
barley	4th June	3.14	62.9
barley	24th June	3.15	66.9
winter wheat	23rd March	0.08	3.4
winter wheat	23rd April	2.03	25.8

The simulated canopies shown in figure **4.2** are (arbitrarily) pictured as $1m^2$ patches. Much larger areas are used for subsequent experimentation, with only small central sub-regions of each canopy being viewed in order to avoid 'edge effects' (see below). Such errors are caused by the divergence of the canopy from the assumption of infinite horizontal extent. During simulation, rays escaping the scene from beyond the horizontal extent of the canopy will lead to inconsistencies in the integration of exitant scene radiation. Additionally, if the modelled canopy is the same area as the area being viewed, some plant organs may extend beyond the edge of the scene leading to the possibility that there may be non-integer numbers of plants in a given area. It should be noted that the canopies in figure **4.3** are simulated over a non-Lambertian soil surface based on observed soil properties. The soil brightness characteristics have been modelled on the observed semivariance of soil properties extracted from photographs from the respective canopies. The height variation of the soil (due to the ploughing and drilling) is modelled using a sine function with the wavelength and amplitude determined from observed soil roughness characteristics. Small amplitude Gaussian noise has been added to the sine function to simulate small-scale surface roughness variations. In subsequent simulations used in this chapter and chapters **5** and **6**, the soil is a simple Lambertian surface (as is assumed in the linear kernel-driven modelling approach).

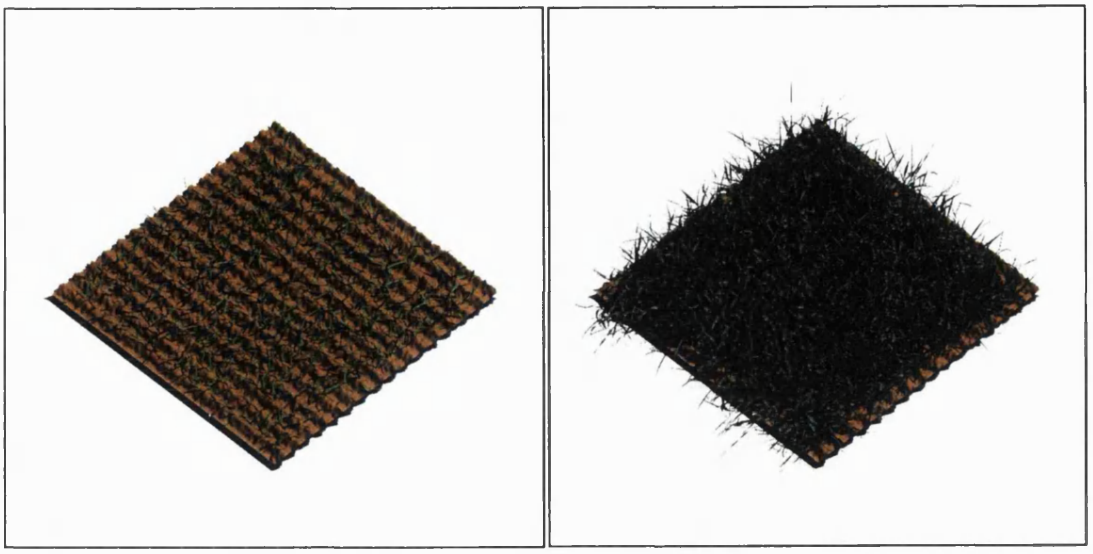

a) barley – 18th April

b) barley – 13th May

c) barley – 4th June

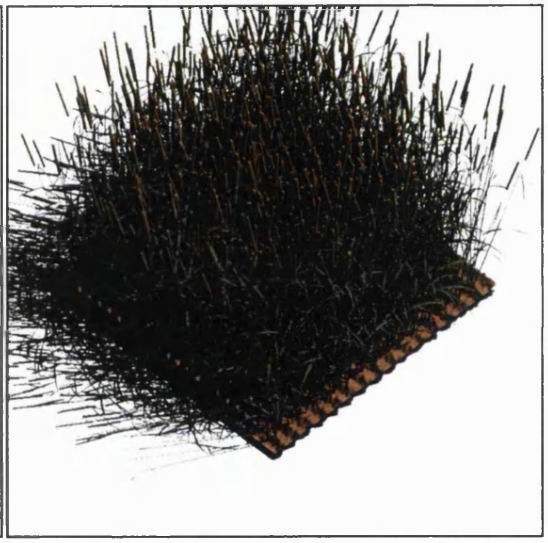

d) barley - 24th June

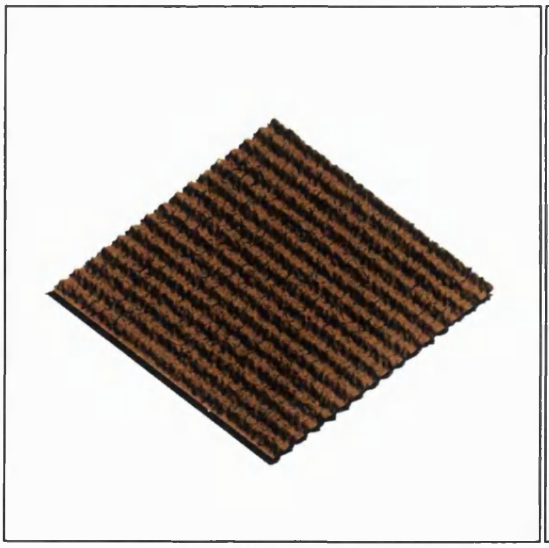

e) wheat – 24th March

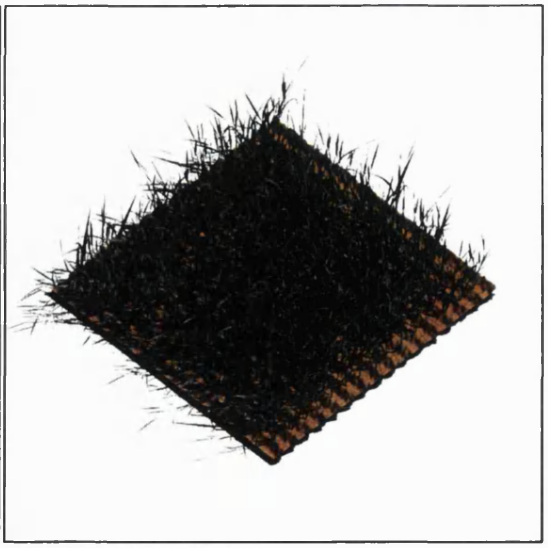

f) wheat – 24th April

Figure 4.2 Simulated images of measured barley and wheat canopies.

The viewed area of each canopy is designed to contain an integer number of rows (seven) resulting in a viewed area of 0.49m on a side (row spacing is 7 cm). The horizontal extent of the canopy, l, is chosen to be 0.49m plus twice the ground projection of the tallest part of the canopy (h) at an angle greater than the maximum θ_v to be used. In order to be safe, θ_v (max) of 70^o is assumed even though in subsequent experiments θ_v never exceeds 60^o. Therefore $l = 0.49 + 2h\tan\theta_v = 0.49 + 5.5h$. This ensures the modelled canopy extends sufficiently either side of the viewed area to eliminate edge effects, even at extreme θ_v. For example, the barley canopy of 13th May has $h_{max} = 0.38$m giving $l = 0.49 + 2(1.04)$ i.e. the canopy is extended to 1.04m on either side of the 0.49m central patch, giving a canopy of 2.57m on a side. Orthographic viewing projection is used to enforce parallel ray geometry. This ensures that the same area of surface is viewed regardless of θ_v. As a result, the linear dimensions of off nadir scenes increase (relative to nadir) to ensure the same area is included in the simulation. This configuration is illustrated in figure **4.3**.

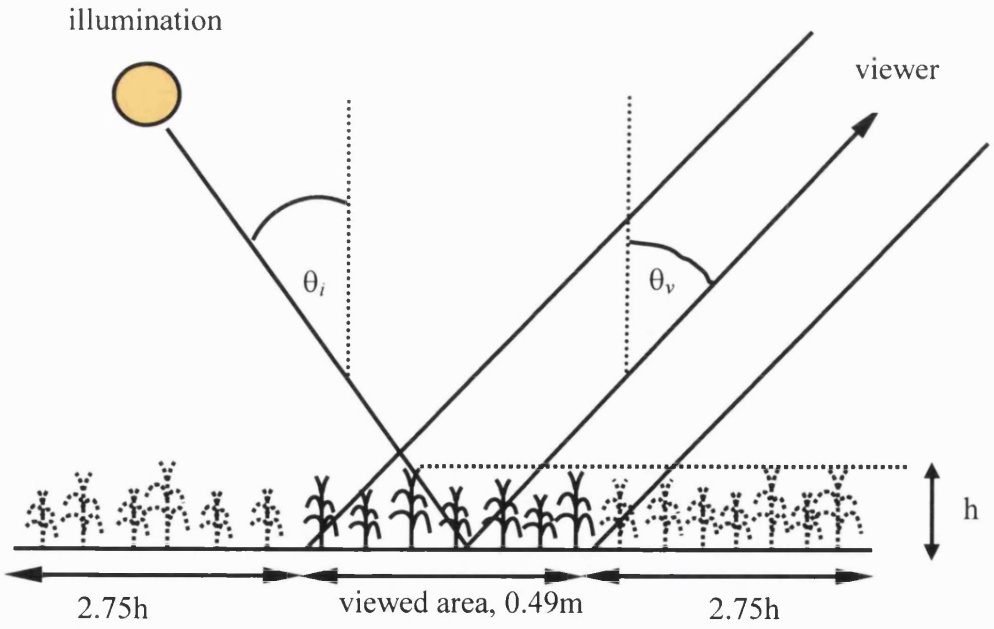

Figure 4.3 Viewing and illumination geometry and canopy extent for simulations.

BRFs were simulated in the manner described above under the explicit assumptions of the linear models (see section **2.5.4**) i.e.:

- single scattering interactions only
- bi-Lambertian leaf reflectance
- $\rho_{leaf} = \tau_{leaf}$ (values: 0.5 or 0)
- ρ_{soil} is Lambertian (values: 0 or 1)
- direct illumination only

Directional reflectance was simulated in the solar principal plane at θ_v from -60^o to 60^o in steps of 10^o, except within the 10^o interval centred on the hotspot, where sampling was increased to every 2^o. The row azimuth angle (ϕ_{row}) of the crop was fixed at angles of 0^o, 45^o, and 90^o to the viewing plane, in order to provide the most extreme cases for analysis. This is likely to affect canopies with noticeable gaps between rows e.g. young crops. As ϕ_{row} increases shadowing will shift from along to across the rows. Figure **4.4** shows an example of simulated directional reflectance of the 13th May barley canopy ($\theta_i = \phi_{row} = 0^o$). The transition of dark to light with increasing view zenith is quite clear, including the bright hotspot image at nadir (differing aspect ratios are caused by the orthographic projection). Three wavebands are simulated: 450, 500 and 650nm, with corresponding $\rho_{leaf} = 0.062$, 0.093 and 0.068; $\tau_{leaf} = 0$; $\rho_{soil} = 0.123$, 0.118 and 0.132.

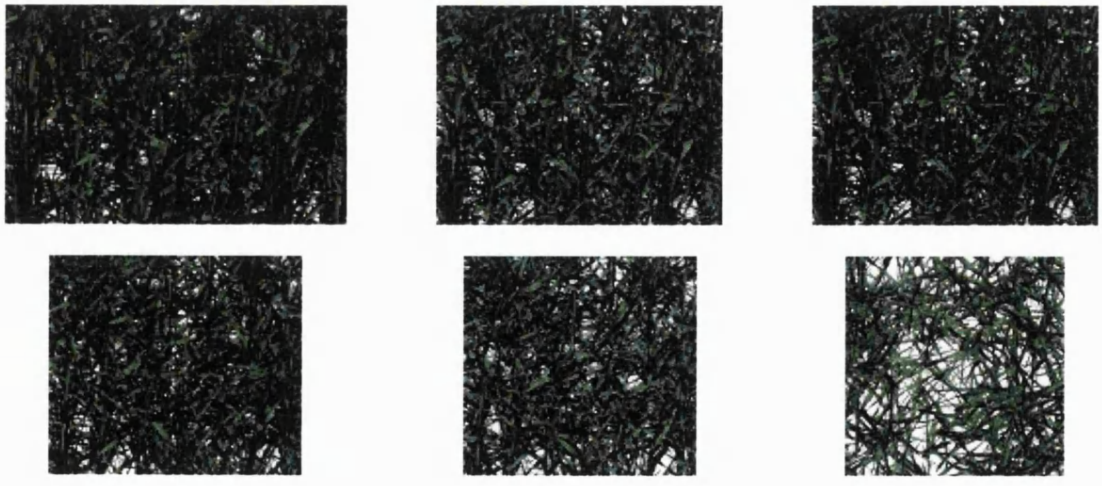

Figure 4.4 Simulated barley reflectance, θ_v from -50^o to 0^o (left to right, top to bottom).

If there is a linear relation between the volumetric and GO components of canopy reflectance and the volumetric and GO kernels, k_{vol} and k_{GO}, then comparing equation **4.1** with the general linear model form of equation **2.27**, k_{vol} must be proportional to α and

k_{GO} must be proportional to β. In this case, it can be said for BPMS-simulated canopy reflectance that (under these specific conditions):

$$k_{vol} = a_{vol}\alpha + b_{vol} \quad \textbf{4.3}$$

$$k_{GO} = a_{GO}\beta + b_{GO} \quad \textbf{4.4}$$

where a_{vol}, b_{vol}, a_{GO}, b_{GO} are constants. Following equation **4.1** the simulated canopy reflectance can be divided into separate volumetric and GO scattering components (scattering from vegetation and soil only) to give values of α and β. If hypothesis 1 is valid then α and k_{vol}, and β and k_{GO} should be linearly related. Slopes of regressions of these parameters will yield a_{vol} and b_{vol}, and the intercepts, a_{GO}, b_{GO}. The following section presents results of the BPMS simulations ρ_{canopy}. Results are also presented from regressing the volume and GO scattering components of the BPMS-simulated ρ_{canopy} (α and β) against the values of k_{vol} and k_{GO} for the same viewing and illumination conditions.

4.2.2 Volumetric and GO components of ρ_{canopy}

The shapes of the volume and GO scattering components of ρ_{canopy} for the barley and wheat canopies are presented here and discussed in section **4.2.3**. Results of the regressions of α and β against k_{vol} and k_{GO}, along with discussion of these results, are presented in section **4.3**.

Figure **4.5** shows the variation of the BPMS-derived volumetric parameter, or leaf-scattered component of simulated reflectance (α from equation **4.2**) as a function of view zenith angle for four dates throughout the development of the barley (**4.5 a-d**) and wheat crops (**4.5 e-f**). Results are shown for θ_v (0°, 30°, 60°) and for ϕ_{row} (0°, 45°, 90°). Figure **4.6 a-f** shows the variation of the BPMS-derived GO parameter of the various canopies (β from equation **4.1**), the soil-scattered component, under the same viewing and illumination conditions (NB note the changes of scale that occur between each of the figures **a-f**).

Figure 4.5 Variation with view zenith angle of BPMS-derived volumetric component of barley and wheat canopy reflectance for six dates.

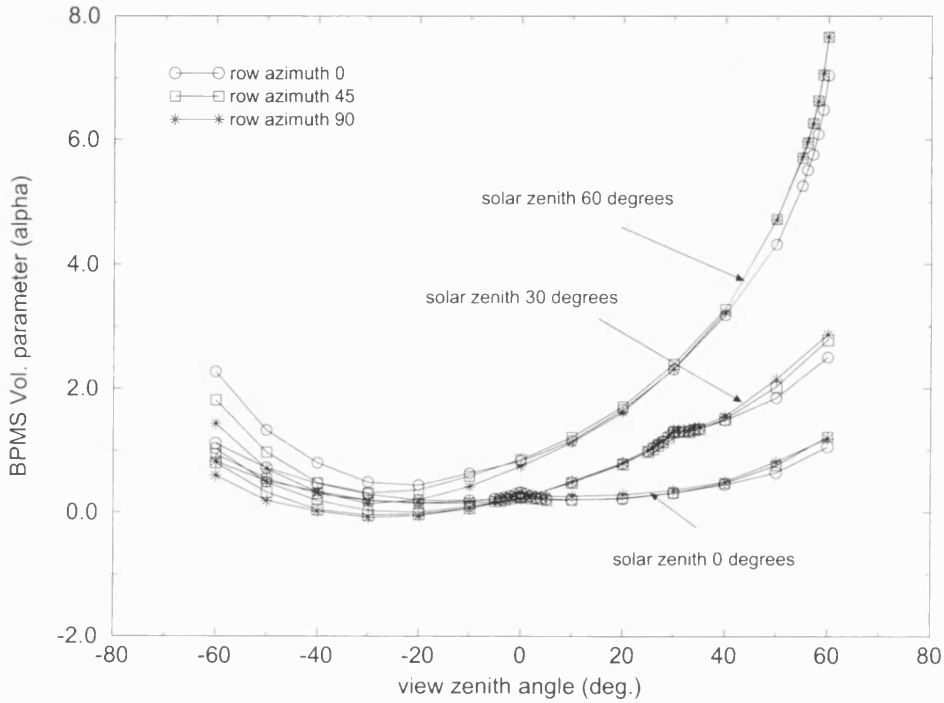

a) barley – 18th April

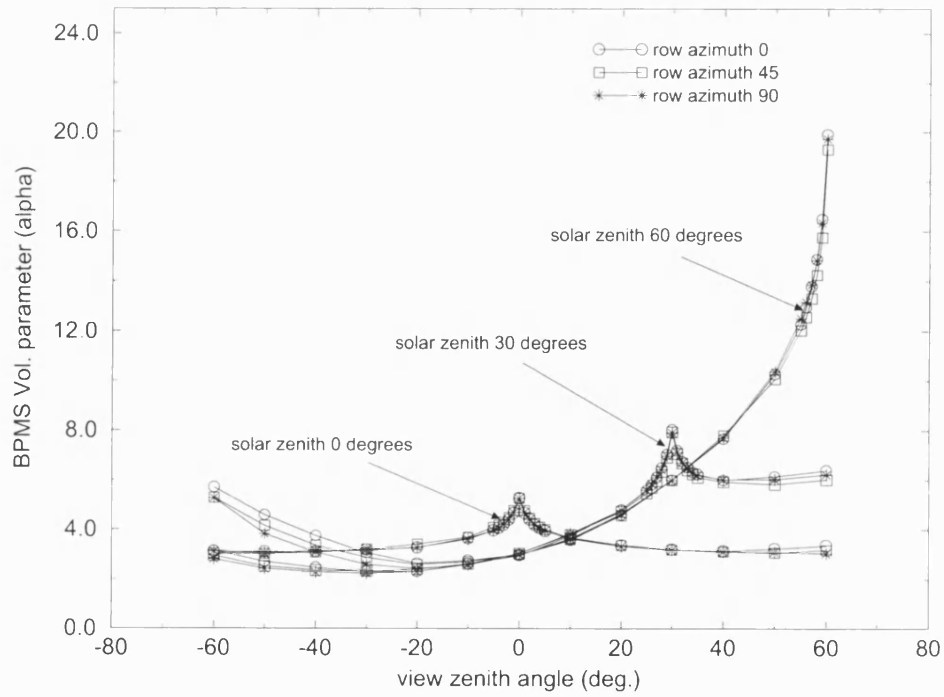

b) barley – 13th May

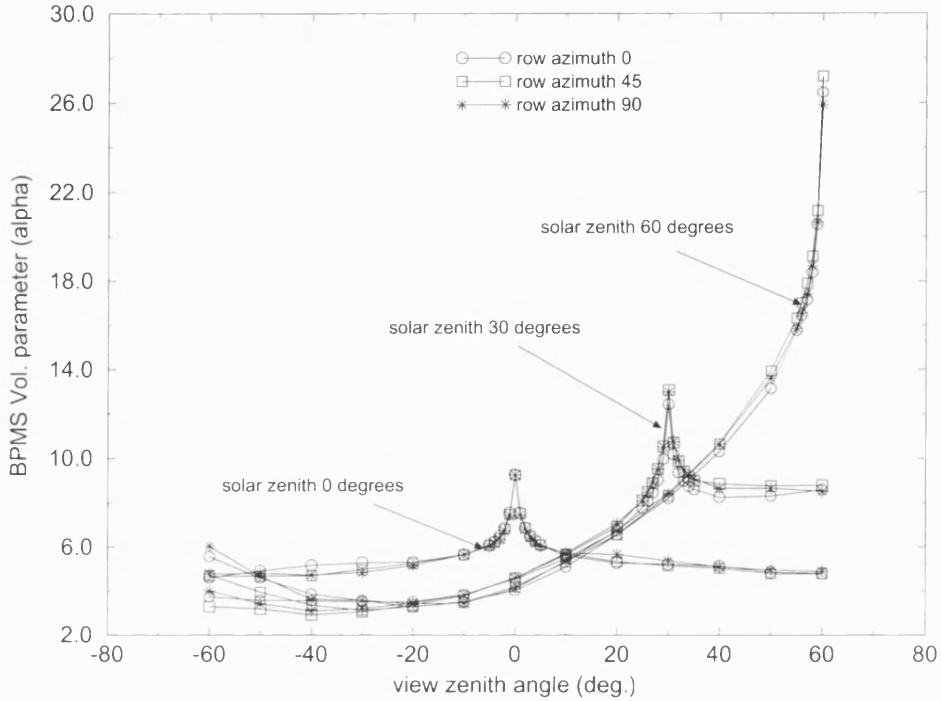

c) barley - 4th June

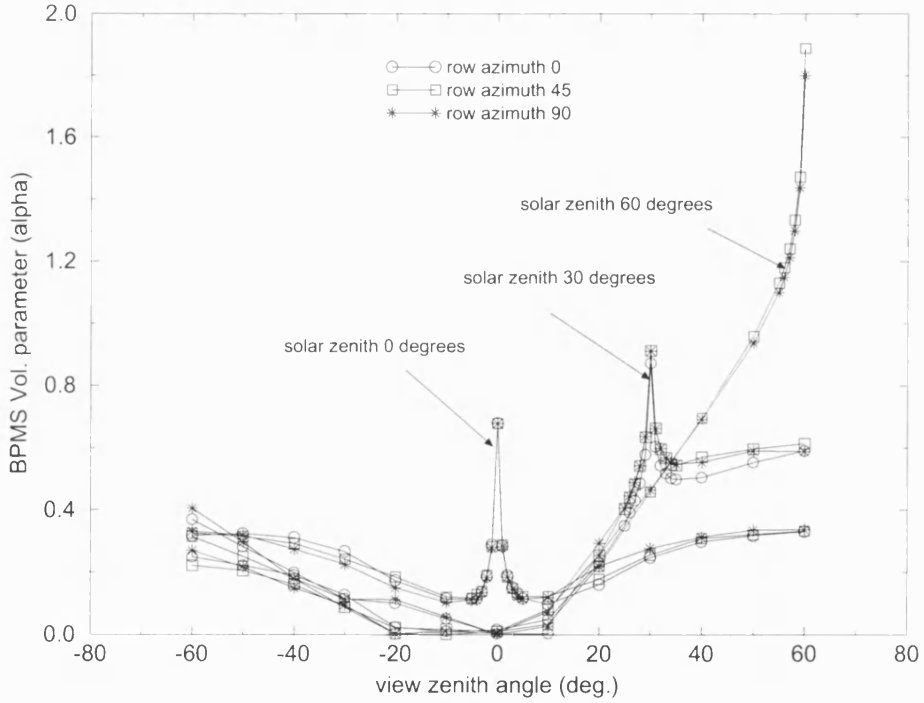

d) barley – 24th June

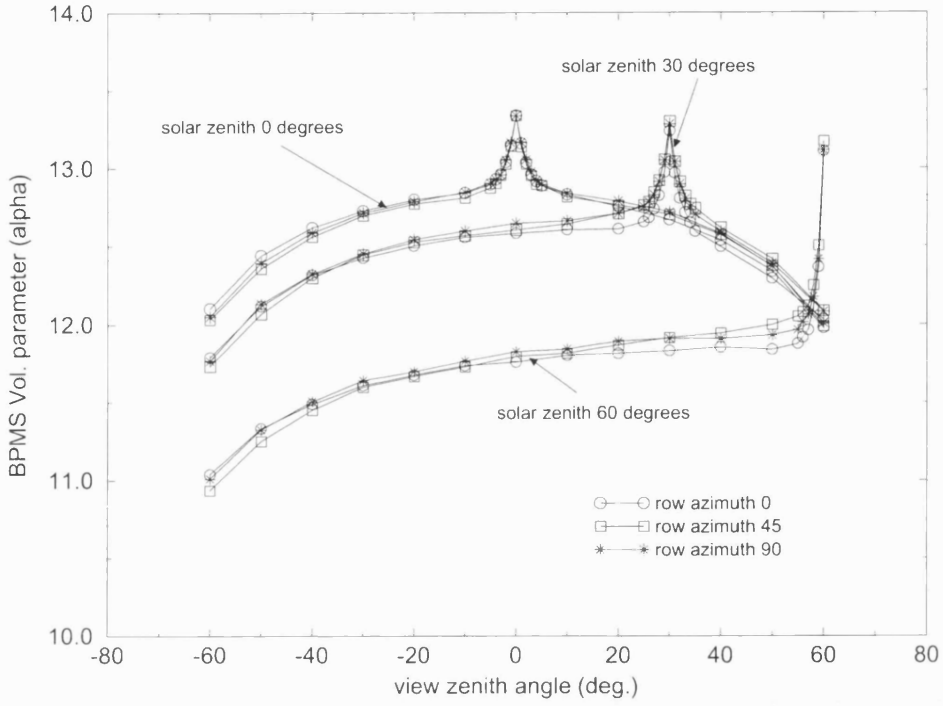

e) wheat –23rd March

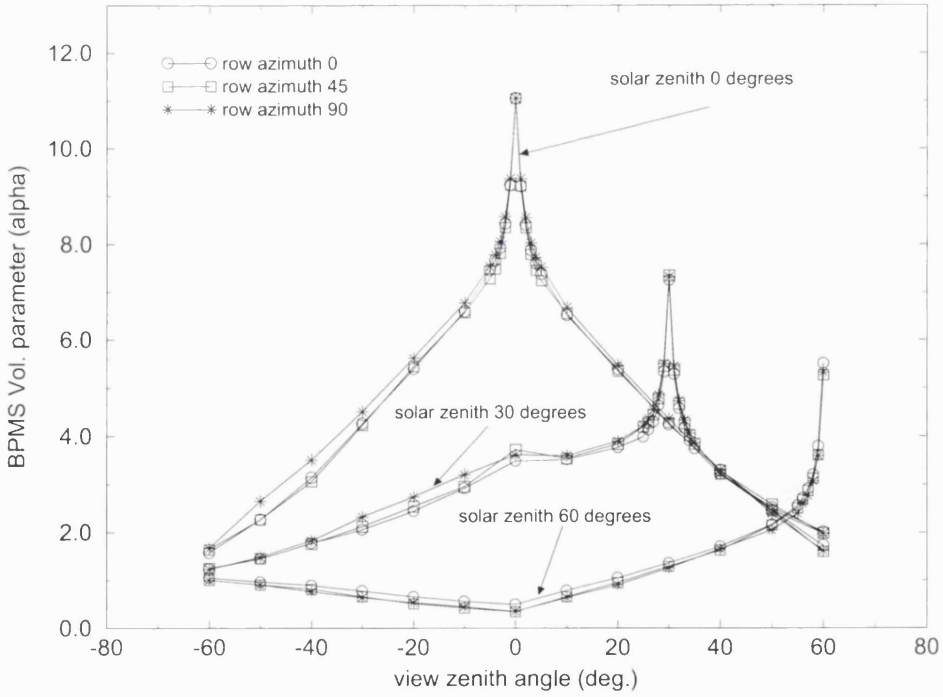

f) wheat - 23rd April

Figure 4.6 Variation with view zenith angle of BPMS-derived GO component of barley and wheat canopy reflectance for six dates.

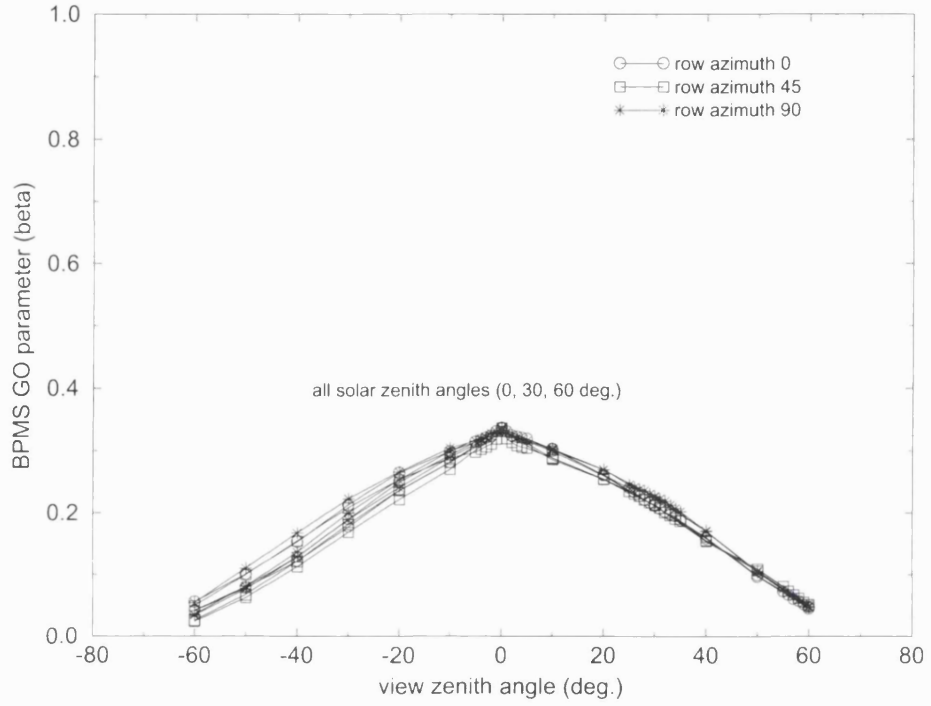

a) barley – 18th April

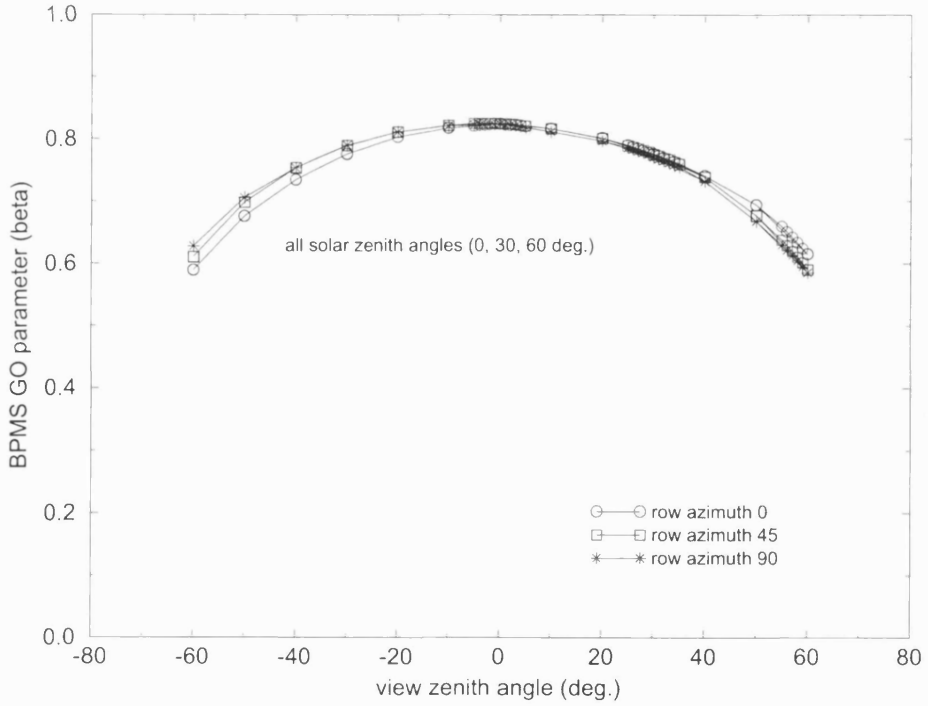

b) barley – 13th May

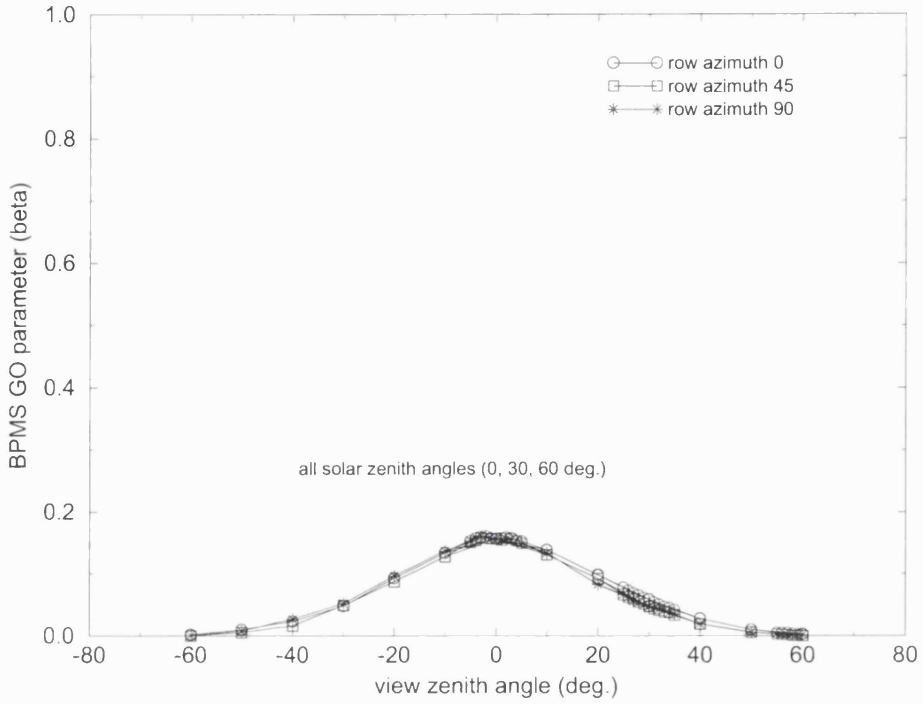

c) barley – 4th June

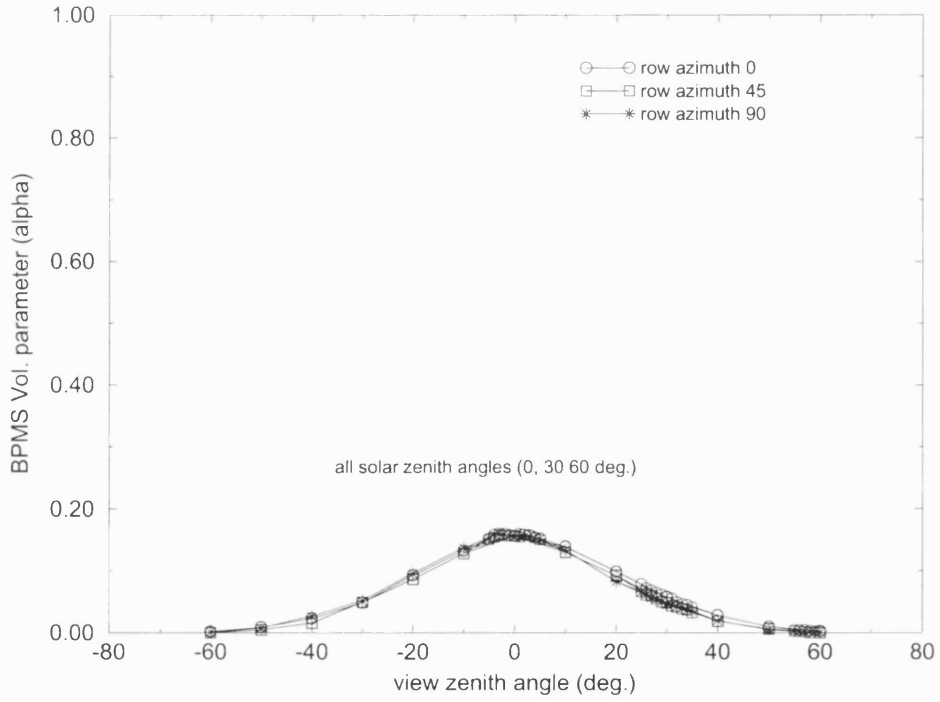

d) barley – 24th June

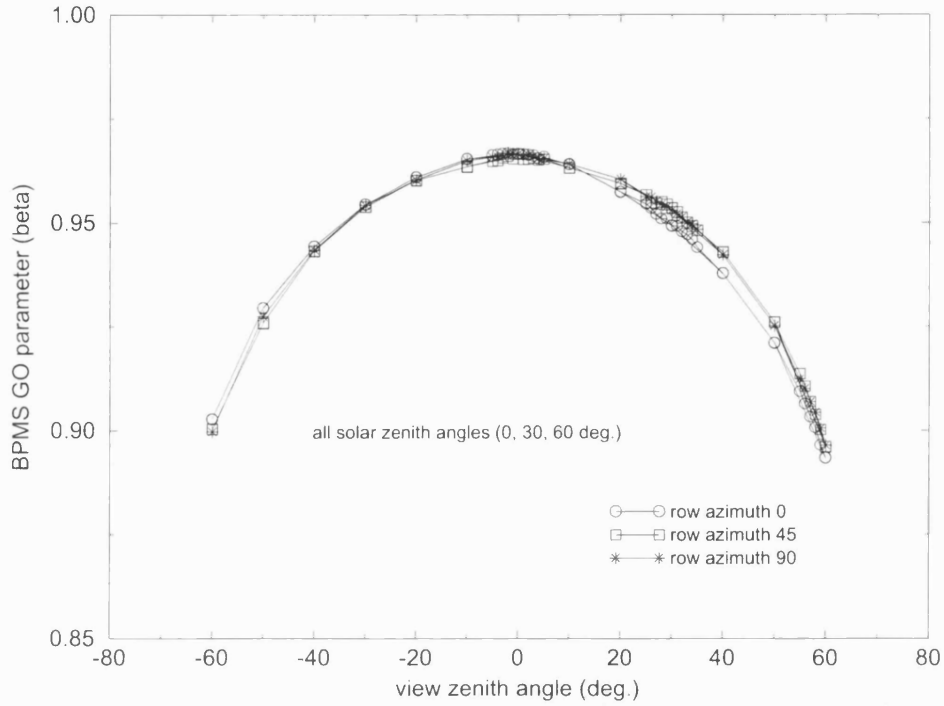

e) wheat – 23rd March

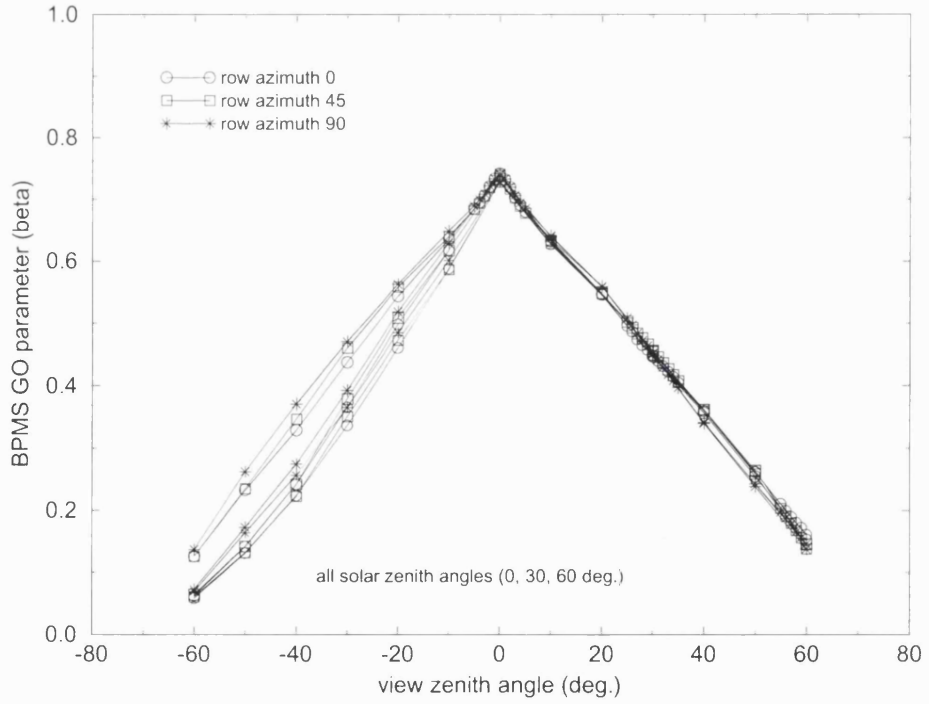

f) wheat – 23rd April

4.2.3 Discussion of directional shapes and magnitudes of α and β

4.2.3.1 Volumetric component of ρ_{canopy}, α

Figure **4.5** shows the volumetric component of BPMS-simulated ρ_{canopy} to have (in general) an asymmetric, upward bowl-shape in the case of the barley canopy (α_{barley}). Reflectance tends to be low (minimum) at nadir or in the forward scattering direction, and increases in the backscatter direction (increasing θ_v) with a sharp peak in the hotspot direction. α_{wheat} is much flatter in comparison, showing a downward bowl-shape for all θ_i, again with a sharp hotspot peak. α_{wheat} decreases between the 23rd March and 23rd April and the shape changes from a peaked downward bowl shape for $\theta_i = 0^o$ to a flat, almost upward bowl shape for $\theta_i = 60^o$. Variation with row azimuth (ϕ_{row}) is negligible in both cases because the row and plant spacing are almost interchangeable (7cm and 5cm respectively).

Differences in the amount of vegetation account for differences in shape between α_{barley} and α_{wheat}. In the wheat canopy of 23rd March there is virtually no vegetation present (LAI = 0.08, see figure **4.2e**) and hence little vegetation scattering. In this case ρ_{canopy} is simply determined by the amount of sunlit soil. The barley canopy of 18th April by contrast, has significant vegetation. Plots of the proportional contribution of the sunlit canopy components to scene reflectance for each canopy, shown in figure **4.7**, support this. In each case, the fractional contribution of each scene component for each ρ_{canopy} simulation (sunlit leaf, sunlit soil) is plotted with varying view zenith angle. Shadowed canopy components are not shown as they do not contribute to scene reflectance (no diffuse component of illumination, $\therefore$ shadows are perfectly black). ρ_{canopy} will in this case be a combination of sunlit leaf and soil only, so the $\text{proportion}_{sunlit\ leaf} = 1 - \text{proportion}_{sunlit\ soil}$ (and vice versa). For comparison, the scene contributions from simulations of the same canopies but including diffuse illumination (i.e. shadowed components are non-zero) are given in Appendix **2**. Recall that in each case, two 'synthetic' wavebands are simulated, the first in which $\rho_{leaf} = \tau_{leaf} = 0.5$ and $\rho_{soil} = 0$ i.e. in this case all signal is (by definition) single scattering from vegetation only; the second waveband has $\rho_{leaf} = \tau_{leaf} = 0$ and $\rho_{soil} = 1$ i.e. in this case all signal is (by definition) single scattering from soil only. Sunlit soil is the dominant scene component in both low LAI cases (figure **4.7a** and **e**) and the behaviour of α reflects this. For wheat, sunlit soil represents greater than 85% of the total reflectance at all $\theta_{v,i}$. As the canopy develops, sunlit soil becomes prevalent.

Figure 4.7 Proportional contribution of sunlit scene components to total scene reflectance, for barley (four dates) and wheat (two dates).

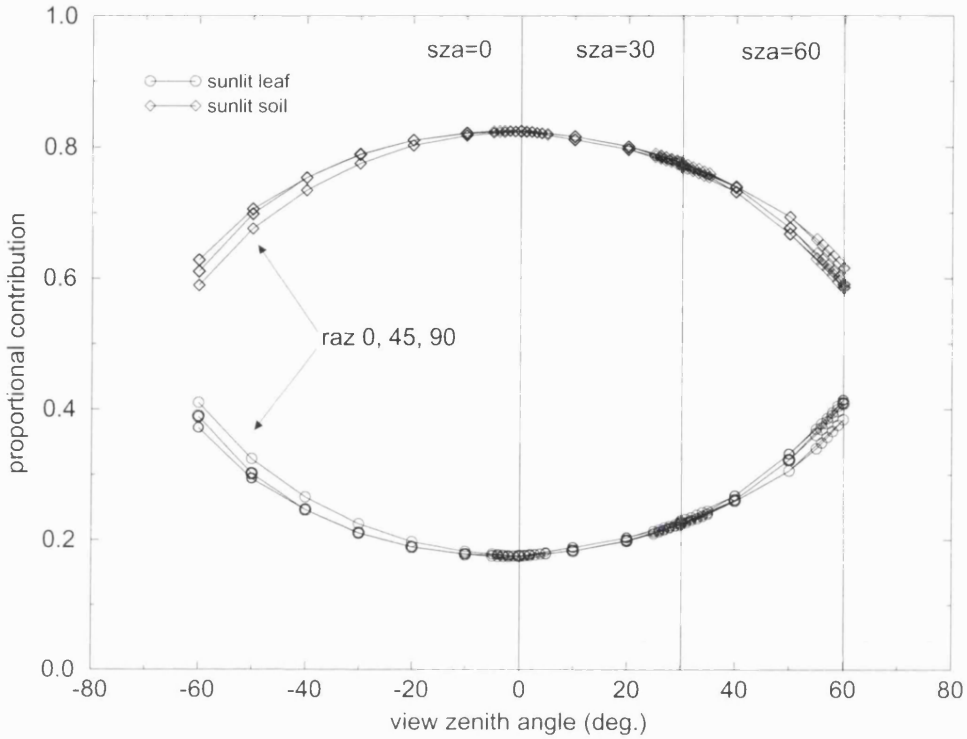

a) barley – 18th April

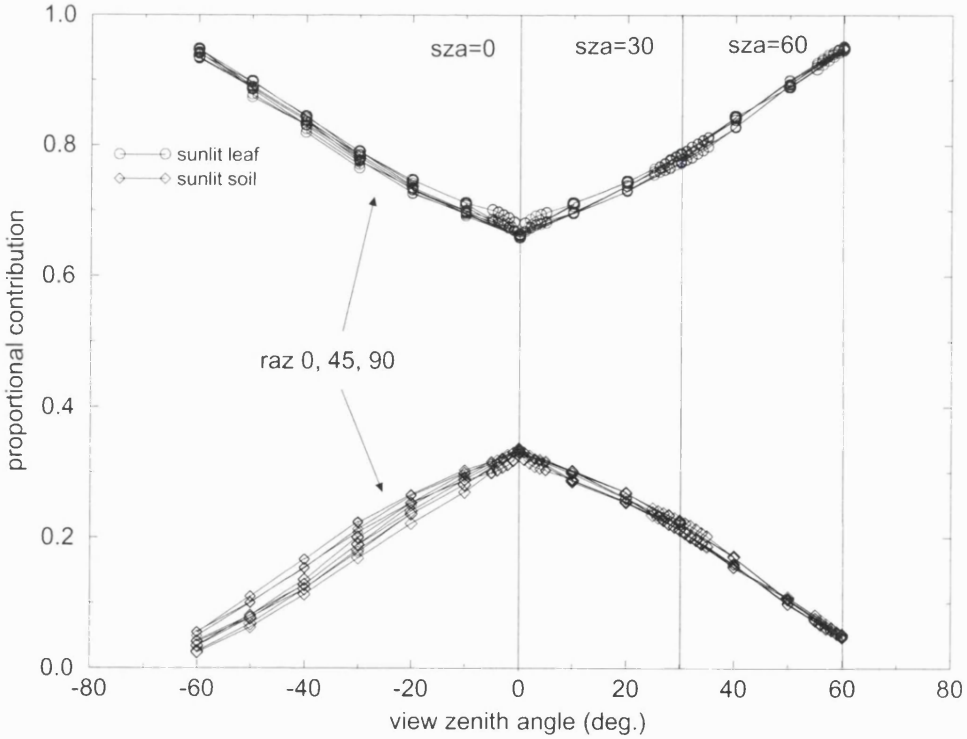

b) barley – 13th May

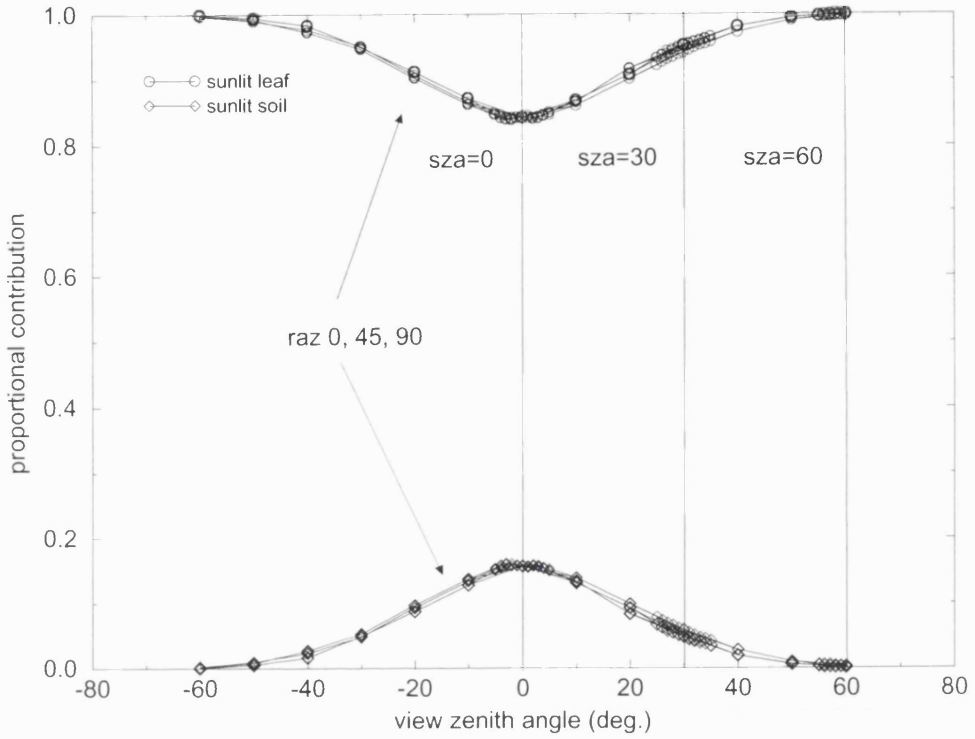

c) barley – 4th June

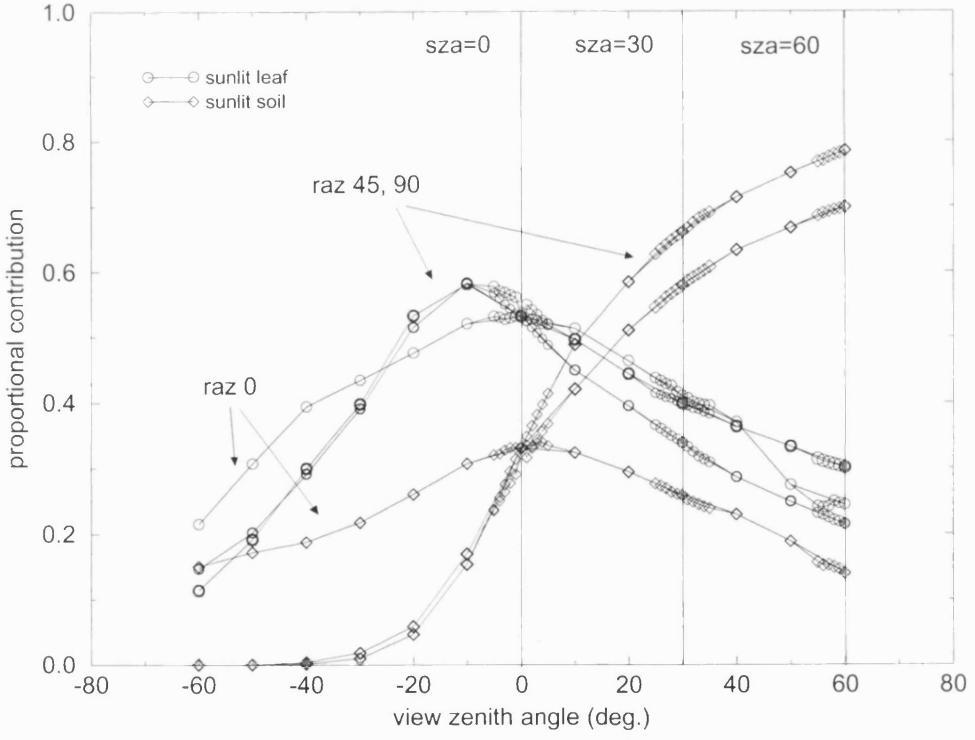

d) barley – 24th June

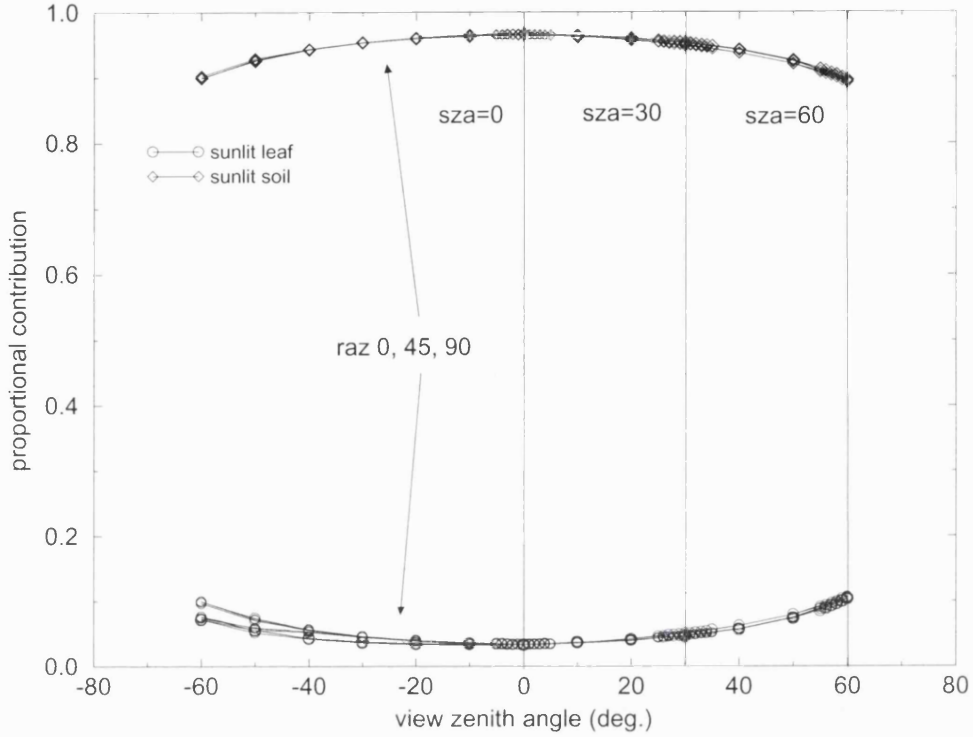

e) wheat – 23rd March

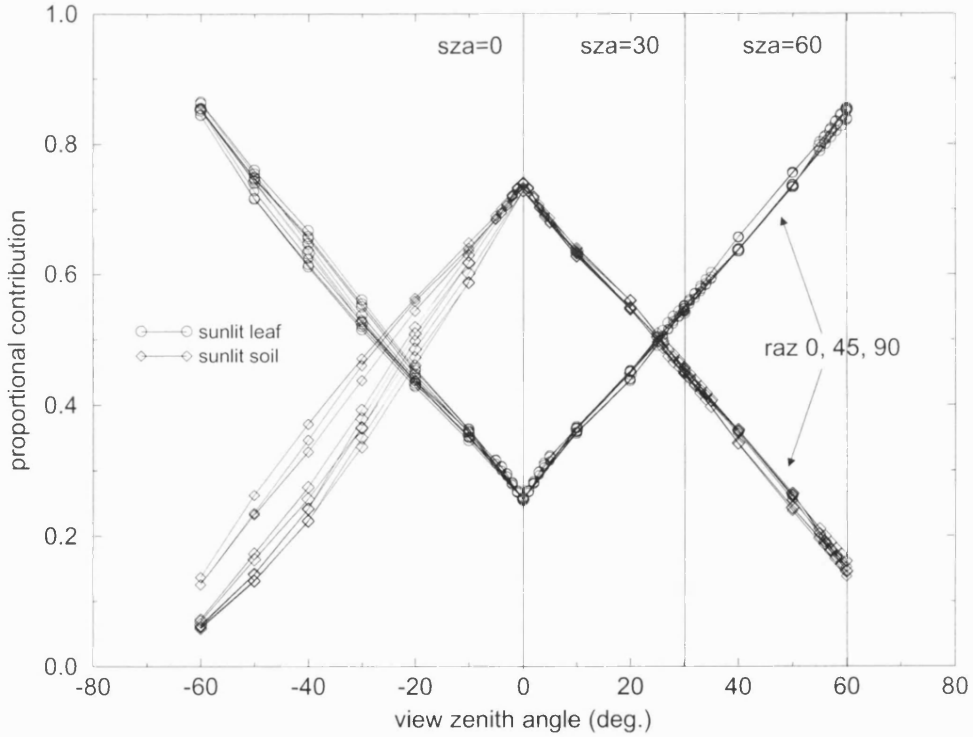

f) wheat – 23rd April

A further difference between the crops which affects α is that in the early stages of growth the wheat canopy is quite strongly erectophile, which can cause dramatic variations in observed reflectance behaviour depending on θ_i and θ_v (Kimes, 1984; Goel, 1992). In an erectophile canopy, the LAD is biased towards higher leaf inclination angles (towards the vertical) so that visible vegetation is at a minimum closer to $\theta_v = 0^\circ$ and increases relatively rapidly with θ_v, while for the visible soil component, the converse applies. The cumulative LADs of the various canopies are shown in figure **4.8**.

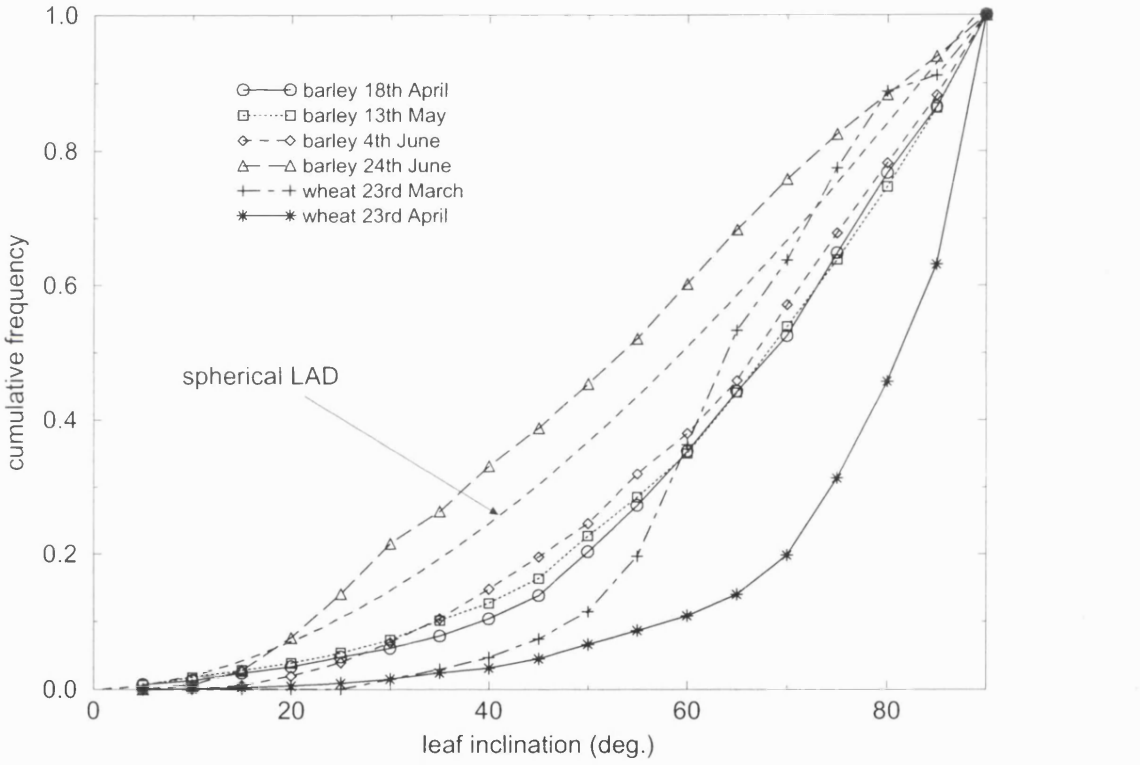

Figure 4.8 Cumulative LAD for four barley and two wheat canopies.

Figure **4.8** shows that the canopies all depart significantly from the assumption of a spherical LAD made in the formulation of the Ross kernels (section **2.5.4.1.1**). The canopies generally tend towards an erectophile LAD i.e. the cumulative frequency distributions rise more slowly than the spherical case to begin with, then much more sharply at higher angles as more leaves are found with relatively high inclination angle. This is true to a greater or lesser extent for all canopies, but particularly wheat. Following the initial growth stages the wheat canopy becomes much more strongly erectophile than the barley. Although the modal LAD for both these canopies lies in the 85-90° range, the increase in frequency from the penultimate 80-85° range is 50% for wheat, and only 14%

for barley. Additionally, the mean LAD of the wheat canopy is 79.3° and 66.5° for the barley. The barley canopy of 24th June is closer to the spherical distribution than the others and also has far more leaves with lower inclination angles than any of the other distributions. However the structure of this canopy is strongly influenced by the seed heads, which cause the stems to 'bend down' under gravity (this can be seen in the photographs of figure **3.8**). This canopy is also the most prone to permanent bending by prevailing winds - as a result of the seed heads again.

It is worthwhile to compare the canopy LADs with a theoretical distribution used in models of ρ_{canopy} such as that of Bunnik (1978). Bunnik's approximation to LAD is a geometrical function with four parameters which can be varied to produce a range of desired distributions. Figure **4.9** shows the variation of Bunnik's theoretical LAD for five cases, erectophile (predominantly upright), extremophile (predominantly either erect or flat), plagiophile (predominantly mid-range), planophile (predominantly flat), spherical (all angles equally likely). Clearly, the barley and wheat canopies used here are closer to the erectophile LAD than any other. This is demonstrated in the correlation of measured canopy LAD values with Bunnik's LAD functions shown in figure **4.10**. All canopies are relatively highly correlated with the erectophile distribution, except the 23rd April wheat canopy which has the lowest correlation with all LADs. The 24th June barley canopy does not follow the trends of the other canopies being nearly equally correlated with the erectophile, plagiophile and spherical distributions. This is a function of the change in canopy structure as it begins to senesce. Clearly, none of the canopies is planophile. The departure of the various canopies from the assumptions of a spherical LAD will tend to cause the scattering components of reflectance α and β, to depart from agreement with their respective kernels and k_{vol} and k_{GO}. This is also likely to have consequences for the separability of scattering components.

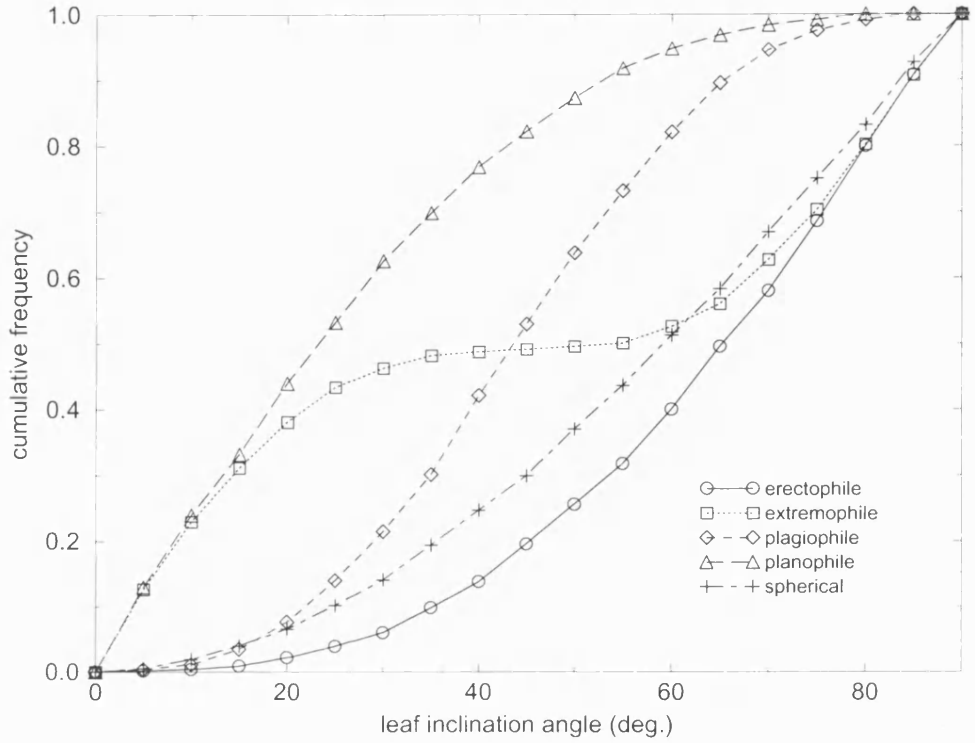

Figure 4.9 Examples of Bunnik's LAD function.

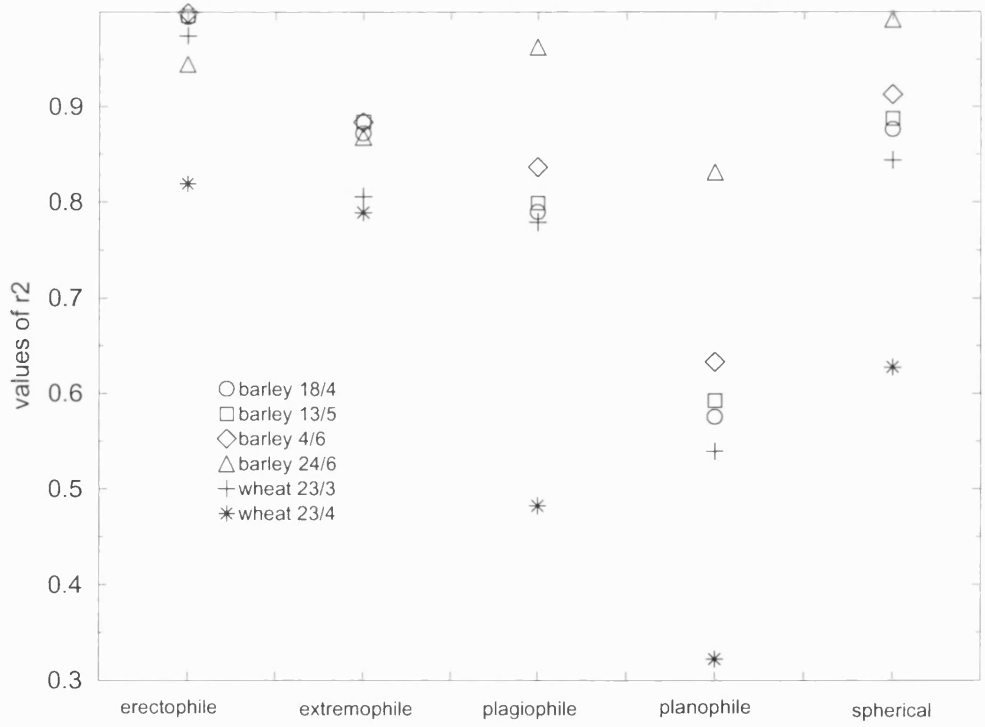

Figure 4.10 Correlation of measured LAD against Bunnik distributions.

It is also instructive to examine the leaf projection functions $G(\Omega)$ (equation **2.21**) and phase functions of the various barley and wheat canopies. Recall that $G(\Omega)$ describes the total fraction of leaf area (per unit volume of canopy) projected into the viewing direction, Ω. Figure **4.11** shows $G(\Omega)$ for the various canopies for which the LAD are given in figure **4.8**. $G(\Omega)$ is shown for $-90^{o} <= \Omega <= 90^{o}$.

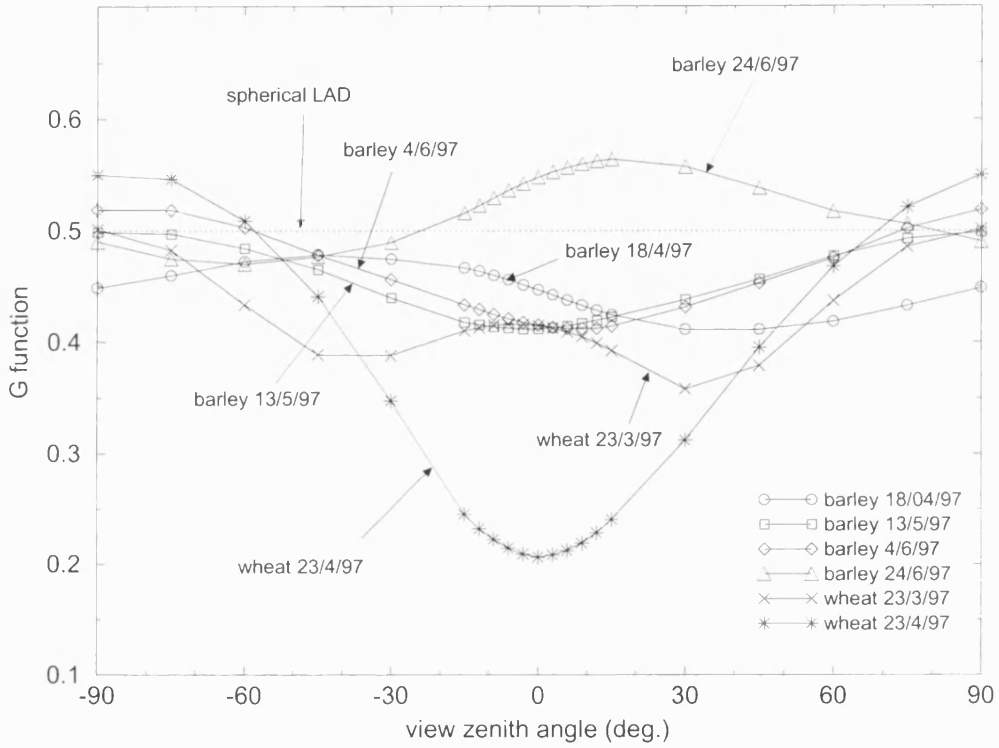

Figure 4.11 Leaf projection function $G(\Omega)$ in viewing direction $\Omega(\theta_v, \phi_v)$.

Figure **4.11** shows the departure from the spherical LAD assumption of the various canopies, particularly the wheat canopy of 23rd April. The closest to the spherical LAD is the barley canopy of 18th April, for which $G(\Omega)$ varies from just below to just above 0.5. The largest departure is seen in the wheat canopy of 23rd April, which has $G(\Omega)$ varying from 0.55 at $\theta_v = \pm 90^{o}$, down to 0.2 at nadir. This highlights the more erectophile nature of the canopy. Phase function is more directly a measure of canopy structure, describing as it does the angular distribution of scattering from the illumination direction Ω' into the viewing direction, Ω, at each photon interaction. Figure **4.12** shows the variation of the phase function with view angle for the six barley and wheat canopies, for nadir illumination. Phase function varies with view angle with the wheat canopy of

23rd April having the lowest values and the barley canopy of 24th June having the highest values (and being most variable).

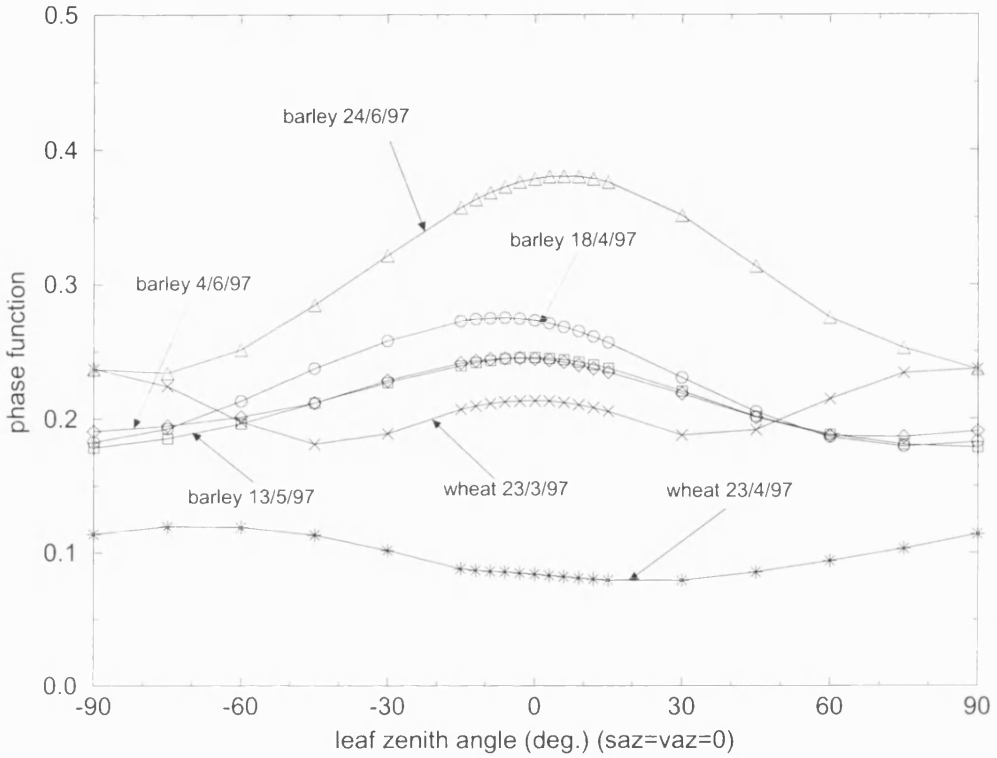

Figure 4.12 Phase function, for $\theta_i = 0^o$.

Returning to the various canopy scattering components, for the barley canopies of 18th April and 13th May (figures **4.5a** and **b**), α_{barley} increases by a factor of four as θ_i increases from 0^o to 60^o at the forward scattering extreme ($\theta_v = 60^o$) where the variation is greatest. This increase of α_{barley} with increasing θ_v is even more pronounced in the developed canopies of figures **4.5c** and **d**, with α_{barley} increasing by a factor of between 8 and 10 at $\theta_v = 60^o$. This behaviour is caused by more vegetation being visible at extreme angles, as seen in figures **4.7b** to **f**. Proportions of sunlit leaf increase with θ_v, with a corresponding reduction in sunlit soil. The shadowed leaf component also increases with θ_v but does not contribute in any way to scene reflectance. The magnitudes of α_{wheat} are similar to α_{barley} for canopies most closely corresponding in terms of LAI (18th April and 13th May). However the variation in magnitude of α_{wheat} with θ_v in the 23rd March case is much smaller than for barley. Values of α_{wheat} lie between 11 and 13 for all θ_v, θ_i, ϕ_{row}. α_{barley} ranges between 0 and 8 and shows large variation with θ_v, θ_i, whilst for the 23rd April case, α_{wheat} varies between 0 and 12 depending on θ_v, θ_i. The contrast in behaviour

of α_{wheat} between the 23rd March (where the LAD resembles that of the 18th April barley canopy) to the 23rd April is again likely to be due to the increasingly erectophile LAD.

A feature of α_{barley} in particular (and α_{wheat} to some extent) is the asymmetry about $\theta_v = 0^\circ$ and the variation with θ_i. This is easily explained by considering the proportions of sunlit leaf in figure **4.7**. By definition, α represents the component of ρ_{canopy} originating from sunlit vegetation. The proportions of sunlit leaf in figure **4.7** are increasingly asymmetric about $\theta_v = 0^\circ$, rising rapidly in the backscatter direction. This explains the behaviour of α. In addition, varying θ_i will cause very different amounts of vegetation to be visible, leading to the variations in α with θ_i.

The trends in magnitude of α_{barley} and α_{wheat} indicate that α is directly related to scattering from vegetation. Figure **4.5a** shows α_{barley} varying from just above zero at nadir to almost 8 at $\theta_v = 60^\circ$ for the 18th April. α_{barley} rises to between 2-20 for 13th May, 3-28 for 4th June and then falls sharply back to below 2 for the 24th June at which point the barley has senesced prior to harvest. From this evidence it is clear that α is related to the quantity of vegetation present in the simulated canopies. The March 23rd (wheat) and April 18th (barley) canopies are characterised as a sparse arrangement of small plants with few tillers and leaves (figures **4.2a** and **e**). Both crops rapidly develop into tall, densely packed canopies with almost complete coverage. The latter stages much more closely approximate the canopy envisioned in the formulation of the volumetric kernels, and reflectance from such a canopy can reasonably be expected to be dominated by the volumetric component. In addition, it is clear from equation **4.2** that the maximum in α will be when the e^{-LAI} term approaches zero i.e. when LAI becomes large, in which case α tends to

$$\alpha = \frac{P(\theta_i, \theta_v, \phi)}{4G\mu\mu'} \qquad \textbf{4.5}$$

A clear feature of the variation of α in figure **4.5** is the increasing prominence of the peak in the backscatter direction at the point where the viewing and solar zenith angles are equal i.e. in the hotspot direction. This peak, caused by a maximum in the amount of visible sunlit scene components (and a corresponding minimum of visible shadow), is barely apparent in figure **4.5a** as the canopy is very sparse. There is a lot of visible sunlit soil and very little shadowing, even at widely differing view and solar zenith angles. As can be seen in figure **4.7** (**a** and **e**) the scene reflectance of the 18th April barley

and the 23rd March wheat canopies are dominated by the amount of sunlit soil present, with shadowed soil and sunlit leaf having similar, much lower proportions. In the extremely sparse wheat canopy of 23rd March the sunlit soil component has a maximum of 0.95 and never falls below 0.8, meaning that the remaining components (sunlit or shadowed) are virtually negligible.

4.2.3.2 GO Component of ρ_{canopy}, β

The behaviour of the GO component of BPMS-simulated reflectance (β) shown in figures **4.6a-f** contrasts with that of α. β_{barley} is initially an inverted bowl-shape (18th April, figure **4.6a**), with a maximum at nadir and decreasing away from this point with increasing θ_v, but becomes slightly peaked at nadir as the canopy develops. β_{barley} has a maximum of approximately 0.8 at nadir viewing in the 18th April canopy and a minimum of 0.6 at $\theta_v = 60^\circ$. The nadir maximum falls to 0.35 by the 13th May, and falls further to between 0.1 and 0.2 in the most developed canopies of 4th and 24th June. For the 23rd March, β_{wheat} varies from 0.97 at nadir to 0.9 at $\theta_v = 60^\circ$ and for the 23rd April β_{wheat} falls almost linearly from 0.8 at nadir to 0.05 at $\theta_v = 60^\circ$. β_{wheat} displays similar trends to β_{barley}, with close agreement in shape between β_{wheat} of 23rd March and β_{barley} 18th April, and β_{wheat} of 23rd April and β_{barley} 13th May. β_{wheat} has a larger range of variation in each case. The β_{wheat} and β_{barley} values of these dates are in much closer agreement than the corresponding α_{barley} and α_{wheat}. These trends (particularly the general downward bowl) are to be expected given that β is the proportion of sunlit soil visible to the viewer. From figure **4.6** it can be seen that in all cases the amount of sunlit soil reduces with increasing θ_v almost symmetrically about $\theta_v = 0^\circ$ as more sunlit vegetation and shadowed soil/vegetation becomes visible. The exception to this is around the hotspot where shadowing is at a minimum. The magnitude of β in all cases is also directly comparable to the proportions of sunlit soil in figure **4.7**. An unexpected result is the absence of a strongly peaked hotspot feature in β, as might be expected. However, this feature is clearly seen in the behaviour of the volumetric component α (where it is not expected), suggesting that α contains elements of behaviour that would only be expected for β. Possible reasons for this behaviour are posited below.

The transition in β_{wheat} from the smooth downward bowl of 23rd March to the more sharply peaked case of 23rd April (seen to an extent in the barley canopy of 13th May) is explained by the much more erectophile LAD of the wheat canopy (particularly for the 23rd April canopy). In this case sunlit soil will tend to be at a maximum at nadir, dropping off sharply with increasing θ_v as the predominantly vertical leaves obscure the soil from view. In contrast, the barley canopy shows a more gradual reduction of sunlit soil with increasing θ_v away from nadir as a result of the less erectophile LAD.

The variations in magnitude of α and β (particularly those of α) support hypothesis 1 above (section **4.2**), namely that ρ_{canopy} can be separated into volumetric and GO components. If this is the case, α would be expected to be low in comparison to β when the canopy is sparse, with ρ_{canopy} dominated by the GO component of reflectance. In addition α might be expected to increase as the canopy develops to more closely resemble the plane parallel homogeneous medium approximated by the volumetric kernels, with a corresponding reduction in the GO component, β. This is precisely the trend observed. Results also show that there is a continuum of volumetric and GO scattering at all stages of growth. GO scattering is prominent at early growth stages when relatively large areas of sunlit soil are visible, with volumetric scattering taking over as the canopy coverage increases from sparse to dense. The fact that there appears to be elements of both volumetric and GO scattering implies that although it may be reasonable to assume two independent components of ρ_{canopy}, they are never likely to be perfectly separable. In particular, the behaviour of β (lack of a hotspot) suggests that the canopies used here depart significantly from the assumptions made in the formulation of the GO kernels. In particular, the assumption of independent scattering crown "envelopes" is not valid.

It is important to note that the semi-empirical kernels were originally formulated based on the idea that the reflectance of heterogeneous scenes observed at moderate resolution could be characterised by proportions of scattering dominated by volumetric and GO scattering respectively (Wanner *et al.*, 1997). These separate scattering components are considered to originate from separate patches within the scene, each contributing to the overall scene reflectance. ρ_{canopy} considered at high resolution will have volumetric and GO scattering components present, although not quite as envisaged above. In the experiments presented in this thesis, the scattering from the canopy is being considered as a sum of volumetric and GO scattering components originating from within the same area of canopy. If the kernels cannot describe this case, then problems will arise

at lower resolution simply because vegetation canopies are not typically homogeneous. At these scales there will be volumetric and GO components of ρ_{canopy} originating from within the IFOV of a given sensor.

4.3 Conclusion

Values of ρ_{canopy} for barley and wheat canopies at various stages of growth were simulated from measured canopy structural properties and field-measured soil and vegetation reflectance data. Simulations were carried out over a wide range of viewing and illumination configurations, under the assumptions made in the linear kernel-driven BRDF models ($\rho_{leaf} = \tau_{leaf}$; Lambertian soil, direct illumination and single scattering only). Volumetric and GO components of simulated ρ_{canopy} were examined to see whether they can be treated as separate components as postulated in the formulation of linear, kernel-driven BRDF models. The trends in the magnitude of the volumetric and GO components of ρ_{canopy} were as expected (other than the lack of a hotspot in the β and the presence of one in α):

- The volumetric component increased with LAI as the canopy developed, with the GO component reducing correspondingly.
- The variation of the volumetric component with θ_v was an asymmetric, upward bowl shape, with a peak in the hotspot direction and large variation with θ_i.
- The GO component (dictated by the proportion of sunlit soil in this case) displayed a downward bowl-shape, symmetric about nadir, varying little with θ_i, but without the expected hotspot.

The GO component of ρ_{canopy} is related to the proportion of visible sunlit soil in each scene and the shapes and magnitudes of β tend to support this. In contrast to α, β has a downward bowl-shape and is generally symmetric about nadir, with a maximum in the hotspot direction. It is important to note that the sharp hotspot peak that would be expected if β were directly equated with sunlit and shaded soil components envisioned in the formulation of the GO kernels is not present. This is a result of the fact that ρ_{canopy} was simulated using a canopy that departs very significantly from the assumptions made in the GO kernels described in section **2.5.4.1.2**. In the formulation, the canopy is considered as

a collection of 'spheroids-on-sticks' (see figure **2.10**) and is modelled as a function of sunlit and shaded scene components. In the simulations presented above (and in subsequent analysis), shadows are perfectly black (no diffuse component of illumination) so the shadowed scene components contribute nothing to reflectance. In addition, the scattering objects in the scene are of a quite different shape and distribution from those shown in figure **2.10**, with a much finer spatial scale and distribution within the canopy. These factors combine to prevent the appearance of the hotspot that would be expected if the canopy were composed of large, well-defined solid geometric objects envisaged in the formulation of the GO kernels. In fact, both the barley and wheat canopies resemble the configuration envisioned in the volumetric scattering kernels (see **2.5.4.1.1**) far more closely than they do the GO scattering configuration (see **2.5.4.1.2**). This would explain why the angular behaviour of β is not quite as expected.

Differences between β_{barley} and β_{wheat} can be explained by differences in the LAD of the two canopies throughout their development: barley more closely approximates the spherical LAD assumed in the linear models; the measured wheat canopy has a more erectophile LAD, particularly for the 23rd April. The observed magnitude and behaviour of α and β during the various stages of canopy development are strong evidence that ρ_{canopy} can be split into volumetric and GO scattering components and that the information contained in each is largely independent of the other. However, results also show that even in canopies with very little vegetation there is a scattering component of reflectance that closely resembles the modelled volumetric component. Similarly, even canopies that have almost total coverage (i.e. virtually zero sunlit soil) a component of GO-like scattering remains. This indicates that although the two components may be generally separable in many cases, the extent to which this is true will depend closely on the nature of the canopy being studied. This implies the kernels need to be applied with care when the nature of the vegetation in the scene departs dramatically from that envisioned in the kernels (in particular mixed regions of clumped and well-distributed vegetation such as widely spaced trees with a grass understorey).

The next stage is to examine the relationship between the volumetric and GO scattering components of ρ_{canopy} and the respective volumetric and GO scattering kernels, k_{vol} and k_{GO}. The ability of the angular kernels to describe the respective scattering components is explored in chapter **5**.

5 Canopy scattering and the linear model parameters

It has been established that the volumetric and GO scattering components of ρ_{canopy} can largely be separated from each other on the basis of their angular behaviour. In addition, the respective scattering components can be related to the respective canopy elements from where they originate. The volumetric component, α, is related to the proportion of sunlit vegetation visible to the viewer and hence the leaf scattering phase function. The GO component, β, can be related to the amount of sunlit soil visible to the viewer and hence reduces with increasing canopy coverage. It should be stressed that these findings relate to single scattering reflectance only. The linear kernel-driven models of BRDF assume single scattering interactions only and this is followed in the simulations of ρ_{canopy} used here. The results discussion in this chapter examine the relationship between α and k_{vol} and β and k_{GO}.

5.1 Relationships between α and k_{vol}, and β and k_{GO}

α has been defined to represent the volumetric scattering component of the BPMS-simulated ρ_{canopy} (equation **4.2**). It would therefore be expected that a **linear relationship between α and k_{vol}**, the volumetric kernels (equations **2.28** and **2.29**) exists (when f_{vol}, the volumetric parameter, is inverted against reflectance data). β is defined as the GO component of BPMS-simulated ρ_{canopy} (equation **4.3**) and it is similarly reasonable to expect a **linear relation between the GO kernels, k_{GO}** (equations **2.30** and **2.31**) and β. The first step in determining how accurately k_{vol} and k_{GO} describe α and β is to plot the volumetric and GO kernels against the respective scattering components of ρ_{canopy}. As in chapter **4**, values of ρ_{canopy} simulated within the BPMS under the assumptions of the linear kernel-driven models of BRDF are employed.

Figure **5.1** shows plots of the BPMS-derived volumetric scattering component of ρ_{canopy}, α, as the abscissa, against the RossThick and RossThin volumetric kernels for barley (four dates) and wheat (two dates). Figures **5.2** and **5.3** show the GO component of ρ_{canopy}, β, plotted against the LiSparse and LiDense kernels respectively[1]. Plots are also

[1] Both the reciprocal and non-reciprocal versions of the GO kernels were used in order to examine any differences in behaviour. Results for both were very similar, with the non-reciprocal version proving to be a marginally better fit in all cases. Consequently results from the non-reciprocal versions only are presented.

shown from two slightly modified versions of these kernels, which treat the reflectance of the sunlit crown and sunlit ground independently, rather than assuming they are of equal brightness as in the standard Li kernels (see figure **2.12**). They are included to explore the possibility that they might prove a better fit to the GO component of ρ_{canopy} than the standard kernels. If so, they may provide a better interpretation of the GO component than is the case in the original formulation of the models, given that sunlit and shaded crown and ground are likely to be of different brightness in practice. The standard and modified kernels are labelled G (for ground only) and GC (for ground and crown) respectively in figures **5.2** and **5.3**. Results are presented from simulated reflectance data from all solar zenith angles and row azimuths combined, but the implications of treating individual solar zenith and row azimuth angles separately are discussed below.

The view and illumination configurations considered in each case are as follows:

- $\phi_{row} = 0°, 45°, 90°$;
- $\theta_i = 0°, 30°, 60°$;
- θ_v in each case between -70° and 70°, in steps of 10° except for the 5° either side of the hotspot, where sampling is every 2°;

As described previously, single-scattering ρ_{canopy} is simulated in each case with two nominal wavebands: one with $\rho_{leaf} = \tau_{leaf} = 0.5$ and $\rho_{soil} = 0$; the other with $\rho_{leaf} = \tau_{leaf} = 0$ and $\rho_{soil} = 0$. This results in scattering either from the vegetation (α) or from the soil (β). These are plotted against their respective kernels in figures **5.1**, **5.2** and **5.3**. The lines in each figure represent the regression line of each data set.

Figure 5.1 BPMS-derived volumetric component (α) against k_{vol} for barley (four dates) and wheat (two dates).

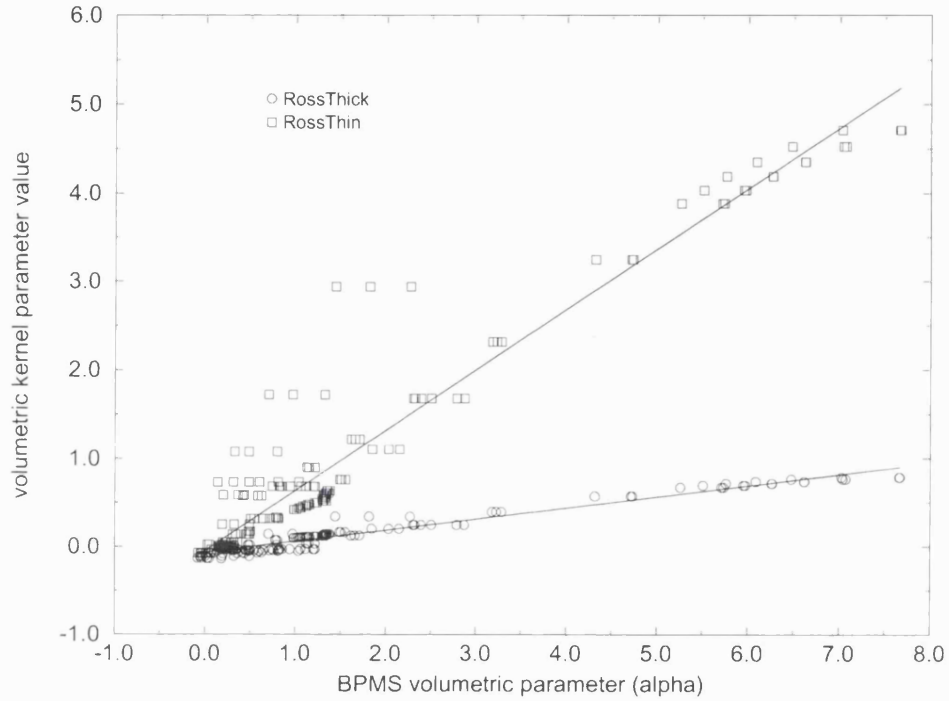

a) barley –18th April

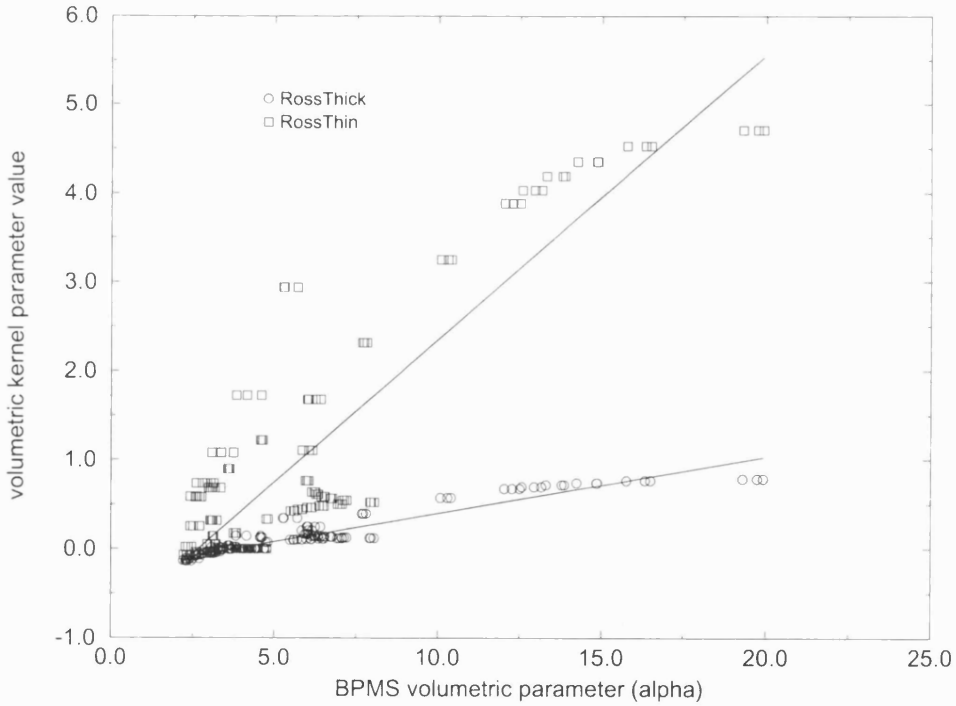

b) barley – 13th May

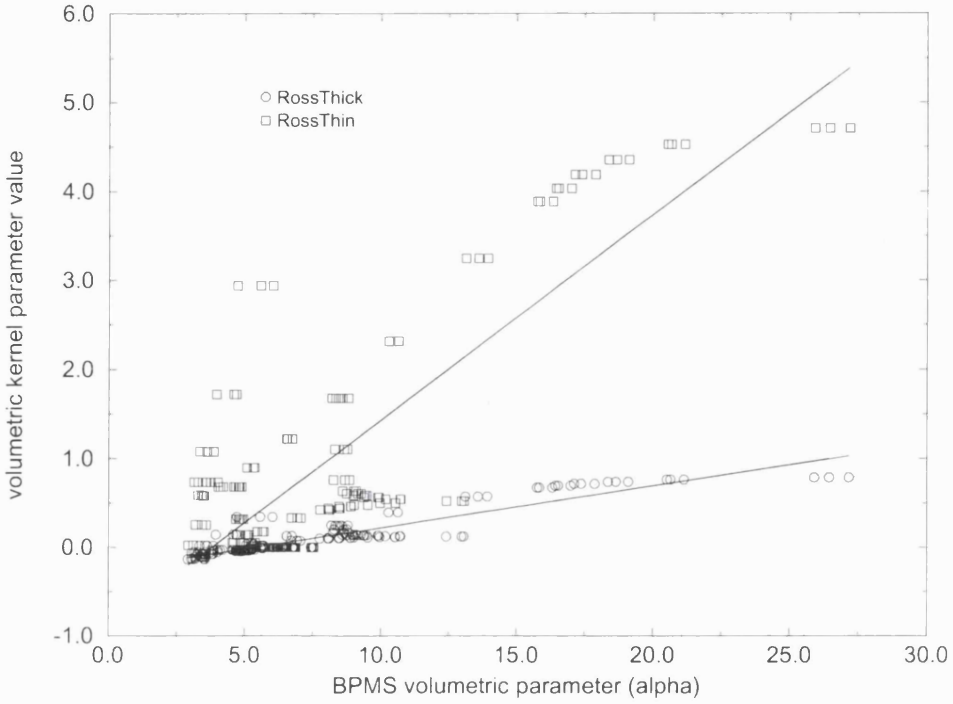

c) barley – 4th June

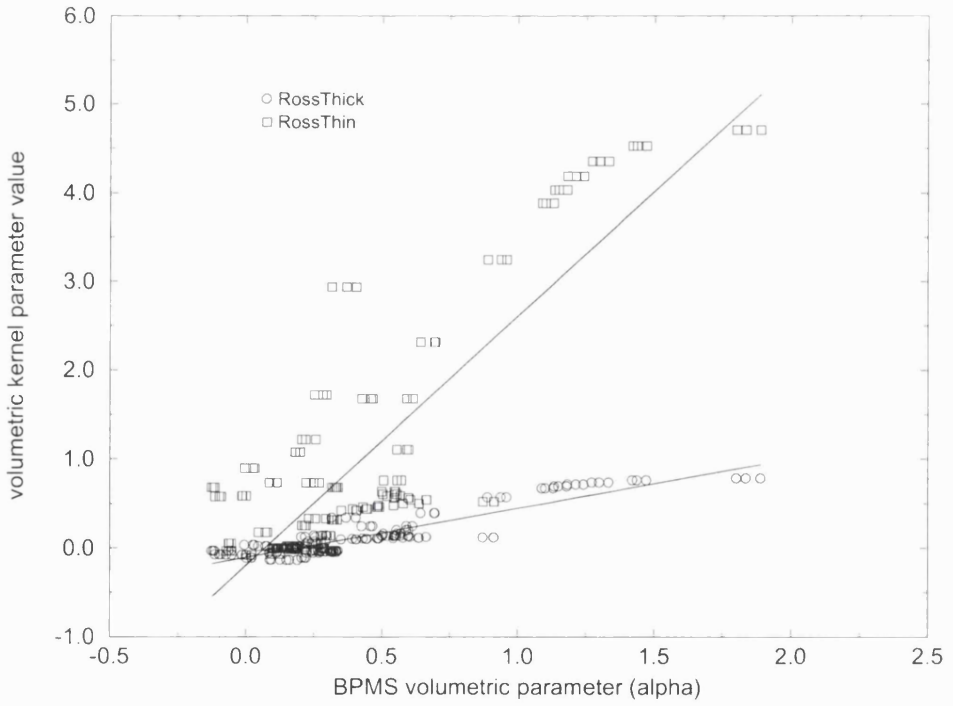

d) barley – 24th June

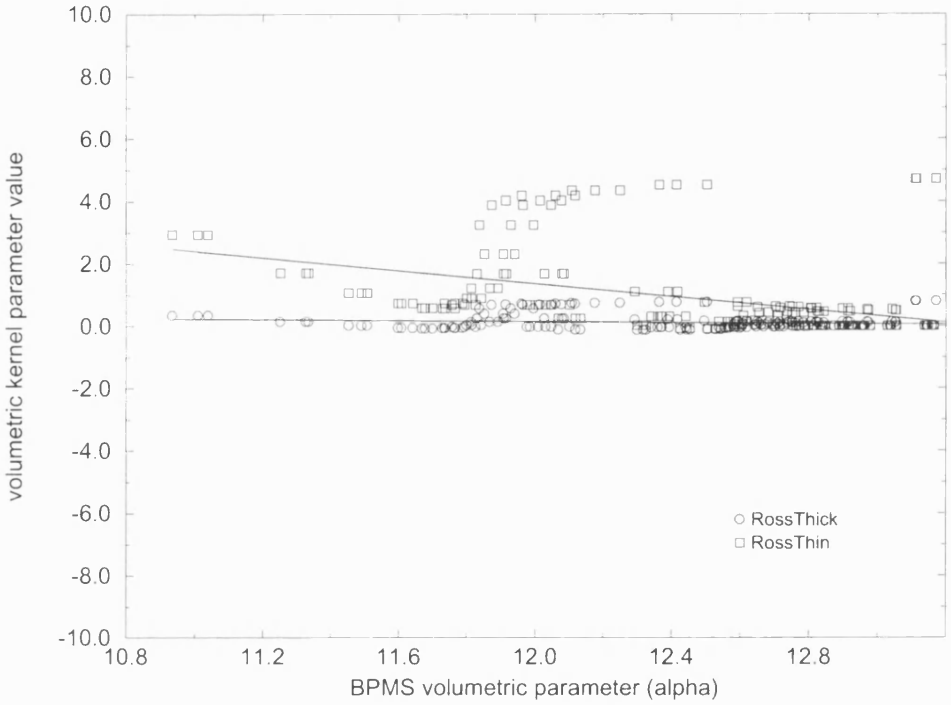

e) wheat – 23rd March

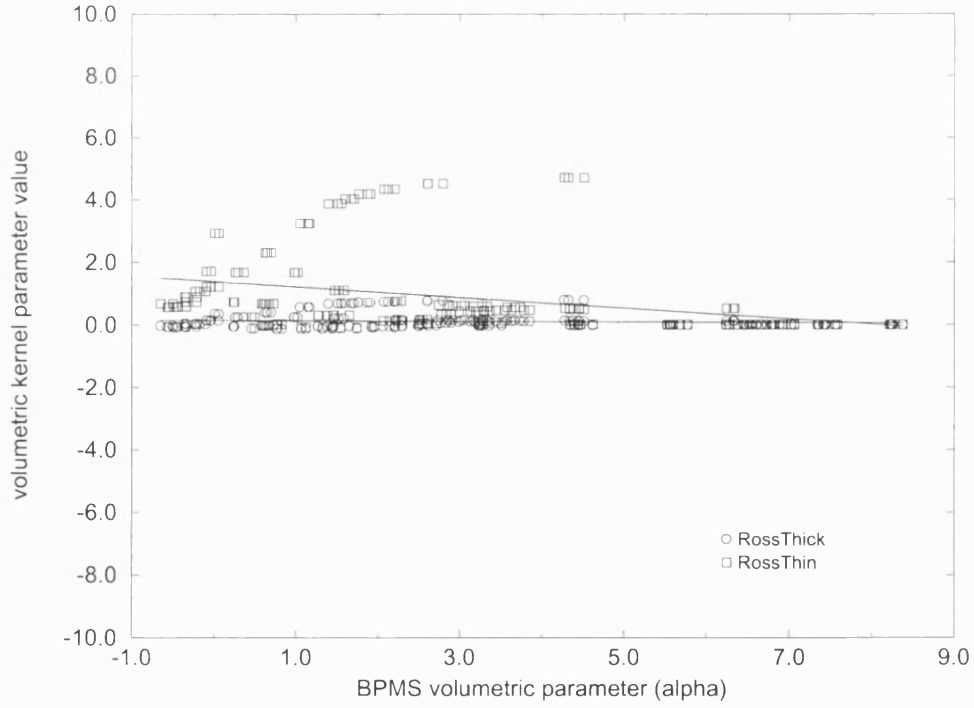

f) wheat – 23rd April

Figure 5.2 BPMS-derived GO component (β) against k_{GO} (LiDense) for barley (four dates) and wheat (two dates).

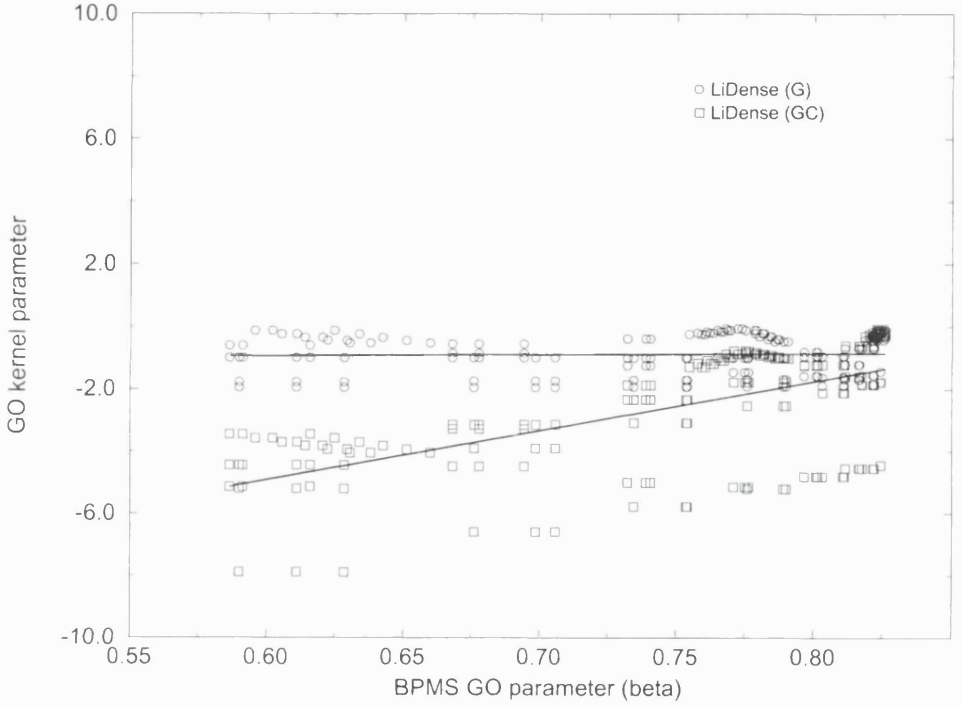

a) barley – 18th April

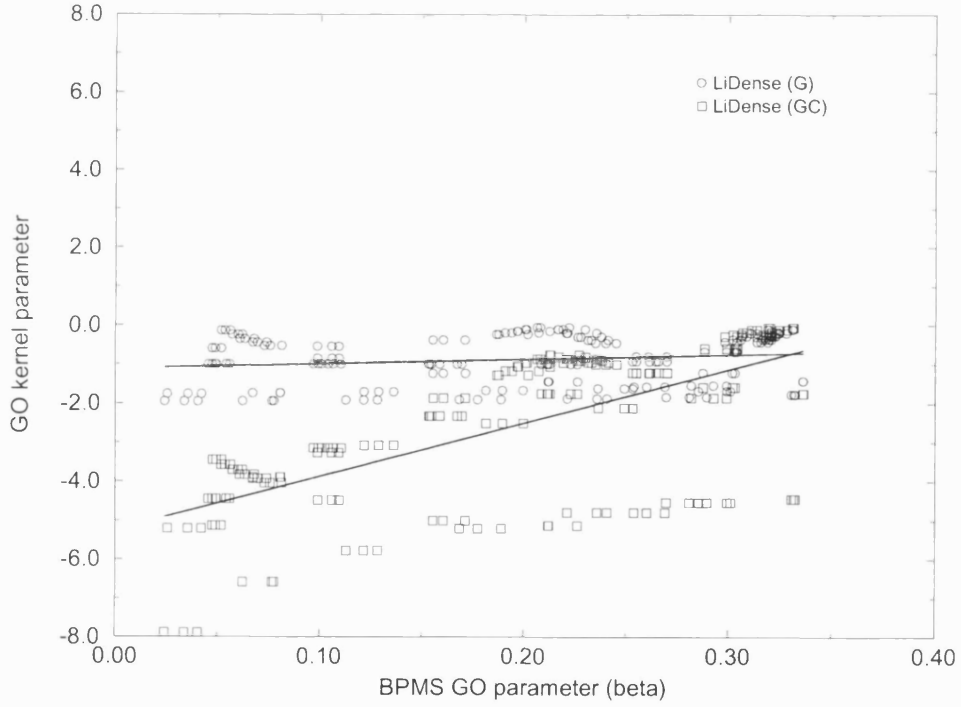

b) barley - 13th May

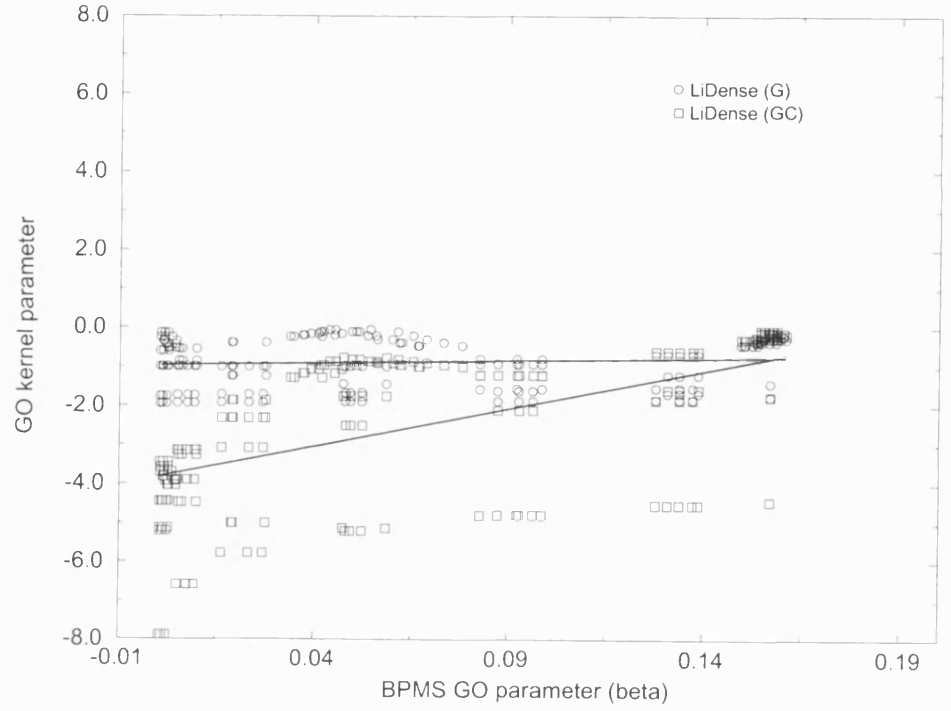

c) barley – 4th June

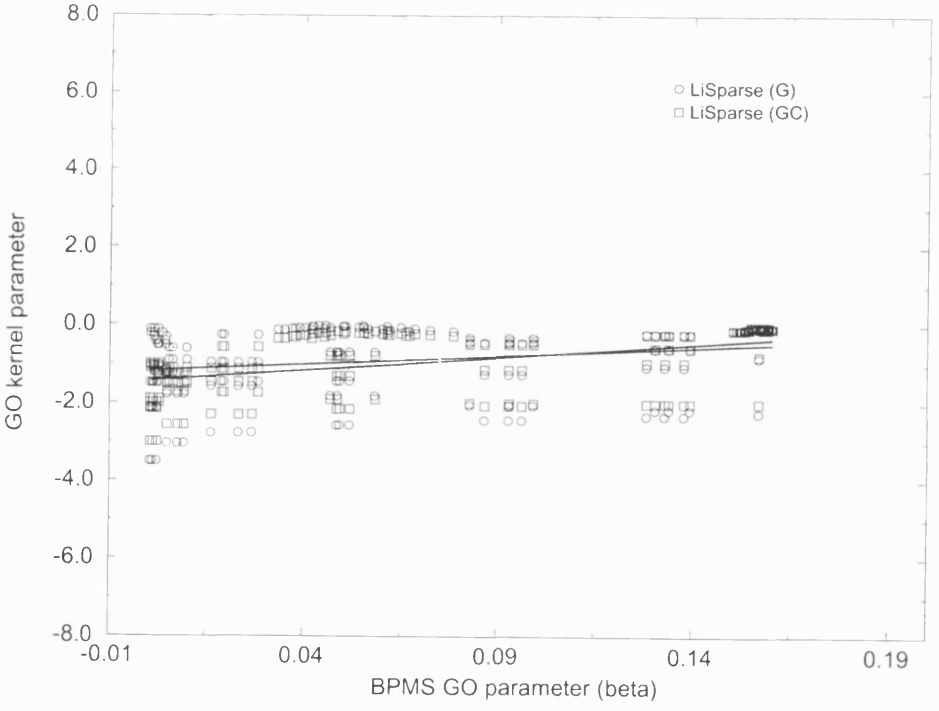

d) barley – 24th June

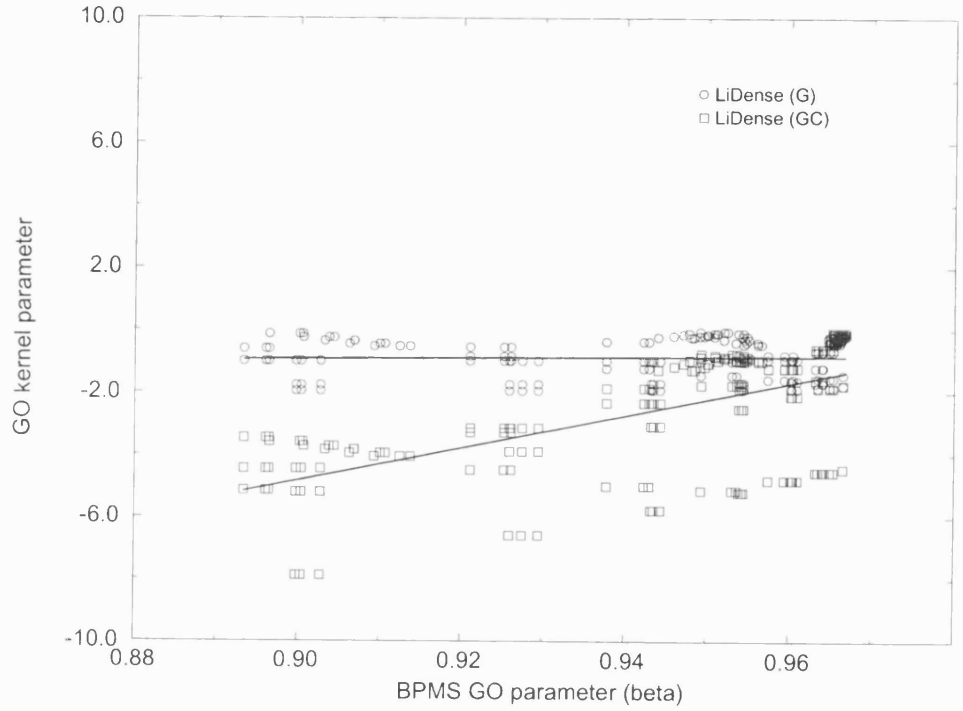

e) wheat – 23rd March

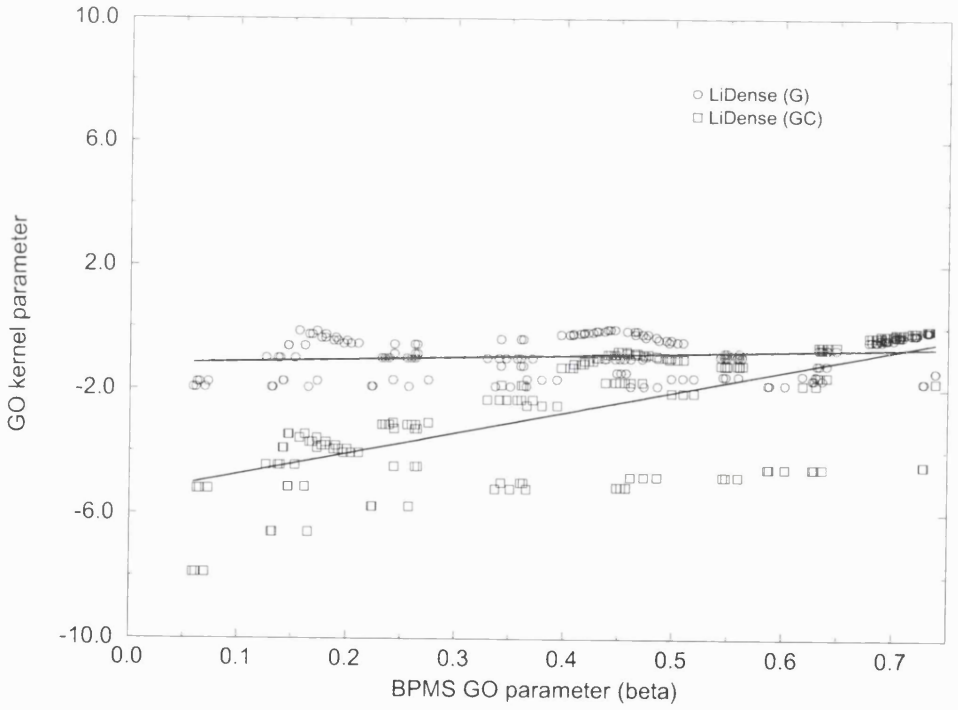

f) wheat – 23rd April

Figure 5.3 BPMS-derived GO component (β) against k_{GO} (LiSparse) for barley (four dates) and wheat (two dates).

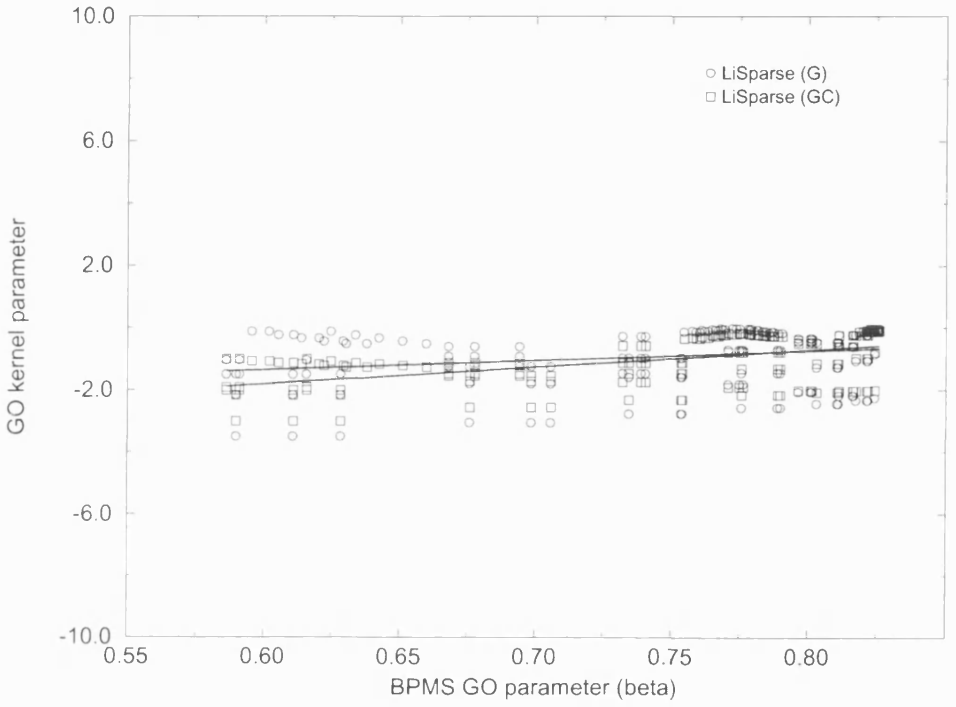

a) barley - 18th April

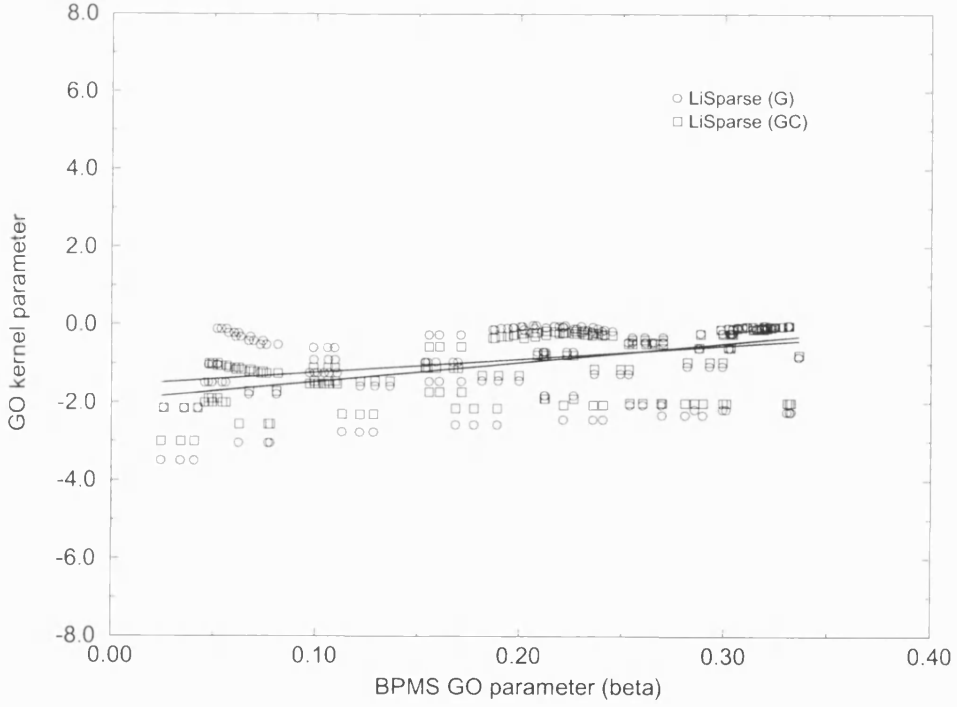

b) barley – 13th May

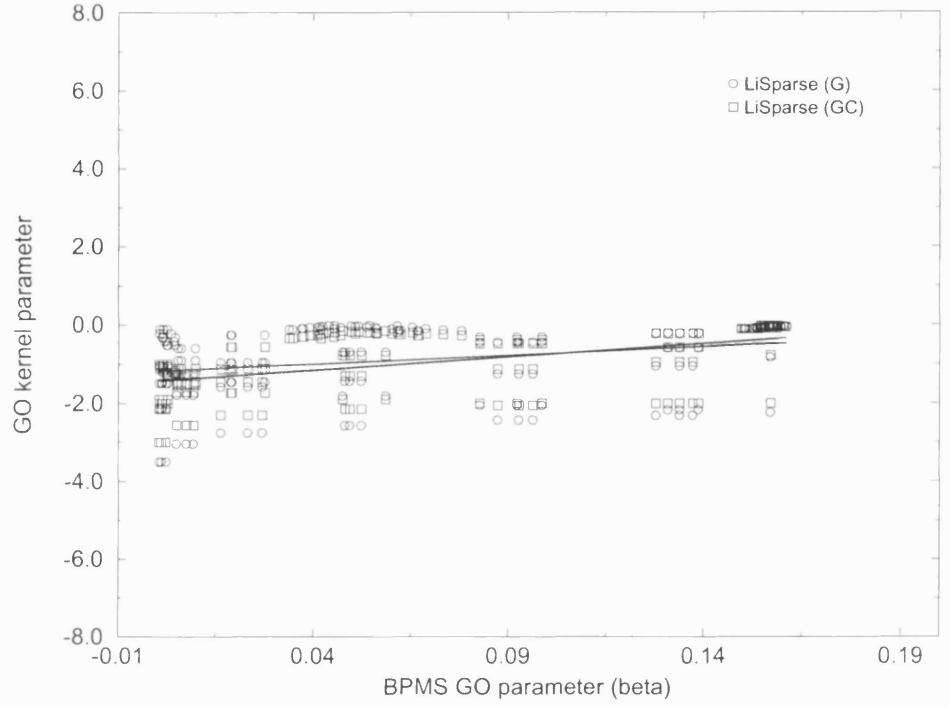

c) barley – 4th June

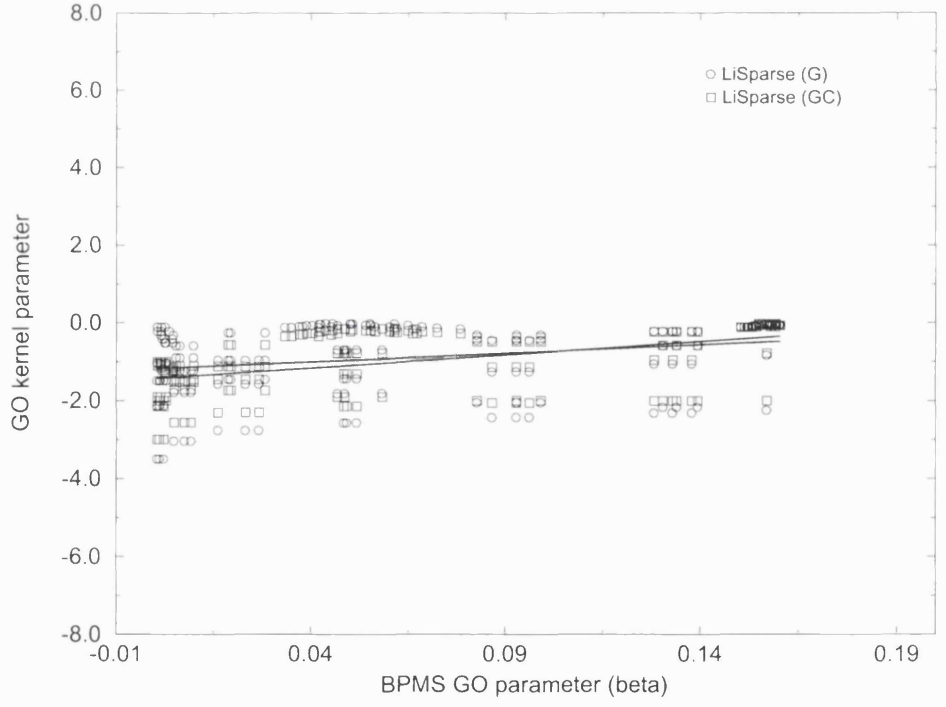

d) barley – 24th June

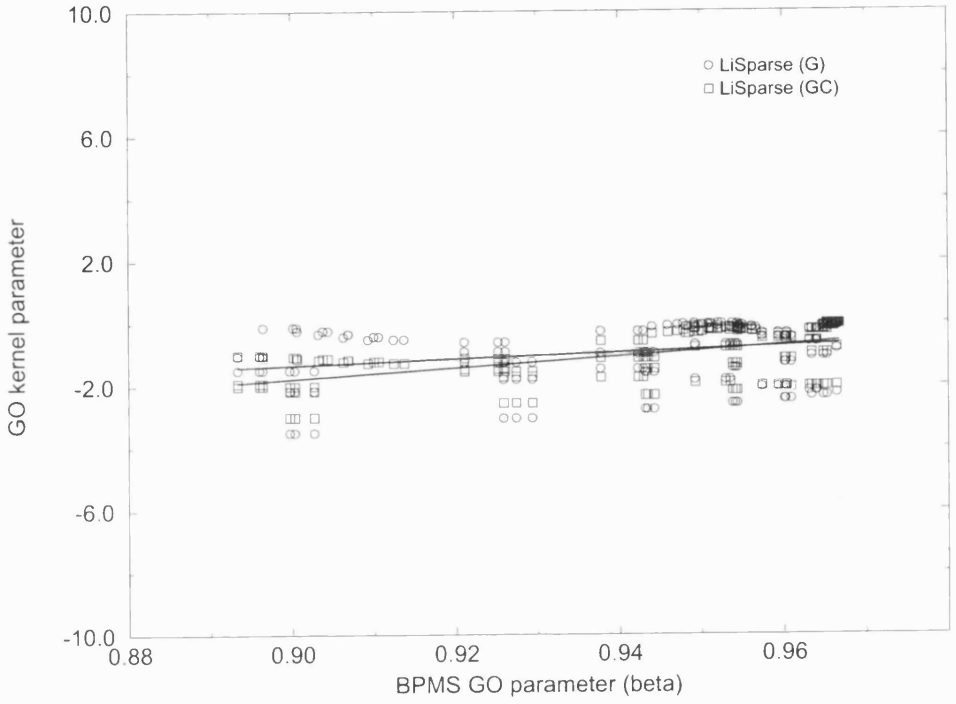

e) wheat – 23rd March

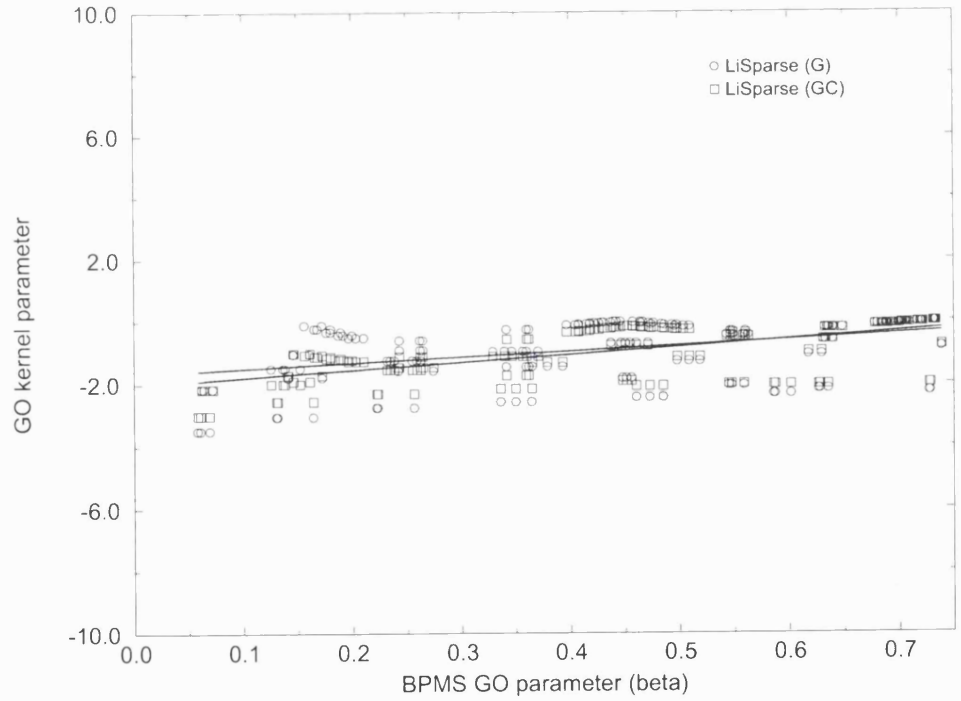

f) wheat – 23rd April

5.2 Variation of volumetric component, α with k_{vol}

5.2.1 Results

Figure **5.1** shows a generally linear relationship between the BPMS-derived volumetric scattering component α and the volumetric kernels, k_{vol}, particularly for the barley canopy. The relationship is less clear for wheat. Values of the correlation coefficient, r, are presented in tables **5.1**. The value of r is a direct measure of the sign of the correlation between two variables (positive or negative), but an indirect measure (square root) of the strength of the correlation. The coefficient of determination, r^2, represents the strength of correlation and is in effect the percent variance of the dependent variable explained by the regression equation. Clearly, r^2 can be calculated from values of r, but it is not possible to determine the sign of r in this way, which is why only values of r are given. Also included in table **5.1** are values of a_{vol} and b_{vol}, the slopes and intercepts of the regression relationships. These results tend to support the first hypothesis presented in **4.2** that α is linearly related to the volumetric scattering kernels. An interesting feature of the results presented in table **5.1** is the variation in r with the illumination (solar) zenith angle, θ_i. While the variation with ϕ_{row} is minimal, θ_i appears to significantly affect the agreement between k_{vol} and α. Although we might expect α to be independent of θ_i, an explanation for the variation is that the increased path length of radiation through the canopy from higher solar zenith angles sun will increase the volumetric scattering component of ρ_{canopy} in relation to β. The values of r increase, in some cases dramatically, with increasing θ_i. The only cases where this is not clear are for the wheat canopies of March and April. In all cases for the barley canopies, the increases of $\alpha$with θ_i are marked.

The RossThin kernel is included in this analysis to see whether evidence supports the adoption of the RossThick kernel for the MODIS albedo product (Lucht *et al.*, 1999). The values of the RossThick and RossThin kernels in table **5.1** are separated by colour, with the RossThin values in red. All correlations presented in table **5.1** are significant to a 95% confidence level. Values in bold are those for which the upper and lower confidence levels lie within ±0.125 of the value of r, the correlation coefficient. This indicates correlations with the smallest confidence interval.

Table 5.1 Slopes, intercepts and regression coefficients for volumetric kernels as a function of solar zenith (θ_i) and row azimuth (ϕ_{row}) (RossThin kernels in red).

5.1a barley - 18th April

kernel	θ_i	ϕ_{row}	a_{vol}	b_{vol}	r
RossThick	0	0	-0.05	0.00	-0.67
RossThick	**30**	**0**	**0.17**	**-0.11**	**0.92**
RossThick	**60**	**0**	**0.14**	**-0.10**	**0.99**
RossThin	**0**	**0**	**0.77**	**-0.18**	**0.99**
RossThin	**30**	**0**	**0.61**	**-0.14**	**0.96**
RossThin	**60**	**0**	**0.64**	**0.43**	**0.98**
RossThick	0	45	-0.04	0.00	-0.63
RossThick	**30**	**45**	**0.15**	**-0.09**	**0.93**
RossThick	**60**	**45**	**0.12**	**-0.06**	**0.98**
RossThin	**0**	**45**	**0.72**	**-0.14**	**0.97**
RossThin	**30**	**45**	**0.55**	**-0.07**	**0.96**
RossThin	**60**	**45**	**0.56**	**0.60**	**0.96**
RossThick	0	90	-0.04	0.00	-0.60
RossThick	**30**	**90**	**0.15**	**-0.08**	**0.95**
RossThick	**60**	**90**	**0.12**	**-0.04**	**0.98**
RossThin	**0**	**90**	**0.76**	**-0.17**	**0.93**
RossThin	**30**	**90**	**0.51**	**-0.03**	**0.94**
RossThin	**60**	**90**	**0.54**	**0.72**	**0.96**

5.1b barley - 13th May

kernel	θ_i	ϕ_{row}	a_{vol}	b_{vol}	r
RossThick	**0**	**0**	**0.03**	**-0.12**	**0.87**
RossThick	**30**	**0**	**0.06**	**-0.22**	**0.91**
RossThick	**60**	**0**	**0.06**	**-0.14**	**0.96**
RossThin	0	0	-0.20	0.86	-0.53
RossThin	30	0	0.13	-0.22	0.63
RossThin	**60**	**0**	**0.27**	**0.18**	**0.96**
RossThick	**0**	**45**	**0.03**	**-0.12**	**0.90**
RossThick	**30**	**45**	**0.06**	**-0.22**	**0.90**
RossThick	**60**	**45**	**0.06**	**-0.15**	**0.96**
RossThin	0	45	-0.20	0.88	-0.60
RossThin	30	45	0.13	-0.19	0.60
RossThin	**60**	**45**	**0.28**	**0.19**	**0.96**
RossThick	**0**	**90**	**0.03**	**-0.12**	**0.88**
RossThick	**30**	**90**	**0.06**	**-0.22**	**0.91**
RossThick	**60**	**90**	**0.06**	**-0.13**	**0.96**
RossThin	0	90	-0.21	0.90	-0.59
RossThin	30	90	0.13	-0.18	0.61
RossThin	**60**	**90**	**0.27**	**0.26**	**0.96**

5.1c barley - 4th June

kernel	θ_i	ϕ_{row}	a_{vol}	b_{vol}	r
RossThick	0	0	0.02	-0.12	0.83
RossThick	**30**	**0**	**0.04**	**-0.21**	**0.87**
RossThick	**60**	**0**	**0.04**	**-0.12**	**0.94**
RossThin	0	0	-0.15	1.00	-0.63
RossThin	30	0	0.08	-0.14	0.56
RossThin	**60**	**0**	**0.20**	**0.30**	**0.94**
RossThick	**0**	**45**	**0.02**	**-0.12**	**0.87**
RossThick	**30**	**45**	**0.03**	**-0.19**	**0.88**
RossThick	**60**	**45**	**0.04**	**-0.10**	**0.94**
RossThin	0	45	-0.14	0.92	-0.61
RossThin	30	45	0.07	-0.08	0.55
RossThin	**60**	**45**	**0.19**	**0.40**	**0.93**
RossThick	0	90	0.02	-0.12	0.85
RossThick	**30**	**90**	**0.03**	**-0.20**	**0.87**
RossThick	**60**	**90**	**0.04**	**-0.14**	**0.95**
RossThin	0	90	-0.15	0.96	-0.59
RossThin	30	90	0.08	-0.10	0.55
RossThin	**60**	**90**	**0.21**	**0.25**	**0.94**

5.1d barley - 24th June

kernel	θ_i	ϕ_{row}	a_{vol}	b_{vol}	r
RossThick	**0**	**0**	**0.01**	**-0.05**	**0.91**
RossThick	30	0	0.05	-0.07	0.64
RossThick	60	0	0.14	0.09	0.84
RossThin	0	0	-0.12	0.49	-0.78
RossThin	30	0	0.05	0.33	0.20
RossThin	60	0	0.64	1.27	0.85
RossThick	**0**	**45**	**0.01**	**-0.04**	**0.88**
RossThick	30	45	0.03	-0.03	0.40
RossThick	60	45	0.08	-0.06	0.74
RossThin	0	45	-0.07	0.30	-0.72
RossThin	30	45	-0.04	0.58	-0.15
RossThin	60	45	0.34	0.79	0.66
RossThick	**0**	**90**	**0.01**	**-0.03**	**0.84**
RossThick	30	90	0.01	0.03	0.13
RossThick	60	90	0.08	0.02	0.52
RossThin	0	90	-0.06	0.25	-0.66
RossThin	30	90	-0.15	0.78	-0.41
RossThin	60	90	0.29	1.22	0.42

5.1e wheat – 23rd March

kernel	θ_i	ϕ_{row}	a_{vol}	b_{vol}	r
RossThick	0	0	0.05	-0.62	0.81
RossThick	30	0	0.12	-1.41	0.33
RossThick	60	0	0.46	-5.17	0.59
RossThin	**0**	**0**	**-0.62**	**7.98**	**-0.92**
RossThin	30	0	-0.28	3.97	-0.22
RossThin	60	0	2.08	-22.18	0.57
RossThick	0	45	0.05	-0.61	0.81
RossThick	30	45	0.14	-1.69	0.43
RossThick	60	45	0.46	-5.10	0.66
RossThin	**0**	**45**	**-0.62**	**7.95**	**-0.93**
RossThin	30	45	-0.15	2.41	-0.14
RossThin	60	45	2.01	-21.51	0.62
RossThick	0	90	0.05	-0.61	0.81
RossThick	30	90	0.13	-1.57	0.39
RossThick	60	90	0.47	-5.21	0.61
RossThin	**0**	**90**	**-0.61**	**7.90**	**-0.93**
RossThin	30	90	-0.21	3.14	-0.18
RossThin	60	90	2.06	-22.04	0.58

5.1f wheat – 23rd April

kernel	θ_i	ϕ_{row}	a_{vol}	b_{vol}	r
RossThick	**0**	**0**	**0.01**	**-0.05**	**0.94**
RossThick	30	0	0.04	-0.05	0.51
RossThick	**60**	**0**	**0.22**	**0.15**	**0.90**
RossThin	0	0	-0.07	0.42	-0.79
RossThin	30	0	0.01	0.45	0.03
RossThin	**60**	**0**	**1.03**	**1.55**	**0.90**
RossThick	**0**	**45**	**0.01**	**-0.05**	**0.94**
RossThick	30	45	0.04	-0.05	0.51
RossThick	**60**	**45**	**0.23**	**0.17**	**0.91**
RossThin	0	45	-0.07	0.42	-0.79
RossThin	30	45	0.01	0.45	0.02
RossThin	**60**	**45**	**1.06**	**1.62**	**0.92**
RossThick	**0**	**90**	**0.01**	**-0.05**	**0.94**
RossThick	30	90	0.04	-0.04	0.48
RossThick	**60**	**90**	**0.22**	**0.17**	**0.90**
RossThin	0	90	-0.07	0.44	-0.80
RossThin	30	90	-0.00	0.48	-0.02
RossThin	**60**	**90**	**1.05**	**1.66**	**0.91**

5.2.2 Analysis of regression relationships

The results for α plotted against k_{vol} presented in tables **5.1a-f**, show r starting high for the 18th April barley canopy, exceeding 0.96 in most cases, then falling slightly for the 13th May canopy to around 0.9. There is little difference between the RossThin and RossThick kernels for 18th April, but by the 13th May, the RossThick kernel has significantly higher values of r than the RossThin at most θ_i and ϕ_{row}. Values remain very similar for the June 4th barley canopy, but fall significantly for the 24th June. The RossThick kernel has significantly higher values of r in this case, particularly for $\theta_i = 0^\circ$. The results for the wheat canopy of 23rd March show little consistency, with values of r between –0.93 (strong negative correlation) and 0.91, due to the fact that there is so little vegetation present. The values of r for the RossThick kernel are always positive, and are relatively high (>0.8) for $\theta_i = 0^\circ$. The values for the RossThin kernel by contrast are predominantly negative. Although the RossThin kernel was formulated for describing the reflectance of sparse canopies (see **2.5.4.1.1**), the vegetation in this case is so sparse as to be almost negligible. This may explain why the RossThin kernel does not correlate with α - there is little or no volumetric scattering. The RossThick kernel appears to fit well regardless, suggesting it is much more flexible than the RossThin in a variety of conditions, a finding supported by other researchers (Lucht *et al.*, 1999; Strugnell and Lucht, 2000).

The results for the wheat canopy of 23rd April are similar to those of the barley canopy of 13th May and 4th June with the RossThick kernel providing a better fit in nearly all cases. For all ϕ_{row}, r values for the RossThick kernel are high for both $\theta_i = 0^\circ$ and $\theta_i = 60^\circ$, but are much lower for $\theta_i = 30^\circ$. Values of r for the RossThin kernel display a clear trend: a strong negative correlation for $\theta_i = 0^\circ$, almost zero correlation at $\theta_i = 30^\circ$, and a relatively strong positive correlation for $\theta_i = 60^\circ$, again for all ϕ_{row}. The RossThick kernel is far more stable in all cases.

As discussed in section **2.5.4.1**, the Ross kernels are based on a solution of radiative transfer in a homogeneous (turbid) medium. The thick and thin versions of the Ross kernels result from approximations for LAI >> 1 and LAI << 1 respectively. It might therefore be expected that the RossThin kernel would correlate with α more closely for the sparse canopies where LAI < 1 (i.e. the 18th April barley and 23rd March wheat canopies) and the RossThick kernel to correlate more strongly for the remaining canopies

where LAI exceeds 2. This is marginally true for the 18th April barley canopy, but not at all the case for the 23rd April wheat canopy, where the RossThin kernel is often negatively correlated with α. This is the sparsest canopy, with very little vegetation present and yet the RossThick kernel is more strongly correlated with α, although only at a significant level for $\theta_i = 0^\circ$. This is a surprising result as the canopy departs not only from the assumption of high LAI, but also from the fundamental assumption of a turbid medium common to both kernels. This suggests that either the two components of ρ_{canopy} cannot be simply separated, or that the k_{vol} kernels not only explain variations in ρ_{canopy} caused by volumetric scattering but also describe some aspects of GO scattering. For the more developed canopies the RossThick kernel is more closely correlated with α, having consistently high (>0.85) values of r. Results for the 23rd April wheat canopy are similar to those of the denser barley canopies. The exception is that values of r for the RossThick kernel fall significantly (to ~0.5) for $\theta_i = 30^\circ$. This may be a result of the erectophile LAD mentioned previously (figure **4.8**).

This behaviour is consistent with previous results: the volumetric component of ρ_{canopy}, α, is strongly linearly related to k_{vol} until the canopy rapidly senesces during the middle of June and there is little or no green vegetation remaining (e.g. although the barley LAI stays constant at around 3.15 in June, by 24th June, very little of the remaining vegetation is green). The RossThick kernel is favoured for nearly all dates except the 18th April barley canopy, despite variations in LAI. This is true even of the 23rd March wheat canopy with LAI = 0.08. The ability of the RossThick kernel to out-perform the RossThin kernel has been found by other researchers (Lucht *et al.*, 1999; Strugnell and Lucht, 2000). This evidence supports the selection of the RossThick kernel as the volumetric kernel for production of global BRDF and albedo products from MODIS (Schaaf *et al.*, 2000a, b).

5.2.3 Slopes and intercepts a_{vol}, b_{vol} of α against k_{vol}

The slopes of k_{vol} against α (a_{vol}) are small and generally positive ($0 < a_{vol} < 1$). The intercepts (b_{vol}) are non-zero and almost exclusively negative. Following the convention of Roujean *et al.* (1992) that the volumetric kernels should equal zero for $\theta_i = \theta_v = 0^\circ$, the RossThick and RossThin kernels contain offsets of $-\pi/4$ and $-\pi/2$ (-0.79 and -1.57) respectively (equations **2.28** and **2.29**). The values of the intercepts in table **5.1** are

close in magnitude to these values - further evidence that the volumetric component of ρ_{canopy} can be separated from the GO component and represented by a relatively simple semi-empirical function. As detailed in section **2.5.4.1** the gradients correspond to the expressions $\frac{4\rho_{leaf}}{3\pi}\left(1-e^{-LAIB}\right)$ for the RossThick kernel, where B is a constant with a value of 1.5 (B is in fact a function of θ_i and θ_v but only varies between 1 and 2, so a value of 1.5 is chosen in order to simplify the kernels) and $\frac{2\rho_{leaf}LAI}{3\pi}$ for the RossThin kernel. Examining the values of a_{vol}, b_{vol} and r in table **5.1** according to solar zenith angle θ_i shows some interesting trends. In the 18th April case the RossThick kernel appears significantly better than the RossThin kernel except for $\theta_i = 0^\circ$, when r is negative and < 0.7, implying a weak negative correlation. For the other dates the regression of the RossThin kernel produces negative values of r where $\theta_i = 0^\circ$.

5.2.4 Summary

k_{vol} is generally strongly correlated with α, the volumetric component of ρ_{canopy}; more so for dense canopies than sparse. There is very little variation in correlation with row azimuth angle, ϕ_{row}, but considerable variation with illumination angle. For the barley canopy, correlation is low between the RossThick kernel and α for the sparse (18th April) canopy. This is particularly true at nadir illumination where little volumetric scattering is present. Correlation between RossThin kernel and α is much higher here. Correlation between RossThick and α increases as the canopy develops, as expected. Conversely, correlation with RossThin reduces and becomes much more strongly dependent on θ_i. This is likely to be a result of increased volumetric scattering at high θ_i due to increased path length though the canopy. For senescent barley (24th June) the correlation between α and RossThick reduces rapidly with increasing θ_i, and correlation with RossThin is generally low.

For wheat the correlation between the volumetric kernels and α is generally much lower than for barley. In addition, RossThick is more strongly correlated than RossThin for the sparse wheat canopy (23rd March), unlike the barley case. Correlation is also generally more variable with θ_i. For the more developed wheat canopy (23rd April)

correlation between RossThick and α is much greater than for the sparse canopy. Correlation of RossThin increases from strongly negative to strongly positive with θ_i. Observed differences between results for barley and wheat are likely to be due to structural arrangement of the canopy (e.g. LAD).

5.3 Variation of GO component, β, with k_{GO}

5.3.1 Results

Results presented in figures **5.2** and **5.3** for the BPMS-derived GO component of ρ_{canopy}, β, against the LiDense and LiSparse kernels do not show such clear linear relationships as the plots of α against the volumetric kernels. There is a far greater spread of points than seen for the volumetric component, largely due to the variation between the separate θ_i cases. The correlation between the values of β and the GO kernel values varies from being close to one in some cases, through zero to strong negative correlation in some cases. In addition, the differences of scale (an order of magnitude between ordinate and abscissa) result in low values of r. The slopes, intercepts and regression coefficients for β against GO kernels are presented in tables **5.2** and **5.3**. Table **5.2** contains the results from the LiDense and LiSparse kernels, while table **5.3** contains the results from the LiDenseGC and LiSparseGC variants. The kernels are labelled in the tables as follows:

LiDense (G) $\Rightarrow$ DG
LiDense (GC) $\Rightarrow$ DGC
LiSparse (G) $\Rightarrow$ SG
LiSparse (GC) $\Rightarrow$ SGC

As in table **5.1**, the kernels are separated by colour, with the LiSparse (SG) values in table **5.2** and the LiSparseGC (SGC) values in table **5.3** being presented in red. Also as in table **5.1**, all correlations are significant to a 95% confidence level. Values in bold are those for which the upper and lower confidence levels lie within ± 0.125 of r. This indicates correlations for which the confidence interval is smallest, suggesting a strong correlation.

Table 5.2 Slopes, intercepts and regression coefficients for the LiDense and LiSparse GO kernels as a function of solar zenith (θ_i) and row azimuth (ϕ_{row}) (LiSparse kernels in red).

5.2a barley - 18th April

k_{GO}	θ_i	ϕ_{row}	a_{GO}	b_{GO}	r
DG	0	0	3.47	-3.33	0.69
DG	30	0	1.79	-2.14	0.17
DG	60	0	-5.37	2.60	-0.62
SG	**0**	**0**	**7.00**	**-5.92**	**0.96**
SG	30	0	5.65	-4.90	0.52
SG	60	0	-5.90	2.55	-0.43
DG	0	45	3.35	-3.24	0.67
DG	30	45	0.58	-1.23	0.06
DG	60	45	-5.93	2.99	-0.74
SG	**0**	**45**	**6.88**	**-5.85**	**0.95**
SG	30	45	4.44	-4.00	0.42
SG	60	45	-7.28	3.53	-0.58
DG	0	90	3.44	-3.31	0.68
DG	30	90	-0.03	-0.76	0.00
DG	60	90	-6.25	3.20	-0.79
SG	**0**	**90**	**7.03**	**-5.95**	**0.95**
SG	30	90	3.92	-3.59	0.36
SG	60	90	-7.94	3.99	-0.64

5.2b barley - 13th May

k_{GO}	θ_i	ϕ_{row}	a_{GO}	b_{GO}	r
DG	0	0	2.98	-1.36	0.82
DG	30	0	0.70	-0.92	0.08
DG	60	0	-4.08	-0.65	-0.58
SG	**0**	**0**	**5.28**	**-1.79**	**0.99**
SG	30	0	3.83	-1.38	0.45
SG	60	0	-4.59	-1.00	-0.42
DG	0	45	3.15	-1.38	0.82
DG	30	45	1.23	-1.02	0.15
DG	60	45	-3.75	-0.71	-0.52
SG	**0**	**45**	**5.61**	**-1.82**	**0.99**
SG	30	45	4.30	-1.46	0.50
SG	60	45	-3.91	-1.12	-0.34
DG	0	90	2.98	-1.38	0.80
DG	30	90	1.16	-1.02	0.14
DG	60	90	-3.94	-0.65	-0.58
SG	**0**	**90**	**5.39**	**-1.83**	**0.99**
SG	30	90	4.18	-1.48	0.50
SG	60	90	-4.35	-1.02	-0.40

5.2c barley - 4th June

k_{GO}	θ_i	ϕ_{row}	a_{GO}	b_{GO}	r
DG	**0**	**0**	**5.02**	**-1.14**	**0.90**
DG	30	0	-2.12	-0.66	-0.14
DG	60	0	-6.99	-0.94	-0.56
SG	**0**	**0**	**7.98**	**-1.30**	**0.98**
SG	30	0	3.40	-0.84	0.22
SG	60	0	-8.11	-1.31	-0.41
DG	**0**	**45**	**4.99**	**-1.12**	**0.91**
DG	30	45	-2.99	-0.62	-0.20
DG	60	45	-6.97	-0.97	-0.55
SG	**0**	**45**	**7.81**	**-1.25**	**0.98**
SG	30	45	2.49	-0.76	0.16
SG	60	45	-8.12	-1.35	-0.40
DG	**0**	**90**	**4.97**	**-1.13**	**0.90**
DG	30	90	-3.75	-0.58	-0.25
DG	60	90	-7.16	-0.95	-0.57
SG	**0**	**90**	**7.82**	**-1.27**	**0.98**
SG	30	90	1.66	-0.72	0.11
SG	60	90	-8.45	-1.32	-0.43

5.2d barley - 24th June

k_{GO}	θ_i	ϕ_{row}	a_{GO}	b_{GO}	r
DG	0	0	4.34	-1.83	0.84
DG	30	0	1.89	-1.25	0.15
DG	60	0	-6.06	0.03	-0.59
SG	**0**	**0**	**7.37**	**-2.52**	**0.98**
SG	30	0	6.51	-2.22	0.51
SG	60	0	-6.96	-0.20	-0.43
DG	0	45	-0.19	-0.56	-0.11
DG	**30**	**45**	**2.42**	**-1.81**	**0.92**
DG	60	45	2.07	-2.12	0.86
SG	0	45	-0.55	-0.27	-0.24
SG	30	45	2.09	-1.48	0.86
SG	**60**	**45**	**3.18**	**-2.96**	**0.90**
DG	0	90	-0.19	-0.55	-0.13
DG	**30**	**90**	**2.10**	**-1.78**	**0.92**
DG	60	90	1.80	-2.09	0.86
SG	0	90	-0.50	-0.27	-0.25
SG	30	90	1.80	-1.46	0.86
SG	60	90	2.76	-2.90	0.89

5.2e wheat – 23rd March

k_{GO}	θ_i	ϕ_{row}	a_{GO}	b_{GO}	r
DG	0	0	11.22	-11.31	0.69
DG	30	0	0.47	-1.22	0.01
DG	60	0	-20.04	17.43	-0.76
SG	**0**	**0**	**22.65**	**-22.05**	**0.95**
SG	30	0	13.39	-13.29	0.38
SG	60	0	-24.92	21.56	-0.60
DG	0	45	11.18	-11.27	0.66
DG	30	45	4.70	-5.24	0.13
DG	60	45	-19.37	16.83	-0.70
SG	**0**	**45**	**23.14**	**-22.52**	**0.94**
SG	30	45	17.31	-17.02	0.49
SG	60	45	-22.97	19.77	-0.53
DG	0	90	11.11	-11.22	0.67
DG	30	90	4.20	-4.77	0.12
DG	60	90	-19.25	16.72	-0.71
SG	**0**	**90**	**22.89**	**-22.30**	**0.95**
SG	30	90	16.79	-16.53	0.48
SG	60	90	-22.93	19.73	-0.54

5.2f wheat – 23rd April

k_{GO}	θ_i	ϕ_{row}	a_{GO}	b_{GO}	r
DG	**0**	**0**	**1.49**	**-1.43**	**0.86**
DG	30	0	0.63	-1.04	0.16
DG	60	0	-1.52	-0.77	-0.43
SG	**0**	**0**	**2.52**	**-1.84**	**0.99**
SG	30	0	2.07	-1.49	0.51
SG	60	0	-1.40	-1.23	-0.25
DG	0	45	1.48	-1.43	0.85
DG	30	45	0.63	-1.05	0.16
DG	60	45	-1.58	-0.75	-0.46
SG	**0**	**45**	**2.53**	**-1.85**	**0.99**
SG	30	45	2.06	-1.49	0.51
SG	60	45	-1.51	-1.20	-0.28
DG	0	90	1.47	-1.43	0.85
DG	30	90	0.39	-0.95	0.10
DG	60	90	-1.73	-0.69	-0.50
SG	**0**	**90**	**2.53**	**-1.86**	**0.99**
SG	30	90	1.87	-1.42	0.46
SG	60	90	-1.78	-1.10	-0.33

Table 5.3 Slopes, intercepts and regression coefficients for GC variants of LiDense and LiSparse GO kernels as a function of solar zenith (θ_i) and row azimuth (ϕ_{row}).

5.3a barley - 18th April

k_{GO}	θ_i	ϕ_{row}	a_{GO}	b_{GO}	r
DGC	**0**	**0**	**19.64**	**-16.54**	**0.98**
DGC	30	0	19.02	-16.32	0.86
DGC	60	0	-0.26	-4.58	-0.02
SGC	**0**	**0**	**9.18**	**-7.71**	**0.98**
SGC	30	0	7.51	-6.41	0.73
SGC	60	0	-2.58	0.07	-0.37
DGC	**0**	**45**	**19.38**	**-16.39**	**0.97**
DGC	30	45	18.07	-15.63	0.82
DGC	60	45	-2.24	-3.16	-0.18
SGC	**0**	**45**	**9.05**	**-7.64**	**0.97**
SGC	30	45	6.80	-5.88	0.67
SGC	60	45	-3.27	0.55	-0.51
DGC	**0**	**90**	**19.73**	**-16.63**	**0.97**
DGC	30	90	17.90	-15.46	0.79
DGC	60	90	-2.98	-2.65	-0.24
SGC	**0**	**90**	**9.23**	**-7.76**	**0.97**
SGC	30	90	6.56	-5.69	0.63
SGC	60	90	-3.60	0.78	-0.57

5.3b barley - 13th May

k_{GO}	θ_i	ϕ_{row}	a_{GO}	b_{GO}	r
DGC	**0**	**0**	**14.42**	**-4.83**	**0.99**
DGC	30	0	13.42	-4.56	0.76
DGC	60	0	0.04	-4.77	0.00
SGC	**0**	**0**	**6.77**	**-2.25**	**0.99**
SGC	30	0	5.27	-1.76	0.65
SGC	60	0	-2.04	-1.48	-0.36
DGC	**0**	**45**	**15.37**	**-4.94**	**0.99**
DGC	30	45	13.87	-4.59	0.79
DGC	60	45	0.86	-4.88	0.07
SGC	**0**	**45**	**7.22**	**-2.30**	**0.99**
SGC	30	45	5.57	-1.80	0.68
SGC	60	45	-1.69	-1.53	-0.28
DGC	**0**	**90**	**14.79**	**-4.98**	**0.99**
DGC	30	90	13.87	-4.76	0.80
DGC	60	90	0.16	-4.78	0.01
SGC	**0**	**90**	**6.95**	**-2.32**	**0.99**
SGC	30	90	5.53	-1.86	0.69
SGC	60	90	-1.92	-1.49	-0.34

5.3c barley - 4th June

k_{GO}	θ_i	ϕ_{row}	a_{GO}	b_{GO}	r
DGC	**0**	**0**	**21.37**	**-3.45**	**0.96**
DGC	30	0	16.62	-2.92	0.52
DGC	60	0	0.62	-4.79	0.03
SGC	**0**	**0**	**10.06**	**-1.60**	**0.96**
SGC	30	0	5.90	-1.08	0.40
SGC	60	0	-3.56	-1.62	-0.34
DGC	**0**	**45**	**20.89**	**-3.33**	**0.95**
DGC	30	45	14.79	-2.71	0.47
DGC	60	45	0.80	-4.79	0.04
SGC	**0**	**45**	**9.83**	**-1.54**	**0.96**
SGC	30	45	4.97	-0.99	0.34
SGC	60	45	-3.53	-1.63	-0.33
DGC	**0**	**90**	**20.92**	**-3.37**	**0.95**
DGC	30	90	13.66	-2.66	0.43
DGC	60	90	0.51	-4.78	0.02
SGC	**0**	**90**	**9.84**	**-1.56**	**0.96**
SGC	30	90	4.26	-0.96	0.29
SGC	60	90	-3.66	-1.62	-0.35

5.3d barley - 24th June

k_{GO}	θ_i	ϕ_{row}	a_{GO}	b_{GO}	r
DGC	**0**	**0**	**20.07**	**-6.82**	**0.97**
DGC	30	0	20.69	-6.98	0.78
DGC	60	0	-0.62	-4.63	-0.04
SGC	**0**	**0**	**9.41**	**-3.18**	**0.98**
SGC	30	0	8.49	-2.80	0.69
SGC	60	0	-3.21	-1.10	-0.38
DGC	0	45	-1.66	-0.62	-0.27
DGC	30	45	1.70	-2.53	0.35
DGC	60	45	2.19	-5.55	0.76
SGC	0	45	-0.76	-0.28	-0.26
SGC	30	45	1.38	-1.28	0.59
SGC	60	45	1.52	-2.38	0.87
DGC	0	90	-1.50	-0.62	-0.29
DGC	30	90	1.49	-2.52	0.35
DGC	60	90	1.87	-5.50	0.74
SGC	0	90	-0.69	-0.28	-0.28
SGC	30	90	1.21	-1.27	0.60
SGC	60	90	1.31	-2.35	0.86

5.3e wheat – 23rd March

k_{GO}	θ_i	ϕ_{row}	a_{GO}	b_{GO}	r
DGC	**0**	**0**	**63.70**	**-61.94**	**0.97**
DGC	30	0	58.32	-57.05	0.80
DGC	60	0	-8.33	3.00	-0.20
SGC	**0**	**0**	**29.73**	**-28.89**	**0.97**
SGC	30	0	21.59	-21.13	0.64
SGC	60	0	-11.23	8.68	-0.54
DGC	**0**	**45**	**65.39**	**-63.54**	**0.97**
DGC	30	45	62.94	-61.52	0.86
DGC	60	45	-6.07	0.91	-0.14
SGC	**0**	**45**	**30.51**	**-29.63**	**0.97**
SGC	30	45	24.51	-23.93	0.72
SGC	60	45	-10.32	7.85	-0.47
DGC	**0**	**90**	**64.63**	**-62.85**	**0.97**
DGC	30	90	61.93	-60.57	0.85
DGC	60	90	-6.01	0.85	-0.14
SGC	**0**	**90**	**30.15**	**-29.30**	**0.97**
SGC	30	90	23.99	-23.45	0.71
SGC	60	90	-10.29	7.82	-0.48

5.3f wheat – 23rd April

k_{GO}	θ_i	ϕ_{row}	a_{GO}	b_{GO}	r
DGC	**0**	**0**	**6.87**	**-4.97**	**0.99**
DGC	30	0	6.32	-4.55	0.75
DGC	60	0	0.92	-5.06	0.16
SGC	**0**	**0**	**3.22**	**-2.31**	**0.99**
SGC	30	0	2.58	-1.80	0.66
SGC	60	0	-0.57	-1.59	-0.19
DGC	**0**	**45**	**6.93**	**-5.02**	**0.99**
DGC	30	45	6.35	-4.59	0.77
DGC	60	45	0.74	-5.00	0.13
SGC	**0**	**45**	**3.25**	**-2.33**	**0.99**
SGC	30	45	2.58	-1.81	0.67
SGC	60	45	-0.63	-1.57	-0.22
DGC	**0**	**90**	**6.91**	**-5.05**	**0.99**
DGC	30	90	6.23	-4.55	0.75
DGC	60	90	0.54	-4.94	0.10
SGC	**0**	**90**	**3.24**	**-2.35**	**0.99**
SGC	30	90	2.47	-1.77	0.64
SGC	60	90	-0.76	-1.53	-0.27

5.3.2 Analysis of regression relationships

The results for β against k_{GO} presented in figures **5.2** and **5.3**, and tables **5.2** and **5.3**, show much greater variation than those seen for α against k_{vol}, although some trends are similar. The variation of the correlation coefficient, r, with ϕ_{row} is negligible on the whole (as above) but there is significant variation with solar zenith angle, θ_i (also as above). Unlike the α case, it is expected for β given that the GO component of ρ_{canopy} will be strongly dependent on the amount of shadowing in the scene, which will vary with θ_i (and with the arrangement of objects within the canopy). The values of r are generally high and positive at nadir illumination, reducing with increasing θ_i, becoming predominantly negative. These trends hold for all kernels. The values of r for the LiSparseGC (SGC) kernel, in the 18th April barley case (table **5.3a**) reduce from 0.96 to -0.43 as θ_i increases from nadir to 60°. The exception to this trend is the barley canopy of 24th June where there is significant variation in r with ϕ_{row}. Although r for $\phi_{row} = 0°$ follows the same trend as for the other canopies, the trend is reversed for $\phi_{row} = 45°$ and $\phi_{row} = 90°$ with r starting low or negative for $\theta_i = 0°$ and increasing to the highest value at $\theta_i = 60°$. This is the only canopy with significantly different canopy structure, having mature seed heads, a somewhat different LAD (from figure **4.10**, correlating much more

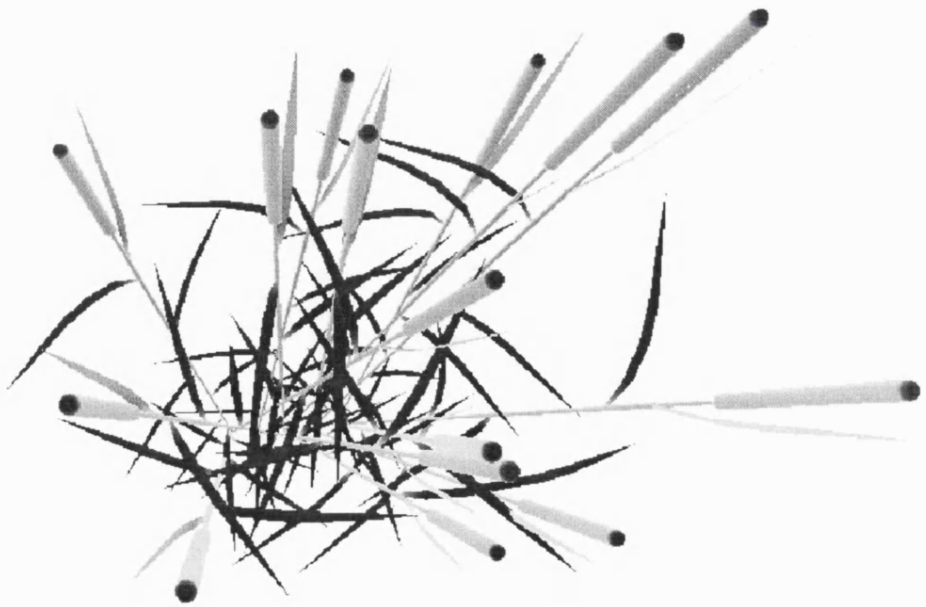

Figure 5.4 Perspective view of barley plants from above.

highly with the plagiophile, planophile and spherical LADs than any other canopy), and less green vegetation. Recent work has shown that the representation of these heads can significantly affect ρ_{canopy}, particularly single scattered radiation (Saich *et al.*, 2001). Figure **5.4** is a perspective view of a barley canopy from above, with seed heads modelled as simple Lambertian cylinders. These cylinders contribute disproportionately strongly to ρ_{canopy}.

The standard LiSparse kernel performs significantly better in all cases than the standard LiDense kernel, with maximum values of r almost always greater than 0.95 (although this is only true at $\theta_i = 0°$) as opposed to values between 0.6 and 0.85 for the LiDense kernel (table **5.2a-f**). In addition both the modified GC versions of the GO kernels perform better than the LiDense kernel, and perform comparably with the standard LiSparse kernel (table **5.3a-f**). Correlations between β and k_{GO} for barley rise as the canopy develops before falling back for 24th June. The wheat canopies of 23rd March and 23rd April show much the same trends as for the barley. The results of the two barley and wheat canopies closest in terms of development (23rd March wheat, 18th April barley and 23rd April wheat, 13th May barley) show close agreement. This is in contrast to the results for correlations between α and k_{vol}.

The values of r for the plots of β against k_{GO} suggest that is less clear that the GO component of ρ_{canopy} is characterised by the linear function of β proposed in equation **4.4** (unlike the situation for α seen in section **5.2**). There is some agreement, but the variability of the results, particularly with varying θ_i, suggests that the GO kernels do not work particularly well when faced with the row-based canopies comprised of relatively fine leaves used here. A consequence of this described in chapter **4** is the absence of a clear hotspot feature in the GO component of simulated ρ_{canopy}, β, and the presence of one in the volumetric component, α. This departure from expectations is not altogether surprising given the departure of the barley and wheat canopies from the assumptions made in the formulation of the GO kernels i.e. spheroids randomly located on a Lambertian surface, with log-normal height distribution and perfectly black shadows. Figure **5.5** illustrates the type of canopy envisaged in the formulation of the kernels: a field of spheroids above a Lambertian surface. The heights are not log-normally distributed (as in the GO kernel formulation), but clearly it may not be realistic to expect the barley and wheat canopies shown in figures **4.2** to behave like the canopy in figure **5.5**. One approach to the dependence on θ_i suggests that the GO kernels may need to be

more flexible in situations where the assumptions underlying the kernels are not met. In some cases, the GO kernels just may not be appropriate. A solution to the row dependent behaviour of the GO kernels might be to define a new set of GO kernels based on canopies with strong row orientations. This would allow a greater degree of confidence to be placed in the ability of the kernels to describe reflectance over agricultural regions.

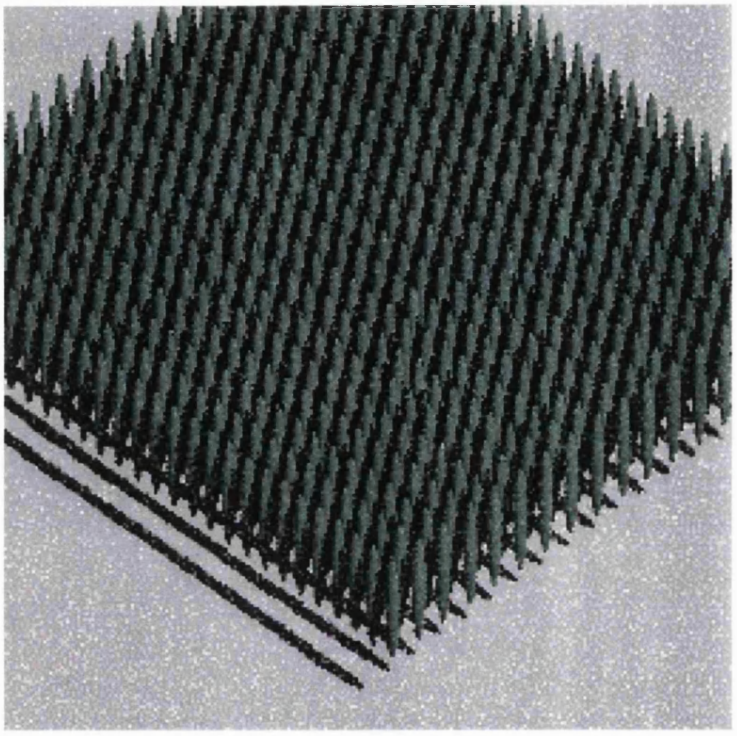

Figure 5.5 Simulated 'spheroids on sticks' canopy.

Such kernels would not have random distributions of spheroids on sticks, but would have a dependency on row azimuth angle, ϕ_{row} (in relation to the viewer). In addition, taking account of the clumped vegetation that predominates when considering these high resolution scenes would improve matters, for instance by using effective LAI (LAI_e), rather than LAI directly for example (Nilson and Kuusk, 1989).

It has already been established that the GO component of ρ_{canopy} as simulated in these experiments is determined by β, the proportion of sunlit soil (it should be noted that this differs from the theoretical case envisioned by Li and Strahler (1985, 1986, 1992) for example, which is driven by scene components including sunlit and shaded crown and ground. In this case, shadowed crown and ground contribute zero to scene reflectance (no diffuse illumination), so the GO component of ρ_{canopy} by definition originates from the sunlit soil). Figure **4.6** shows that the proportion of sunlit soil is the dominant component of ρ_{canopy} in the 18th April barley and 23rd March wheat canopies, accounting for the similarity in results of these two canopies. Although the proportion of sunlit soil varies in

the same way with θ_v for all canopies (downward bowl-shape, peak in the hotspot direction), the magnitude is very different, reducing from 0.6-0.8 (18th April, 23rd March) when the canopy is sparse, to close to zero for the 4th June (LAI = 3.19, 80-90% cover). The assumptions behind the GO kernels are more closely adhered to in the sparse canopies when the proportion of sunlit soil is highest and the regularly spaced plants with small leaf area are well-separated. Subsequent increases in cover reduce the proportion of sunlit soil, as well as the separability of the plants; they become a dense canopy rather than individual scattering objects. Consequently the GO component of ρ_{canopy} is less-well characterised by equation **4.4**. The decline in strength of the correlation with increasing θ_i suggests that the projected area of plants departs from the projections assumed in the GO kernels. Although the proportion of sunlit soil reduces with increasing θ_i it clearly does not do so in the manner assumed in theory (particularly in the case of the LiDense kernel). This is hardly surprising: the plants begin small, with leaves large in proportion to plant height; in the latter stages the plants are tall and very thin, with proportionally much smaller leaves. These plants are further removed from the spheroidal assumption than their immature counterparts. In addition, as the proportion of visible soil (sunlit or otherwise) reduces, the projected area of the plants will become proportionally more important.

5.3.3 Slopes and intercepts a_{GO}, b_{GO} of β against k_{GO}

In the same manner as seen in **5.2.3** for the volumetric kernels, the values of a_{GO}, b_{GO} in tables **5.2a-f** and **5.3a-f** correspond to the slopes and intercepts of the regressions of β against k_{GO}. The LiDense kernel contains an offset of –2 (equation **2.31**) to ensure that the kernel is zero for nadir viewing and illumination (the LiSparse kernel is zero anyway under these conditions). The gradients are $C\lambda\pi r^2$ for the LiSparse kernel, where C is the reflectance of the sunlit crown (equal to 1), and λ is the number density of spheroids on the surface of width 2r, and $C/2$ for the LiDense kernel. Table **5.3a** shows that in the 18th April case the values of a_{GO} are mostly positive and vary from close to zero up to 14 or 15 for the LiDense (GC) kernel. Values of b_{GO} are almost exclusively negative, varying from just below zero in most cases, down to –15 for the LiDense (GC) kernel. The values of a_{GO} gradually increase for the barley canopy as it develops and the total scattering component increases, with the values of b_{GO} remaining similar for each

date. The biggest changes are seen between the wheat canopies of 23rd March and 23rd April (tables **5.2** and **5.3 e** and **f**). For the earlier canopy, the values of a_{GO} and b_{GO} are extreme, ranging from –25 to 65 in the case of a_{GO}, with a_{GO} following similar patterns. However, for the 23rd April canopy the gradients and intercepts are comparable to the values in tables **5.2** and **5.3 a** and **b** for the 18th April and 13th May canopies.

5.3.4 Summary

In most cases the correlation between β and k_{GO} (as measured by r, the correlation coefficient) is lower than that between α and k_{vol}. Results suggest that in certain cases the volumetric and GO scattering components can be separated and are generally linearly related to the respective kernels used to describe them in the linear kernel-driven models of BRDF, although there is significant variation in this relationship. For both barley and wheat there is little variation with ϕ_{row} in correlation in the earlier stages of the canopy. This changes for the 24th June barley canopy, when values of r increase dramatically with increasing ϕ_{row}. This is likely to be related to the structural variation in the canopy described above, with far less shadowed soil being visible as well as the presence of seed heads. There is significant variation in the strength of correlation with increasing θ_i, with values of r moving from high positive values at nadir to zero or negative values for θ_i = 60°. This trend is true for each barley canopy.

In the early stages of growth of both the barley and wheat canopies the sparse and dense variants of k_{GO} are similar, with the sparse version having a slight edge in terms of correlation with β. The sparse variants become increasingly better as the canopy develops. This is further evidence to support the choice of the sparse family of kernels as the GO kernels-of-choice for BRDF and albedo production from MODIS reflectance data. The GC variants of k_{GO}, treating ground and crown as having separate reflectance, perform better in nearly all cases, in the sense of being more closely correlated with β. The only exception to this is in the 24th June barley case. In terms of implementation the GC variants require extra parameters (shadowed crown and ground reflectance) but this evidence does suggest that these kernels may be better equipped to describe the GO component of ρ_{canopy} in a wider variety of cases (for the type of canopy examined here). At the very least the GC variants should be considered a viable alternative to the standard GO kernels.

5.4 Conclusion

The hypothesis that ρ_{canopy} can be represented as a linear combination of volumetric and GO components, α and β, was tested by separating these components from BPMS-simulated ρ_{canopy}, and plotting their relationship with the respective linear model kernels, k_{vol} and k_{GO}. Results from barley and wheat canopies show that there is generally a linear relationship between α and k_{vol}, which becomes stronger as the canopies develop. The values of r for the regressions of α against k_{vol} generally increase with θ_i and decrease with ϕ_{row} until the canopy no longer adheres to the assumptions used in the kernels exemplified by the 24th June barley canopy (LAI of 3.19, but little green vegetation and lots of seed heads). This behaviour is likely to be due to an increase in the proportion of volumetric scattering caused by increasing path length (of incoming radiation) through the canopy.

Results show a much weaker relationship between β and k_{GO}, than between α and k_{vol}. There is also greater variability in the values of r in this case. The values of r for β against k_{GO} tend to fall as the canopy develops and volumetric scattering increases at the expense of GO scattering. Also in contrast to α, r falls with θ_i in all cases except for the 24th June barley canopy. There is little variation in correlation between β and k_{GO} with ϕ_{row}, except (again) for the 24th June barley canopy. Although results for α (in particular) and β indicate that ρ_{canopy} may be separated into a linear combination of volume and GO scattering components in some cases, it is clear that this separability will depend on canopy configuration. The canopies used here depart (deliberately) from those envisioned in the linear kernels (particularly the GO case): they are row-oriented, with non-spherical LAD and small, widely distributed scatterers rather than GO "envelopes". In particular, as the canopies develop, they resemble the idealised 'spheroids on sticks' assumption of the GO kernels less and less. The key issue is that ρ_{canopy} can always be approximated (badly) by a linear combination of volumetric and GO components. However, results presented in this chapter illustrate that in cases where the canopy configuration more closely resembles that envisioned in the formulation of the kernels, the linear assumption is reasonable, particularly in the volumetric case. The barley and wheat canopies used for the simulation of ρ_{canopy} in this chapter resemble the configuration envisioned in the volumetric kernels far more closely than that envisioned in the GO kernels, so it is not surprising that agreement between k_{vol} and α is far higher than that between k_{GO} and β.

The canopies used in this experiment were deliberately chosen to diverge from the assumptions of plane-parallel homogeneity and distinct crown-shape on which k_{vol} and k_{GO} respectively are based. This was done in order to explore the applicability of the kernels in cases where their assumptions are not met directly (which perhaps applies to most cover types). When the assumptions underlying the kernels are not met, the assumption that ρ_{canopy} can be described as a linear combination of volumetric and GO scattering components tends to break down. These cases are listed below:

i) The canopy is very sparse, and there is almost no scattering from vegetation (k_{vol} attempts to explain some GO scattering). This is seen in the variability (and general reduction) of r with k_{vol} in table **5.1e**.

ii) The canopy is very dense, but the LAI is (relatively) low e.g. when the canopy reaches maturity and is largely stems and seed heads with little green leaf area (see variation of r with k_{vol} in table **5.1d**)

iii) There is noticeable azimuthal variation in the vegetation density due to row planting patterns (assumption of azimuthal uniformity invalidated). This is true for k_{GO} in the 24th June barley canopy case (table **5.2d**). However, the large variation seen in the correlation between k_{vol} and α, and k_{GO} and β with θ_i is also a function of variation in ϕ_{row}. As the canopy is seen across and along rows, the density of (viewed) vegetation changes significantly, causing variation in the amount of visible sunlit (and shaded) soil and vegetation (clumping). This is especially true for the barley canopy of 24th June. Figure **5.6** shows the large variation in sunlit leaf and soil with ϕ_{row}, at high θ_i. The variation is not as pronounced for younger canopies or for lower θ_i.

iv) Canopy LAD departs from the assumed spherical distribution (see figure **4.8**) i.e. 23rd March wheat (see variability of r values in table **5.1e**)

v) Inappropriate kernel choices are made i.e. RossThick kernel when LAI is low (table **5.1a** and **e**), or RossThin when LAI increases (table **5.1b-d**). This is not true of k_{GO} as the LiSparse kernel proved a better fit in nearly all circumstances (table **5.2**). So, interestingly, the "wrong" kernel choice can in some cases provide a better fit to reflectance. This indicates some kernel combinations may be inherently more flexible than others, although any biophysical information contained in the model parameters in these cases should not be trusted.

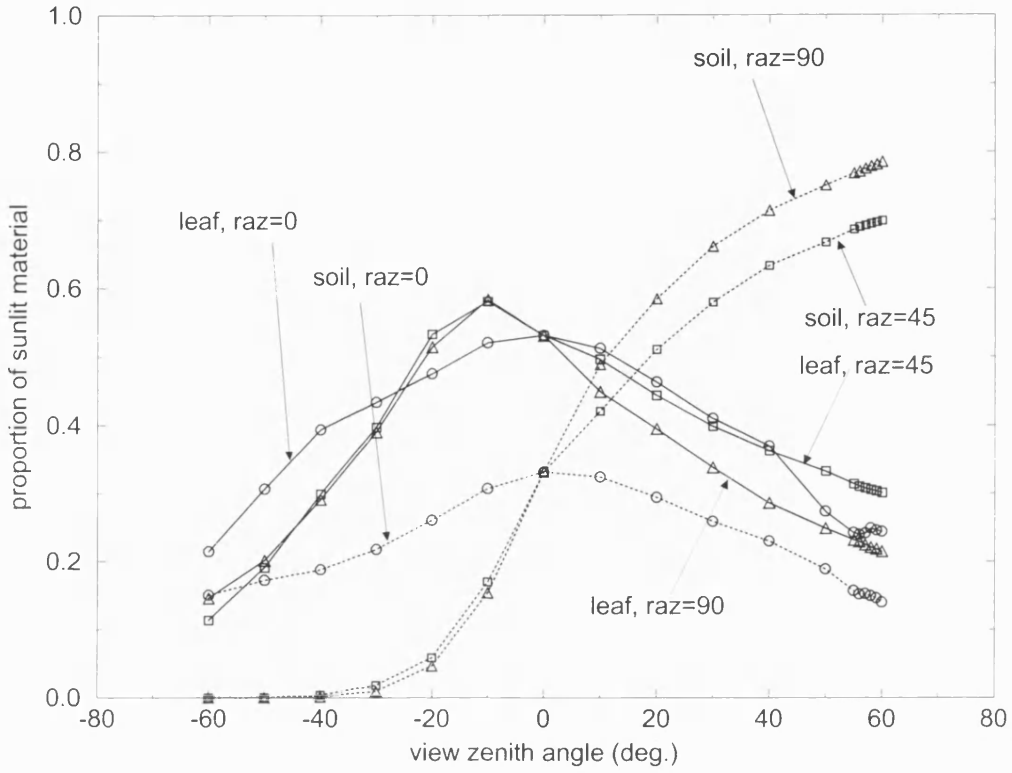

Figure 5.6 Variation in sunlit leaf and soil, 24th June barley canopy, $\theta_i = 60^o$.

The factors listed above highlight the importance of interpretation when using model parameters derived from satellite and airborne reflectance measurements. It is preferable that a minimum of assumptions regarding the type and distribution of cover be made. However results presented here suggest that the assumption of ρ_{canopy} as a linear combination of volumetric and GO scattering components is not always true. If cover types do not conform to the approximations underlying the linear models, attempts to evaluate parameters such as LAI and shadow fraction **should not be made**. Conversely, the parameters may directly indicate regions of departure from the assumptions made in the linear models. In these cases it is still possible to derive integrated products such as albedo, but no conclusions should be drawn regarding surface biophysical parameters. Constraints may be applied in these cases to ensure adherence to physical principles such as energy conservation (see appendix **1**). The next stage of analysis is to examine more closely the information content of volumetric and GO model parameters inverted against simulated ρ_{canopy}. It is important to understand whether it may be possible to retrieve biophysical information from the inverted model parameters (and if so, what sort) or whether the kernels should only ever be used for generating integrated products such as albedo, or predicting reflectance behaviour (Roy *et al.*, 2001).

6 Separability of canopy scattering components and information content

6.1 Introduction

Evidence presented in chapters **4** and **5** supports the first hypothesis of section **4.2** i.e. that ρ_{canopy} can (in general) be modelled as a linear combination of volumetric and GO kernels describing the (angular) variation of the separate components. However as the structure of the canopy departs from the assumptions made in the formulation of the kernels this hypothesis tends to break down. For sparse canopies k_{vol} can apparently explain a significant part of the variation seen in ρ_{canopy} even though there is likely to be very little volumetric scattering in these cases (reflected in the high values of the correlation coefficient, r, seen in table **5.1**). Likewise, k_{GO} generally seems to explain variations in ρ_{canopy} for the dense canopies when the scattering will be predominantly volumetric. This poses the question of whether the kernels can be said to be acting independently of each other. If not, attributing meaning to derived biophysical parameters will be much more difficult as the model parameters will be coupled in some way.

The issue of information in linear BRDF model parameters will be addressed in the subsequent section with reference to the second hypothesis of section **4.2**, namely that the kernels describing the volumetric and GO scattering components of ρ_{canopy} act independently of each other. If this hypothesis is true, then the volumetric component of ρ_{canopy} should be adequately modelled by the volumetric kernel alone and the GO component of ρ_{canopy} should be described solely by the GO kernel. This implies that **no part of the variation of either component should be explained by the other kernel**. In this case the components are separable and orthogonal. In practical cases where the models do not satisfactorily describe the BRDF, and assuming that angular sampling is reasonable (Lucht and Lewis (2000) have shown that poor angular sampling can severely affect the kernels' ability to fit BRDF), it is assumed that the basic kernel shapes are inadequate to describe the primary reflectance variations or that the assumptions underlying the kernels may not be fully met. The possibility that there may be secondary (and higher) components of the volumetric or GO components of the scattered reflectance field which may be described in part by the other kernel is not considered.

Kernel-driven models are specifically designed to cope with spatially heterogeneous surfaces where both volume and GO scattering may be present due to the

variety of cover types that may be contained in a single pixel (Wanner *et al.*, 1995). This permits inversion against moderate resolution reflectance data where heterogeneity can otherwise present severe problems. An example of this type of surface might be sparse woodland interspersed with grassland, where the shadows cast by the tree crowns conform to the GO model, whilst scattering within the tree crowns and from the grass is likely to be predominantly volumetric. Such a surface suggests that a continuum of the two scattering components exists, potentially operating at different scales (Wanner *et al.*, 1997). Is it reasonable in such a case to assume that all variation in each of the two components can be completely described by the respective kernels? If not, it is likely that the model parameters cannot be ascribed the direct physical meaning given in their formulation (see equations **4.3** and **4.4**), but rather that the parameters are coupled in some sense.

If we wish to invert the linear models against reflectance data in order to derive biophysical information it is essential to understand the physical meaning of the model parameters, whether the parameters are coupled, and if so, in what sense. As an example, consider equation **4.2**: knowing $P(\theta_i, \theta_v, \phi)$, G and G', μ and μ', is it possible to invert LAI explicitly from ρ_{canopy}, or will LAI and ρ_{leaf} be coupled in some way? If so, then to derive LAI by inverting a kernel-driven model against measured ρ_{canopy} would require knowledge of specific ρ_{leaf} for the observed canopy. The following section investigates the possibility that ρ_{canopy} cannot necessarily be separated into volumetric and GO scattering components and that some part of each component may actually be described by the other kernel. In addition, spectral variation of the angular kernels is discussed.

6.2 Method

If the linear relationships between k_{vol} and α and k_{GO} and β described in equations **4.3** and **4.4**, and demonstrated experimentally in chapter **5**, are substituted into equation **4.1**, a simplified expression for ρ_{canopy} is obtained in terms of the coefficients of the linear relationships presented in tables **5.2** and **5.3** ($a_{vol,GO}$ and $b_{vol,GO}$):

$$\rho_{canopy} = \underbrace{-\left(\rho_{leaf}\frac{b_{vol}}{a_{vol}} + \rho_{soil}\frac{b_{GO}}{a_{GO}}\right)}_{\text{isotropic term}} + \underbrace{\rho_{leaf}\frac{k_{vol}}{a_{vol}}}_{\text{volumetric term}} + \underbrace{\rho_{soil}\frac{k_{GO}}{a_{GO}}}_{\text{GO term}} \qquad \textbf{6.1}$$

Equation **6.1** contains a purely volumetric term, a purely GO term and a term comprising ρ_{leaf} and ρ_{soil} multiplied by the ratio of b to a (slope over intercept) from equations **4.3** and **4.4**. If equation **6.1** is compared with the general expression for a full kernel-driven model (equation **2.27**) it can be seen that (except for the role f_{iso} has in taking up the multiple scattering component) there is a direct equivalence between the model parameters i.e.

$$f_{iso} \equiv -\left(\rho_{leaf}\frac{b_{vol}}{a_{vol}} + \rho_{soil}\frac{b_{GO}}{a_{GO}}\right) \qquad \textbf{6.2a}$$

$$f_{vol} \equiv \frac{\rho_{leaf}}{a_{vol}} \qquad \textbf{6.2b}$$

$$f_{GO} \equiv \frac{\rho_{soil}}{a_{GO}} \qquad \textbf{6.2c}$$

where $f_{iso,GO,vol}$ are the model parameters (equivalent to the kernel weightings as described in section **2.5.4.1**, ignoring multiple scattering effects). We can now obtain estimates of the volumetric and GO parameters f_{vol} and f_{GO} from two directions:

1. From the values of a_{vol} and a_{GO} in tables **5.1** and **5.2** in combination with appropriate spectral estimates of ρ_{leaf} and ρ_{soil}, using the relationships in equations **6.2b** and **6.2c**.

2. From inverting a full linear kernel-driven model (as expressed in equation **2.27**) against ρ_{canopy} calculated from substitution of $a_{vol,GO}$ and $b_{vol,GO}$ back into equation **6.1**.

If the separate (single) scattering components of ρ_{canopy} can be modelled by isolating the purely geometric parameters controlling them (i.e. f_{vol} and f_{GO}, all other factors being equal) by assuming that ρ_{canopy} can be represented as a linear combination of volumetric and GO components α and β, then clearly the same values of f_{vol} and f_{GO} should be obtained from method 1 above as from method 2. This is illustrated schematically in figure **6.1**. If there are significant differences between the values of f_{vol} and f_{GO} derived from $a_{vol,GO}$ and $b_{vol,GO}$ and those obtained through full model inversion then we must conclude that the volumetric and GO kernels are not entirely separable i.e. hypothesis two of section **4.2** is false, and, as a result, the retrieval of uncoupled biophysical parameters from linear model inversions may not be possible. In this case it may be possible to identify coupled parameter relationships which might be inverted, but the nature of the coupling will need to be understood. This has important consequences for the operational use of linear kernel-driven BRDF models: without a clear understanding of the physical meaning of model parameters inverted from reflectance data, they are likely to be wrongly used and interpreted.

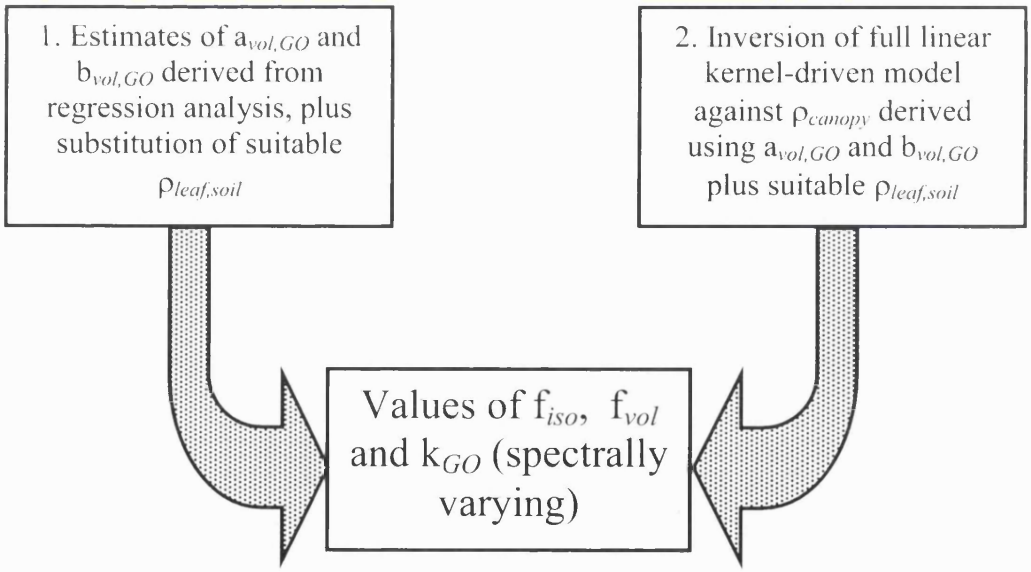

Figure 6.1 Estimates of model parameters f_{iso}, f_{vol} and f_{GO} obtained from two directions.

6.3 Results

The values of $a_{vol,GO}$ and $b_{vol,GO}$ presented in tables **5.1** and **5.2** were used in conjunction with suitable values of ρ_{leaf} and ρ_{soil} to calculate (spectrally varying) values of model parameters f_{GO} and f_{vol} according to equations **6.2b** and **c**. The ρ_{leaf} and ρ_{soil} spectra used are shown in figure **6.2**. These spectra were obtained during the field campaign described in chapter **3** using the PSII radiometer. Leaf spectra recorded in this manner (with leaves still attached to the plants) may not be a totally accurate measure of leaf reflectance as some radiation impinging on the leaf is lost via transmission through the lower surface of the leaf, while some reflected radiation will not fall within the instrument IFOV. Laboratory measurements are generally made using an integrating sphere, in order to ensure all incident radiation is recorded. However, in these experiments the absolute values of reflectance are not so important, it is the behaviour across the spectrum that is of interest. From figure **6.2**, the values of leaf are higher in the NIR than might be expected.

At the same time as values of f_{GO} and f_{vol} are derived via the regression relationships of chapter **5**, a full kernel-driven model of the type described in equation **2.27** was inverted against values of ρ_{canopy} calculated by substituting the parameters $a_{vol,GO}$

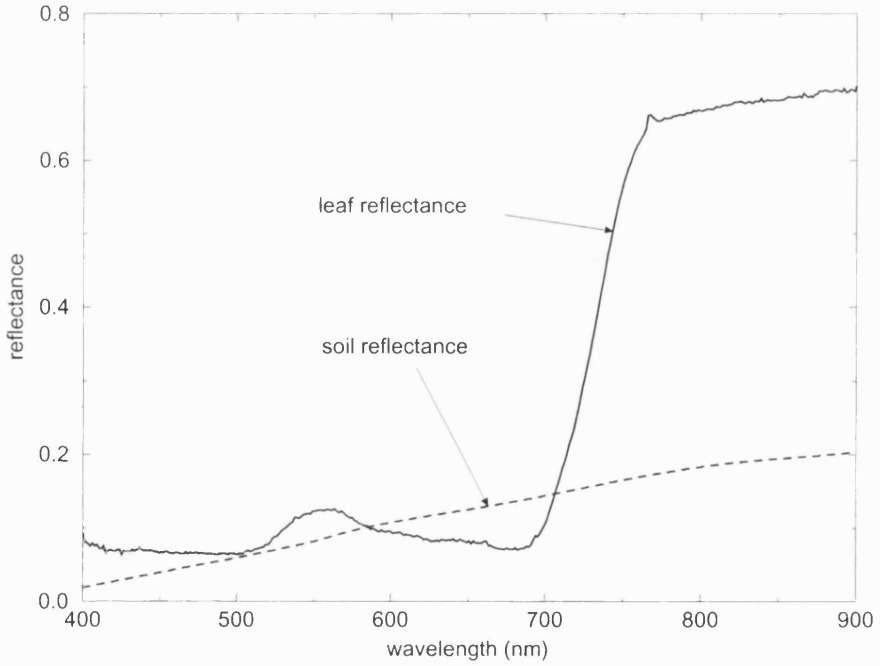

Figure 6. 2 ρ_{leaf} and ρ_{soil} used in BPMS ρ_{canopy} simulations

$b_{vol,GO}$, ρ_{leaf} and ρ_{soil} into equation **6.1**. These spectrally varying f_{GO} and f_{vol} are presented alongside the values of f_{GO} and f_{vol} calculated directly from tabulated values of a_{vol} and a_{GO} (plus ρ_{leaf} and ρ_{soil}) via equations **6.2b** and **c**. Figures **6.3** and **6.4** show the comparisons between the two sets of model parameters. Results are shown for the isotropic, RossThick and LiSparse kernel combination (figure **6.3**) as well as the isotropic, RossThin, LiDense combination (figure **6.4**). In figures **6.3** and **6.4** the parameters derived through the use of the derived $a_{vol,GO}$ and $b_{vol,GO}$ values are referred to as "**BPMS**" (or "BPMS-derived") parameters, and those through the inversion of a full linear model as "**inverted**". These distinctions are artificial as both sets of parameters are derived from BPMS simulations and both are obtained by inversion (although in different senses), but they need to be distinguished in subsequent discussions.

Figure 6.3 Comparison of isotropic, volumetric (RossThick) and GO (LiSparse) parameters derived from BPMS simulations and inversion of a full linear model.

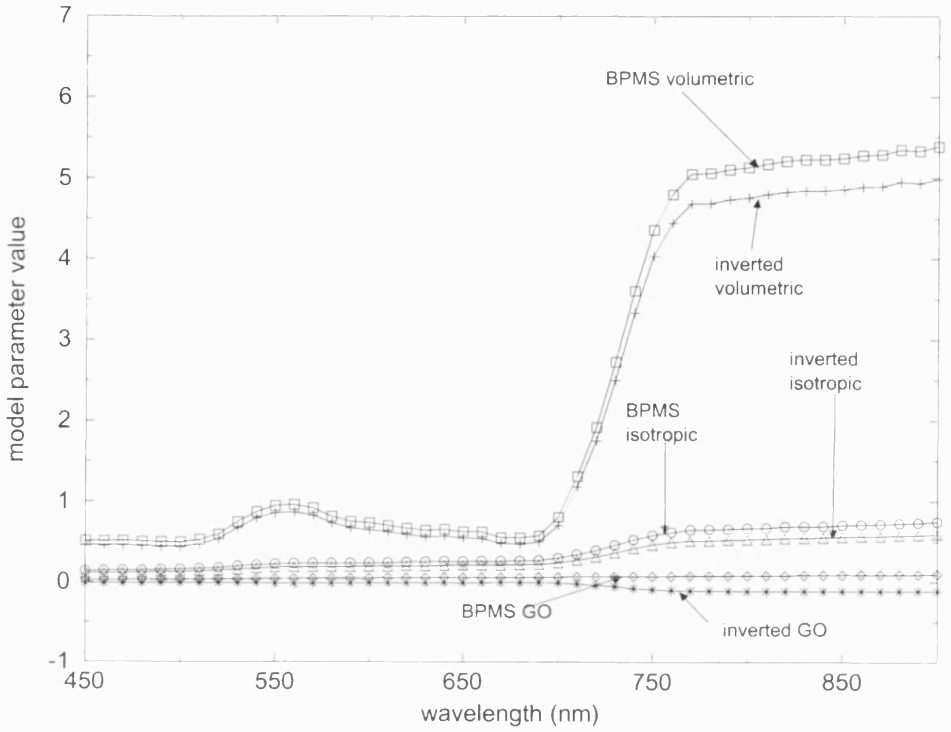

a) barley - 18th April

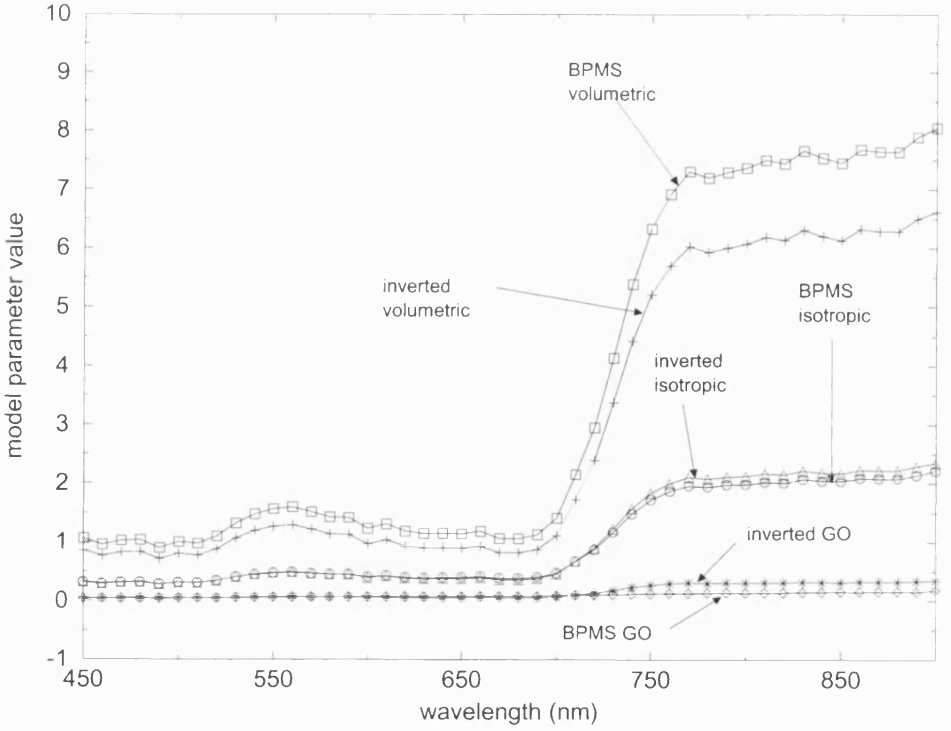

b) barley - 13th May

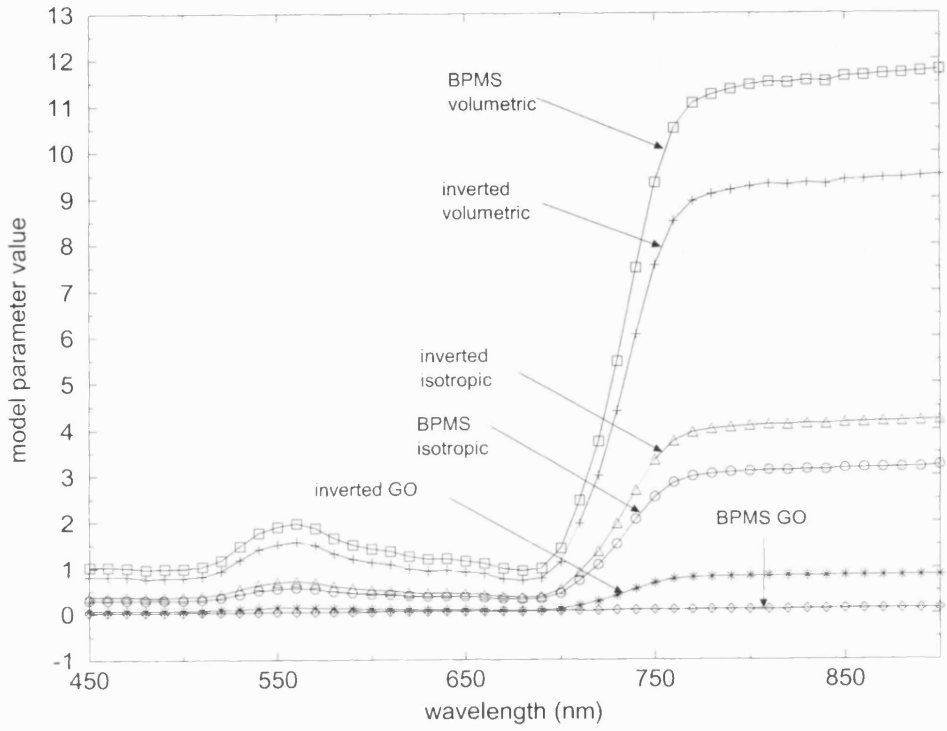

c) barley - 4th June

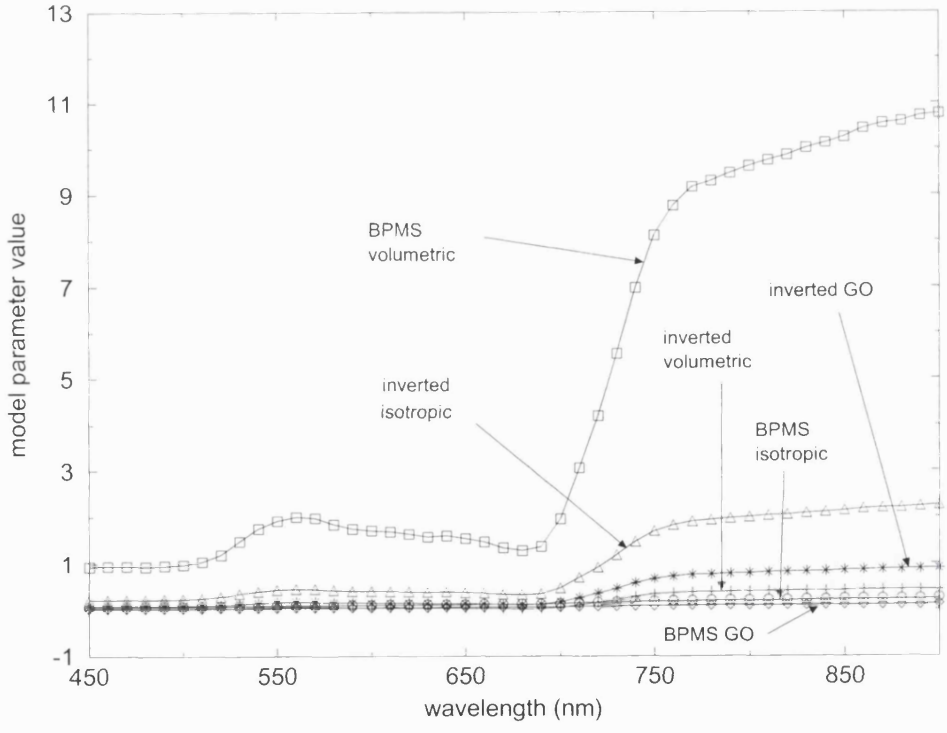

d) barley - 24th June

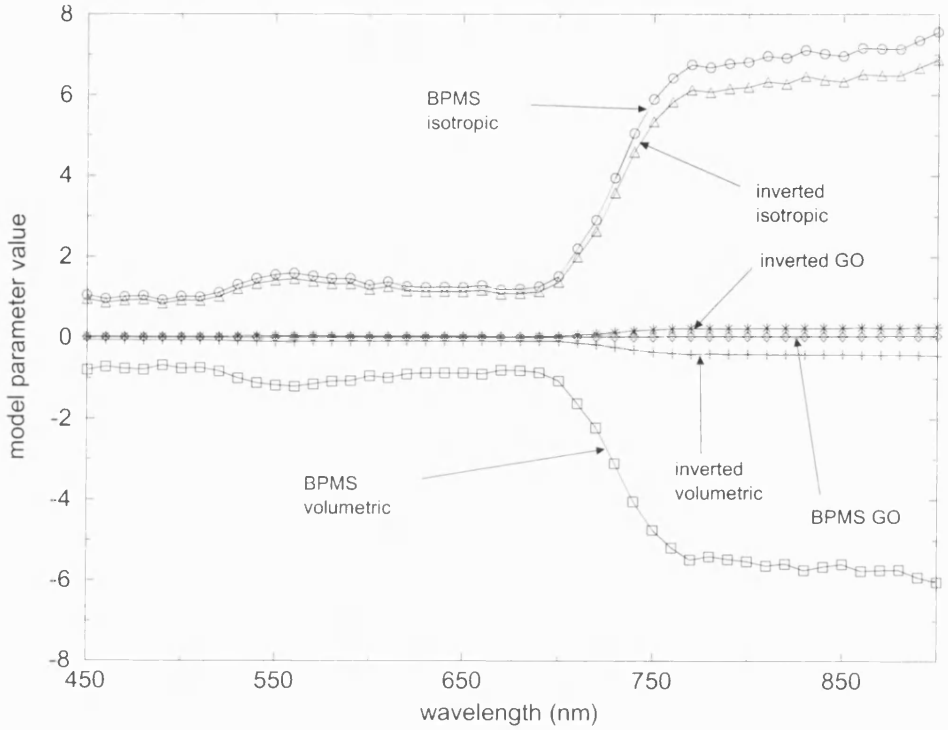

e) wheat - 23rd March

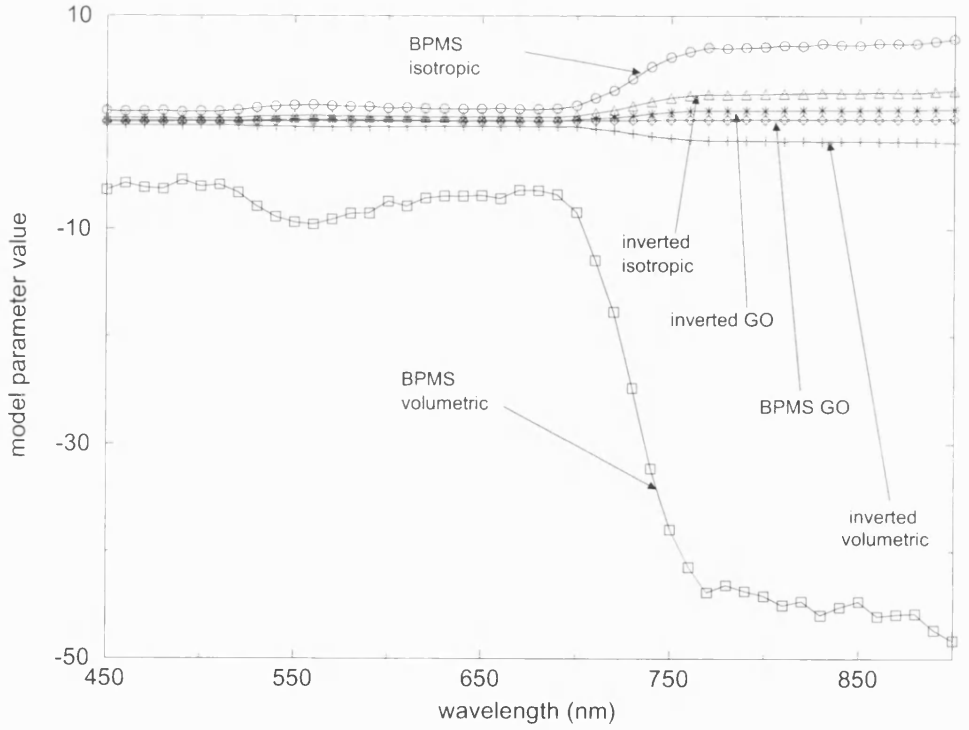

f) wheat - 23rd April

Figure 6.4 Comparison of isotropic, volumetric (RossThin) and GO (LiDense) parameters derived from BPMS simulations and inversion of a full linear model.

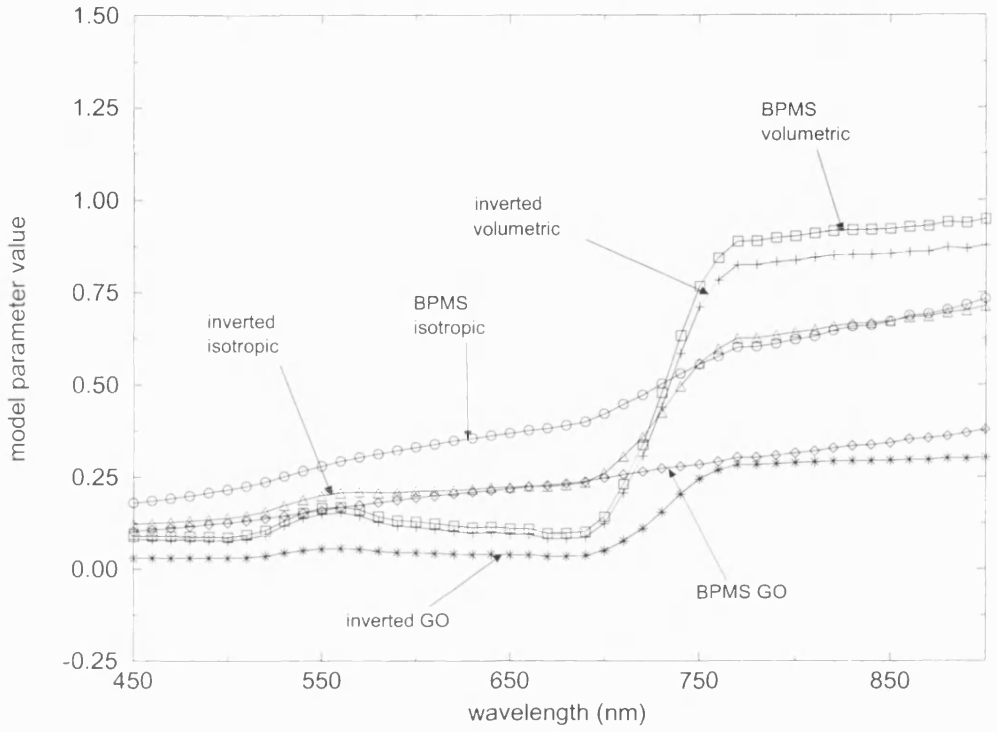

a) barley - 18th April

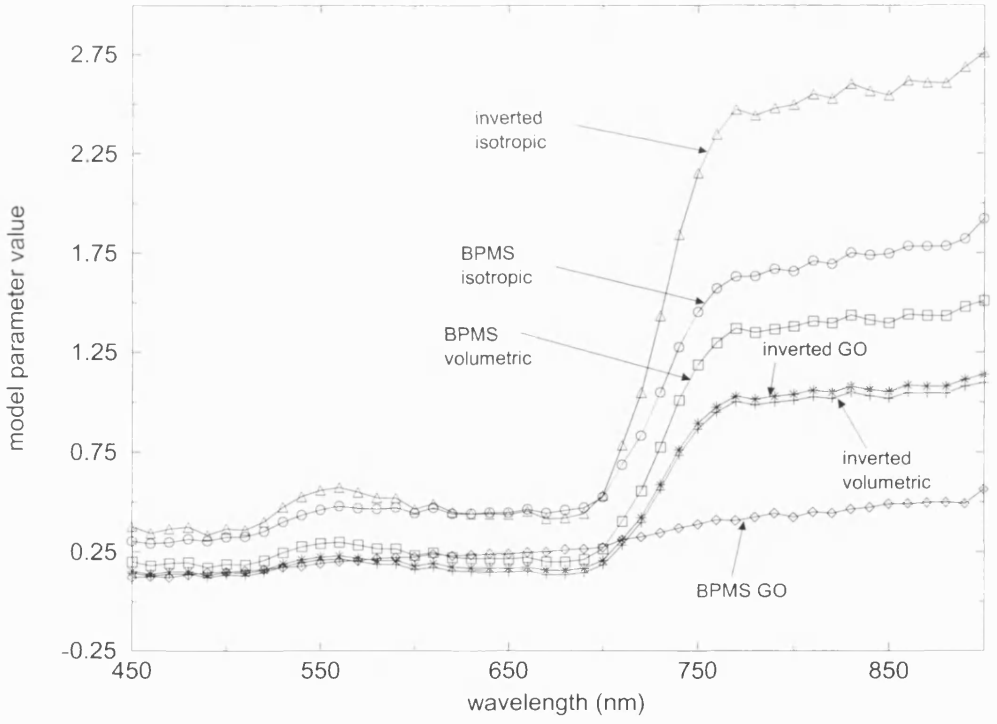

b) barley - 13th May

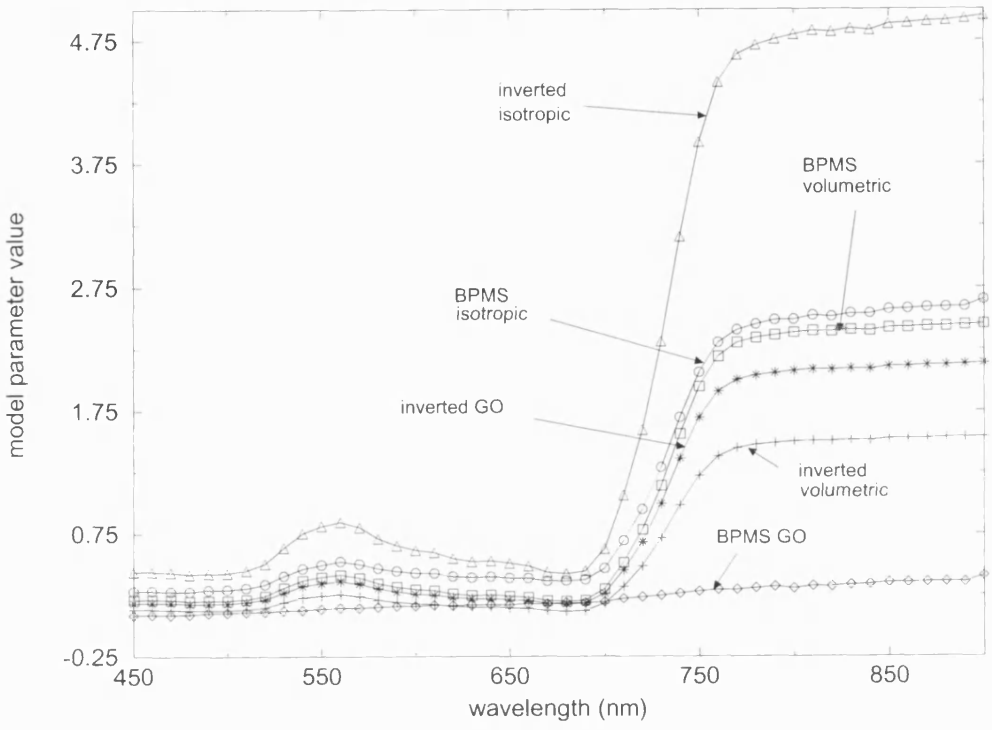

c) barley - 4th June

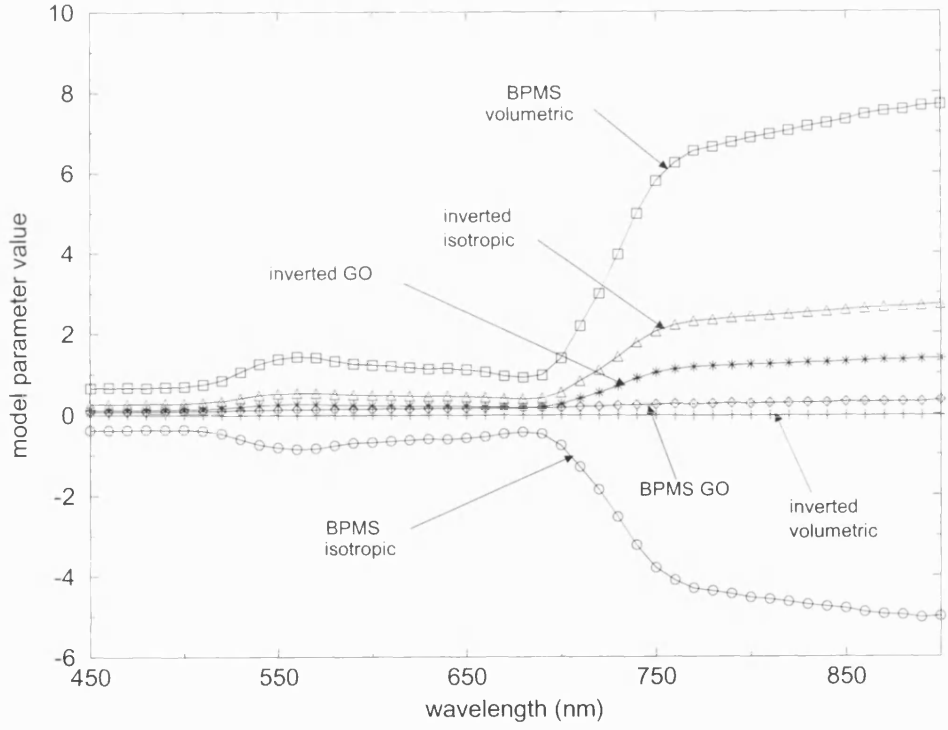

d) barley - 24th June

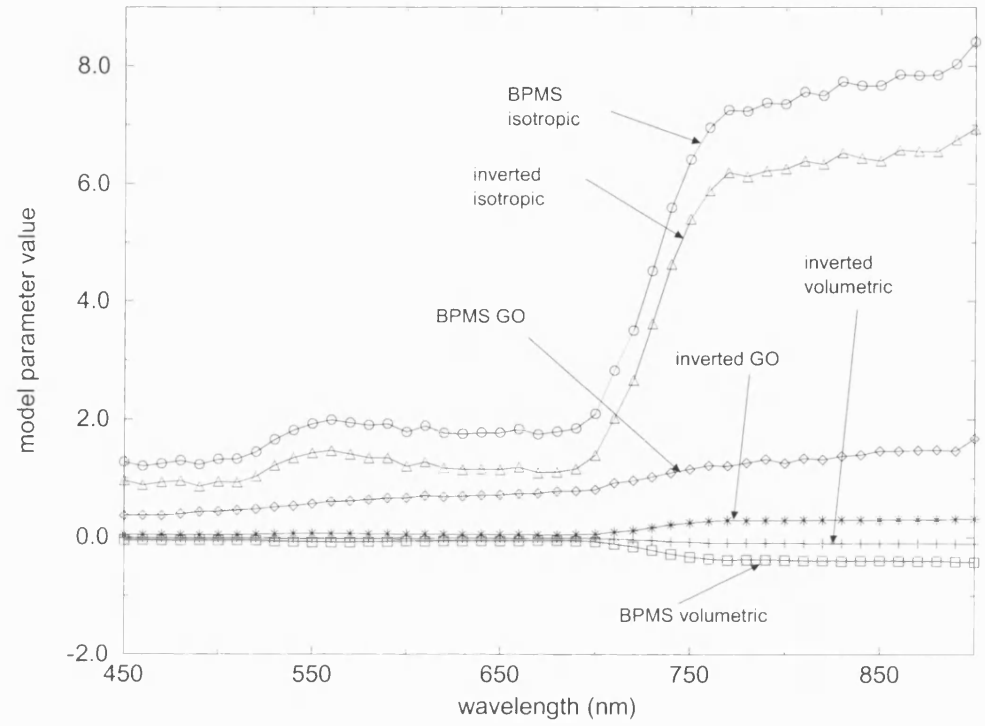

e) wheat - 23rd March

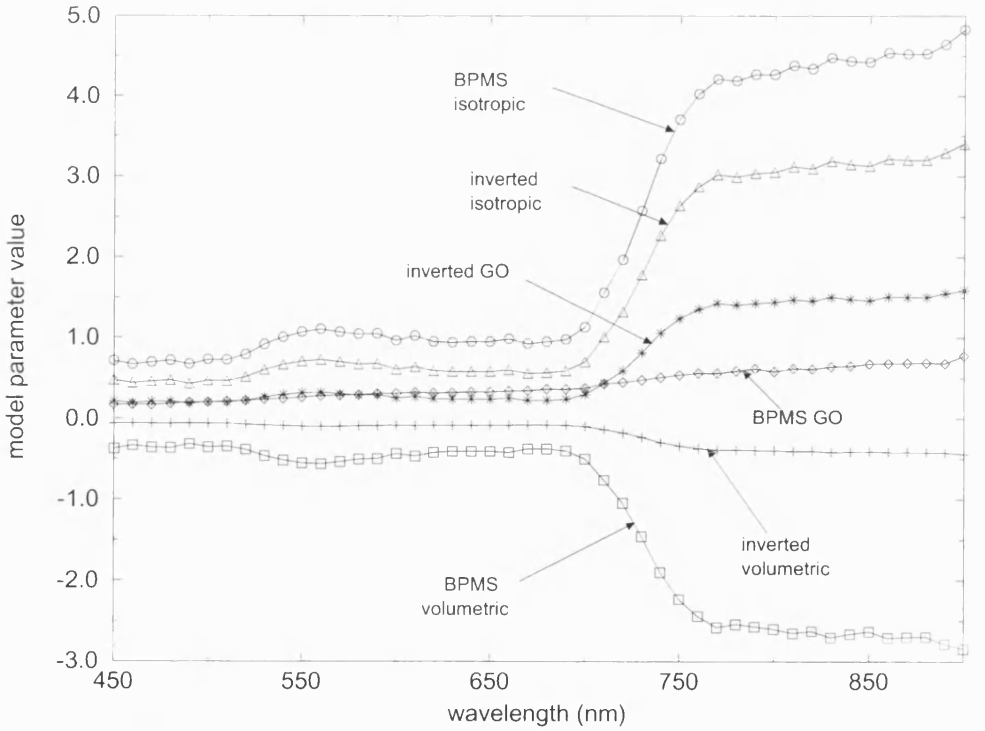

f) wheat - 23rd April

6.4 Discussion

Figures **6.3** and **6.4** show comparisons of the isotropic, volumetric and GO parameters (f_{iso}, f_{vol} and f_{GO}) obtained from:

i) Substituting values of $a_{vol,GO}$ and $b_{vol,GO}$ (derived from relating the volumetric and GO components of BPMS-simulated ρ_{canopy}, α and β, to k_{vol} and k_{GO}) along with selected ρ_{leaf} and ρ_{soil} back into equations **6.2a-c** (in essence 'calibrating' the kernels to each canopy under consideration).

ii) Inversion of a full linear kernel-driven BRDF model against values of ρ_{canopy} derived by substituting values of $a_{vol,GO}$, $b_{vol,GO}$, ρ_{leaf} and ρ_{soil} into equation **6.1**. Inversion in this case is performed fitting three kernels (isotropic, volumetric, GO) to the BPMS-simulated values of ρ_{canopy} by the standard linear (matrix) inversion methods described in **2.4.1**. Inversion is performed against values of ρ_{canopy} simulated at all θ_v (-70° to 70°), θ_i (0°, 30°, 60°) and ϕ_{row} (0°, 45°, 90°).

The aim of this is to establish what information might be contained within the model parameters, f_{iso}, f_{vol} and f_{GO}. This has implications for how the inverted kernel-driven model parameters are used in practice and what information they can be expected to yield. Results for each canopy are discussed separately in turn in sections **6.4.1** to **6.4.6**. In general terms however, the correlation between the two sets of parameters is very high as would be expected (values of the correlation coefficient higher than 0.95 in all cases). The main discrepancy is a tendency for the inverted GO parameter to 'flip' negative sometimes, in a mirror image of the BPMS-derived value. This is discussed below.

6.4.1 Barley canopy, 18th April

For the isotropic, RossThick, LiSparse kernel combination the two sets of parameters agree well, particularly in the visible, with some divergence in the near IR. Both estimates of f_{iso} are relatively small in magnitude and spectrally 'flat', with a small rise in the near IR. The largest spectral variation by far is in f_{vol}. The volumetric

component of ρ_{canopy}, α, is proportional to the $1-e^{-LAI}$ term in equation **4.2**, but the spectral shape indicates that α is also a function of ρ_{leaf} (the leaf-scattering phase function $P(\theta_i,\theta_v,\phi)$ and the leaf projection function $G(\theta_i,\theta_v,\phi)$ are both geometric terms i.e. not a function of λ). Both estimates of f_{vol} exhibit spectral variation: very low reflectance at visible wavelengths due to chlorophyll absorption including a peak in the visible green centred at around 560nm, and a large increase of reflectance across the red edge from the visible to the near IR wavelength regions at around 700-800nm. The form of f_{vol} in figures **6.3** and **6.4** follows exactly the form of ρ_{leaf} shown in figure **6.2**. This is unsurprising as α is defined as the component of ρ_{canopy} due to scattering from vegetation (equation **4.3**). It is independent of ρ_{leaf} (a geometric parameter only) but the insertion of the spectra described above re-introduces this dependence. The degree of correspondence of f_{vol} to ρ_{leaf} effectively defines the degree of dominance of the volumetric component of ρ_{canopy} by scattering from vegetation, and is a further indicator of the fact that ρ_{canopy} can be separated into volumetric and GO components.

In contrast f_{GO}, controlled by the amount of visible sunlit and shadowed soil, shows little spectral variation (compared to the assumed soil spectrum, ρ_{soil}, of figure **6.2**). The relation between the spectral variations of f_{vol} and f_{GO} and the spectral components of ρ_{canopy}, ρ_{leaf} and ρ_{soil}, suggest that model parameter estimates of this sort may well be useful for spectral discrimination of cover types i.e. classification. In such an application, the absolute values of the parameters are unimportant but the relative magnitudes could be used to map spatial distribution of volumetric and GO scattering components (equivalent to vegetated and non-vegetated regions). This is of consequence in applications where estimates of total vegetation amount are required, such as in analysis of carbon budgets and net primary productivity.

The isotropic, RossThin and LiDense kernels (figure **6.4a**) are almost an order of magnitude smaller than for the previous case, with k_{vol} barely rising to 1, as opposed to around 5.5 above. Values of f_{vol} still agree within a few percent but there are discrepancies between the BPMS-derived and inverted isotropic parameters in the visible region, with the inverted parameter showing a distinct "vegetation-like" rise in magnitude from the visible to the near IR. The same is true of the inverted f_{GO}, unlike the BPMS-derived f_{GO}, which closely resembles the ρ_{soil} of figure **5.2**. This suggests that perhaps f_{iso} and f_{GO} are describing some of the scattering due to vegetation that is not being explained

by f_{vol}. This would also explain why the contrast between f_{iso}, f_{GO} and f_{vol} in the near IR is not as great as would be expected. This combination of kernels is not as effective at describing ρ_{canopy} as the previous one, although in this case f_{GO} follows ρ_{soil} more closely than in the previous case. As in chapter **5** this adds further weight to the choice of the isotropic, RossThick and LiSparse kernel combination for inversion against reflectance data where no *a priori* knowledge of cover type is assumed (Hu *et al.*, 1997; Wanner *et al.*, 1997).

6.4.2 Barley canopy, 13th May

The trends in the inverted isotropic, RossThick plus LiSparse model parameters for the 13th May barley canopy are similar to those of 18th April. Agreement in magnitude between the BPMS-derived and inverted parameters is very good, particularly f_{iso} (greater than 95%). Notable differences are the increased magnitude, particularly of the volumetric parameter (maximum of nearly 8 as opposed to 5.5 for 18th April), the 20% increase in magnitude of the BPMS-derived volumetric parameter over the inverted volumetric parameter in the near IR, and the clear rise of the isotropic parameters across the red edge. This last factor again suggests that some of the variation due to volume scattering may be being taken up by f_{iso}. Both the f_{GO} are spectrally flat and very small in magnitude.

The isotropic, RossThin LiDense parameters for the 13th May are quite different (**6.4b**). The magnitudes are again much lower than for the isotropic, RossThick LiSparse combination, as was seen for the 18th April canopy (compare figures **6.3a** and **6.4a**). The f_{iso} show the greatest spectral variation, increasingly resembling the volumetric parameter in figure **6.3**. In addition, the BPMS-derived GO parameter, still relatively flat, differs markedly from the inverted GO parameter, which is much closer in appearance to the inverted volumetric parameter. These observations suggest that **if non-optimal kernel combinations are selected, the information content of the model parameters becomes increasingly difficult to explain**.

6.4.3 Barley canopy, 4th June

The magnitude of both sets of parameters in the isotropic, RossThick, LiSparse combination increases again (figure **6.3c**) up to a maximum of between 8.5 and 11.5 for both f_{iso}. Both isotropic parameters again appear to explain some of the spectral variation due to scattering from vegetation. The inverted values of f_{GO} also display a slight increase with wavelength, but this is not true for the BPMS-derived k_{GO}. This may indicate that the parameter space of the full linear model inversion is larger than that for the parameter values derived using the estimates of $a_{vol,GO}$ and $b_{vol,GO}$, allowing spectral components of volumetric scattering to be spread across all three parameters rather than confined to one. The results presented in section **5.3** illustrate that in some cases the relationship between the GO component of ρ_{canopy}, β, and the GO kernels is not clear. It is predictable in these cases that the inverted model parameters are likely to describe a combination of both volumetric and GO components of ρ_{canopy}. Apart from the BPMS-derived GO parameter, all the parameters in figure **6.4c** (isotropic, RossThin, LiDense) except the BPMS-derived GO parameter show a sharp rise in magnitude across the red edge suggesting that the volumetric component increasingly dominates ρ_{canopy} as the canopy develops.

6.4.4 Barley canopy, 24th June

Results from this canopy are different again, as the canopy has matured and begun to senesce. The BPMS-derived values of f_{vol} still display the strong vegetation-like shape, but, in contrast to previous results, the inverted parameters do not follow this pattern at all and are very much lower in magnitude. The inverted f_{iso} is the only parameter which rises significantly above zero. It is perhaps ill-advised to attempt to explain the variations in this case as the canopy is now divergent from the assumptions made in the formulation of either the volumetric or GO kernels. It has already been shown that this divergence results in the inability of the linear kernel-driven models to describe the directional and spectral features of ρ_{canopy} adequately (see section **5.3.2**). This inability is strongly apparent in the results of the isotropic + RossThin + LiDense kernel combination for the same date (figure **6.4d**). The BPMS-derived isotropic parameter in this case has become virtually a negative reflection about the x-axis of the BPMS-derived volumetric parameter. The other parameters generally follow the same shapes as in the previous case.

6.4.5 Wheat canopy, 23rd March

Results from the isotropic + RossThick + LiSparse combination for the wheat canopy of March 23rd (figure **6.3e**) show a number of differences from the results of the barley canopies. The two isotropic parameters agree closely but are similar in shape and magnitude to the volumetric parameter of the barley canopies of 18th April and 13th May. However, both f_{vol} in this case are negative, with the BPMS-derived estimate of f_{vol} being a virtual reflection of both f_{iso} about the x-axis. This suggests the volumetric parameter is over-compensating for the vegetation element contained in the isotropic parameter. All other parameters are close to zero. Similarly, the isotropic + RossThin + LiDense combination has both isotropic parameters following closely the shape of ρ_{leaf} (in a similar manner to the behaviour of the volumetric parameter in the barley cases). This canopy is very sparse (LAI = 0.08) and the volume scattering component has been shown to be small (figure **4.5**). This further illustrates how scattering originating from one component of ρ_{canopy} may be 'taken up' by another parameter if the assumptions underlying the kernels are not met and/or an unsuitable combination of kernels is selected. The BPMS-derived GO parameter is similar in shape (and relative magnitude compared with f_{vol}) to ρ_{soil} which is less surprising, as it might be expected that ρ_{canopy} be dominated by ρ_{soil} with so little vegetation being present.

6.4.6 Wheat canopy, 23rd April

The behaviour of the isotropic, RossThick and LiSparse parameters for this canopy are similar to those of the previous wheat case, with an exaggeration in magnitude. Both isotropic parameters are (relatively) high and similar in shape to ρ_{leaf}, although agreement between the two is less than for the previous wheat canopy, particularly in the near IR where the BPMS-derived parameter is significantly higher than the inverted parameter. As the volumetric component of ρ_{canopy} increases from 23rd March to 23rd April, differences between the two sets of parameters become more apparent. The BPMS-derived and inverted volumetric parameters are both negative as in the 23rd March case but even more so, suggesting over-compensation during inversion. In terms of shape and magnitude the inverted estimates of the GO parameter lie somewhere between the inverted isotropic and the BPMS-derived GO parameter, which is close to zero across all

wavelengths. This is due to the structure of the wheat canopy. It has been shown that this canopy has a somewhat different structure from the other canopies in this experiment, with a strongly erectophile LAD (figure **4.8**). If θ_v departs significantly from nadir, very little soil will be visible to the viewer (see figure **4.7**). In this case, scattering from the canopy (under the assumption of single scattering interactions only) will be dominated by the component originating from the vegetation alone.

Results from the isotropic + RossThin + LiDense kernel combination (figure **6.4f**) are even more variable than for the various barley canopies. Both isotropic parameters are similar in shape to the parameters inverted from the isotropic + RossThick + LiSparse kernel combination for this canopy (figure **6.3f**) with the BPMS-derived parameter being similar in magnitude and the inverted isotropic parameter being significantly lower. The GO parameters also show similar behaviour but with the BPMS GO parameter rising above zero in this case. The volumetric parameters in both cases are negative.

6.4.7 Summary

Results show that there is good agreement in some cases between the two sets of model parameters - those derived from inversion of a full kernel-driven model against ρ_{canopy} and those derived from regression of the BPMS-derived reflectance components α and β against the separate volumetric and GO kernels. However, agreement is not always good and for some canopies the two parameter sets differ markedly, notably when the BPMS parameters turn negative. Table **6.1** shows values of r^2 for the two sets of f_{iso}, f_{vol} and f_{GO} parameters. In each case, the values are given from the isotropic + RossThick + LiSparse kernel combination and the isotropic + RossThin + LiDense kernel combination.

As the barley canopy develops, the parameters (including the isotropic parameter, f_{iso}) increasingly resemble ρ_{leaf}. This indicates the parameters are not limited to dependence on purely geometric terms as intended (if this were the case, we would expect f_{vol} to resemble leaf, f_{GO} to resemble soil, and f_{iso} to be spectrally flat). The relative magnitude of the parameters generally varies as expected, with the volumetric parameter (and to an extent the isotropic parameter) increasing with LAI relative to the GO parameter but at the expense of increased coupling. As the canopy departs from

assumptions underlying the kernels (geometrically and radiometrically) the parameters become negative, or become coupled. This is most obvious in the case of the wheat canopy of 23rd April, which has a strongly erectophile LAD. Discrepancies between the two sets of parameters also become more apparent in the barley canopy as it develops, particularly for the 24th June case (figures **6.3d** and **6.4d**) which least resembles the assumptions made in the kernel-driven models. In the case of the isotropic + RossThick + LiSparse kernel combination, the BPMS isotropic parameter is far larger then the corresponding inverted isotropic parameter, in fact larger than all other parameters by far. For the isotropic + RossThin + LiDense kernel combination, the BPMS isotropic parameter turns negative, indicating an unsuitable choice of kernels.

Table 6.1 r^2 values for BPMS-derived against inverted values of f_{iso}, f_{vol} and f_{GO}.

	Values of r^2 for correlation (BPMS v inverted)					
	Isotropic RossThick LiSparse			Isotropic RossThin LiDense		
Canopy	f_{iso}	f_{vol}	f_{GO}	f_{iso}	f_{vol}	f_{GO}
barley 18/4	0.99	0.99	-0.88	0.98	0.99	0.89
barley 13/5	0.99	0.99	0.95	0.99	0.99	0.95
barley 4/6	0.99	0.99	0.94	0.99	0.98	0.94
barley 24/6	0.96	0.99	0.96	-0.99	-0.99	0.96
wheat 23/3	0.99	0.98	0.95	0.99	-0.99	0.95
wheat 23/4	0.99	0.98	0.95	0.99	-0.99	0.95

6.5 Implications of coupling between model parameters

It is clear from results presented above (and previously) that the volumetric and GO components of ρ_{canopy} are separable in many cases. However, it is also clear that as a canopy develops and the magnitude of the respective volumetric and GO parameters increases (particularly k_{vol}), observed behaviour departs from that which might be expected if the components were completely separable. The relationships between α and k_{vol} and β and k_{GO} presented in chapter **5** show that a proportion of both the volumetric and GO components of ρ_{canopy} are not described by the corresponding kernel: the relationships are not perfectly linear by any means. There is a possibility that a residual

part of the volumetric component, α, not described by k_{vol} may be described by k_{GO}, and conversely, some proportion of the GO component, β, may be explained by k_{vol}. As an example, the rise of the volumetric parameter across the red edge for the barley canopies of 13th May and 4th June and the wheat canopy of 23rd April are coupled to a similar increase in the GO parameter (figures **6.3** and **6.4**). Clearly α is not completely described by k_{vol}; the GO parameter, f_{GO}, also contains information related to α. From equation **4.2**, for a given (θ_i, θ_v, ϕ), α is proportional to $(1-e^{-LAI})$ (all other terms in equation **4.2** being purely dependent on θ_i, θ_v, ϕ). From equation **4.2** it can also be seen that the spectral variation of the volumetric component of ρ_{canopy} is controlled by ρ_{leaf}. In all cases, the accuracy with which the kernels can describe ρ_{canopy} will be dependent on angular sampling (Lucht and Lewis, 2000). In the experiments presented in this thesis ρ_{canopy} can be simulated at arbitrary (θ_i, θ_v, ϕ) as required and consequently angular sampling is not an issue. However, in practice the impact of poor angular sampling will compete with (and possibly outweigh) the coupling of volumetric and GO parameters to reduce the kernels' ability to describe ρ_{canopy}.

Having shown in chapter **5** that it is possible (in the main) to isolate the geometric factors controlling ρ_{canopy} through wavelength-independent simulations, the results of the previous section present spectrally varying estimates of model parameters. It is immediately obvious from figures **6.3** and **6.4** that α is proportional to ρ_{leaf}. This implies that the geometric and spectral parts of the volumetric component of ρ_{canopy} are linked. The question is whether they are inextricably linked. If so, it may not be possible to invert parameters such as LAI directly from reflectance data as the geometric factors are likely to be coupled to spectral information (i.e. ρ_{leaf}). In order to separate LAI from a coupled $\rho_{leaf}(1-e^{-LAI})$ term, an estimate of ρ_{leaf} would be needed. A requirement for ancillary data of this sort potentially limits the use of inverted biophysical parameter information unless: (i) ρ_{leaf} data are available; or (ii) *a priori* assumptions are made regarding the cover types over which such models are applied. Option (i) is generally not practical if specific ρ_{leaf} data are required, simply because of the variety of vegetation types and the scarcity of high quality field-measured spectral reflectance data. Option (ii) is not desirable given that one purpose of the linear kernel-driven approach is to allow application of models to reflectance data of arbitrary cover types, at a range of scales (neglecting adjacency effects). In relation to (i) above it should be noted however that it is clear that most (if not

all) green ρ_{leaf} spectra share many attributes, namely a maxima of reflectance at visible green wavelengths, a minima in the visible red, and a sharp rise across the NIR region. The possibility that this can be exploited, in a manner similar to the generalisation of BRDF shape made in the linear kernel-driven models, is explored in chapter **7**. At any rate, evidence presented here and in chapter **4** demonstrates that inverted parameters from reflectance data must be interpreted carefully if they are to be used directly (rather than for deriving integrated parameters such as albedo, or for classification).

If such parameter coupling is significant, then we might expect that the data used in chapter **4** to explore the relationships between i) k_{vol} and α, and ii) k_{GO} and β, would show two distinct dimensions of information related to the two components of scattering behaviour. These data are the (supposedly) separate volumetric and GO scattering components of BPMS-simulated ρ_{canopy}, α and β. If canopy information is not coupled, α will describe only volumetric scattering, and β will describe only GO scattering, as defined in equation **4.1**. If there is coupling however, each component of ρ_{canopy} will contain information related to the other. In order to examine this possibility, principal component analysis (PCA) was performed on the respective combinations of α and k_{vol} and β and k_{GO}. PCA allows a set of correlated observations to be transformed to a set of uncorrelated (principal) components (pcs) by calculating the eigenvectors and eigenvalues of the variance-covariance matrix of observations (Jolliffe, 1986). The percent variance in the data described by each pc is simply the corresponding eigenvalue, scaled by the sum of all eigenvalues. In this case, the magnitudes of the first two principal components will indicate the relative importance of the scattering components. If α describes only the volumetric component of canopy scattering, it would be expected that pc1, the first principle component, would be completely dominant, with pc2 having a far lower magnitude. The same argument applies to β and k_{GO}. If there is significant coupling in either case however, it would be expected that the magnitude of pc1 and pc2 might be comparable. Results of the PCA are presented in figure **6.5**. Results are presented for the simulations carried out with $\phi_{row} = 0^{\circ}$, for all three values of θ_i i.e. 0°, 30°, and 60°.

The main feature of the results presented in figure **6.5** is that in all cases the first principal component is always larger than the second. This indicates that in each case there is a "dominant" component to the observed variance in the data. This is particularly true for the volumetric component of the early barley canopies, where pc1 of the

volumetric components (represented by the RossThick of RossThin kernels) rises as high as 99% (hence pc2 = 1%). In these cases nearly all the variance in α is explained by k_{vol}, and it is safe to assume that coupling is minimal. The case for β is not quite so clear cut, with pc1 for the various k_{GO} falling to between 60% and 70% in many cases, and down to almost 50% for the 23rd April wheat canopy. In this case there is significant variation in β which is not being explained by k_{GO}. This supports the results presented in section **5.3** where the relationship between β and k_{GO} is not demonstrably linear as was the case for α and k_{vol}.

A second feature of figure **6.5** is the variation in the magnitude of the principal components with θ_i. For the 18th April barley canopy, pc1 for the RossThick kernel starts at 85% for $\theta_i = 0^o$, rises to 96% for $\theta_i = 30^o$, and again to 98% at $\theta_i = 60^o$. There is even more variability for the various k_{GO}. The respective pc1s are virtually identical for $\theta_i = 0^o$ at 98%, except for the LiSparse kernel, where pc1 = 85%. For $\theta_i = 30^o$ there is a variability between the kernels in the magnitude of pc1 of around 20%, and by $\theta_i = 60^o$, they have fallen again to around 70%. This is the opposite trend to that observed for α.

Figure 6.5 Principal component analysis of the separate α and β components of ρ_{canopy} for barley (four dates) and wheat (two dates).

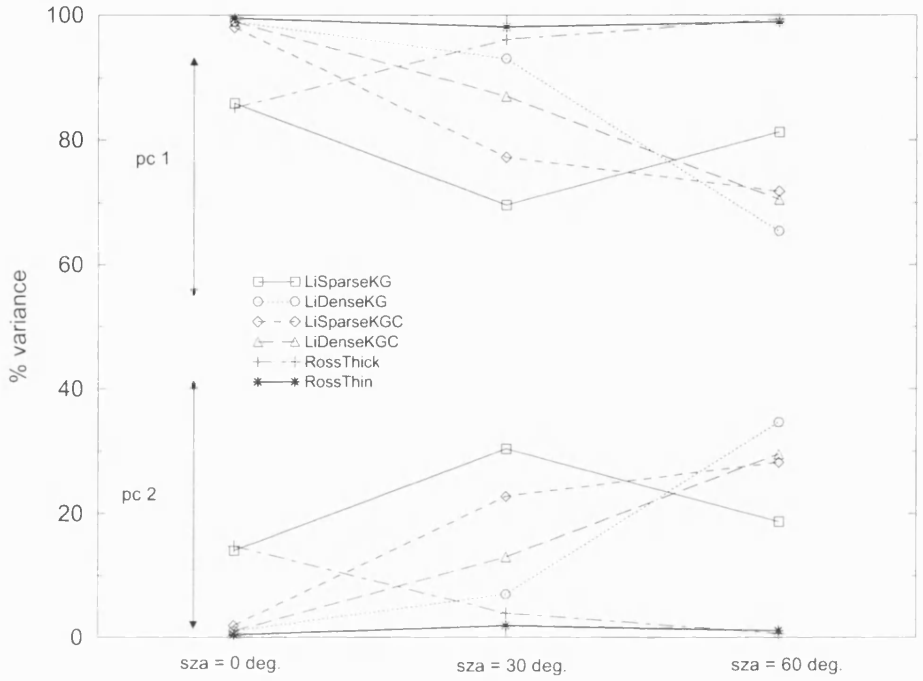

a) barley - 18th April

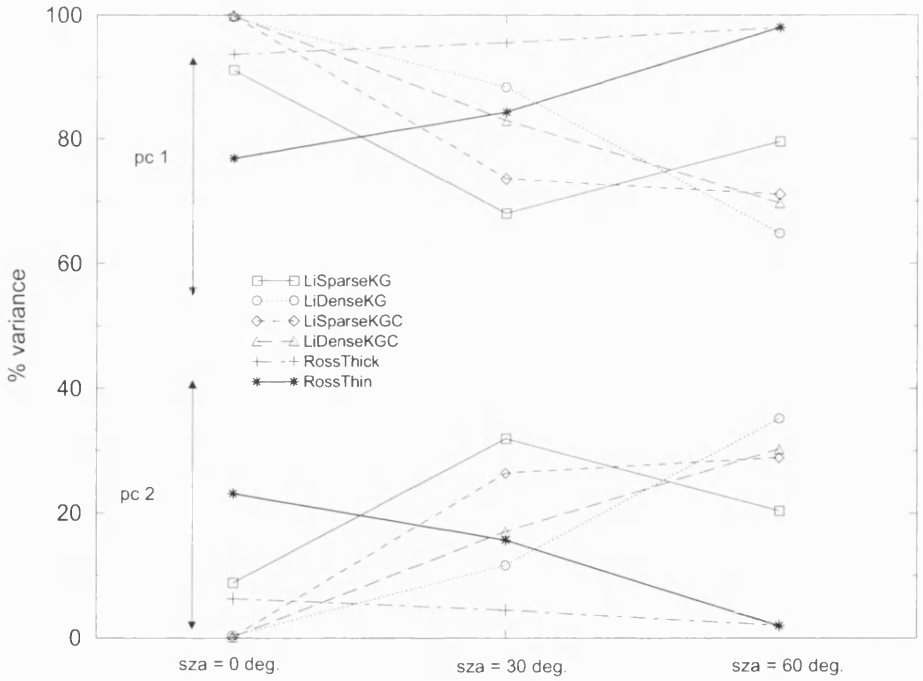

b) barley – 13th May

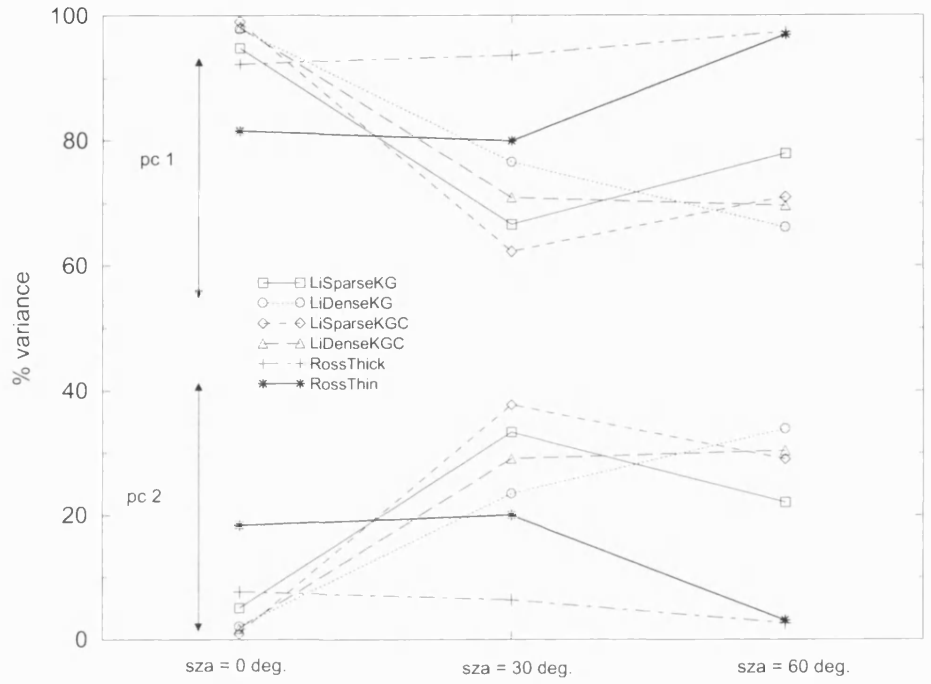

c) barley - 4th June

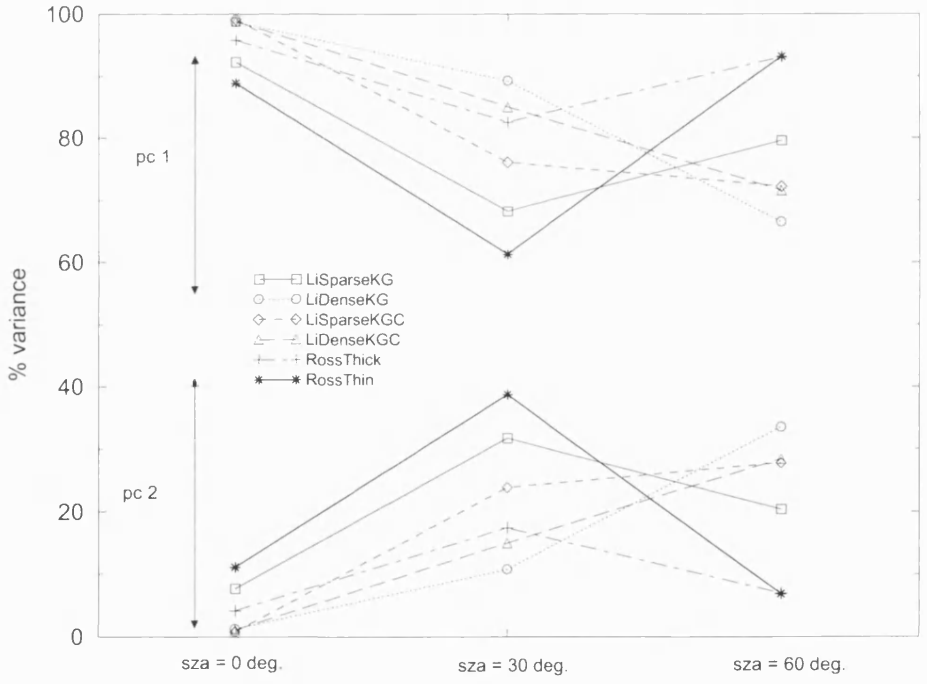

d) barley - 24th June

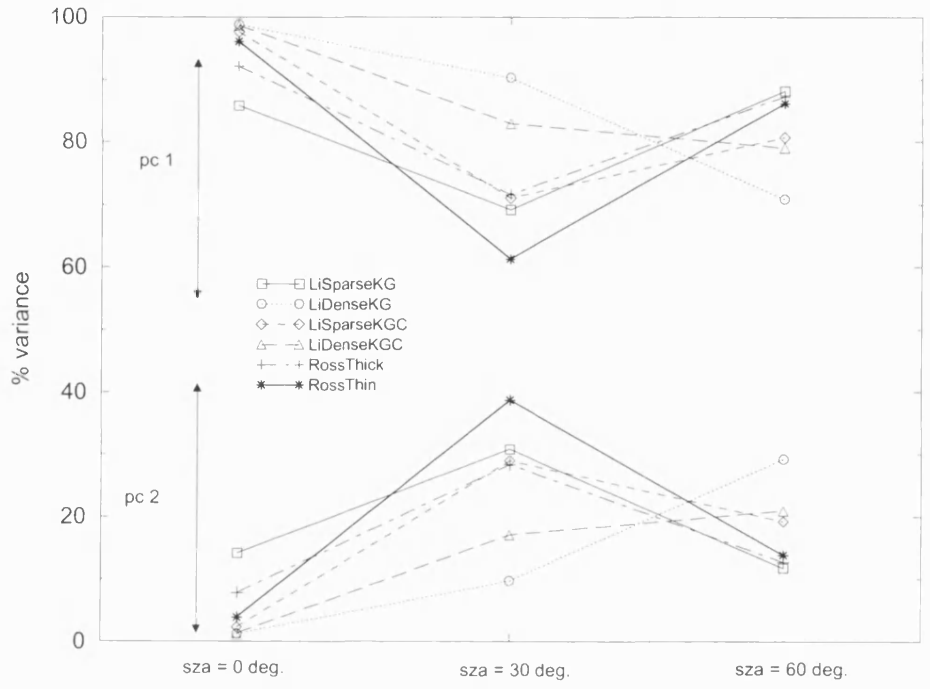

e) wheat - 23rd March

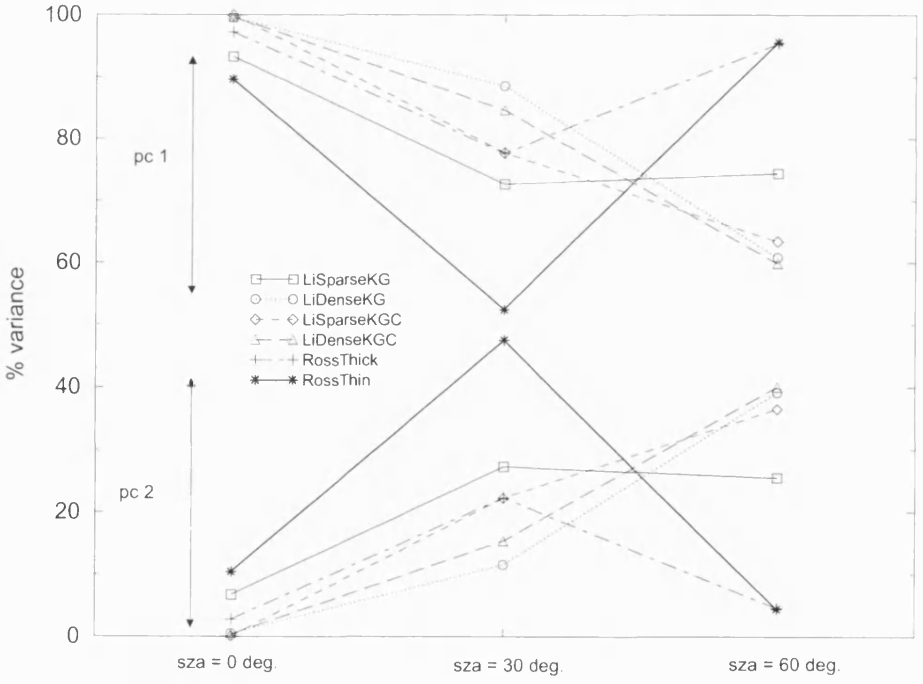

f) wheat - 23rd April

The trends observed in figure **6.5** of both the magnitude of pc1 for α and β, and the variability with θ_i are broadly similar for all the canopies under investigation. The major differences lie in the spread of points, with the more developed canopies having lower values of pc1 (and correspondingly higher pc2). For the 23rd March wheat canopy where very little vegetation is present, pc1 and pc2 of α are relatively close, implying that there is no dominant "dimension" of the data to be explained by k_{vol}. This agrees with the results presented in section **5.2**.

For nearly all canopies the volumetric component has lower pc1 for $\theta_i = 0^o$ than the GO component, and higher pc1 for $\theta_i = 60^o$. In all cases except the barley canopy of 18th April, α is better described by the RossThick kernel. For β there is considerable variation with θ_i within each canopy, but from one canopy to the next the pattern is the same: pc1 of β starts high for all kernels except LiSparse, then falls for $\theta_i = 30^o$, where in all cases the LiDense canopy explains the most variance; pc1 falls again to $\theta_i = 60^o$ where the LiSparse kernel performs the best. The consistency from one case to another suggests that the choice of kernel is more important than the variability of the data.

Conclusions to be drawn from the results presented above are simply that in most cases there is good reason to believe that ρ_{canopy} can be separated into volumetric and GO components. The caveat is that under certain where either the assumptions of the kernels are not met (as is the case in these experiments) or an unsuitable choice of kernels is used, this is not necessarily the case and care must be taken. In the canopies studied here the volumetric component tends to dominate ρ_{canopy}, except in cases where the canopy is extremely sparse. The RossThick kernel tends to explain most variance in the volumetric component of ρ_{canopy}, while the LiSparse kernel explains most variance in the GO component. The results for the GO kernels are less conclusive than those for the volumetric kernels.

The RossThick LiSparse kernel combination has been chosen for operational use as it appears to be the best at describing reflectance irrespective of surface, allowing it to be applied without *a priori* knowledge of cover type. However this disguises the fact that over cover types where the assumptions underlying the kernels are not met, the RMSE of fit may not be significantly worse, yet the inverted model parameters are likely to have some very different, coupled meaning.

New techniques are being developed to alleviate this situation. Strugnell and Lucht (2000) have implemented a LUT relating land cover classes to field-measured BRDF shapes. The shapes of these measured class "archetypes" - BRDFs representative of each land cover class, are used to constrain the inversion of linear BRDF models against measured data. The assumption is made that BRDFs of cover types lying within a particular class will typically be closely related in shape with intra-class differences being one of magnitude rather than shape. By contrast, whilst unrelated cover types may have very similar spectral reflectances, their respective BRDFs will tend to differ as the underlying structure of the cover types is likely to be different. This use of existing knowledge of BRDF shapes of different cover types may be one way in which to inform the inversion of biophysical parameter information from linear models such that the most (physically) appropriate kernel combination is selected wherever possible. This method has been implemented for the initial surface reflectance and albedo products from MODIS. This so-called "magnitude inversion" method is used where insufficient angular samples of reflectance are available over a given 16-day period to permit a full inversion (the uncertainty is reflected in the associated QA information). A modification to the method of selecting appropriate kernel combinations for production of albedo where sufficient angular samples are available has recently been proposed. Gao *et al.* (2001) use least variance of white-sky albedo (bihemispherical reflectance) to select kernel combinations, rather than conventional least-squares fitting as proposed previously. Least variance of white-sky albedo appears to be a more effective way of selecting kernel combinations than RMSE, particularly when angular sampling is non-optimal which it will be in many situations. White-sky albedo also has the advantage that, as an integral of directional reflectance over the viewing and illumination hemisphere rather than an angular measure, it is an intrinsic surface property. Variance of observed white-sky albedo is a function of measurement noise, angular sampling and the number of observations. It is therefore a direct indication of the quality of any particular set of reflectance observations used to generate a retrieved albedo value. This can be compared with the constrained model inversion discussed in appendix **1**, based on specifying that reflectance and directional hemispherical reflectance should lie between physically realistic limits (0 to 1).

6.6 Implications of negative model parameters

The negative values of the isotropic and volumetric model parameters seen in the 24th June barley and 23rd April wheat canopies raises the issue of what such negative model parameters mean and how they arise. In a physical sense a negative model parameter is meaningless: there cannot be negative volumetric or GO scattering, or by extension (and from energy conservation), negative reflectance. It is clear from these results however, and from other work (Disney *et al.*, 1997; Hobson *et al.*, 1999; Grant, 2000) that negative parameters can and do occur in practice. They arise as a result of the inversion process, with one parameter over-compensating for another in a case where reflectance is poorly described by the chosen kernel combinations. This implies that the correct choice of kernels may determine whether model parameters obtained through inversion have any physical meaning.

Practically, a better fit to measured reflectance data is generally obtained by allowing parameters to go out of physical bounds (i.e. to go negative) in order to compensate for the inability of the kernel combination to describe the shape of ρ_{canopy}. One or more parameters being out of physical bounds indicates that the kernel combination is fundamentally unable to describe the surface reflectance. Different approaches can be applied to this problem depending on the use to which the parameters are to be put. Negative model parameters may mean there is simply not enough information in the reflectance signal to provide an unequivocal solution to model inversion. In this situation, known as overfitting (Gershenfeld, 1999) the model has too much flexibility (too many free parameters) and can fit the data in a way that will not provide a physically meaningful solution. If inverted model parameters are to be interpreted directly e.g. for deriving LAI or crown density say, it may be appropriate to reduce the number of kernels (and hence model parameters) in order to reduce the number of degrees of freedom of the inversion and recalculate the parameter values. This was carried out for two of the canopies in figures **6.3** and **6.4** for which negative model parameters were obtained from the full linear model inversions (24th June barley and 23rd April wheat). Scatter plots showing the comparisons of the isotropic, volumetric and GO parameters, obtained from inverting two kernels with the corresponding parameters obtained from the three inverting kernels are presented in figures **6.6** and **6.7**.

The scatter plots of figures **6.6** and **6.7** are laid out as follows:

Figure **6.6a** (24th June barley canopy)

- isotropic (isotropic + RossThick) v isotropic (isotropic + RossThick + LiSparse)
- isotropic (isotropic + RossThin) v isotropic (isotropic + RossThin + LiDense)
- isotropic (isotropic + LiSparse) v isotropic (isotropic + RossThick + LiSparse)
- isotropic (isotropic + LiDense) v isotropic (isotropic + RossThin + LiDense)

Figure **6.6b** (24th June barley canopy)

- volumetric (isotropic + RossThick) v volumetric (isotropic + RossThick + LiSparse)
- volumetric (isotropic + RossThin) v volumetric (isotropic + RossThin + LiDense)
- GO (isotropic + LiSparse) v GO (isotropic + RossThick + LiSparse)
- GO (isotropic + LiDense) v GO (isotropic + RossThin + LiDense)

Figure **6.7a** (23rd April wheat canopy)

- isotropic (isotropic + RossThick) v isotropic (isotropic + RossThick + LiSparse)
- isotropic (isotropic + RossThin) v isotropic (isotropic + RossThin + LiDense)
- isotropic (isotropic + LiSparse) v isotropic (isotropic + RossThick + LiSparse)
- isotropic (isotropic + LiDense) v isotropic (isotropic + RossThin + LiDense)

Figure **6.7b** (23rd April wheat canopy)

- volumetric (isotropic + RossThick) v volumetric (isotropic + RossThick + LiSparse)
- volumetric (isotropic + RossThin) v volumetric (isotropic + RossThin + LiDense)
- GO (isotropic + LiSparse) v GO (isotropic + RossThick + LiSparse)
- GO (isotropic + LiDense) v GO (isotropic + RossThin + LiDense)

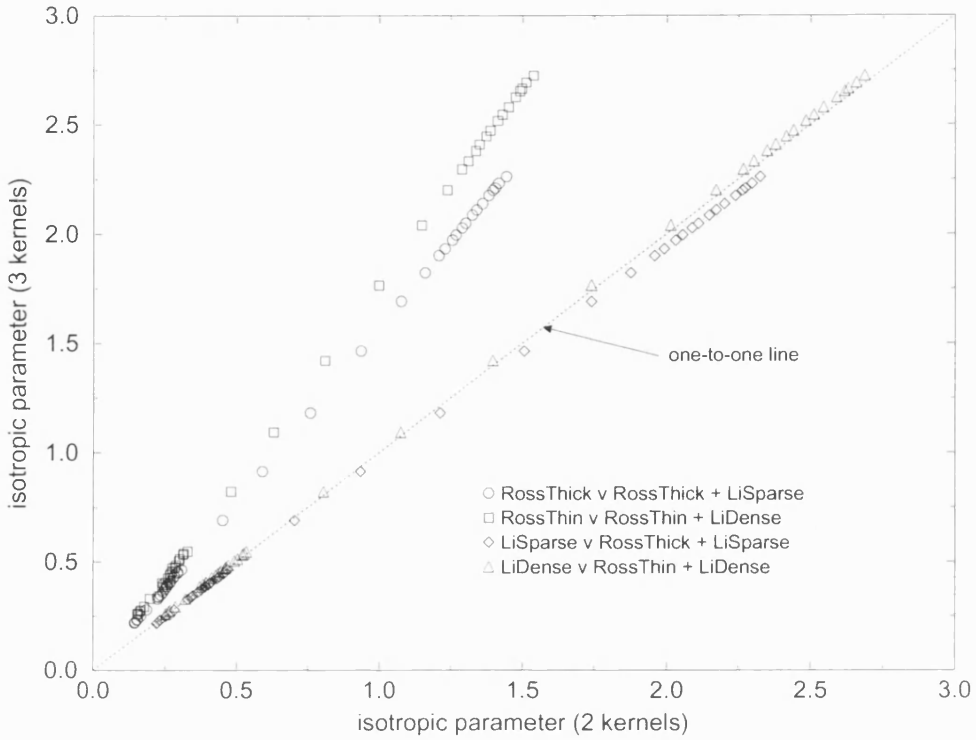

a) 2 kernel v 3 kernel isotropic parameters.

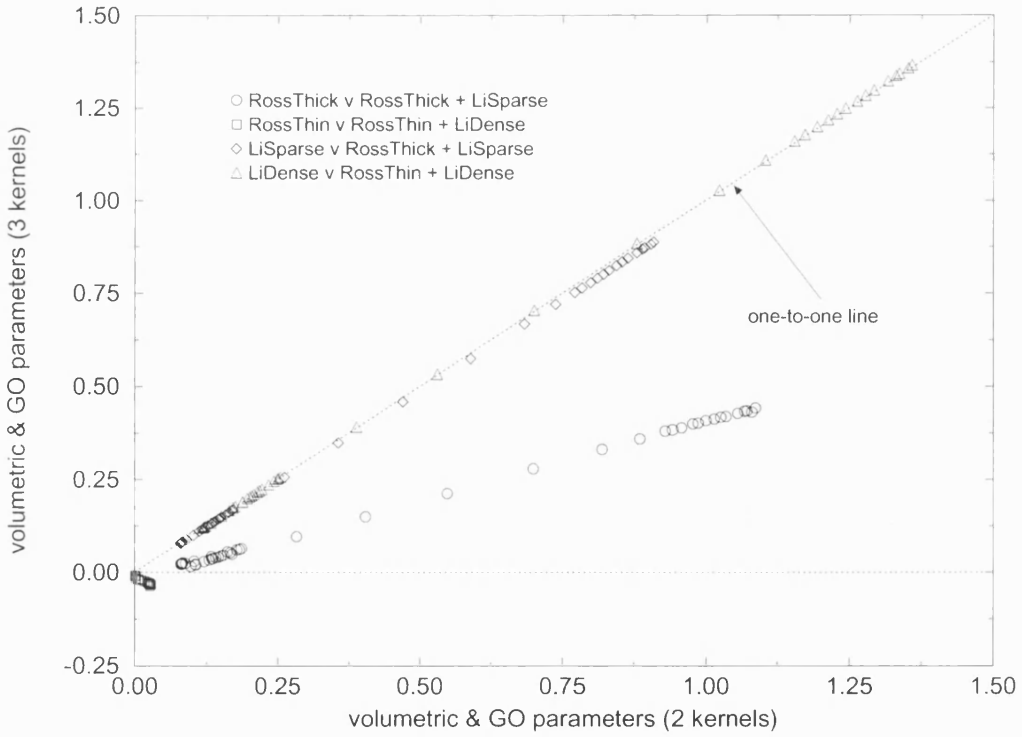

b) 2 kernel v 3 kernel volumetric and GO parameters.

Figure 6.6 Comparison of model parameters from 2 and 3 kernel inversions, 24th June barley.

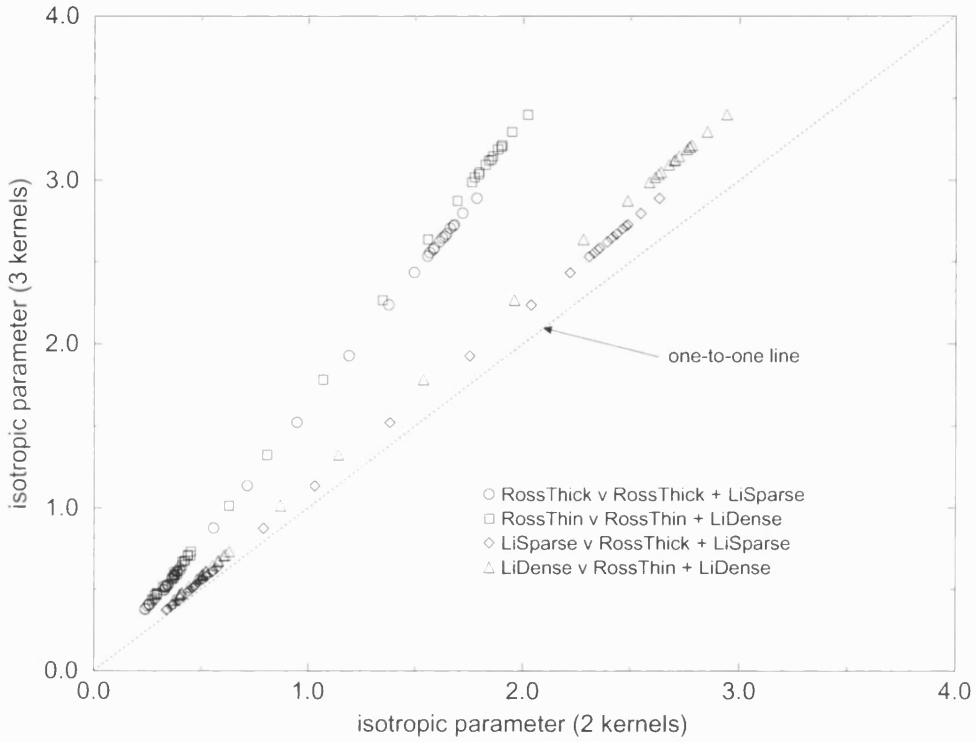

a) 2 kernel v 3 kernel isotropic parameters.

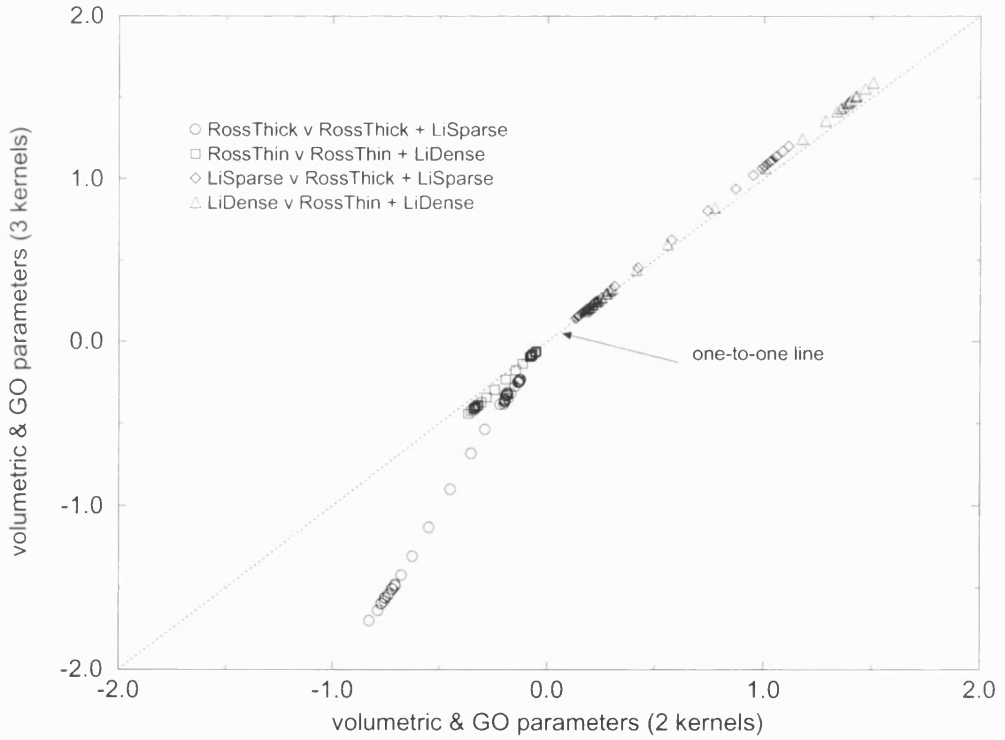

b) 2 kernel v 3 kernel volumetric and GO parameters.

Figure 6.7 Comparison of model parameters from 2 and 3 kernel inversions, 23rd April barley.

6.6.1 Discussion of two parameter inversions

Results presented in figures **6.6a** and **6.7a** show that where two kernels are inverted (isotropic and either k_{vol} or k_{GO}), the correlation with their three kernel counterparts is generally high in all cases, as would be expected. The differences are mostly ones of magnitude. The two kernel isotropic parameter is generally smaller than the three kernel version. The only exception to this is the isotropic parameter of the 24th June barley canopy (figure **6.6a**) derived from inversion of the isotropic + LiSparse kernel combination, which is slightly higher than the three kernel (isotropic + RossThick + LiSparse) isotropic parameter. Conversely, the volumetric and GO parameters from two kernel inversions are generally larger than their three kernel counterparts (figures **6.6b** and **6.7b**). In the case of the barley canopy the difference is only significant for the two kernel volumetric parameters. In this case the volumetric parameter obtained from inverting the isotropic + RossThick kernels is significantly larger than the three kernel volumetric parameter.

Most importantly, the volumetric parameter obtained from inverting the isotropic + RossThin kernels remains negative as it was in the original three kernel case (figure **6.4f**). Neither the two kernel (isotropic + RossThin) nor the three kernel (isotropic + RossThin + LiDense) combinations are capable of describing reflectance behaviour and these kernels are clearly inappropriate for this canopy. The two kernel GO parameters are virtually identical to the three kernel versions suggesting that a combination of an isotropic and a GO kernel (either LiSparse or LiDense) is sufficient to describe reflectance for this canopy. Similar behaviour is apparent for the wheat canopy of 23rd April (figure **6.7b**). In this case, both the two kernel volumetric parameters are negatively correlated with their three kernel counterparts (almost perfectly in the case of the parameter derived from inversion of the isotropic + RossThin kernel combination), while the GO parameters are very similar to the three kernel versions.

These results indicate that in cases where inverted model parameters are negative, using two kernels as opposed to three is not likely to help. Two kernels are apparently sufficient to describe directional reflectance behaviour in some cases, particularly when appropriate choices of kernels are made (i.e. for these canopies, not the RossThin and/or LiDense kernels). Both the RMSE of model fit and the expected error in the derived

model parameters are higher in the inversion of the two kernel combinations than in the three kernel case. This is to be expected as the model has fewer degrees of freedom, and is unable to fit the measured reflectance so accurately. If the parameter values are to be directly interpreted however, the validity of the inverted parameters is of greater importance than the overall RMSE of model fit. If on the other hand the parameters are to be used indirectly e.g. for classification as mentioned previously, the requirement for physical constraint of model parameters is less clear. In this case the parameters are being used to provide only an indication of the relative spatial variation in scattering behaviour. Results presented above support this statement, suggesting that the relative magnitudes and spectral shapes of the inverted parameters are representative of the types of scattering occurring within the canopy even if their absolute magnitudes may be not be physically realistic (and should not be interpreted).

In the operational processing of reflectance data using linear models, the inversion process can be constrained to prevent negative parameters arising, via the use of Lagrange multipliers for example (see appendix **1**). Constraints can also be imposed to ensure that products derived directly from model parameters such as directional-hemispherical and bihemispherical integrals of BRDF (so-called 'black-sky' and 'white-sky' albedos) lie within physically realisable limits i.e. between 0 and 1. Albedo values for given conditions of illumination and sky radiance can then be interpolated from these two limiting cases (Wanner *et al.*, 1995). As discussed above, this type of approach is being taken for the processing of the EOS MODIS data products (Schaaf *et al.*, 2000a,b; Gao *et al.*, 2001; Schaaf *et al.*, 2001a,b).

6.7 Conclusion

This chapter presents the results of experiments following on directly from those of chapter **4**, which demonstrated that (with caveats) ρ_{canopy} can be described as a linear combination of volumetric and GO scattering components. The experiments described in this chapter are designed to answer the second fundamental question regarding linear kernel-driven approach to modelling BRDF, namely whether the volumetric component of ρ_{canopy} completely described by the volumetric kernel, and the GO component by the GO kernel i.e. are they separable? The simple answer is "No", but with provisos.

Understanding this issue is vital to determining the information it may be possible to retrieve by inversion of semi-empirical kernel-driven models against measured reflectance data.

Isotropic, volumetric and GO model parameters ($f_{iso,vol,GO}$) were derived from ρ_{canopy} in two distinct ways: i) via substitution of the parameters derived from regressing the volumetric and GO scattering components of (BPMS-simulated) ρ_{canopy} against k_{vol} and k_{GO} (a and b in tables **5.1**, **5.2** and **5.3**) into equations **6.2b** and **c**, along with appropriate spectral estimates of ρ_{leaf} and ρ_{soil}; and ii) via inversion of a full linear kernel-driven model against ρ_{canopy} calculated from substitution of the values of a and b (tables **5.1**, **5.2** and **5.3**) back into equation **6.1**. This yielded **spectral** estimates of the **angular** model parameters. It was demonstrated that the volumetric and GO components of ρ_{canopy} are separable in some cases, with the volumetric parameter, f_{vol}, closely approximating the shape of the chosen ρ_{leaf}, and likewise f_{GO} and ρ_{soil}. If the components were not separable, we would not expect f_{vol} and f_{GO} to resemble ρ_{leaf} and ρ_{soil} respectively, but would expect f_{iso} f_{vol} and f_{GO} to (equally) resemble some combination of them. This is apparent in some cases, where a significant proportion of the scattering from the canopy (k_{vol}) is taken up by the GO parameter, f_{GO}. In all cases the isotropic parameter, f_{iso}, showed some component of both f_{vol} and f_{GO}, which is as expected. As the canopies developed the volumetric parameter came to more closely resemble the GO parameter implying that there is a degree of redundancy between the two kernels.

In order to examine the dimensionality of the separate components of ρ_{canopy} principal component analysis was performed on the volumetric and GO components. Results showed that the majority of the variance of each component was described by the corresponding kernel, as pc1 in most cases was often greater than 80% and in many cases greater than 95% (mean value pc1 was 81.6%). There was significant variation in the magnitude of pc1 with ϕ_{row}. This implies that for certain canopies (e.g. those with relatively strongly row azimuth variation such as managed forest stands, or developing crops) there can be significant coupling of the kernels. This is another important fact in assessing the usefulness of parameter information derived from model inversion. The RossThick and LiSparse kernels are able to explain the most variance of the volumetric and GO components of ρ_{canopy} respectively. This supports the choice of the isotropic, RossThick LiSparse kernel combination as a model for use in general BRDF applications.

The occurrence of physically impossible (negative) model parameters arising from inversion was investigated. Such values typically occur when there are more degrees of freedom in the model than there are dimensions to the data (e.g. ρ_{canopy} might only vary with in relation to two parameters, but three are used to try and describe it), or an inappropriate choice of kernels is used. In this case the model has too much freedom to fit the data and overfitting occurs. This is typical of an overdetermined system of more than N equations in N unknowns. Such a system can be very sensitive to small changes in the parameter values, particularly where measurement methods and approximations introduce noise into the parameter estimates (Twomey, 1996). This is the case for the inversion of semi-empirical BRDF models against measured reflectance data and the error inherent in inverted model parameters will be determined by the sampling strategy (Lucht and Lewis, 2000). The results presented here are all based on good angular sampling (in the solar principle plane, θ_v every 10^o and every 2^o around the hotspot). It is known that the linear kernel-driven models do not perform so well in cases where angular sampling is much poorer (Lucht and Lewis, 2000; Gao *et al.*, 2001). It was shown that in some cases, two kernels can describe reflectance nearly as well as three kernels, but the choice of kernels becomes crucial in determining whether model parameters are negative. Where inverting three kernels resulted in strongly negative model parameters, using two kernels did not appear to give much better results. However, where three kernels results in parameters which are just negative, using two kernels can result in positive (and more physically realistic) model parameters.

If inverted model parameters are to be used indirectly, for example in spatial classification, then physically unrealistic parameter values are not necessarily a problem, as the kernels may still contain information related to (spectral and directional) scattering behaviour, although this is not the case if overfitting occurs. If the parameters are to be used directly however, then the inversion should be reduced to a constrained model parameter space. In this case, a combination of an isotropic term (there will always be a "brightness" component of surface reflectance) and either volumetric or GO kernels with parameter values constrained to lie within physically realisable limits, will prove a better solution. The choice of kernel becomes important in this case and for the barley and wheat canopies, the RossThick volumetric and LiSparse GO kernels appeared to work much better, either separately (in combination with the isotropic kernel) or as a three kernel combination.

It has been shown that although the inverted model parameters contain biophysical information, it is likely to be coupled to a greater or lesser extent. Indeed, spectral estimates of the angular model parameters show the influence of ρ_{leaf} on the inverted parameter estimates. This characteristic reflectance shape is common to all types of green vegetation in the same way that BRDF shapes for certain surfaces have significant commonality. The next chapter explores the idea that it may be possible to develop a spectral analogue of the angular kernels in order to model spectral variations of observed reflectance. This would have particular use for interpolating and extrapolating limited spectral reflectance samples and could augment the angular kernels to provide a full spectral, directional kernel-driven model of ρ_{canopy}.

7 Development and application of spectral kernels

7.1 Introduction

The previous chapters have explored the detailed operation of the **angular** kernels in describing angular variations of canopy reflectance. Despite their approximate nature it is clear that they can be very successful in describing BRDF. The caveat is that care is required in order to interpret biophysical information contained in the model parameters. Importantly, the end result of providing a viable, working description of BRDF is promoted at the expense of physical accuracy (given the severely approximations nature the semi-empirical kernels). One reason for this is that the kernels were primarily designed with their integrated properties in mind, particularly for production of broadband albedo at moderate spatial resolutions, rather than for parameter retrieval and interpretation. They are intended merely to act as angular interpolants for limited samples of directional reflectance. As a result, the angular kernels take **no account** of spectral reflectance behaviour – they are independent of wavelength. Consequently, the analyses presented in chapters **4**, **5** and **6** were expressly undertaken to be independent of wavelength. Despite this, it was shown that the angular kernels *are* sensitive to spectral variations in reflectance behaviour.

Accurate estimates of albedo are required in order to characterise the shortwave energy fluxes at the Earth's surface, in particular for climate modelling. Land surface albedo is a measure of the proportion of incoming solar radiation reflected at the surface, and, more importantly, the quantity absorbed. As a result broadband albedo - across the spectral range of incoming solar radiation - is a lower boundary condition in models of global climate. However, albedo is generally parameterised in some way to overcome issues of measurement and spatial variability (Pinty *et al.*, 2000; Strugnell *et al.*, 2000). Henderson-Sellers and Wilson (1983) suggested that albedo is required to an accuracy of ±5% in order to be useful for climate studies. Sellers (1993) has since proposed a standard of accuracy in albedo measurements of ±2%. Given these constraints, the general insensitivity of the angular kernels to spectral variation, and the resulting limitation to production of narrowband estimates of albedo is clear. More than 40% of the total incoming solar energy lies in the visible to mid-IR region of the spectrum (0.35 and 0.7μm). In order to effectively describe surface energy fluxes, accurate estimates of albedo are required across this shortwave region (Justice *et al.*, 1998). Conversion of limited spectral samples of albedo to a single broadband value requires a number of

assumptions and approximations. As outlined in section **2.1.1**, spectral albedo can be convolved with the solar spectrum (Brest and Goward, 1987). In this case, albedo, α, is calculated as

$$\alpha = \int_{solarspectrum} p(\lambda)\alpha(\lambda)d\lambda \qquad \textbf{7.1}$$

where $p(\lambda)$ is the proportion of the total downwelling solar radiation at wavelength λ (dependent on current atmospheric state); and $\alpha(\lambda)$ is spectral albedo, derived from the integration (with respect to the viewing and illumination geometry, Ω and Ω') of the angular kernels. These integrated terms provide estimates of (spectral) directional hemispherical and bihemipsherical reflectance ($\overline{\rho}(\lambda,\Omega')$ and $\overline{\overline{\rho}}(\lambda)$ respectively). $\alpha(\lambda)$ is then a weighted sum of these two components, with the weights determined by the relative quantities of direct and diffuse illumination. A drawback of this method is that it relies on being able to characterise the current atmospheric state, and success or failure in this respect will largely determine the accuracy of the results (Lewis *et al.*, 1999). Liang *et al.* (1999, 2000) and Liang (2000) have shown that it is possible to use a series of pre-calculated conversion factors to calculate 'inherent surface albedo' (as opposed to 'apparent surface albedo' observed in the presence of atmospheric scattering) from narrowband measurements of reflectance. This method works quite well for calculating visible albedo, but less so for total shortwave albedo (Liang, 2000). In addition, radiative transfer simulations of atmospheric scattering are required to decouple surface and atmospheric components of TOA reflectance, which in turn rely on assumptions about atmospheric state, and/or the use of standard models of atmospheric scattering. Another approach is to use hyperspectral measurements of reflectance as a first pass at a spectral interpolant. Lucht *et al.* (2000) employed an observed hyperspectral reflectance profile as a spectral interpolant to convert spectral samples of satellite-observed albedo to broadband albedo (305-2800nm), rather than use an arbitrary spline curve. There is also a large body of work on spectral unmixing which seeks to extract (sub-pixel) areal proportions of so-called spectral end-members ('pure' vegetation and soil spectra) from multispectral reflectance measurements (Settle and Drake, 1993; van Leeuwen *et el.*, 1997; Bateson *et al.*, 2000).

This chapter presents a method of directly exploiting existing knowledge of variations in the **spectral** reflectance behaviour of soil and vegetation in order to interpolate limited samples of spectral canopy reflectance, $\rho_{canopy}(\lambda)$, over a much wider

range of wavelengths (in particular 450-2500nm). In a direct analogy with the development of the angular kernels, it is proposed that $\rho_{canopy}(\lambda)$ can be split into constituent components of spectral soil and vegetation spectral reflectance, ($\rho_{soil}(\lambda)$ and $\rho_{veg}(\lambda)$) (c.f. separation of the volumetric and GO components of $\rho_{canopy}(\Omega, \Omega')$). Further, it is demonstrated that a small number of simple $\rho_{soil}(\lambda)$ and $\rho_{veg}(\lambda)$ terms can be combined in a weighted linear summation to describe the majority of observed variance in the behaviour of $\rho_{canopy}(\lambda)$. It will be shown that such terms (subsequently referred to as spectral kernels) can be readily derived and applied. More usefully, these spectral kernels can potentially be coupled with the angular kernels in order to provide a linear kernel-driven description of spectral directional canopy reflectance, $\rho_{canopy}(\lambda, \Omega, \Omega')$. There are several key areas where such a development is likely to prove extremely useful:

i. **Generation of broadband albedo (across the visible, SWIR and NIR regions) from a potentially small number of narrowband samples.** As described above this is currently problematic as it is reliant on an ability to accurately characterise the atmospheric conditions under which reflectance measurements are obtained. The ability to interpolate limited spectral samples across the observed spectrum (essentially a spectral integral of $\rho_{canopy}(\lambda)$) is analogous to the use of the angular kernels to derive angular integrals of directional reflectance samples in order to derive $\overline{\rho}(\lambda, \Omega')$ and $\overline{\overline{\rho}}(\lambda)$ (so-called black-sky and white-sky albedo).

ii. **Separation of the soil and vegetation scattering components of $\rho_{canopy}(\lambda)$.** This is of particular use for studies of radiation interception and photosynthetic efficiency. Parameters such as fAPAR are directly related to absorption of the photosynthetically active part of incoming solar radiation by vegetation within the canopy. The ability to isolate the spectral component of scattering originating from the vegetation would clearly be of benefit to such studies. The separation of the soil and vegetation components of $\rho_{canopy}(\lambda)$ is analogous to the separation of the volumetric and GO components of $\rho_{canopy}(\Omega, \Omega')$.

iii. **Making better use of limited directional/spectral sampling to improve BRDF model inversion.** The spectral kernels have the potential for exploring the meaning of derived spectral model parameters in the same manner as has been achieved with the directional kernels. This would permit better understanding of the impact of

spectral sampling on the accuracy of BRDF retrievals, similar to the way in which angular sampling has been explored (Lucht and Lewis, 2000).

iv. **Permitting the combination of multispectral data from sensors with different spectral bands and band-pass functions**. This would have the benefit of maximising the information extraction from of sensors with complementary spectral, spatial and temporal capabilities e.g. Meteosat Second Generation (MSG) (www[**7.1**]) and POLDER (www[**7.2**]). 'Data synergy' has long been an aim of remote sensing studies. Spectral kernels could be used to 'normalise' samples of spectral reflectance to a common set of wavebands. This is analogous to the use of angular kernels to normalise samples of directional reflectance obtained under arbitrary viewing and illumination conditions to a common viewing and illumination geometry (usually nadir).

7.2 Concept of spectral kernels

What is proposed is a series of simple functions that can be superposed in a weighted linear combination to describe the dominant shortwave (visible and NIR) reflectance characteristics of **spectral** canopy reflectance. This assumes that $\rho_{canopy}(\lambda)$ can be considered as follows

$$\rho_{canopy}(\lambda) = \underbrace{a_1\rho_s + a_2\rho_v}_{\text{single scattering component}} + \underbrace{\left(a_3\rho_s\rho_v + a_4\rho_s\rho_v^2 + a_5\rho_s^2\rho_v + a_6\rho_s^2\rho_v^2 + \ldots\right)}_{\text{multiple scattering component}} \qquad \textbf{7.2}$$

where a_i are constants; ρ_s and ρ_v are the single scattering contributions to ρ_{canopy} from the soil and vegetation (reflectance or transmittance); terms in brackets are multiple scattering contributions representing higher order interactions between soil and vegetation (truncated). It should be recalled that the single scattered component of directional reflectance is the dominant feature, with successively higher orders of multiple scattering interactions becoming increasingly isotropic. The work of Price (1990) for soil, and Price (1992) and Hurcom *et al.* (1996) for vegetation suggest this is a reasonable assumption for $\rho_{canopy}(\lambda)$. Figure **7.1** demonstrates the dominance of the single scattered component of $\rho_{canopy}(\lambda)$ (note that the plot is logarithmic with respect to the reflectance

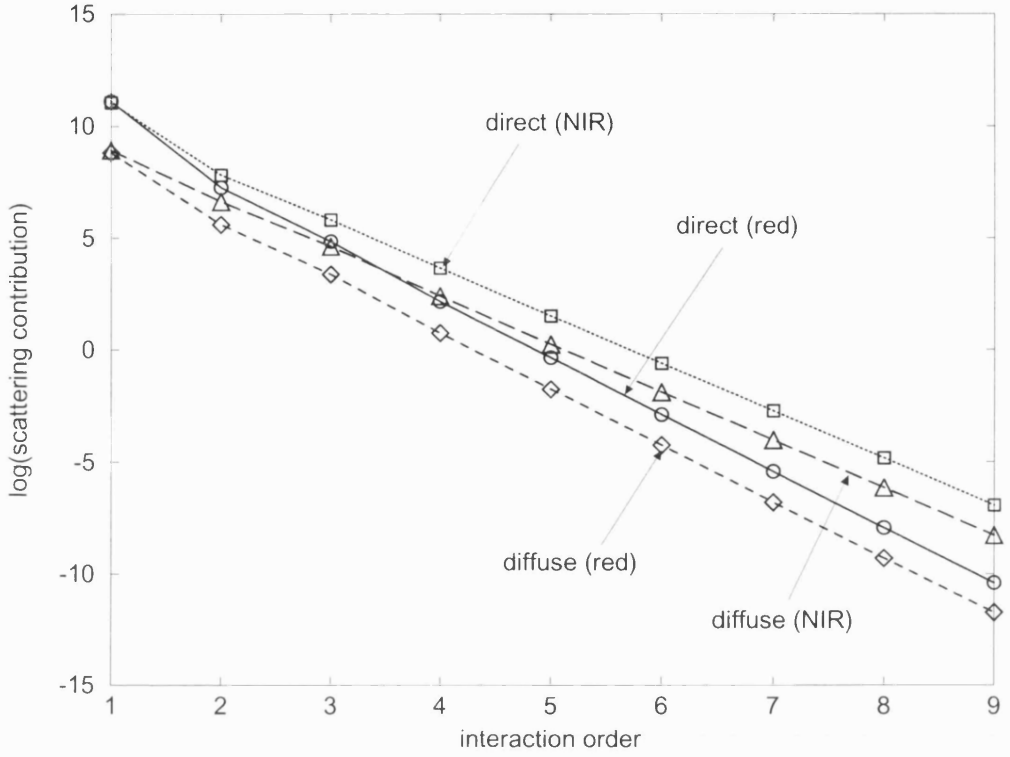

Figure 7.1 Direct and diffuse scattering contributions to simulated ρ_{canopy} as a function of scattering order (barley canopy, 15th May, nadir viewing and illumination).

contributions). In this example, the single scattered components contain 98% and 95% of the total contribution to reflectance in the direct and diffuse cases respectively (this is low, and is a result of the relatively sparse canopy).

If $\rho_{canopy}(\lambda) = (\rho_1, \rho_2, ... , \rho_n)$ is an observed reflectance spectrum for the set of n wavelength values $\lambda = (\lambda_1,\lambda_2, ... \lambda_n)$ then the desired spectral kernels (referred to by Price (1990) as basis functions) are $k(\lambda_1,\lambda_2, ... \lambda_n)$, and

$$\rho_{canopy}(\lambda) = \sum_{i=1}^{M} f_i k_i(\lambda) \qquad \textbf{7.3}$$

where the f_i are the weights associated with each spectral kernel. The total number of basis functions, M, clearly cannot exceed the number of available bands, n, in the observed data (e.g. four in the case of MISR, and typically seven for MODIS), and ideally, $M << n$. This must suffice for a description of both the soil and vegetation components of $\rho_{canopy}(\lambda)$.

If such spectral kernels are plausible, they could be combined with the angular

kernels to create a spectral directional kernel-driven model of canopy reflectance. This situation is described in equation **7.4**.

$$\rho_{canopy}(\lambda,\Omega,\Omega') = \underbrace{\left[\rho_{veg}(\lambda)+\rho_{soil}(\lambda)\right]}_{\text{spectral component}} + \underbrace{\left[\rho_{VOL}(\Omega,\Omega')+\rho_{GO}(\Omega,\Omega')\right]}_{\text{directional component}} \qquad \textbf{7.4}$$

The spectral kernels would then provide a link between the spectral and directional domains, which is currently missing in the kernel-driven approach to modelling ρ_{canopy}. The full spectral directional kernel-driven approach is then of the form

$$\rho_{canopy}(\lambda,(\Omega,\Omega')) = \sum_{i=1}^{M} f_i k_i(\lambda) + \sum_{j=1}^{N} f_j k_j(\Omega,\Omega') \qquad \textbf{7.5}$$

where N is the number of angular reflectance samples, and k_i and k_j are the spectral and directional kernels respectively. This approach considers the spectral and directional components of ρ_{canopy} as separate, and models each of them correspondingly as a linear sum of terms (kernels).

The remainder of this chapter presents a derivation of spectral kernels for $\rho_{soil}(\lambda)$ and $\rho_{veg}(\lambda)$ and demonstrates their use, in combination with the angular kernels, in describing modelled and observed spectral directional ρ_{canopy}. The structure is as follows:

i) Derivation of spectral kernels from laboratory reflectance spectra, in particular $\rho_{veg}(\lambda)$.

ii) Demonstration of kernels' ability to describe $\rho_{soil}(\lambda)$ and $\rho_{veg}(\lambda)$ individually, and $\rho_{canopy}(\lambda)$.

iii) Demonstration of ability of spectral and directional kernels to describe $\rho_{canopy}(\lambda, (\Omega, \Omega'))$.

iv) Discussion of implications, particularly in relation to the calculation of spectrally integrated products such as albedo.

7.3 Derivation of spectral kernels

The kernel-driven models of BRDF arose from the observation that it is possible to consider $\rho_{canopy}(\Omega, \Omega')$ as a sum of separate volumetric and GO terms (Roujean *et al.*, 1992; Wanner *et al.*, 1995). This approach considers $\rho_{canopy}(\Omega, \Omega')$ to be a sum of the dominant volumetric and GO "shapes" governing reflectance behaviour. The derivation of the angular kernels was described in detail in chapter **2**, and the separability and information content of the two components was explored in chapters **4** and **5.** The spectral kernels outlined below are derived from a similar observation: that $\rho_{canopy}(\lambda)$ can be considered as a combination of the spectral reflectance behaviour of soil and vegetation respectively. This work is based on that of several authors, notably Price (1990, 1992, 1998), who have noted that the major variations in reflectance behaviour of both soil and vegetation can largely be described by a few simple basis functions (spectral kernels).

7.3.1 Reflectance features of vegetation

It is well known that that both vegetation and soil exhibit characteristic reflectance features (Carlson *et al.*, 1971; Huete, 1989; Jacquemoud and Baret, 1990; Price, 1990; Curran *et al.*, 1992; Asner, 1998). Different types of vegetation tend to differ far more in the relative magnitude of characteristic reflectance features than the wavelengths at which these features occur. Examples of leaf and soil spectra in figures **7.2** and **7.3** illustrate this.

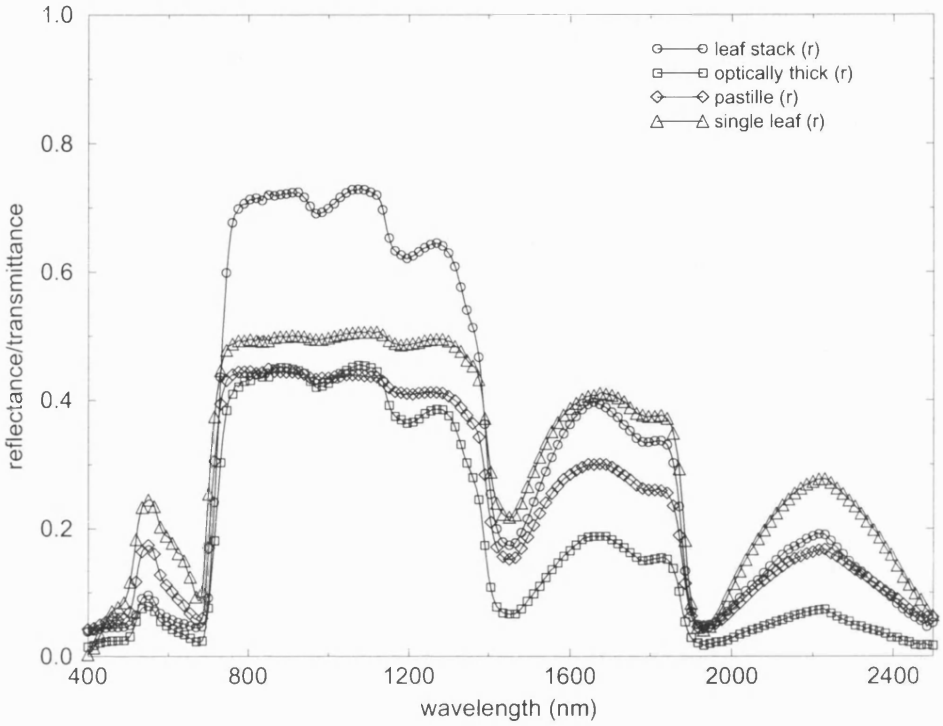

Figure 7.2 Laboratory-measured vegetation reflectance spectra (Hosgood *et al.*, 1994).

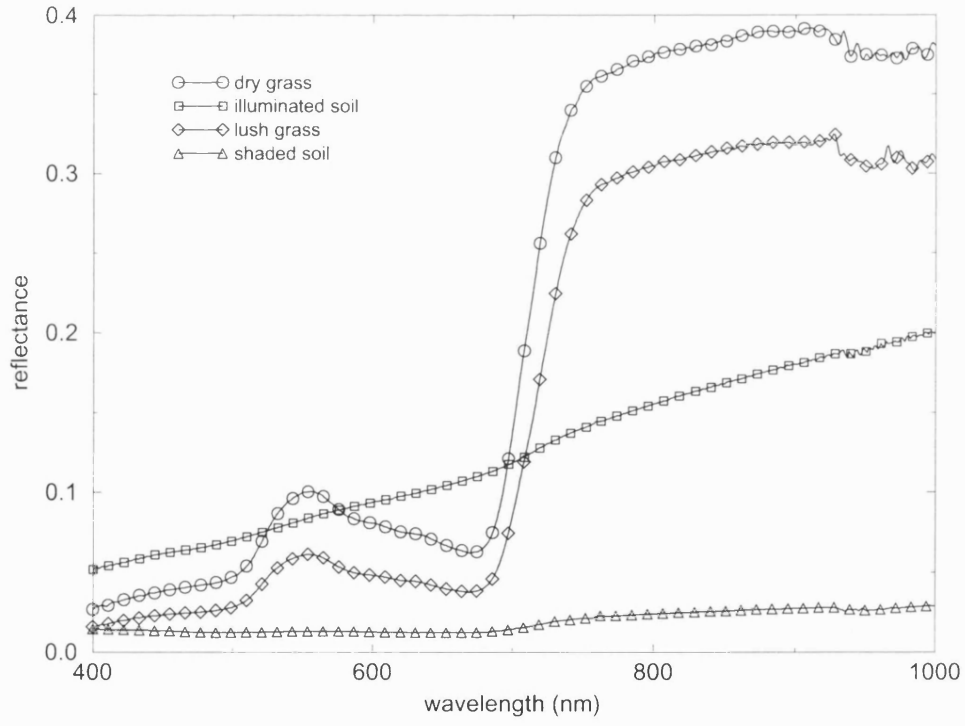

Figure 7.3 Field-measured soil and vegetation reflectance spectra (Milton, *pers. comm.*).

Figures **7.2** and **7.3** show both laboratory- and field-measured reflectance spectra of a variety of vegetation. Figure **7.3** contains spectra of a single leaf, a layered leaf medium, an optically thick leaf stack, and a pastille of powdered green leaf material. These spectra represent an extremely wide range of physical conditions (some artificial), yet the characteristic leaf reflectance features are present in all cases: the reflectance peak in the visible green (~550nm) due to chlorophyll pigments; the sharp rise in reflectance from the visible red to the shortwave IR (the so-called red-edge); water absorption features in the NIR at around 1450 and 1900nm. The spectra in figure **7.3** also display these similarities, albeit with wider variation due to external factors present in field measurements (atmospheric conditions, field of view considerations etc.). The difference between the soil spectra (in the visible at any rate) is essentially a linear transformation of scene brightness caused by the presence or absence of direct sunlight. The question remains as to whether the variation in the soil and/or the vegetation reflectance can be represented using simple terms in linear combination.

7.3.2 Soil kernels: the soil component of $\rho_{canopy}(\lambda)$

Price (1990) showed that the soil component of $\rho_{canopy}(\lambda)$ can be well-represented by a linear combination of basis functions, or kernels derived from measured spectra. Price (*ibid.*) applied principal component analysis (PCA) to laboratory-measured soil spectra of a wide range of soil types. PCA allows a set of correlated observations to be transformed to a set of uncorrelated (principal) components, or basis functions, by calculating the eigenvectors and eigenvalues of the variance-covariance matrix of observations. The percent variance in the data described by each PC is simply the corresponding eigenvalue, scaled by the sum of all eigenvalues (and multiplied by 100). The first PC describes the largest variance within the data, with subsequent PCs describing successively less of the observed variance. PCA permits the decomposition of observed spectra into PCs (spectral basis functions) which can then be summed to regenerate the original reflectance spectra.

Price (*ibid.*) showed that the first four PCs of laboratory-measured soil reflectance explained nearly 98% of the observed variance in the data, with the remaining variance attributable to measurement noise. Price's first four soil basis functions are shown in figure **7.4** (the functions are scaled in this case - the first basis function described over

95% of observed variance). Huete (1986) used factor analysis (closely related to PCA) to separate soil and vegetation spectral mixtures, whilst Huete and Escadafal (1991) applied spectral decomposition techniques (also closely related to PCA) to field-measured soil spectra. They found that four basis functions were sufficient to reconstruct observed spectra. Given the success of the spectral decomposition/PCA analysis of soil reflectance, and the use of Price's basis functions by a number of other researchers, notably by Nilson and Kuusk (1989) to describe $\rho_{soil}(\lambda)$ in their physically-based canopy reflectance model, it makes sense to use these basis functions as the soil spectral kernels in the spectral kernel-driven model of $\rho_{canopy}(\lambda)$. It then remains to derive corresponding vegetation kernels.

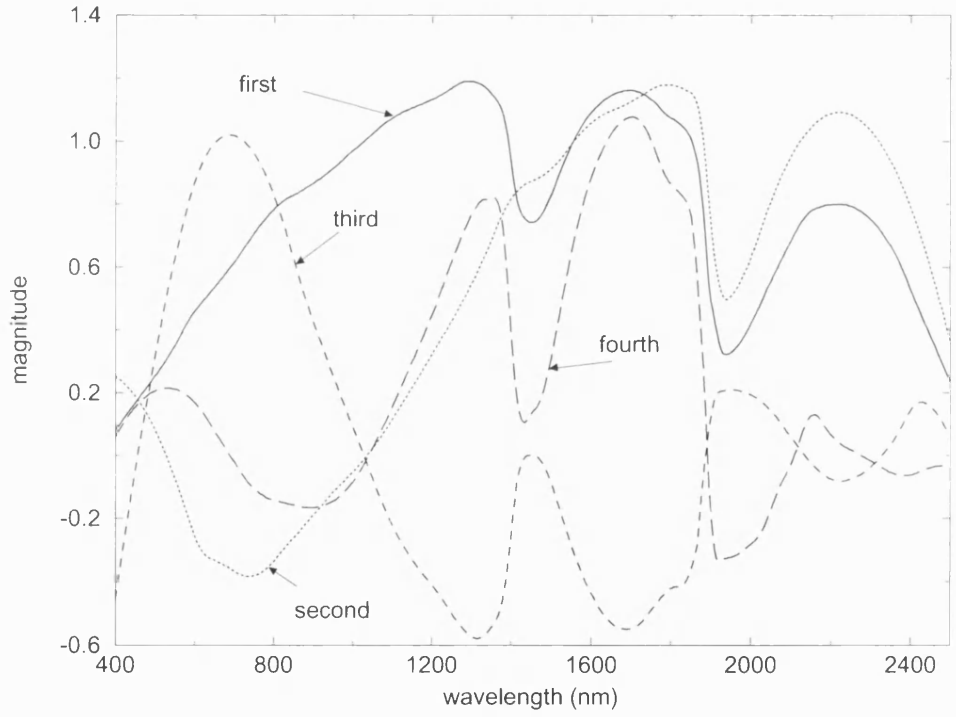

Figure 7.4 Price's first four basis functions of observed soil reflectance spectra.

It is apparent from figure **7.4** why Price's first basis function describes so large a proportion of the observed variance of soil reflectance. The rise across the visible and NIR parts of the spectrum is characteristic of soil reflectance, as are the water absorption features at around 1300 and 1900nm. The second and higher basis functions can act to moderate the first basis function depending on the visible and NIR reflectance behaviour of the soil being modelled.

7.3.3 Vegetation kernels: the vegetation component of $\rho_{canopy}(\lambda)$

The fact that spectral reflectance of vegetation has certain common features has been exploited by a number of researchers. Price (1992) showed that high resolution crop reflectance spectra measured in the field could largely be described using a weighted linear summation of the first five PCs of the observed data. Hurcom *et al.* (1996) used spectral decomposition to demonstrate that four factors (closely related to PCs) described 99.86% of observed spectral variance of semi-arid Mediterranean vegetation species. Some of these factors appeared to be correlated with biophysical properties such as the proportion of directly irradiated green leaf area viewed by the measurement instrument, and spectral response in the chlorophyll absorption region. Hurcom *et al.* (*ibid.*), and Hurcom and Harrison (1998), have also suggested that these vegetation factors could be used to describe the variation of spectrally similar vegetation types in terms of biophysical properties, rather than as mixtures of various spectral classes as in the standard mixture modelling approach. Indeed, work by Jacquemoud and Baret (1990), Baret *et al.* (1994) and Jacquemoud *et al.* (1996) has demonstrated that leaf reflectance is mainly controlled by a small number of physical parameters affecting leaf absorption behaviour (as opposed to scattering behaviour), such as leaf mesophyll structure, pigment concentration (chlorophyll a and b), and water, lignin and cellulose content. These are the minimum terms required to model leaf reflectance accurately. However, these terms are non-linear and so cannot be combined in a linear fashion as required here.

Following the approach of Price (1990, 1992), and Hurcom *et al.* (1996), vegetation spectral reflectance kernels (basis functions) have been derived through PCA of a large number of measured reflectance spectra. The primary difference between the analysis described here and Price's work is the availability of both transmittance and reflectance spectra. This potentially permits the derivation of single scattering albedo kernels, given that single scattered albedo $\omega = \rho + \tau$. One of the aims of developing a linear kernel-driven model of ρ_{canopy} is to allow broadband estimates of albedo to be derived from limited spectral samples. The most logical way to achieve this (and the most consistent with respect to energy conservation) is to use single scattering albedo from the outset.

Other differences from the analysis of Price (1990, 1992) are that the spectra used here were measured under laboratory conditions, rather than in the field where

measurement error increases due to atmospheric effects. In addition, the number and variety of spectra used are much greater, with nearly two thousand vegetation spectra, from one hundred and twenty distinct vegetation types. This compares with less than two hundred spectra of at most five crop types in Price's analysis. Finally, due to advances in computational capability it is now straightforward to carry out robust and accurate numerical inversions of matrices of the order of 2000 x 2000 in a few minutes. Price was forced to use numerical approximations in order to carry out piecewise inversions of significantly smaller matrices.

The reflectance and transmittance data used in this analysis were measured in the controlled environment of the European Goniometric Observatory (EGO) facility, at the Joint Research Centre (JRC), Ispra, Italy[1]. These data were the result of the Leaf Optical Properties Experiment (LOPEX) (Hosgood *et al.*, 1994), and formed the basis of work relating biochemical properties to reflectance (Jacquemoud *et al.*, 1995) as well as for development of the PROSPECT-REDUX leaf reflectance model (Jacquemoud *et al.*, 1996). A range of optical configurations are included within the LOPEX data, such as optically thick media (bark), fresh and dry (oven-dried) leaf samples, in addition to pastilles of powdered leaf samples, and fresh and dry leaf stacks (layered media) which are included to represent leaf-scale multiple scattering. It is known that the reflectance of oven-dried leaf spectra is not quite the same as naturally dry, brown vegetation and this will affect results slightly, in particular in the transition from visible to NIR wavelengths. However, it is intended that if/when naturally dry leaf spectra become available, these will be added to the analysis presented below. The spectra in figure **7.2** are drawn from the LOPEX data. Figures **7.5a** and **b** show the (normalised) spectral vegetation kernels derived from the fresh and dry single scattered spectral albedo. These kernels are likely to be the most widely applicable, as they are derived from fresh and dry reflectance and transmittance spectra, as well as the pastille and leaf stack spectra. The latter spectra will potentially allow the kernels to describe at least the first order (spectral) multiple scattering terms of equation **7.2**.

[1] Kindly provided by B. Hosgood, technical director of the EGO facility.

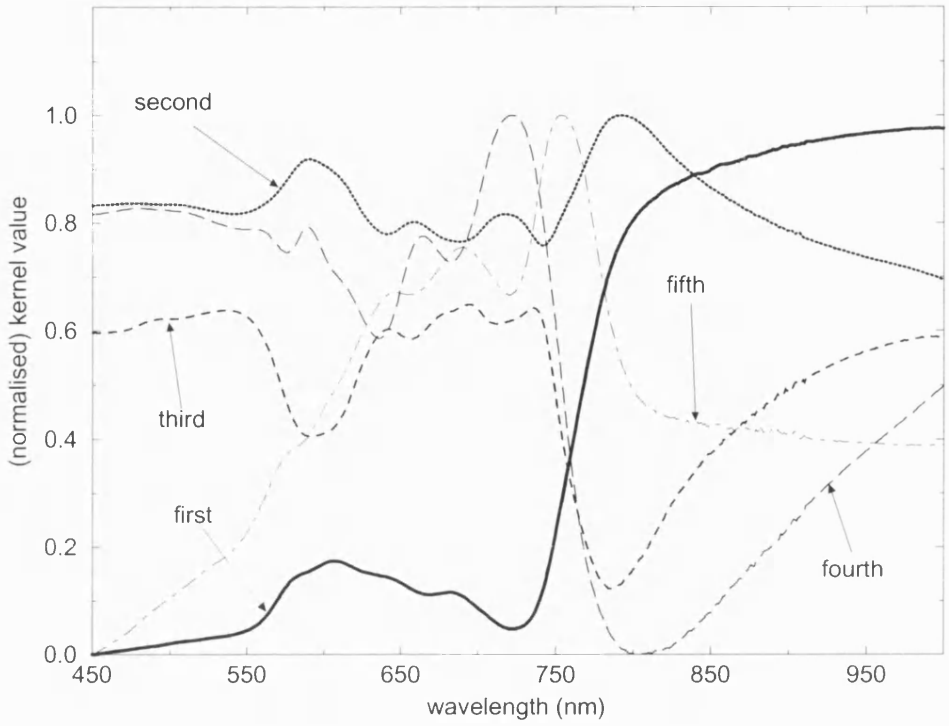

Figure 7.5a First five vegetation spectral kernels derived from fresh and dry single scattered albedo (450-1000nm).

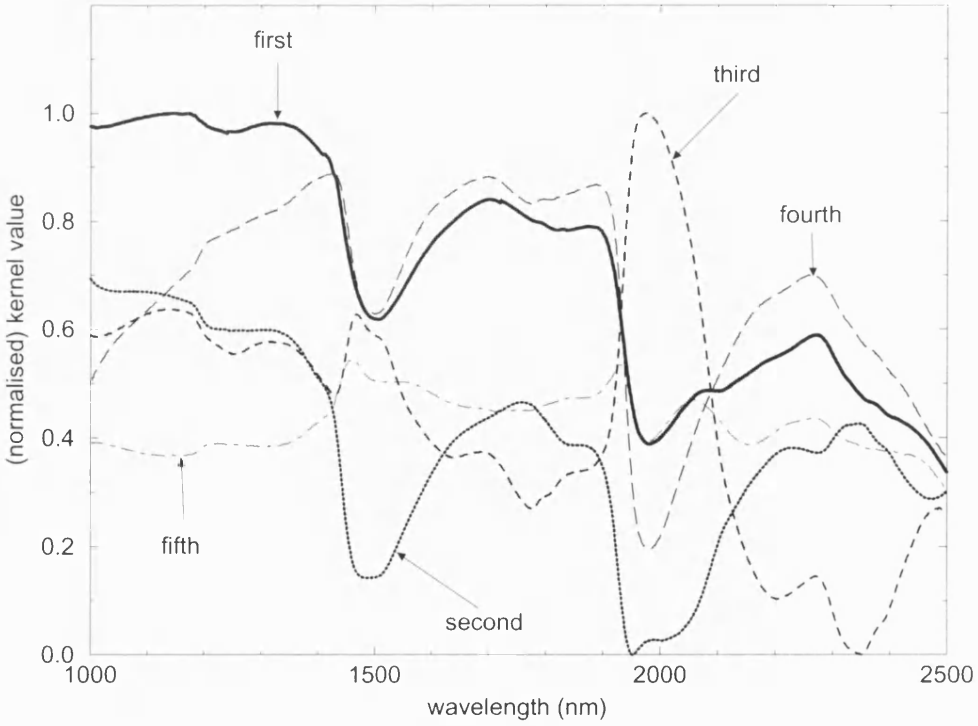

Figure 7.5b First five vegetation spectral kernels derived from fresh and dry single scattered albedo (1000-2500nm).

The cumulative variance of the original data explained by each of the spectral kernels is given in table **7.1**. The first and second kernels explain 83.9% and 14.5% of the observed variance respectively. The third component explains less than 1% of observed variance. This suggest that **in most cases, two to three vegetation kernels should be sufficient to describe the majority of observed variance**, particularly in the case of green vegetation. More kernels can be used (at the expense of requiring more spectral samples), but this will generally only serve to significantly improve fitting when the spectra diverge from healthy vegetation.

Table 7.1 First five eigenvalues of PCA of LOPEX fresh and dry single scattering albedo, and the corresponding percent variance.

PC	eigenvalue	cumulative variance (%)
1	43.85	83.85
2	7.56	98.31
3	0.39	99.05
4	0.11	99.50
5	0.067	99.71

The reduction in explained variance from PC 1 to 2 in this case is smaller than for any of the other possible combinations of LOPEX spectra. For example, if only fresh leaf reflectance is used, the first PC explains 95.8% of observed variance, and the second, 3.4%. If dry leaf transmittance is used, the first PC explains 96.5% of observed variance, and the second PC, 2%. As a result, these combinations are likely to permit fewer vegetation kernels to be used to model a given set of observations of $\rho_{canopy}(\lambda)$. However, the ability to describe albedo directly is of greater importance, and hence the combination of fresh and dry single-scattered albedo is thought the most appropriate at this stage.

7.4 Testing the spectral kernels

The first step in demonstrating the applicability of the spectral kernels is to show they can reconstruct independently measured soil and vegetation spectra. These data are provided by the Natural Environment Research Council Equipment Pool for Field Spectroscopy (NERC EPFS), based at Southampton University[2], from spectra measured in a variety of locations and (field) conditions. The EPFS data comprise 85 spectra of various cover types (not just soil and vegetation), measured using a 15° FOV hand-held radiometer, with a wavelength range of 400 to 1000nm in steps of 1nm. Results are presented from inversions of spectral kernels derived from fresh and dry leaf reflectance and transmittance as well as fresh and dry single scattered albedo, against all available observed spectra. This is to examine the limitations (if any) of using only the fresh and dry single scattered albedo spectral kernels to reconstruct observed spectra. Following this, specific examples of inversions of the derived spectral kernels against field-measured reflectance are presented, such as green and senescent vegetation. Following this, results are presented for inversion of both spectral **and** directional kernels simultaneously against spectral, directional reflectance samples generated using a physically-based (radiative transfer) model of canopy reflectance (the model of Nilson and Kuusk, 1989). In this case, samples of reflectance are simulated with θ_v varying from -75 to 75 degrees ($\theta_i = \phi_{i,v} = 0^o$) in steps of 5°, with spectral bands from 400 to 2500nm in steps of 20nm. This is designed to test the kernels' ability to fit the spectral component of ρ_{canopy}, related to ρ_{leaf}. Although ρ_{canopy} contains a significant (non-linear) multiple scattering component, a linear combination of kernels (including a kernel related to multiple scattering, derived from leaf stack spectra) may be capable of describing spectral variation in this case. Lastly, the spectral kernels are inverted against multi-spectral ATM data (described in section **3.1.5**).

[2] Many thanks to Dr. E. Milton and colleagues at EPFS for use of the field data.

7.4.1 Inversion against all NERC EPFS spectra

The results presented in figures **7.6**, **7.7** and **7.8** illustrate the kernels' performance in inversion against the entire EPFS data, containing spectra of (amongst other things) concrete, water, gorse, limestone and vegetation. These surfaces cover a variety of spectra that are likely to be found in the pixels of a moderate (km-scale) resolution satellite image of the land surface.

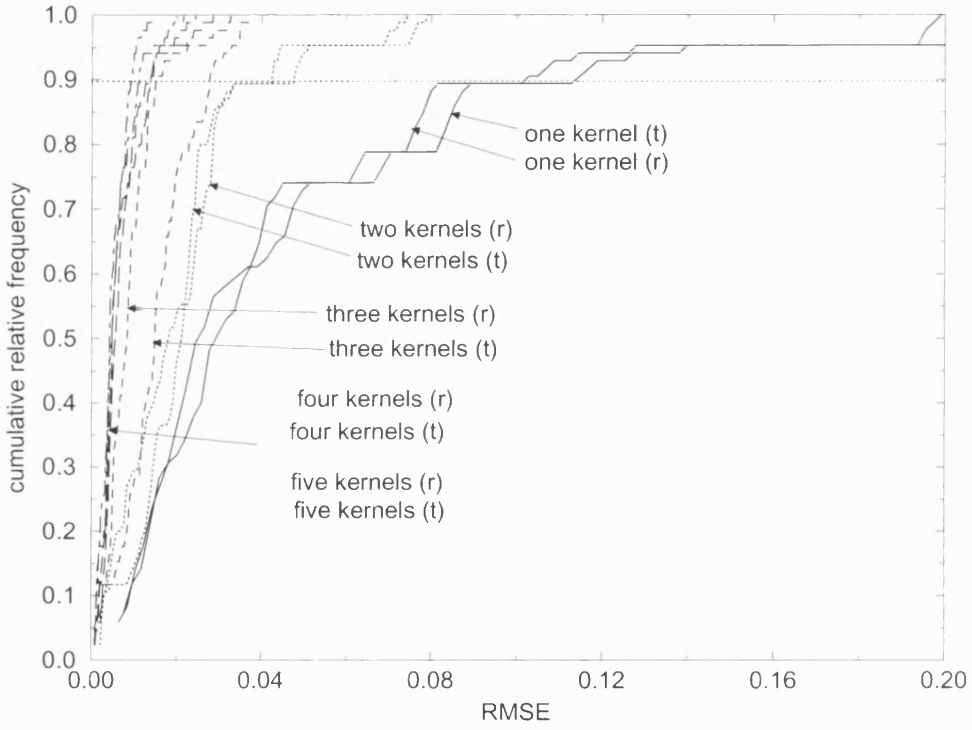

Figure 7.6 Cumulative relative error of inversion of vegetation spectral kernels derived from fresh and dry reflectance and transmittance spectra, against all EPFS spectra.

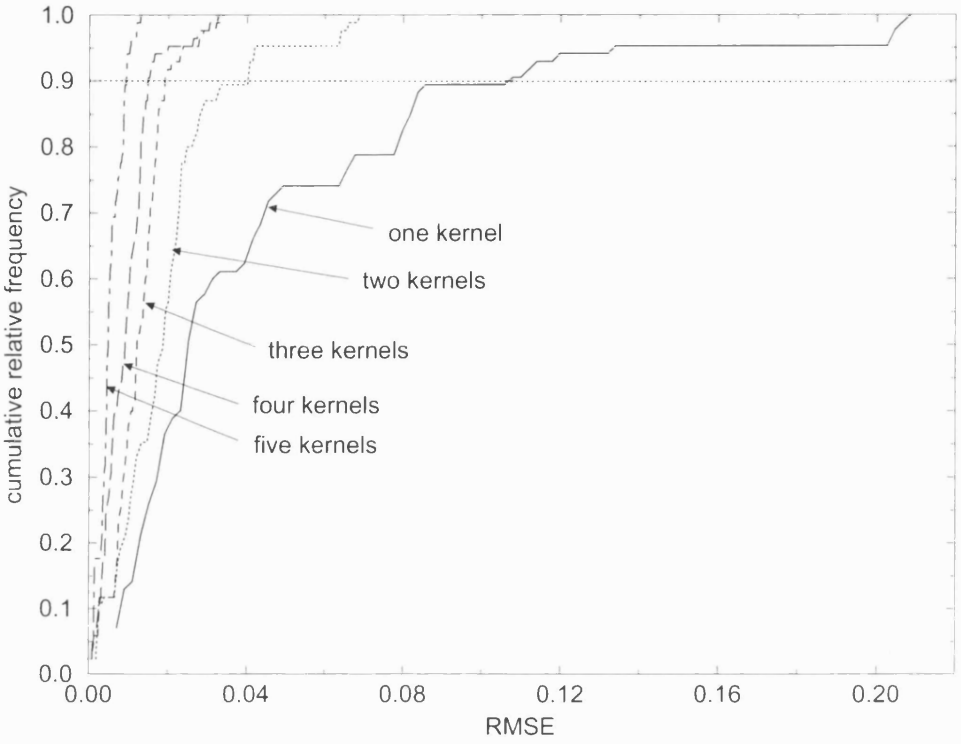

Figure 7.7 Cumulative relative error of inversion of vegetation spectral kernels derived from fresh single scattering albedo only, against all EPFS spectra.

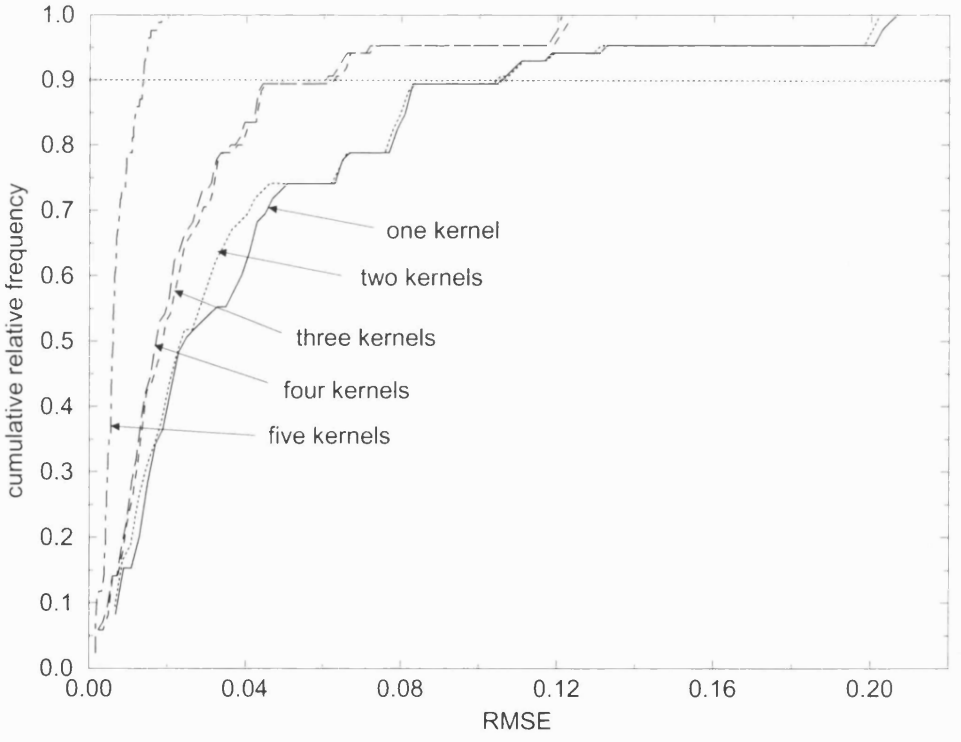

Figure 7.8 Cumulative relative error of inversion of vegetation spectral kernels derived from fresh and dry single scattering albedo, against all EPFS spectra.

Figures **7.6**, **7.7** and **7.8** shows the cumulative (relative) error frequency for inversion of the kernels against all 83 spectra included in the EPFS data set. The vertical axis represents the percentage of samples in total with RMSE below this level and the horizontal axis shows the RMSE at that cumulative error level. There is a noticeable increase in RMSE at around the 90% cumulative relative frequency level (except for the five kernel case). This error level, at which 90% of inversions have a lower error, is used as a comparison between the various cases. The fresh and dry reflectance and transmittance (ρ and τ) case (figure **7.6**) is included to examine whether using single scattering albedo confers any advantage over using reflectance or transmittance spectra alone. The ρ and τ cases are separable on RMSE at the 90% level, particularly in the one to three kernel cases. Results are presented in table **7.2**.

Table 7.2 RMSE of inversion of various kernel combinations against field-measured spectra.

	RMSE (at 90% cumulative error level)			
no. of kernels	**fresh + dry ρ**	**fresh + dry τ**	**fresh ω**	**fresh + dry ω**
1	0.09	0.1	0.11	0.106
2	0.046	0.042	0.04	0.106
3	0.016	0.028	0.02	0.064
4	0.019	0.013	0.014	0.063
5	0.009	0.009	0.008	0.013

As might be expected, increasing the number of kernels improves the ability of the spectral kernels to recreate measured spectra. As might also be expected, increasing the number of kernels produces progressively less improvement each time. Kernels derived from reflectance or transmittance spectra alone exhibit broadly similar characteristics. For a fixed number of kernels those derived from fresh spectra tend to perform slightly better than the same number derived from dry spectra. Kernels derived from both fresh and dry reflectance spectra generally performed better than those derived from fresh and dry transmittance spectra. Operationally, it is preferable to keep the number of spectral kernels to an absolute minimum so that the number of bands required for inversion is kept small (ideally less than seven). Given that between two and four soil kernels will be required in order to describe the $\rho_{soil}(\lambda)$ component of $\rho_{canopy}(\lambda)$, it is desirable that the $\rho_{veg}(\lambda)$ component of $\rho_{canopy}(\lambda)$ can be described by two or three vegetation kernels.

Figures **7.9a** and **b** show the relative error of inversion (mean RMSE as a fraction of mean reflectance) for all the various EPFS field-measured reflectance spectra. RMSE

for the one and four kernel cases are shown for all samples. In the cases where the spectra resemble green vegetation spectra closely, the relative error is between 5% and 10%. The difference in error between using one or four kernels is small. As the spectra depart from green vegetation (asphalt, concrete, limestone and water), relative error increases and the difference between the one and four kernel cases becomes larger, doubling in the most extreme cases. This demonstrates further that two kernels may well be sufficient to describe reflectance of green vegetation. Figures **7.10a** and **b** show spectral plots of measured and modelled lush and dry grass spectra in the visible and NIR respectively. Although there is excellent general agreement, it can be seen that differences tend to be concentrated in the visible part of the spectrum. This is not necessarily desirable for studies of albedo, as the incoming solar radiation is at a maximum here, which will tend to exacerbate such errors.

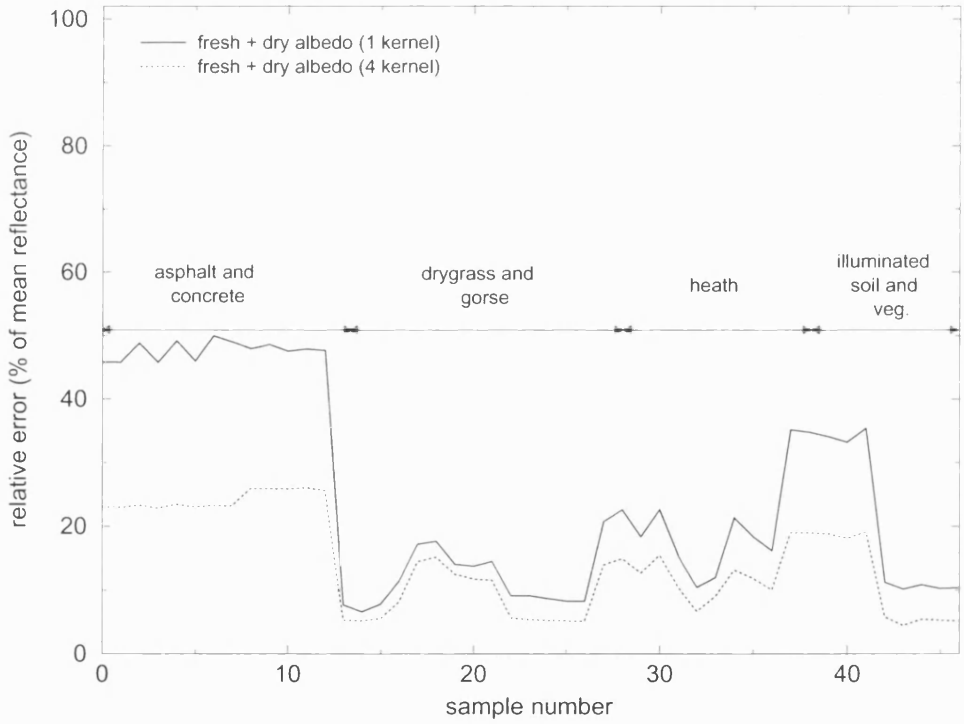

Figure 7.9a Relative error of inversion, EPFS reflectance spectra samples 1-47, 1 and 4 kernels.

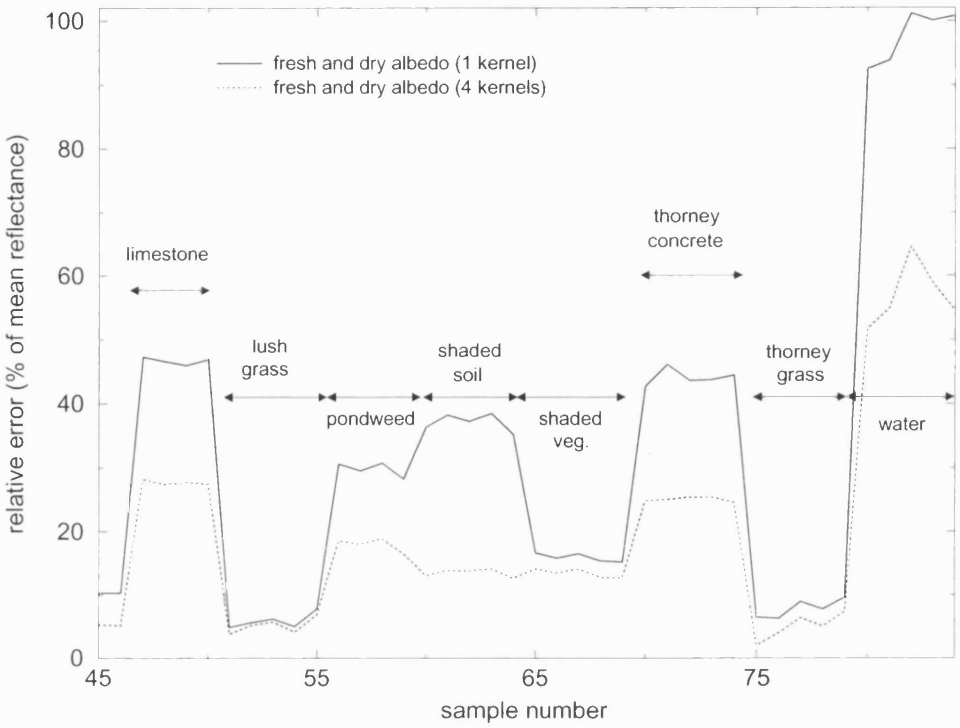

Figure 7.9b Relative error of inversion, EPFS reflectance spectra samples 48-83, 1 and 4 kernels.

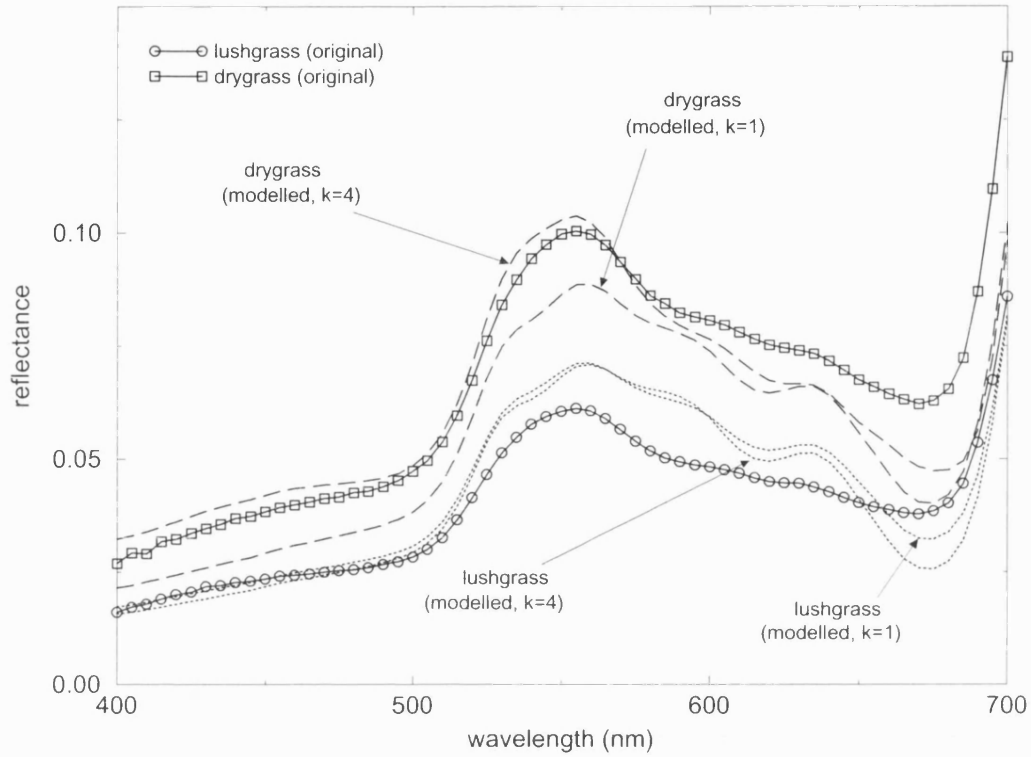

Figure 7.10a Original and modelled lush and dry grass spectra, 1 and 4 kernels, visible.

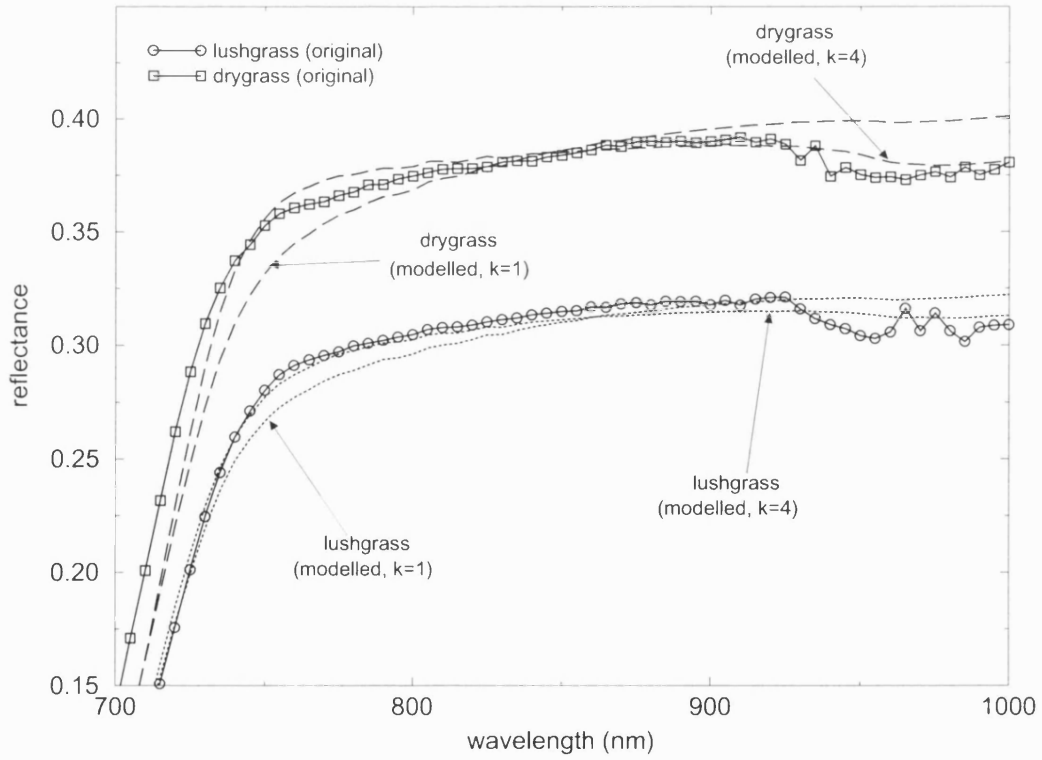

Figure 7.10b Original and modelled lush and dry grass spectra, 1 and 4 kernels, NIR.

7.4.2 Demonstration of vegetation spectral kernels against specific measured spectra

Figures **7.11 a** and **b** show scatter plots of measured against modelled reflectance of the lush grass and dry grass spectra shown in figure **7.10**. These spectra representing a broad range of vegetation reflectance characteristics, from healthy, green vegetation to senescent. The spectra were measured in the field under varying atmospheric conditions, so providing a stern test of the kernels' flexibility. In each case, one to five vegetation kernels are used to derive the forward modelled reflectance spectra. Using more kernels is always more likely to provide a better fit to the observed data due to the increased degree of freedom (assuming overfitting is not occurring), at a cost of requiring more spectral bands.

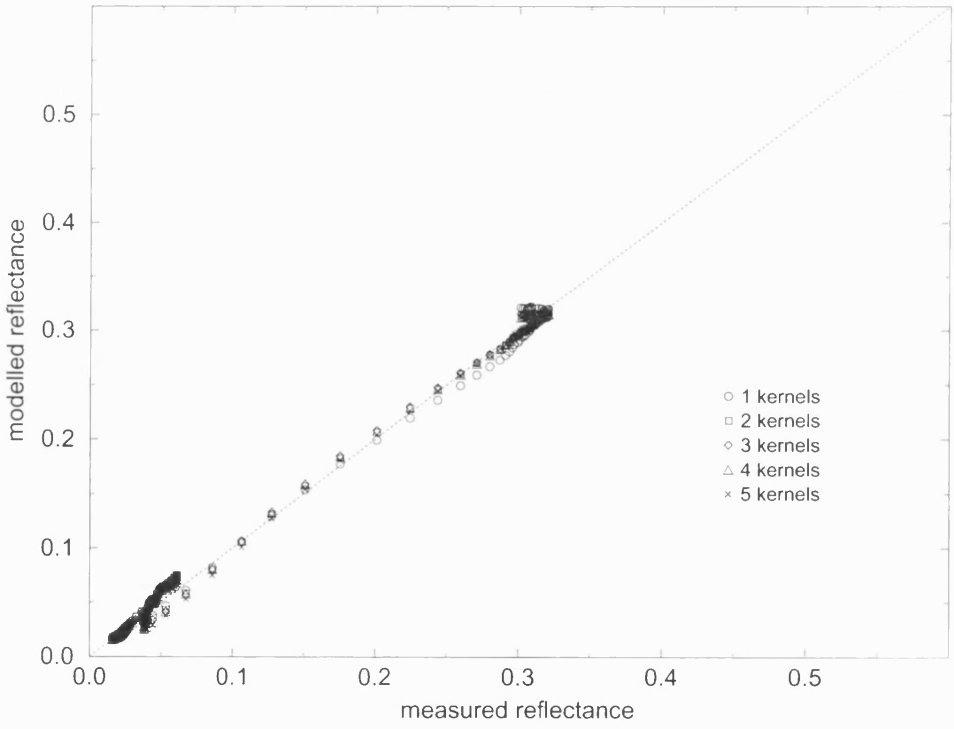

Figure 7.11a Measured against modelled lush grass reflectance, 1 - 5 vegetation kernels.

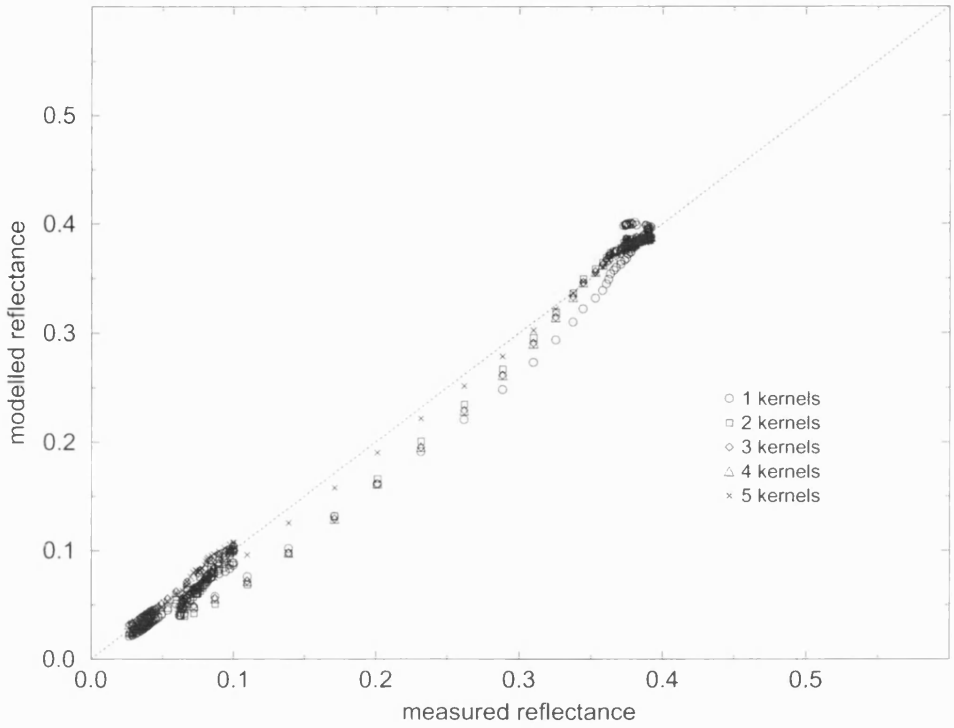

Figure 7.11b Measured against modelled dry grass reflectance, 1 - 5 vegetation kernels.

It can be seen from figure **7.11a** that there is close correlation between the measured and modelled lush grass reflectance (r values greater than 0.98 in all cases). There is greater variation in the scatter of the dry grass reflectance values (figure **7.11b**, r around 0.95), in particular at visible parts of the spectrum (lower values of reflectance). The pattern of variation in the RMSE is not unexpected. The lush grass has by far the lowest RMSE and, although the error reduces as the number of kernels increases, the reduction is relatively small (0.0099 for 1 kernel to 0.0065 for 5 kernels). This illustrates that when fitting spectra of green vegetation, only one or perhaps two kernels are necessary to achieve a good fit, simply because of the close resemblance of, in particular the first kernel, to the general green leaf reflectance shape. The RMSE in the case of dry grass is approximately double that of the lush grass case, with the exception of the five kernels case where the RMSE values are comparable (0.020 for 1 kernel, 0.0056 for 5 kernels). This demonstrates that a larger number of vegetation spectral kernels can, if necessary, fit a wide range of spectra. The addition of more kernels will allow more flexibility, but it is not necessarily desirable to allow the kernels to fit any kind of reflectance as they are intended in part to allow the separation of vegetation and soil spectra from $\rho_{canopy}(\lambda)$.

Figure **7.12** shows the residual error between the measured and modelled lush and dry grass reflectance values shown in figure **7.10**. There are two main areas of difference - firstly in the visible green and red (500-650nm) where the modelled reflectance tends to be on the low side in the lush grass case, particularly in the regions of strong chlorophyll absorption at around 580nm. The one and four kernel cases are virtually identical. However, for the dry grass case they differ in the visible region, with the one kernel case over-estimating reflectance, while the four kernel case has a much smaller residual error. Across the red edge and into the NIR the lush grass case has a very low residual error, while the modelled dry grass reflectance overestimates the measured values. This is largely a function of the difference in the position of the red edge in the dry grass spectra. The gradient of the spectral reflectance at this point is such that if the red edge position is very slightly out, the differences between measured and modelled values will be amplified.

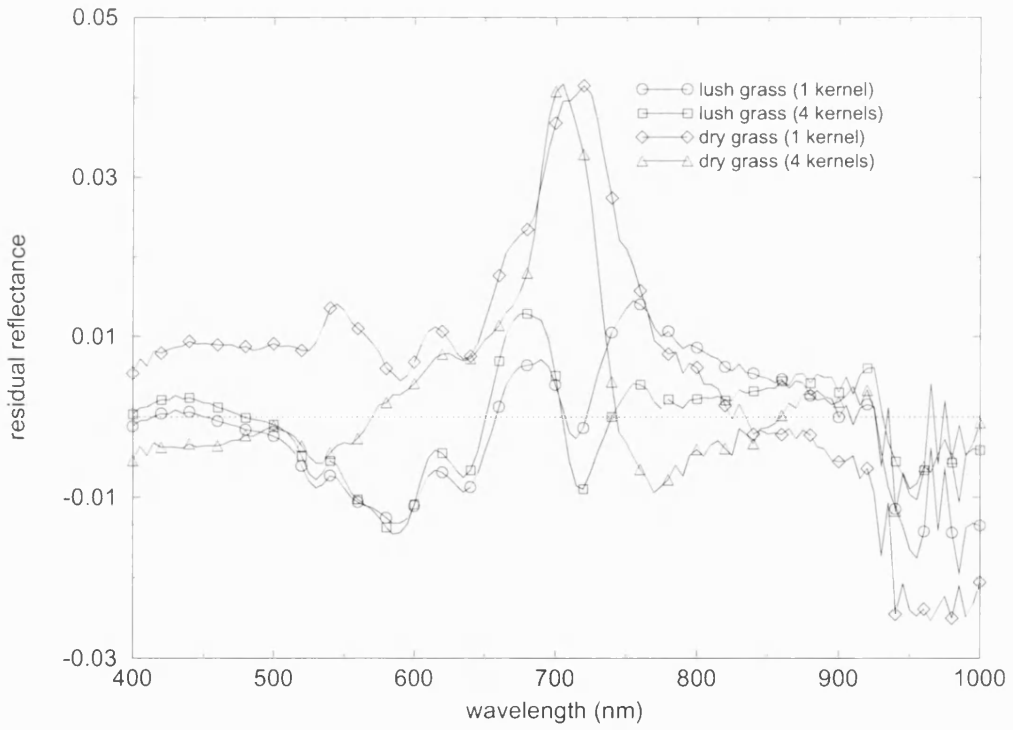

Figure 7.12 Residual error between measured and modelled lush and dry grass reflectance, one and four kernel cases.

It is worth noting that RMSE may not be the most appropriate measure of fitting error in the case of modelling vegetation spectra. There may be regions of close agreement between measured and modelled spectra in some parts of the spectrum and disagreement in others and RMSE over the whole spectrum will not reflect this. Other

error measures based on specific features of observed vegetation reflectance may be more instructive. For example, discrepancies in the red edge position between measured and modelled spectra may represent the ability of spectral kernels to reconstruct spectral reflectance in the visible and NIR more accurately than RMSE. Red edge position also has the advantage of being (empirically) related to the biophysical properties of vegetation (particularly in the visible and NIR).

Another measure of goodness of fit might be a spectral index such as NDVI (Normalised Difference Vegetation Index) (Rouse *et al.*, 1974) which is simply the difference between the NIR and visible red signal divided by their sum. A more general measure of the suitability of a particular model (in this case represented by type and number of spectral kernels) is an information criterion (IC) such as that of Akaike (1974) (AIC). AIC balances the (log) maximum likelihood selection of a particular model against both the number of observations and the number of free model parameters. Table **7.3** shows the results of applying these three criteria to the inversions of one and five (fresh and dry single scattering albedo) spectral kernels against lush and dry grass spectra (Δ values represent differences from the original spectra; lower AIC values represent better model fit). The red edge position in table **7.3** is calculated by finding the wavelength at which $\frac{\partial^2 \rho}{\partial \lambda^2} = 0$. Red edge position in this case is defined as the wavelength (between 670 and 750nm) where the gradient of $\rho(\lambda)$ is at its steepest. At this point, the derivative of $\rho(\lambda)$ will be at a maximum, and hence the second derivative will be zero.

Table 7.3 Comparison of RMSE to alternative estimates of model fit (k is kernels).

Grass spectra	**RMSE**		**Δ(NDVI)**		**Δ(red edge)/nm**		**AIC**	
	1 k	5 k	1 k	5 k	1 k	5 k	1 k	5 k
dry1	0.043	0.019	0.089	0.021	5	2	-414.3	-646.6
dry2	0.042	0.019	0.098	0.015	5	2	-465.8	-630.0
dry3	0.050	0.017	0.123	0.016	0	3	-433.9	-684.4
dry4	0.068	0.015	0.195	0.015	6	2	-379.4	-699.6
lush1	0.025	0.024	0.026	0.069	10	9	-587.2	-653.2
lush2	0.032	0.027	0.019	0.089	14	10	-549.7	-626.3
lush3	0.038	0.027	0.001	0.084	14	9	-519.3	-633.1
lush4	0.028	0.024	0.012	0.067	11	9	-571.9	-648.1
lush5	0.048	0.033	0.018	0.097	14	9	-457.3	-583.9

In this case, the various measures exhibit broadly the same trends as RMSE (particularly AIC). However certain features are emphasized e.g. Δ(NDVI) varies more strongly then RMSE in the 1 kernel lush grass case and is actually more sensitive

generally. Table **7.3** highlights the fact that RMSE may not always be the best (or most appropriate) measure of model fit, particularly when modelling biophysical processes. This fact should be considered (along with parameter constraint and energy conservation requirements) in any implementation of a full spectral directional kernel-driven model of ρ_{canopy}.

7.5 A spectral directional kernel-driven model of ρ_{canopy}

In order to test the spectral kernels fully (as they would be applied in practice) they must be applied in conjunction with the angular kernels (equations **7.4** and **7.5**) to samples of spectral directional reflectance. In order to provide a stable comparison (avoiding the ambiguities that may be introduced at all stages during field measurement of such data), spectral directional reflectance data were generated using the physically-based canopy reflectance model of Nilson and Kuusk (1989). This model was used as it can be run in forward and inverse modes quite rapidly. Reflectance data were generated for canopy configurations as follows:

- LAI of 0.1 and 4 (sparse and dense canopy cases).
- θ_v varying from -75 to 75 degrees ($\theta_i = \phi_{i,v} = 0^\circ$) in steps of 5°.
- Spectral bands varying from 400 to 2500nm in steps of 20nm.

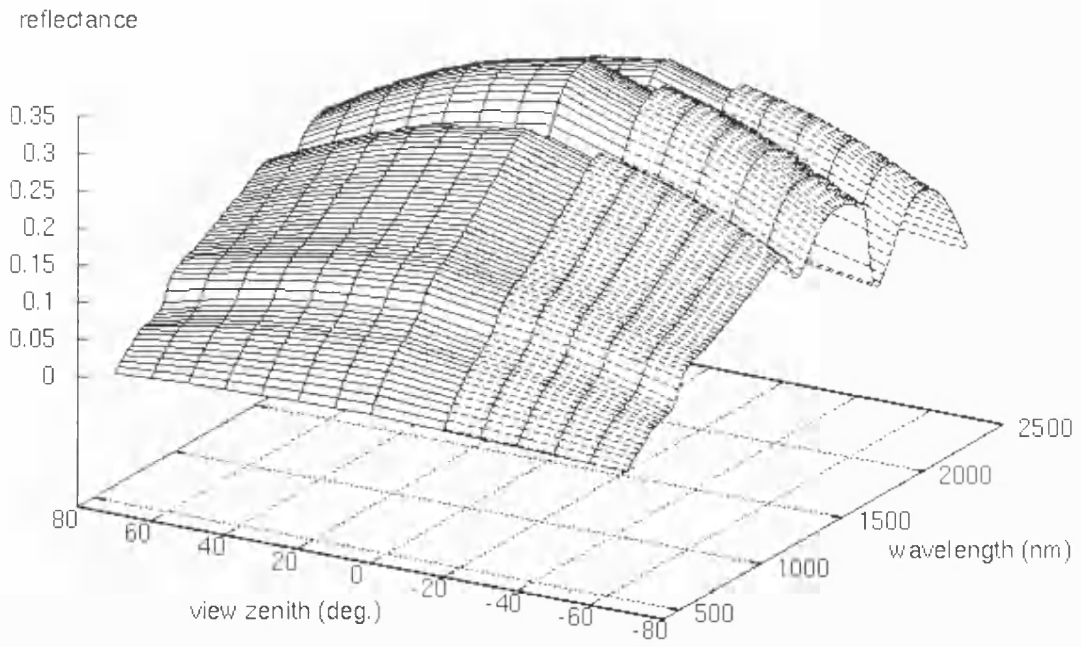

Figure 7.13 Simulated ρ_{canopy}, LAI = 0.1, $\theta_i = 0^\circ$.

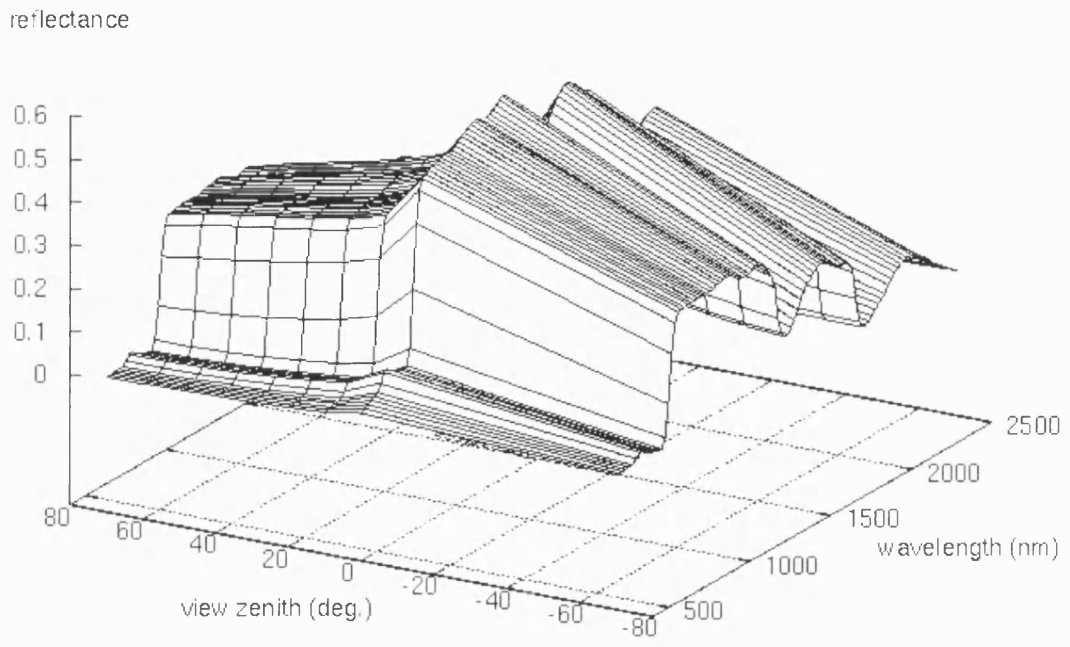

Figure 7.14 Simulated ρ_{canopy}, LAI = 4, $\theta_i = 0°$.

Figures **7.13** and **7.14** show the simulated spectral directional ρ_{canopy} data for low and high LAI cases (0.1 and 4 respectively). The LAD for each canopy was uniform. Spectrally, the low LAI case is unsurprisingly very close in shape to soil reflectance, while the high LAI case is typically characteristic of vegetation. In directional terms, the low LAI canopy possesses a shallow, inverted 'bowl-shape' with a relatively low overall magnitude (maximum of around 30%). The high LAI case is relatively flat in the visible region, with a peak in the hotspot direction but is more significantly peaked across the red edge and into the NIR. Reflectance is generally higher overall in this case, rising to close to 70% at nadir in the NIR.

The full spectral directional linear kernel-driven model (equations **7.2** and **7.4**) was inverted against the simulated ρ_{canopy} data, generating modelled estimates of directional and spectral reflectance, each with the associated model kernel weights, forward modelled reflectance components, and RMSE values. The spectral kernels were inverted against the spectral estimates of ρ_{canopy} (first term of equation **7.5**) while the angular kernels were inverted separately against the angular samples of ρ_{canopy} in each waveband (second term of equation **7.5**). It should be noted that in future applications the set of kernels will include spectral and angular terms, which will be inverted together against ρ_{canopy}. In this way the kernels will be explicitly linked. This raises the possibility that the spectral kernels may end up fitting angular reflectance variations (and vice versa),

as the inversion process simply minimises e^2 between observed and modelled values of $\rho_{canopy}(\lambda, (\Omega, \Omega'))$, and does not discriminate between "angular" and "spectral" variation. However it is likely that the fit of spectral kernels to $\rho_{canopy}(\lambda)$ and angular kernels to $\rho_{canopy}(\Omega, \Omega')$ will achieve this. If necessary, constraints can be applied to enforce this.

As in previous chapters, the RossThick and LiSparseModis kernels are used (volumetric and GO kernels respectively). The spectral kernels are applied in varying combinations to modelling the spectral component of the simulated samples of ρ_{canopy}. The number of separate soil and vegetation spectral kernels applied to each set of simulated ρ_{canopy} (varying LAI) is varied between one and three. Hence, the minimum total number of spectral kernels is two (one soil and one vegetation) and the maximum is six (three soil and three vegetation). Results are presented as follows:

- **Original spectral reflectance against reflectance reconstructed using spectral kernels and scatter plots of one against the other.**
- **Analysis of RMSE and residuals for different numbers of kernels.**
- **Original directional reflectance against reflectance reconstructed using angular kernels and scatter plots of one against the other.**
- **Directional component of reconstructed spectral reflectance and comparison with spectral component of reconstructed directional reflectance (c.f. chapter 6).**

7.5.1 Performance of spectral kernels against simulated spectral directional ρ_{canopy}

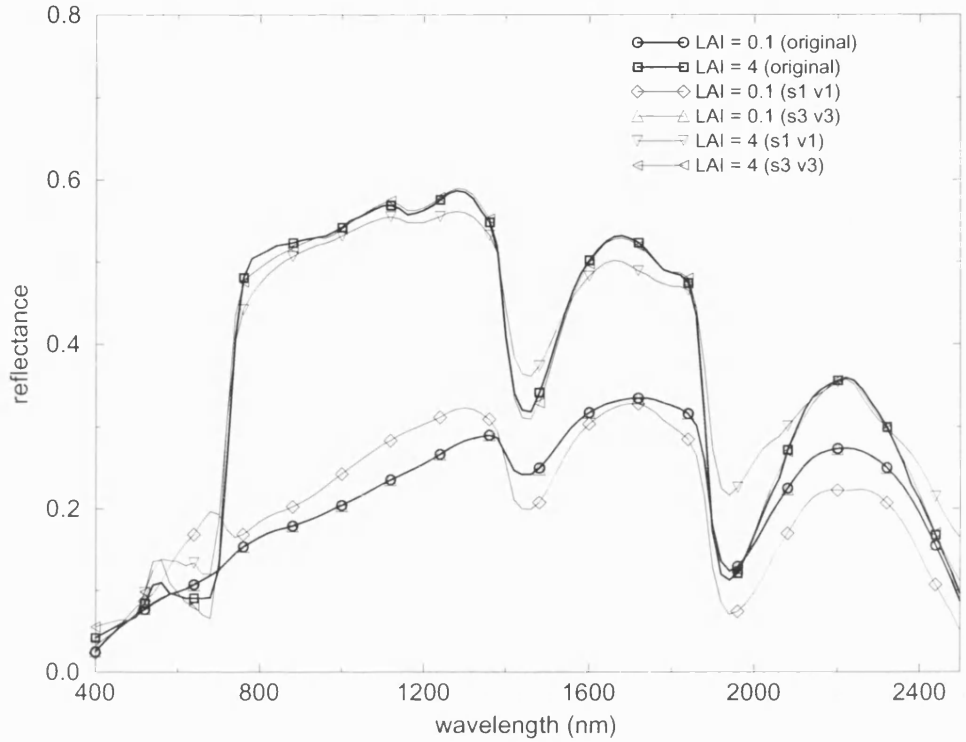

Figure 7.15 Demonstration of spectral kernels' ability to reconstruct spectral reflectance for two LAI cases, for two separate kernel combinations ($\theta_v = \theta_i = 0°$).

Figure **7.15** shows results from inverting a spectral kernel-driven model against simulated ρ_{canopy} (labelled **original**) for low and relatively high LAI canopies (0.1 and 4 respectively). Inversions of one soil plus one vegetation kernel (labelled **s1v1**), and three soil plus three vegetation kernels (labelled **s3v3**) are shown. It can be seen immediately that in most cases the spectral kernels do an excellent job of reconstructing $\rho_{canopy}(\lambda)$, particularly across the red edge in the high LAI case and in the NIR. An exception to this is for the low LAI canopy when only two kernels are used. This configuration lacks the flexibility required to accurately reconstruct observed reflectance. As a result the forward modelled reflectance spectra overestimate reflectance in the visible and SWIR and underestimate at longer wavelengths. This inflexibility is also apparent in the high LAI case, particularly in the water absorption features at 1600 and 1850nm where reflectance is over-estimated by the **s1v1** kernel combination. RMSE values for these inversions are given in table **7.4**. In terms of using a spectral kernel approach to derive albedo, the magnitude of RMSE suggests that more than one soil and vegetation kernel should be used, in order to keep error below 1 or 2% if possible.

Table 7.4 RMSE of inversion of spectral kernels against reflectance data.

LAI	kernel combination	RMSE (%)
0.1	s1v1	3.96
0.1	s3v3	0.086
4	s1v1	3.67
4	s3v3	0.981

Figures **7.16** and **7.17** show scatter plots of original against forward modelled reflectance for the low and high LAI cases, for each kernel combination (s1v1, s2v3, s3v3) and for three separate view zenith angles (nadir, 30° and 60°). For the LAI = 0.1 case, correlation increases dramatically from the two to four kernel cases, less so for the four to six kernel cases. Again, the largest discrepancies appear at lower reflectance values, particularly for the s1v1 case. The LAI = 4 case shows distinctly higher correlation for the s1v1 cases. In the low LAI case, r^2 tends to decrease with decreasing view zenith angle, particularly for the s1v1 case. The reverse is true for the high LAI case.

Figure **7.18** shows a scatter plot of the combined results presented in figures **7.16** and **7.17**. The correlation for both LAI cases is generally high, with the LAI = 4 having a slightly higher value of r^2. The disagreement is greatest at lower reflectance values (below 0.15) as observed previously. Figure **7.18** illustrates clearly the effectiveness with which the spectral kernels can model the spectral component of $\rho_{canopy}(\lambda,(\Omega,\Omega'))$, particularly if more than one soil and vegetation kernel are used. Results illustrating the separation of the vegetation and soil component are shown in the next section.

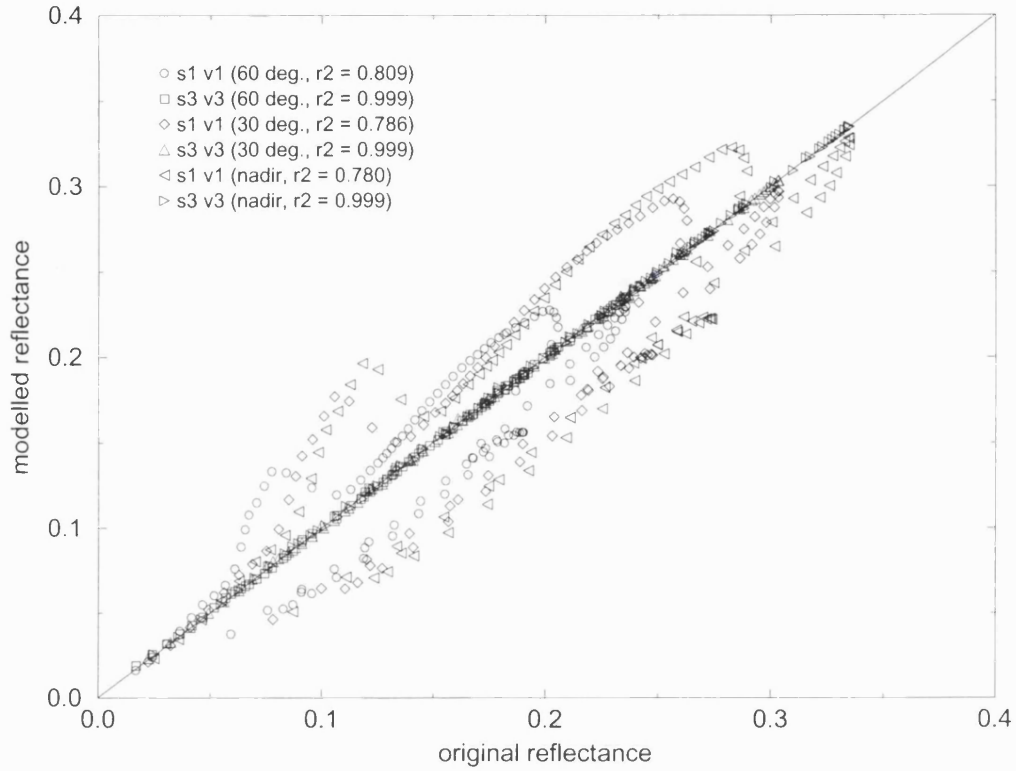

Figure 7.16 Original against modelled reflectance, LAI = 0.1.

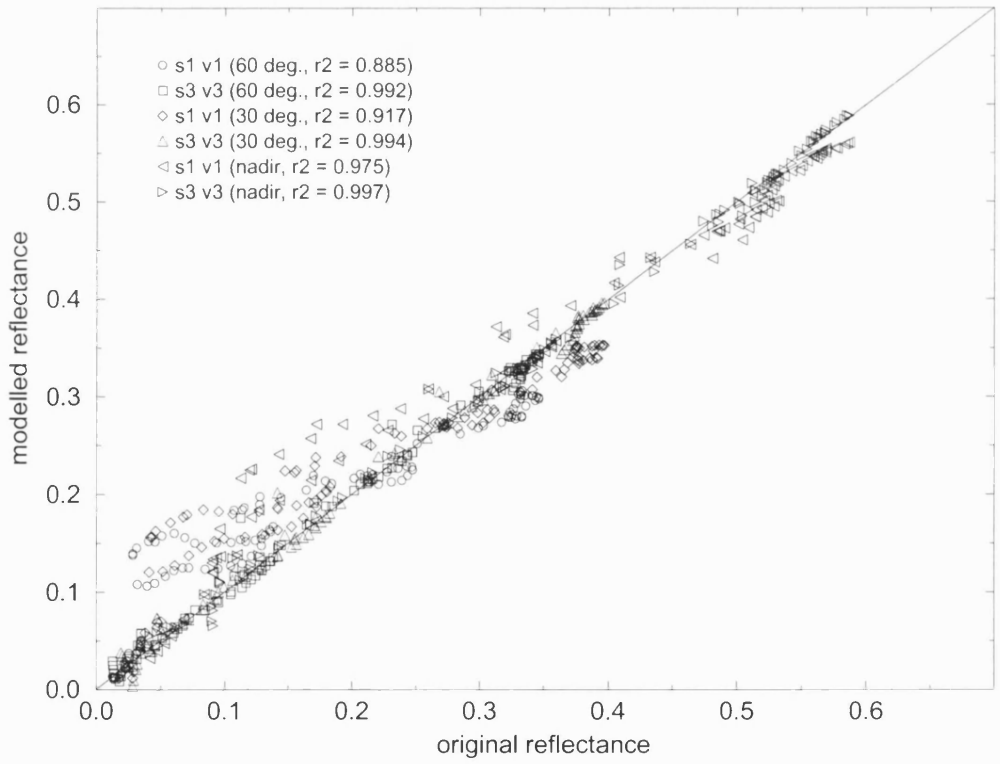

Figure 7.17 Original against modelled reflectance, LAI = 4.

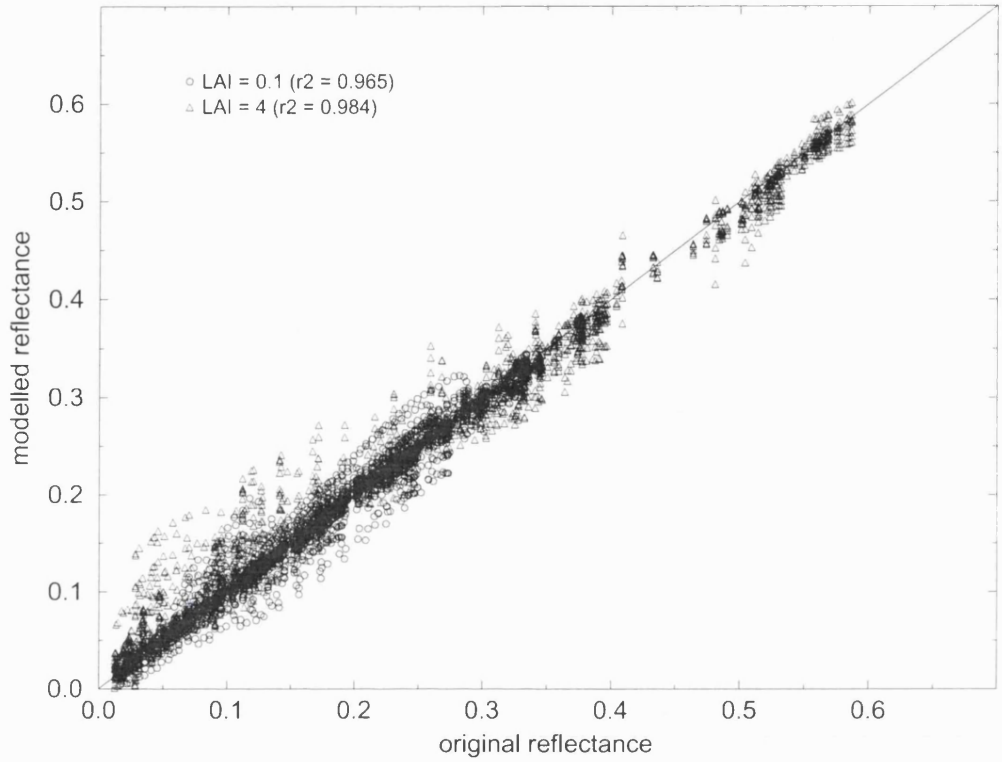

Figure 7.18 Scatter plot of all view zenith angles and kernels combinations.

Figure **7.19** shows the residuals associated with the model fitting of figures **7.16** and **7.17**. The residuals indicate that the model fit is (unsurprisingly) poorest for the two kernel case (**s1v1**) for both canopies. In particular, the kernels underestimate reflectance in the visible by up to 7% for both canopies. In the NIR, results differ for the two canopies, with the kernels continuing to underestimate reflectance in the LAI = 0.1 case, and overestimate in the LAI = 4 case. The residuals swap signs at around 1380nm before fluctuating in the 2000nm range as a result of the inability to follow the water absorption features. The residuals for the six kernel cases (**s3v3**) are very much smaller, indicative of the better fit obtained. The residuals in the case of the low LAI canopy are close to zero across the spectrum, while for the high LAI case, the only significant residuals are in the visible region, with residuals of around +/-3%.

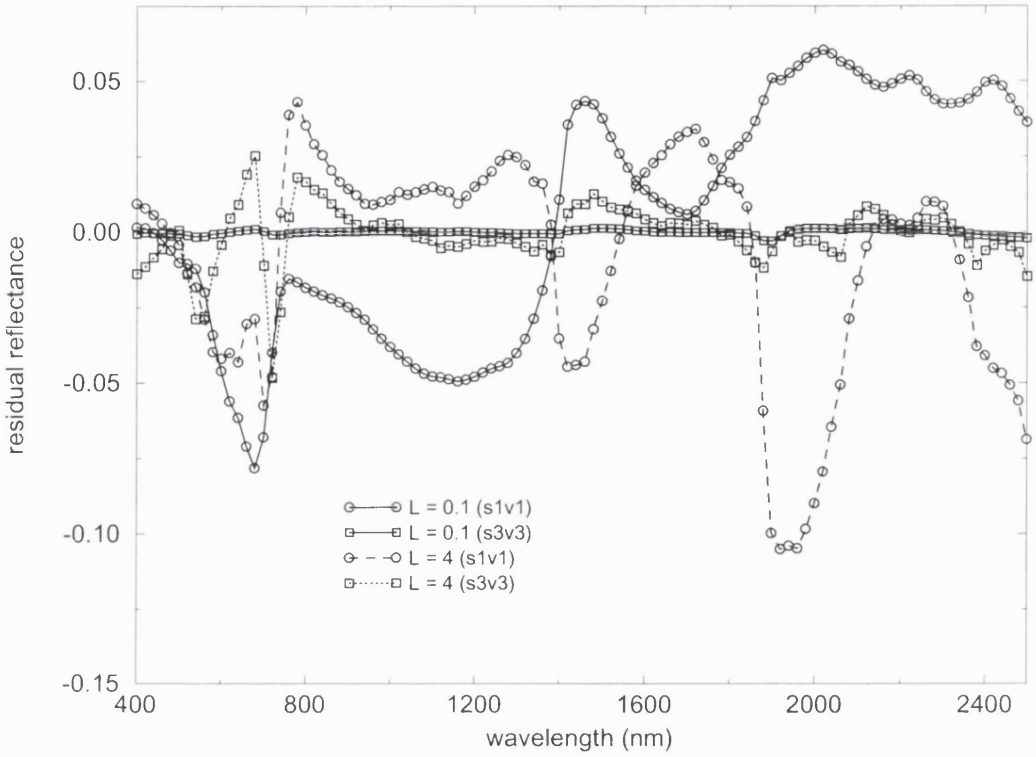

Figure 7.19 Residuals from fitting spectral kernels to reflectance data.

7.5.2 Separation of soil and vegetation components

One aim of developing the spectral kernels is to allow the separation of the spectral soil and vegetation components of $\rho_{canopy}(\lambda)$. Results presented below show the spectral components of soil and vegetation reflectance extracted with the spectral kernels from the original ρ_{canopy} values. Figures **7.20** and **7.21** show the original spectral reflectance, as well as the modelled soil and vegetation components for the low and high LAI canopies respectively. The components of the two and six kernel inversions are shown and labelled respectively as **s1, v1 (k=2)** and **s[1,2,3] v[1,2,3] (k=6)**, where the s and v represent the number of soil and vegetation kernels respectively, as before. If the kernels *are* able to separate the spectral soil and vegetation components of ρ_{canopy}, it would be expected that the soil kernels would dominate the soil component with minimal contribution from the vegetation kernels and the vegetation kernels would dominate the vegetation component.

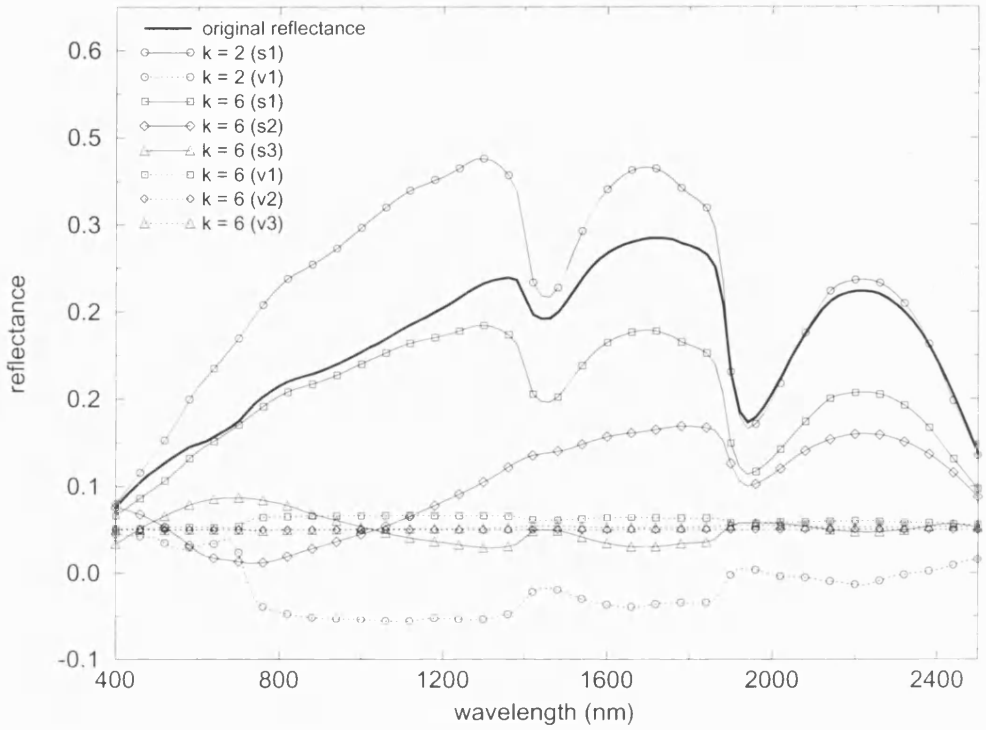

Figure 7.20 Soil and vegetation model parameters, LAI = 0.1.

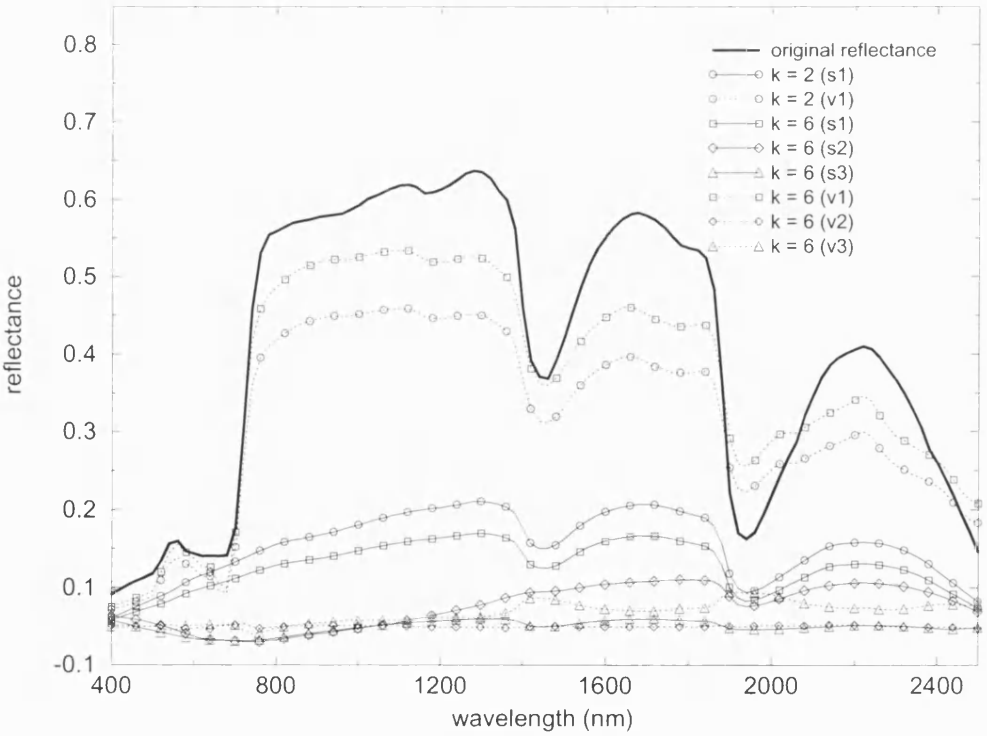

Figure 7.21 Soil and vegetation model parameters, LAI = 4.

For the low LAI canopy **s1v1** case, the single soil parameter dominates reflectance as would be expected. However, the vegetation parameter is exclusively negative (acting to reduce overall reflectance) indicating that one soil kernel is not sufficient to describe the soil component accurately. The soil parameter strongly overestimates reflectance in the visible and SWIR but matches reflectance quite closely at longer wavelengths, particularly in the water absorption feature at 1850nm. For the six kernel case, the first two parameters dominate the modelled reflectance and the third soil parameter is very much smaller, suggesting that two soil kernels may well be enough in some cases. The vegetation parameters are all close to zero.

For the high LAI case, the separation of the soil and vegetation components is even clearer. In both the two and six kernel cases the vegetation parameters dominate reflectance. In the former case, although the single vegetation parameter dominates, particularly in the visible and NIR regions, the soil parameter contributes up to about 15% of total reflectance, mainly beyond 1000nm. For the six kernel case, the first vegetation parameter is significantly larger than the corresponding parameter in the two kernel case, with the first soil parameter being lower. The remaining two soil parameters are close to zero. These results indicate that the kernels are quite capable of separating soil and vegetation components of spectral reflectance, even in a potentially tricky case such as a high LAI canopy where the single scattering contribution to soil reflectance is likely to be small due to the density of the canopy.

Figures **7.22** and **7.23** are scatter plots of all soil and vegetation components of forward modelled reflectance respectively, for both LAI cases. Correlation for the soil component is almost identical for both canopies (r^2 values of 0.837 and 0.833 respectively). There is, however, a significant negative component for the high LAI canopy, where the magnitude of the original soil component is very low, and is generally much smaller than the vegetation component. However, the primary conclusion is **that the soil kernels can successfully separate the soil component of ρ_{canopy} and do it equally well for high or low LAI canopies.**

Correlation between the original and forward modelled vegetation components of the low LAI canopy shown in figure **7.23** is close to zero. This suggests that the vegetation kernels have trouble separating out the vegetation component of ρ_{canopy} when it is small in comparison to the soil component. For the high LAI case correlation is

virtually the same as in both the soil cases (r^2 value of 0.83). The modelled vegetation component is overestimated by around 7-10% across all values. This is reflected in the slope of the regression relation (0.9) and the intercept of 0.09. These two results suggest the soil kernels are perhaps more flexible in being able to separate out the soil component in both high and low LAI canopies. The vegetation kernels can also separate out the vegetation component from ρ_{canopy}, but tend to struggle when the soil component dominates.

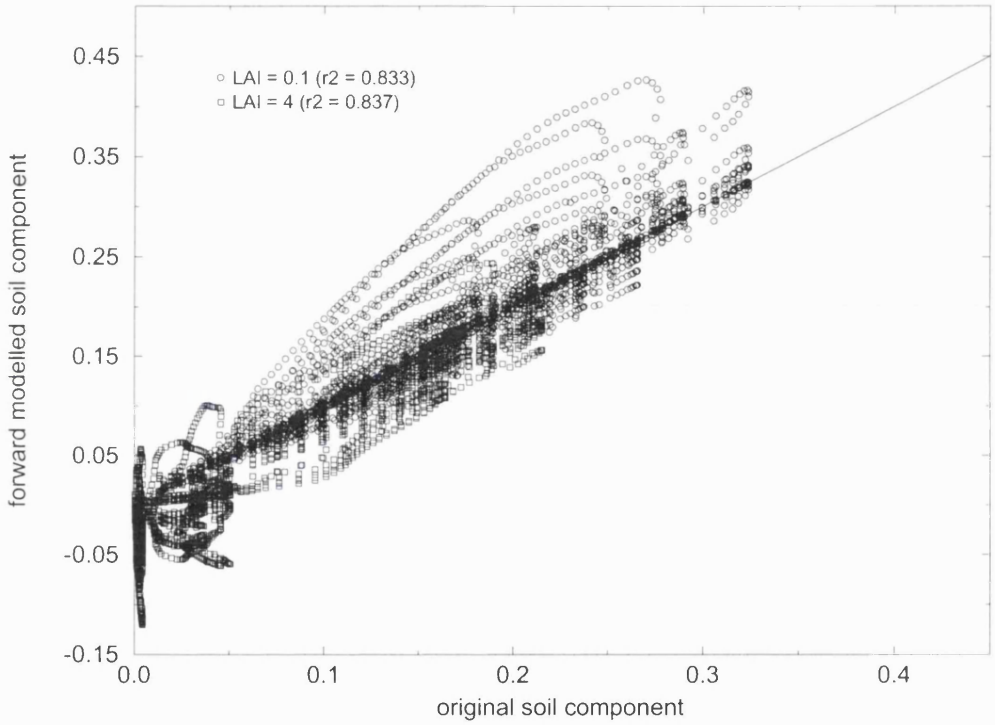

Figure 7.22 Scatter plot of soil components of ρ_{canopy}, two LAI cases.

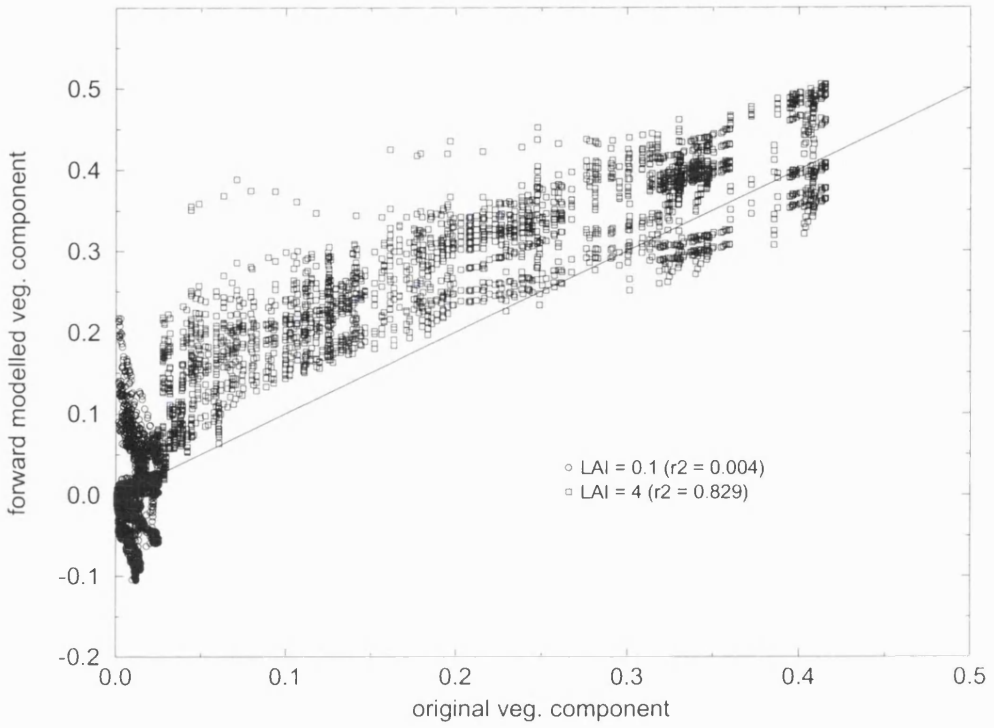

Figure 7.23 Scatter plot of vegetation components of ρ_{canopy}, two LAI cases.

7.5.3 Reconstruction from limited wavebands

Reconstruction of full spectrum reflectance has so far been carried out by inverting kernels against reflectance samples generated at wavelength intervals of 20nm from 400 to 2500nm. In order to demonstrate the kernels' ability to interpolate from limited samples of reflectance, a brief demonstration of the inversion of the kernels against selected MODIS wavebands at visible and NIR wavelengths is presented. A limited set of available MODIS wavebands was selected to coincide with (in particular) visible blue, green and red, as well as NIR reflectance features. These bands are **443.0**, **469.0**, **555.0**, **645.0**, **858.5**, and **940.0nm**. The small number of bands provides a more stringent test of the kernels' ability to interpolate (and potentially extrapolate) limited reflectance samples and reconstruct full spectra. Figure **7.24** shows the inversion of the s1v1 and s3v3 kernel combinations against six reflectance bands.

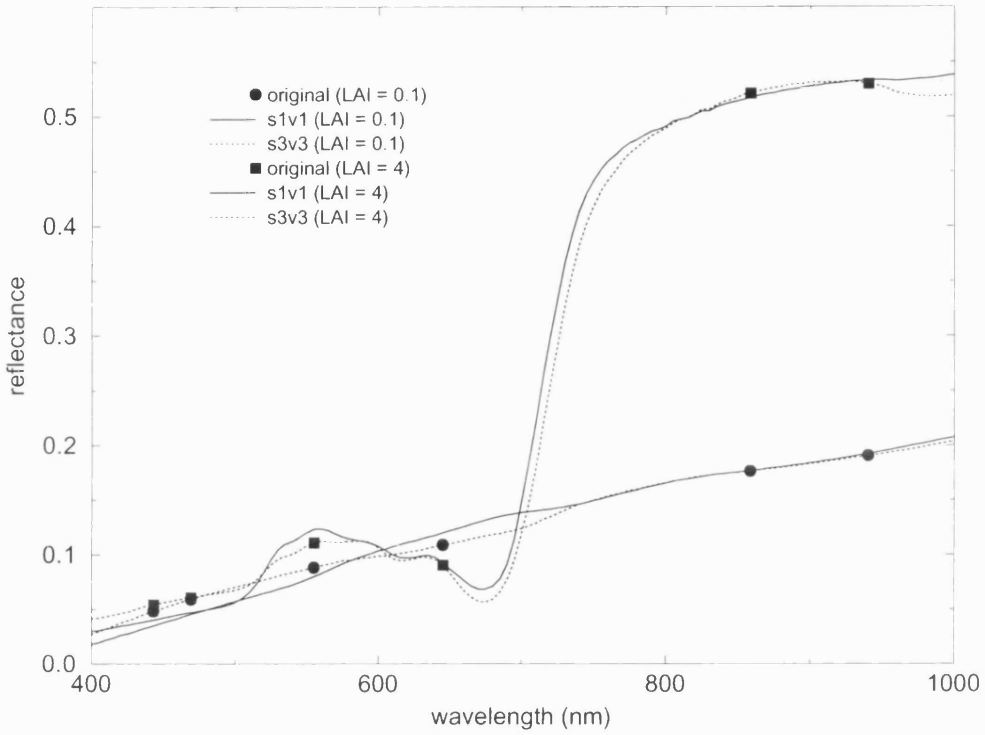

Figure 7.24 Reflectance generated from samples at selected MODIS wavebands.

Figure **7.24** shows that the spectral kernels can reconstruct full spectrum reflectance from limited wavebands very effectively. Even with only six reflectance bands (just enough to perform a valid inversion) the forward modelled reflectance agrees extremely closely with the original values, particularly for the **s3v3** case. The RMSE values in each case are correspondingly small, 9×10^{-3} for both **s1v1** cases and 4×10^{-7} for the **s3v3** cases. If the reconstructed spectra are to be used for spectral interpolation (e.g. for production of broadband shortwave albedo), rather than direct interpretation, then the spectral kernels may permit better use to be made of available reflectance information than is currently the case. Typically, broadband albedo is derived from limited samples using simple convolution across the solar spectrum, or with empirical coefficients derived for particular sensors (Liang, 2000; Liang *et al.*, 2000c).

Figure **7.25** shows scatter plots of original against forward modelled reflectance values given in figure **7.24**. The correlation is extremely high, with r^2 values exceeding 0.99 in all cases. It should be noted that in practice, spectral sampling will become an issue for the application of spectral kernels as angular sampling is for the angular kernels (Lucht and Lewis, 2000). The location of spectral samples (and the bandpass of the

instrument under consideration) will have an impact on the error associated with inversion of the spectral kernels against spectral reflectance data.

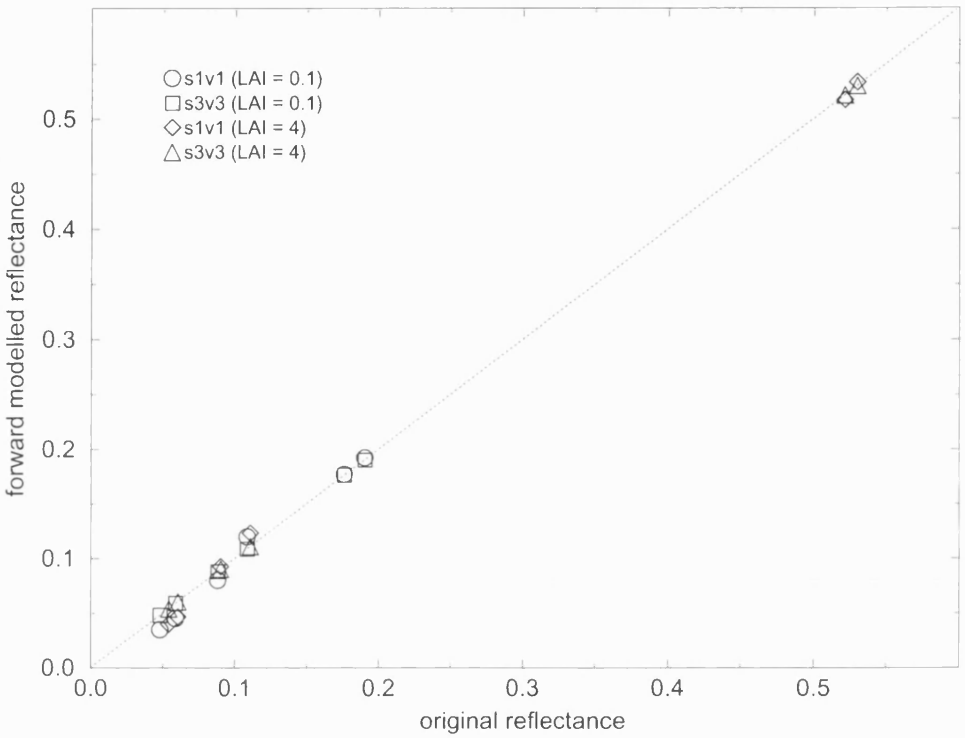

Figure 7.25 Scatter of reflectance generated at selected MODIS wavebands (1 soil + 1 vegetation and 3 soil + 3 soil kernels).

7.5.4 Directional component

Following analysis of the spectral kernels' ability to reconstruct the spectral component of $\rho_{canopy}(\lambda,(\Omega, \Omega')$ the directional component of the spectral kernels is briefly examined. Although the spectral kernels are independent of view zenith angle (in the same way that the angular kernels are independent of wavelength), they may contain directional information. This is analogous to the spectral variation seen in the inverted directional kernels shown in chapter **6**. Figure **7.26** shows the soil and vegetation spectral kernel parameter values for the **s1v1** case plotted as a function of view zenith angle (the **s3v3** cases are not shown as they follow the same patterns but with each successively reducing in magnitude). For the low LAI canopy the soil kernel, **s1,** dominates as expected. The angular variation of **s1** is characteristic of the GO component of $\rho_{canopy}(\Omega,$

Ω') seen in chapter **4**. The vegetation kernel, **v1**, is close to zero, as expected. For the high LAI canopy, the soil kernel is slightly above zero while the vegetation kernel is sharply peaked in the hotspot direction. This strongly resembles the directional variation of the volumetric component of $\rho_{canopy}(\Omega, \Omega')$ seen in chapter **4**.

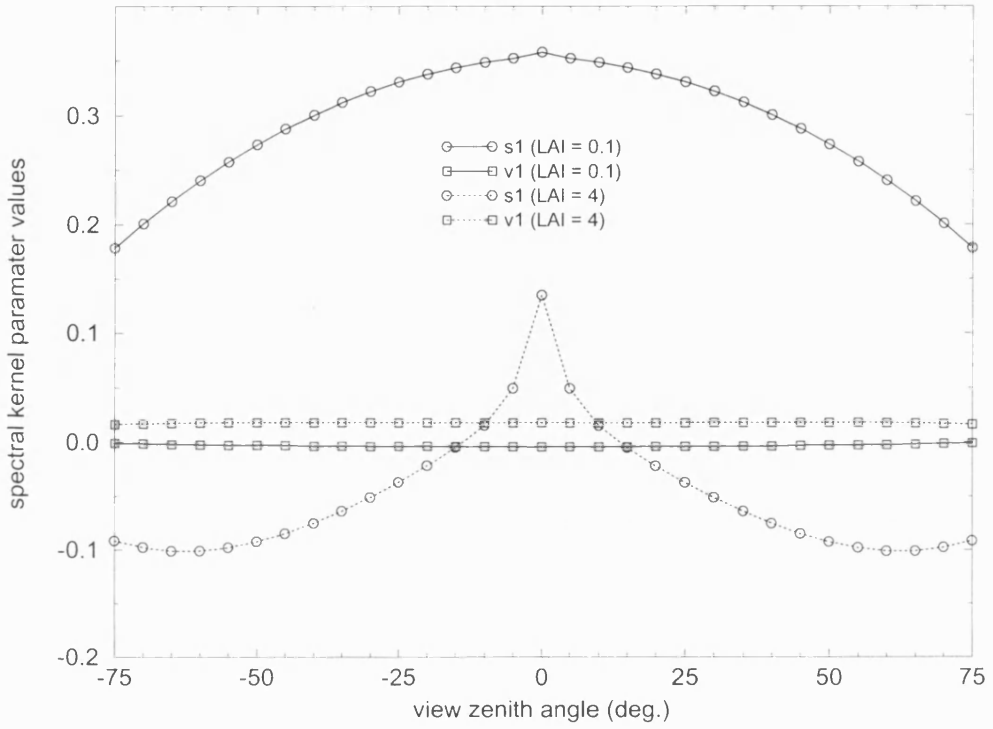

Figure 7.26 Angular variation of inverted spectral kernel parameter values (s1v1 case).

The observation that the soil and vegetation spectral kernels contain angular information related to the GO and volumetric angular kernels is confirmed by regression of the spectral kernel parameter values against the respective volumetric and GO components of BPMS simulated canopy reflectance. Using volumetric and GO components of BPMS-derived canopies with similar LAI to those used above (wheat canopy of 23rd March, LAI = 0.9; barley canopy of 13th May, LAI = 3.9) r^2 values of greater than 0.95 were obtained for the GO components of both canopies. Values of r^2 for the relationship between volumetric components were greater than 0.85. These results indicate that the spectral kernels are likely to contain angular information when inverted against directional data.

It is intended that the spectral kernels be developed more fully, integrated with the angular kernels into a spectral directional kernel-driven model and tested on airborne and spaceborne remote data, with the eventual aim of producing spatial estimates of spectral

estimates of albedo. This is discussed in more detail in chapter **8**, but a demonstration of spectral kernels ability to retrieve spatial estimates of soil and vegetation parameter information is given below.

7.5.5 Demonstration of spectral kernels against airborne reflectance data

The effectiveness of the spectral kernels to reconstruct spectral reflectance has been demonstrated. The final part of this experiment presents a brief example of the application of the spectral kernels (three soil and three vegetation) to airborne data over Barton Bendish, shown in figure **7.27**. This demonstrates the possibilities for using the spectral kernels to generate spatial estimates of spectral model parameters.

The false colour composite (FCC) original ATM image shown at the top left of figure **7.27** forms part of multiple flight lines of data collected over the Barton Bendish area on various dates (described in section **3.1.5**). These data are geometrically but not atmospherically corrected (due to a lack of information on atmospheric conditions during the overpasses, such as aerosol optical depth, water vapour and ozone concentrations). Pixel radiance values are weighted by a solar irradiance spectrum calculated for the date and time of the overpass. The inverted soil and vegetation parameters are also shown as FCC images i.e. first, second and third soil parameter on the red, green and blue channels respectively and the same for the vegetation parameters.

It can be seen in figure **7.27** that the soil parameters are bright where the original false colour composite ATM image is blue-ish, corresponding to soil areas and darker where there is likely to be vegetation (red in FCC). The third soil parameter is dominant over the farm area (see figure **3.1**) which comprises harvested crops (stubble) and sugar beet. This behaviour contrasts with that over the airfield at the top of the image (areas covered by short grass and tarmac) where the first soil parameter is dominant. The vegetation parameters are generally bright where the likelihood of vegetated cover is highest in the original FCC image. The first parameter (and the third parameter to a lesser extent) is dominant except over the airfield, where the second parameter is bright resulting in a green colour. Interestingly, the RMSE image shows consistently lower values for areas of vegetation, than for bare soil. This figure demonstrates that there is significant information in spatial estimates of spectral model parameters, not only in

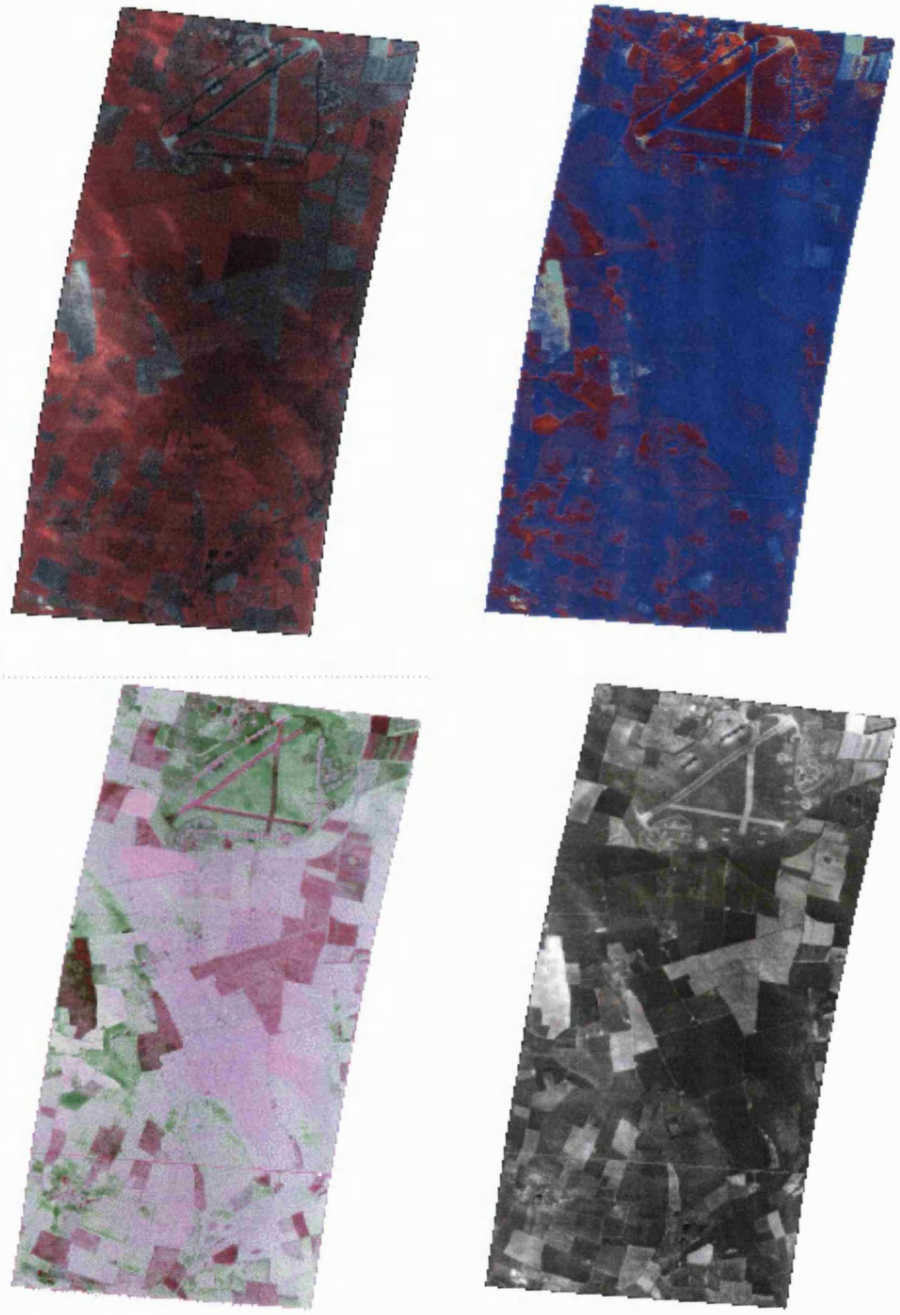

Figure 7.27 Top left, FCC of NIR, red and green bands, ATM image, June 6th 1997; top right, soil parameters (FCC parameters 1, 2 and 3); bottom left, vegetation parameters (FCC parameters 1,2 and 3); bottom right, RMSE image of inversion.

regard to differentiating areas of soil and vegetation cover but also in separating the spectral behaviour of different soil and vegetation types.

Figure **7.28** shows a scatter plot of original against modelled pixel values selected randomly from the original ATM image. Agreement between the two is high with an r^2 value of 0.96 when all bands are considered together. Individually, the only bands where

r^2 values fall below 0.9 are 435nm (possibly due to atmospheric scattering which is significantly higher at shorter wavelengths), 615nm and 830nm. The close agreement overall demonstrates the ability of the spectral kernels to describe spectral reflectance of soil and vegetation. In addition, the kernels appear to be capable of generating spatial estimates of soil and vegetation scattering components. This has far greater theoretical justification than an empirical estimate of vegetation such as NDVI and is nearly as rapid to apply. It will be straightforward to apply the full spectral directional kernel driven model to spectral directional reflectance data in the future, and use the resulting parameter values to interpolate estimates of narrowband albedo to broadband. This is discussed briefly in chapter **8**.

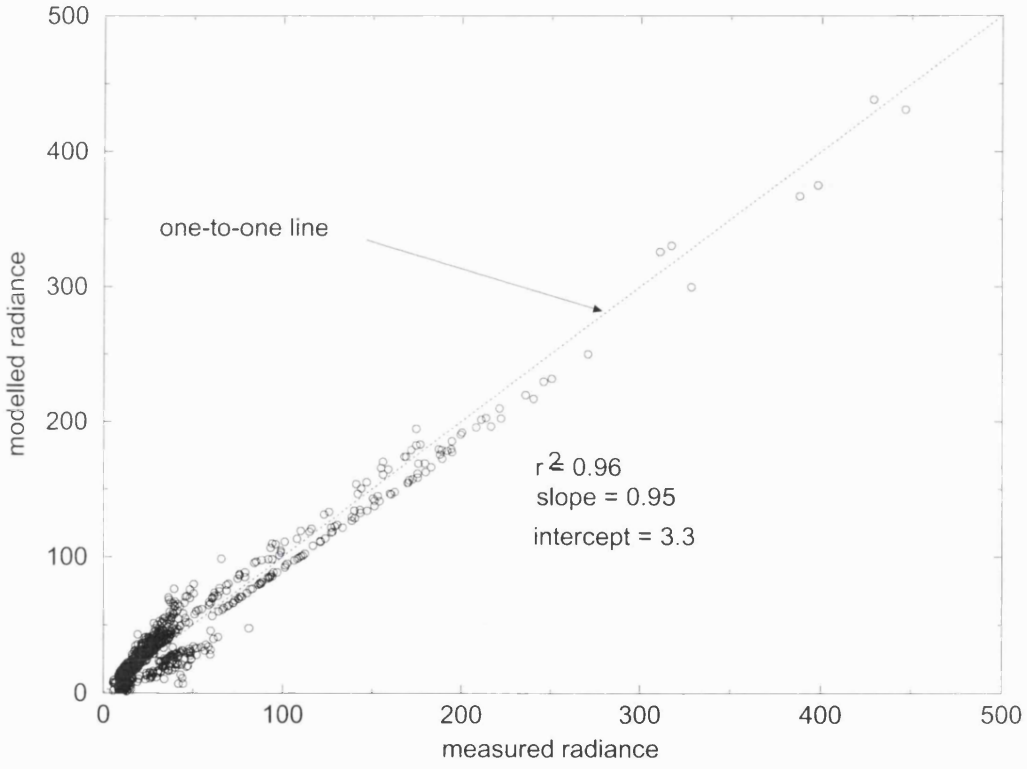

Figure 7.28 Scatter of original against modelled radiance values (using spectral kernels) for random points within ATM image of figure **7.27**.

7.6 Conclusion

It has been demonstrated that the concept of a spectral directional kernel driven model of $\rho_{canopy}(\lambda, (\Omega, \Omega'))$ is feasible. Results indicate that such a model is likely to provide significant improvement over current kernel-driven models of directional reflectance, which operate independently of wavelength. It is shown that vegetation kernels derived from PCA of measured laboratory reflectance and transmittance spectra (combined as single scattering albedo) are capable of accurately describing spectral reflectance of a number of vegetation types. Some green vegetation spectra can be described adequately using only one vegetation kernel, but in most cases two or three kernels are necessary. In conjunction with two or three soil kernels, derived by Price (1990), it is shown that spectral canopy reflectance can be modelled very accurately. This approach is similar in some ways to linear unmixing (Settle and Drake, 1993), but differs in that the aim is to allow spectral interpolation of limited samples of reflectance, rather than the derivation of spectrally 'pure' end-members.

Results also show that the spectral kernels are highly effective in separating the constituent soil and vegetation components of spectral canopy reflectance. This is of significance for studies of photosynthetic activity (fAPAR), canopy efficiency and general vegetation influence, where it is desirable to be able to isolate the contribution of the vegetation component to total ρ_{canopy}. The vegetation spectral kernels are particularly successful for canopies with LAI > 0.5. Even with only two or three vegetation spectral kernels it is likely that the majority of the single scattering contribution of vegetation reflectance to $\rho_{canopy}(\lambda)$ can be extracted in most cases. The implication is that in cases where limited spectral sampling is available (e.g. MISR data, with only four bands), the kernels can act as spectral interpolants to generate full spectrum estimates of reflectance.

The spectral kernels can be simply combined with the directional kernels discussed in previous chapters to provide a full spectral, directional kernel-driven model of $\rho_{canopy}(\lambda, (\Omega, \Omega'))$. Inversion of this type of model against simulated reflectance data indicates that full spectrum reconstruction of spectral directional reflectance from limited spectral directional samples is very accurate. As an example, reconstruction from selected MODIS wavebands is demonstrated. Derived spectral model parameters may well contain directional information, similar to the spectral information contained in the derived angular parameter values seen in chapter **6**.

The success of the spectral kernels in reconstructing spectral reflectance confirms their utility as spectral interpolants, although much further validation is required in order to confirm their applicability. This will be of use for converting narrowband to broadband albedo and this will comprise the main direction for further research based on the spectral kernels. The next stage will be to test the kernels on aerial and spaceborne reflectance data in order to produce full shortwave spectrum reconstructions of reflectance data from limited spectral samples (an example of the spectral kernels' ability to describe spatial estimates of surface scattering and separate soil and vegetation scattering components is shown). These will then be used to generate shortwave albedo from airborne and spaceborne remote sensing data. A full spectral directional kernel-driven model can then be inverted against remotely sensed directional spectral reflectance data, such as that currently being produced by the MODIS instrument. Shortwave albedo can then be compared with the current operational MODIS albedo product. It is foreseen that the spectral directional kernel-driven model will greatly reduce the need for assumptions regarding atmospheric state and instrument band pass behaviour when interpolating narrowband samples of directional reflectance to produce broadband albedo. This is discussed in more detail in chapter **8**.

Recent follow-up work by colleagues on the spectral kernels has indicated that it may be more effective to separate fresh and dry reflectance and transmittance spectra when generating the kernels in order to generate separate fresh and dry kernels (Collings, 2001). Using a suite of kernels in this manner (using the best fitting for a given circumstance) may be operationally feasible given that the computational overhead of inversion is very small. This is equivalent to the original AMBRALS (**A**lgorithm for **M**ODIS **B**idirectional **R**eflectance and **AL**bedo) algorithm proposed for MODIS processing (Wanner *et al.*, 1997), where a range of angular kernel combinations are inverted against each reflectance sample.

The final chapter sums up the results presented in this thesis, highlighting the most significant results. Areas related to this work where research is currently progressing are described, particularly in regard to the extension and application of the spectral kernels as part of a full spectral directional kernel-driven model. Suggestions are also made for where future research related to these topics might be directed.

8 Conclusions and directions for further work

8.1 Exploring the concept of linear kernel-driven models

This thesis sets out to explore the assumptions underlying the development and application of linear kernel-driven models of BRDF. The simplified semi-empirical approach to modelling ρ_{canopy} underlying such models is examined, as is their potential for extracting biophysical information from reflectance data. Results presented here show that the linear kernel-driven models largely conform to the assumptions made in their formulation. In particular, evidence indicates that it is often justifiable to consider canopy scattering as a linear combination of volumetric and GO scattering components. This justification is less clear-cut in cases where the canopy departs markedly from the assumptions made in the kernel-driven models, particularly in a structural sense (strongly clumped, non-spherical LAD etc.). It has also been demonstrated that the volumetric and GO kernels are, in general, linearly related to the volumetric and GO components of canopy scattering, as would be expected if the kernels operate as intended. The relationship is generally much stronger for the volumetric component than for the GO component. This relationship has not previously been established quantitatively. In the past, the fact that the linear kernel-driven models tend to fit observed reflectance well has been used to justify their simplified nature.

Detailed 3D structural models of vegetation based on field measurement of canopy structure were used to simulate barley and wheat ρ_{canopy} over a growing season. Validation against measured data indicated that the models represented the radiometric response of the vegetation reasonably well. Variation between measured and modelled reflectance values was due to variability in both field measurements and intra-field crop density. Simulations of ρ_{canopy} were carried out under the same assumptions made in the formulation of the kernel-driven models i.e. independently of wavelength and considering only single scattering interactions and using a Lambertian soil surface.

The linear kernel-driven models assume that ρ_{canopy} can be treated as separate (purely geometric) volumetric and GO components. In practice, these components are described using a linear superposition of separate volumetric and GO kernels (with an isotropic brightness term representing the multiple scattering contribution). Simulated ρ_{canopy} was separated into its constituent volumetric and GO components. The volumetric component, related to scattering from vegetation only, was shown to behave as expected

for vegetation reflectance. The GO component (related to the proportion of visible sunlit soil in this case) does not agree precisely with expectations, in that a hotspot feature was not apparent due to the departure of the canopies used in the experiments from the ideal GO canopy visualised in the formulation of GO models of CR. The respective volumetric and GO canopy components were shown to change with the developing canopy as expected during the growing season. The volumetric component increased with increasing LAI until the canopy reached senescence. Conversely, the GO component reduced over time as a result of the soil becoming obscured by the developing vegetation.

Two fundamental hypotheses were presented, both of which must hold true for the kernel-driven models to be valid. Firstly, it must be possible to describe ρ_{canopy} as a linear combination of separate volumetric and GO terms. Results showed that in many cases this hypothesis was true, with strong linear relationships between the volumetric and GO scattering components and their respective kernels. However, there was significant variation, particularly in the relationship of the GO component to k_{GO}, the GO scattering kernel. This is a result of the fact that the GO component being modelled is significantly different from the theoretical GO component of ρ_{canopy} envisioned in the kernels (Li and Strahler, 1985, 1986; Wanner *et al.*, 1997), in particular, the canopy is composed of many relatively small leaves rather than scattering 'spheroids-on-sticks' (see **2.5.4.1.2**).

The agreement between the scattering components and their respective kernels was particularly noticeable in canopies with one dominant scattering component. The assumption broke down in more extreme cases when either there was very little vegetation present (and hence virtually no volume scattering) or else the canopy had senesced, with little green vegetation remaining. In these cases the canopy had diverged even further from the general assumptions of the linear models. Departure from the assumption of spherical LAD was shown to have a significant impact on the relation of the volumetric and GO components of canopy scattering to the respective model kernels. The tendency of agricultural canopies to have regular planting patterns exacerbates this by violating the assumption of azimuthal invariance. This can lead to significant clumping, particularly at early stages of growth. This appeared to impair the ability of the models to describe the reflectance of this type of canopy. Forests also tend to have non-uniform distributions of vegetation and/or LAD and may pose similar problems.

The second hypothesis examined was that the volumetric and GO components of

ρ_{canopy} can be described adequately by the volumetric and GO kernels alone. Results indicated that this hypothesis is true in some cases, with the individual scattering components of ρ_{canopy} being largely separable. Again, discrepancies tended to occur where the canopy departed from the assumptions of azimuthal invariance and spherical LAD. In these cases it was clear that some proportion of volumetric scattering was explained by the GO kernel, while conversely, some GO scattering was taken up by the volumetric kernel. This indicated an element of coupling between the kernels. The implication is that model parameter values need to be interpreted very carefully in practice. In cases where the vegetation canopy departs from the (structural) assumptions underlying the kernel-driven models it will not be possible to relate the model parameters directly to their respective scattering components.

Spectral estimates of the angular kernels were derived. As expected, the volumetric kernel tended (spectrally) to resemble ρ_{leaf} and the GO kernel resembled ρ_{soil}. In some cases the respective kernels clearly contained information regarding the other scattering component. In particular, the isotropic kernel appears to be correlated with ρ_{leaf} in some cases. As the canopies developed, the volumetric and GO parameters increasingly resembled each other, indicating an increased degree of coupling as well as the difficulty of separating the components in these cases. As a consequence it may not be possible to interpret parameter values directly without ancillary data, such as estimates of ρ_{leaf}. This may not be practical in many cases, for example in applications involving moderate resolution data with large areal coverage (thousands of km^2).

In nearly all cases the RossThick LiSparse kernel combination was the best fit to observed reflectance, supporting the choice of this combination as the primary model for processing MODIS reflectance data. The behaviour of the spectral estimates of the angular kernels indicates that they may be suited to classification of reflectance data, as they might be used as extra channels of information regarding scattering from soil and vegetation. In particular, the model parameters may be able to separate soil and vegetation scattering components, which will prove useful for studies of carbon budget, fAPAR and NPP. It was noted that, in some cases, derived values of the model parameters could take physically unrealistic (negative) values. This is not a problem if the parameters are to be used for classification for example, as in this case it is simply the relative values that are important. However, if the parameters are to be interpreted then inversion should be constrained so that parameter values are physically realistic.

8.2 Extension of the kernel-driven modelling concept

The linear kernel-driven models are based on the idea that simple volumetric and GO 'shape' terms can be combined to describe the dominant angular features of surface BRDF. This concept was adapted and extended into the spectral domain based on the observation that vegetation (and soil) spectral reflectance displays a number of common features. There are a number of benefits that a combined spectral directional kernel-driven model of ρ_{canopy} confers. Chief amongst these is the ability to interpolate narrowband samples of reflectance over a wide range of wavelengths. This is analogous to the application of the angular kernels to interpolate/extrapolate limited directional samples of reflectance to arbitrary viewing/illumination angles. This ability to interpolate (and possibly extrapolate) narrowband reflectance samples would be extremely useful in deriving albedo, which typically requires assumptions to be made regarding spectral weightings of narrowband reflectance samples and the shape of the solar spectrum. A spectral kernel-driven model will obviate the need for such assumptions. Another benefit is the ability to separate the spectral components of scattering from soil and vegetation. This is of particular importance in studies of fAPAR and NPP, where only scattering from vegetation is of interest. A further advantage is that spectral kernels will permit the combination of data from sensors with different bandpass functions. Spectral kernels could be used to 'normalise' spectral reflectance to some common set of wavebands. This is analogous to normalisation of directional reflectance to specified viewing and illumination angles (typically nadir) using the angular kernels.

Based on previous work deriving soil basis functions (or spectral kernels), a number of vegetation spectral kernels were derived from measured reflectance and transmittance spectra. It was demonstrated that three or four of these spectral kernels are sufficient to describe greater than 98% of observed variance in a large range of measured vegetation spectra. It was shown that a combination of five or six soil and vegetation kernels were able to describe observed spectral ρ_{canopy} extremely well. In some cases as little as two or three spectral kernels in total were required to adequately fit observed data. This is likely to be sufficient for many multispectral sensors, which tend to have four or more spectral bands. The spectral kernels were applied in conjunction with angular kernels to simulated values of spectral directional ρ_{canopy}. The full spectral directional kernel-driven model fitted the simulated reflectance values extremely well, with RMSE of $< 4\%$ in all cases. In cases where three soil and three vegetation kernels are used, RMSE

of fit falls to between 0.1% and 1%. The kernels were also shown to be capable of separating soil and vegetation spectral components of ρ_{canopy} successfully. Spectral estimates of the angular kernels were derived which illustrated that some angular information was contained in the spectral kernels. Full spectrum reconstruction of spectral reflectance from limited (MODIS) wavebands also showed the success of the spectral kernels. These results indicate that the spectral directional kernel-driven model is likely to provide significant improvement over current kernel-driven models of directional reflectance, which operate independently of wavelength. Further work is needed to explore the ability of the kernels to generate albedo but initial results suggest they may be very effective.

8.3 Directions for future research

The work presented in this thesis is part of ongoing research into the scattering behaviour of vegetation canopies and how this behaviour can be modelled and hence exploited. However, there are a several specific areas in which the work in this thesis will be built upon and extended and these are briefly outlined below.

8.3.1 Application of full spectral, directional kernel-driven model

A full spectral directional linear kernel-driven model is under development. This will be applied to airborne thematic mapper (ATM) and compact airborne spectrographic imager (CASI) data obtained over the Barton Bendish site in 1997. ATM data are limited to 11 visible and NIR wavebands, whilst CASI has up to 288 bands (depending on the chosen configuration). It is proposed that the spectral kernels be used to reconstruct the CASI data spectrally from the ATM data. This will provide an excellent test of the spectral kernels ability to model spectral reflectance. Once these data are atmospherically and geometrically corrected to the required accuracy (sub-pixel registration accuracy is required for BRDF studies) they will be used to derive broadband albedo. These values will then be compared with MODIS albedo estimates over the same area. This will provide a link between high resolution albedo derived from the airborne data and the moderate resolution (km scale) MODIS product, contributing to ongoing MODIS validation work (www[8.1]). Validating albedo is difficult given that field-measured

albedo is typically a point measure from an albedometer and relatively few samples can be collected over areas covered by even a very small number of MODIS pixels (Lucht *et al.*, 2000). The spectral kernels will also be used to generate spatial estimates of soil and vegetation spectral and directional reflectance components (as in section **7.5.5**). These will be compared with estimates derived from field measurements. If this is successful it will demonstrate the use of the spectral kernels for applications requiring scattering information from vegetation alone.

It is intended that the full spectral directional kernel driven model be applied to the spectral directional reflectance data as described above and that the resulting parameter values be used to interpolate estimates of narrowband albedo to broadband. This has typically been a laborious process requiring a number of approximations and assumptions (see chapter **2**). Conversion of narrowband to broadband albedo will be carried out once the ATM and CASI airborne data have been pre-processed to the required accuracy. This includes sub-pixel geometric correction required for BRDF model inversion (Barnsley *et al.*, 1997) and accurate atmospheric correction based on the MISR algorithm of Martonchik *et al.*, 1998a). In addition, data from the CHRIS mission (launched in October 2001 aboard the PROBA platform) will be available for comparison with airborne estimates of albedo. CHRIS is a pointable high resolution optical instrument with selectable bands (www[1.11]). It is anticipated that the spectral directional kernel-driven models will be ideal for inversion against CHRIS data. Estimates of albedo (and biophysical parameters) can then be compared directly with MODIS products over the same area. It is expected that this will provide better understanding of the issues involved in scaling albedo from ground-based, to moderate resolution data.

8.3.2 Other canopy types

Much of the work in this thesis is intended as a benchmark for the application of the kernel-driven models, as well as an indication of the information it may be possible to derive from their parameters. The methods employed here can be used in the future to test modifications to the kernels and try out new formulations. In addition, it is now possible to simulate the reflectance of forest canopies using the explicit 3D geometric BPMS model (given suitable field measurements). It is likely to be an interesting and worthwhile

exercise to apply the methods used in this thesis to such different canopies. This would give a more direct indication of the applicability of the kernel-driven models to a wide range of land cover types.

A further possibility is to construct detailed 3D models of the GO and volumetric scattering arrangements postulated in the kernel-driven models. In the case of the GO kernels this requires constructing arrangements of 'spheroids on sticks'; the volumetric kernels require approximating the horizontally homogeneous scattering 'cloud'. It would then be possible to explore what size and shape of scattering objects and/or combinations most closely correspond to 'real' plant canopies. Figure **8.1** shows an example of this approach carried out as part of the RAMI exercise (Pinty *et al.*, 2001). This is a simulation of a vegetation canopy with spherical 'clumps' of vegetation of fixed LAI, comprised of randomly located disks with specified LAD.

Figure 8.1 Simulated 'vegetation' canopy

8.3.3 Multiple scattering

The assumption of single scattering interactions made in the formulation of the kernel-driven models has (intentionally) received little attention in this thesis. It is clear that single scattering interactions do dominate ρ_{canopy}, particularly in the visible part of the spectrum (see figure **7.1**). However, this is not necessarily the case in the NIR where reflectance is much higher. Application of the spectral kernels over the wider spectrum means that multiple scattering is likely to become more important. It may also be possible to derive information regarding the canopy structure from analysis of multiply scattered information. It is known that there are approximations that can represent multiple scattering reasonably well (Knyazikhin and Marshak, 2000). If this information can be modelled using relatively simple terms it may be possible to construct a kernel-driven expression for the multiple scattering component, rather than lump it in as 'brightness' term as is currently the case in the kernel-driven models. An advantage of this is it may lead to a better description of ρ_{canopy}. In addition, the multiple scattering component is known to contain information regarding canopy structure, which it may be possible to extract.

Some analysis of the multiple scattering component of ρ_{canopy} from the canopies used in this thesis has already been attempted (Disney and Lewis, 1998). This work has shown that there may be a simple approximation for describing multiple scattering as a function of scattering order within the canopy. This may not be so important for studies of albedo, due to differences in scattering behaviour between the visible and SWIR regions: single scattering dominates in the visible, whilst multiple scattering dominates in the SWIR and NIR. Visible radiation has a larger impact on shortwave albedo than SWIR and NIR, as around 40% of total solar energy arriving at the surface lies between 0.3 and 0.8μm (see figure **1.3**). However, a simple approximation for representing the multiple scattering component of ρ_{canopy} is likely to be useful for deriving biophysical information. Lewis and Disney (1998) have shown that such an approach is very similar to theoretical work by other groups based on solutions to the 3D radiative transfer equation in a vegetation canopy (Knyazikhin, *pers. comm.*). It is intended that studies of multiple scattering will be fully incorporated into future analysis of kernel-driven BRDF modelling, again through the use of full 3D structural models of vegetation.

8.3.4 Improved fieldwork measurements

The fieldwork described in chapter **3**, intended to validate canopy radiometric simulations, was subject to a number of problems. Chief amongst these was poor weather, which (unfortunately) cannot be legislated for. However, part of ongoing research into linear kernel-driven models of ρ_{canopy} will be to refine the methods used here in an effort to generate a significantly better set of fieldwork measurements. Following the fieldwork of 1997, it is much easier to determine what needs to be measured in the future, how accurately these measurements can be expected to be, and how existing measurements may be improved.

The scope and detail of what can be measured is partly determined by available manpower. Most of the measurements used in this thesis were carried out by two groups of two people (often less). This severely restricts the degree of spatial sampling that can be carried out as well as the overall number of parameters which can be measured. However, within these limitations, a number of improvements can be made. Firstly, radiometric measurements can be carried out using a larger FOV (15^{o}) radiometer head. The advantage of this is that it is not as sensitive to the pointing accuracy of the radiometer (a few degrees at best). The disadvantage of this is that features of measured BRFD such as the hotspot will become 'smeared out'. However, for validation it is more important to characterise the general magnitude and angular variation of BRDF than to measure features such as hotspot width, say.

Another way of significantly improving future field radiometric measurements is with the use of a sun photometer to characterise atmospheric scattering. This is vital not only for ground-based radiometric measurements (seen figure **3.7**), but also for atmospheric correction of airborne and satellite remote sensing data. One of the difficulties of processing the airborne data collected in 1997 has been the lack of contemporaneous measurements of atmospheric aerosol and water vapour properties. This is considered essential for studies of BRDF (and hence albedo). A CIMEL (www[8.2]) sun photometer has been made available for fieldwork at Barton Bendish, as part of the NASA Aerosol Robotic Network (AERONET, www[8.3]) and general MODIS validation effort. This will allow accurate characterisation of atmospheric scattering during future campaigns. Walthall *et al.* (2000) describe a number of protocols including angular and spatial sampling regimes and atmospheric measurements which are generally accepted as

essential in field measurement of BRDF. These protocols will be adopted for future fieldwork. Finally, in order for useful comparisons to be made between spatial albedo values generated at high spatial resolution (e.g. from airborne data) and satellite-derived values, some validation at the surface is required. The use of an albedometer through the growing season would achieve this. It is limited essentially to point measurements, but if large, relatively homogeneous (at the field scale), fields of barley and wheat are used, the albedo can be assumed to be fairly constant over a whole field. This would provide the required link between albedo generated from airborne and spaceborne using the spectral kernels and albedo measured (and simulated) at canopy scale.

8.3.5 Optical and microwave scattering

One final, broad area where the work carried out in this thesis will be continued and extended is the marrying of scattering in vegetation in the optical and microwave domain. Currently, physical descriptions of scattering these two domains are very different. This is because the dimensions of canopy scattering objects (such as leaves) are far larger than optical wavelengths, but typically of the same order of magnitude as microwave radiation (λ of mm to cm). This leads to a number of problems for those constructing models of canopy scattering in this domain, in particular the consideration of absorption and scattering at the leaf level. It is not a simple matter of reflectance, transmittance and absorptance behaviour as in the optical domain. Nor can useful simplifications such as Lambertian scattering be applied. In microwave models of canopy scattering, gross simplifications are required such as the use of 'equivalent disks' to represent leaves, and cylinders representing stems. Complex phase scattering matrices and assumptions about dielectric behaviour are required to solve even these cases. However, the fundamental representations of canopy structure are the same. It may be possible to apply the type of assumptions regarding simple scattering 'shapes' made in the kernel-driven models to microwave backscatter models. This would prove extremely useful, given the advantages that RADAR instruments hold over optical ones in being able to penetrate cloud and operate on the Earth's dark side. It has already been recognised that the conceptually different approaches to modelling of vegetation in the optical and microwave domains are in fact linked by a common need to consider vegetation structure (Saich *et al.*, 2001). It is intended that methods developed in this thesis will be applied to examining possible linkages between microwave scattering and the kernel-driven approach to modelling canopy reflectance in the optical domain.

Appendix 1

Constraint of linear model parameters for inversion (Lewis, *pers. comm.*)

The inversion of linear kernel-driven BRDF models against measured reflectance data can, in practice, result in model inverted parameter values that are physically unrealisable (Strugnell and Lucht, 2000). This tends to occur when a chosen kernel combination cannot describe surface reflectance adequately. There are two reasons for this failure. Firstly, the selected kernel combination may simply be inappropriate for the cover type under observation. This typically occurs in areas where the surface may be at the extremes of what was envisioned in the kernel formulation e.g. sparse canopies over very bright/rough soils; canopies with extreme LAD (departure from spherical assumption of volumetric kernels); dense forest canopy where the assumptions of discrete crown and ground areas break down. Secondly, there may be insufficient information in the signal (variation related to surface structure in the reflectance data) for a full linear model comprising an isotropic, volumetric and GO kernel, to be inverted, hence the best-fit solution (lowest RMSE) may be physically unrealistic.

If the parameters are to be used indirectly e.g. as an additional channel of information for classification (beyond the spatial and spectral) then the absolute values are not important, only the spatial variations. As demonstrated in chapters **5** and **6**, inverted linear model parameters do contain biophysical information related to the volumetric and GO scattering properties of a surface, and this is the important issue for indirect use. If parameters are to be used directly however e.g. to extrapolate/interpolate directional reflectance values, or to derive associated surface properties such as directional hemispherical reflectance or spectral albedo, then clearly it is sensible to place physical constraints on the derived properties. These constraints can then be used to direct the inversion procedure.

Recall from section **2.5.4.1** that a linear model of BRDF can be represented as $\rho_{canopy} = f_0 + f_1 k_1 + f_2 k_2$. Recall also that the unconstrained inversion of such a model against a set of observations over varying k_1, k_2 is simply the minimisation of e^2, the sum squared error between modelled and measured reflectances i.e.

$$e^2 = \frac{1}{N}\sum_{i=1}^{i=N}\left(\rho_i - \left(f_0 + f_1 k_1 + f_2 k_2\right)\right)^2 \qquad \text{A 1.0}$$

which results in a series of linear equations, one for each observation. This can be simply solved using matrix algebra (see section **2.4.1.1**, after Lewis, 1995) i.e. $P = M^{-1}V$ where

$$V = \frac{1}{N}\sum_{i=1}^{i=N}\left(\rho_i, \rho_i k_{1i}, \rho_i k_{2i}\right)^T \qquad \text{A 1.2}$$

and

$$M = \frac{1}{N}\sum_{i=1}^{i=N}\begin{bmatrix} 1 & k_{1i} & k_{2i} \\ k_{1i} & k_{1i}^2 & k_{1i}k_{2i} \\ k_{2i} & k_{2i}k_{1i} & k_{2i}^2 \end{bmatrix} \qquad \text{A 1.3}$$

Lagrange multipliers can be applied to such a system to impose arbitrary constraints under which inversion may be carried out. Lagrange multipliers allow the minimum (or maximum) of a function $f(f_0, f_1, f_2)$ to be found by using a relationship between the function parameters and some constant i.e. $\varphi(f_0, f_1, f_2)$ = constant (e.g. Boas, 1983). In this case, the function $\varphi(f_0, f_1, f_2)$ is the constraint equation, based on some physical limits. e^2 can now be minimised based on the original model in addition to the constraint equation i.e. we wish also to minimise $\varphi = af_0 + bf_1 + cf_2 - d = 0$ or $C \cdot P = d$ where C is the transpose of the matrix containing the Lagrange multipliers i.e. $C = (a, b, c)^T$ and the minimisation is now a function of the constraint equation in addition to the original expression i.e.

$$e^2 = \frac{1}{N}\sum_{i=1}^{i=N}\left(\rho_i - \left(f_0 + f_1 k_1 + f_2 k_2\right)\right)^2 - 2\lambda\left(af_0 + bf_1 + cf_2 - d\right) \qquad \text{A 1.4}$$

Minimisation therefore leads to $V = MP + \lambda C$ and $V - \lambda C = MP$ and multiplying by the inverse of M i.e. $M^{-1}V - \lambda M^{-1}C = P$ or $P' - \lambda C' = P$ where $P' = M^{-1}V$ and $C' = M^{-1}C$, and P' is the parameter values obtained from unconstrained minimisation. Now, clearly $P' \cdot C - \lambda C' \cdot C = P \cdot C$ and we have already seen that C.P=d, so that we can derive an expression for λ i.e.

$$\lambda = \frac{P' \cdot C - d}{C' \cdot C} \qquad \text{A 1.5}$$

and since we know that $M^{-1}V - \lambda M^{-1}C = P$ then

$$P' - \left(\frac{P' \cdot C - d}{C' \cdot C}\right)C' = P \qquad \text{A 1.6}$$

i.e. if M^{-1} and P' are calculated in an unconstrained manner then the inverse matrix can be multiplied by the constraint vector C to obtain C', and hence P, the set of constrained parameters, can be calculated. Practically the difficulty is to find a constraint equation that relates the model parameters to some constant. The most obvious physical constraint is that the surface reflectance should be ≥ 0. In this case, we can say that $f_0, f_1, f_2 \geq 0$ i.e. $f_0 + f_1 + f_2 \geq 0$ and $f_0 + f_1 k_1 + f_2 k_2 \geq 0$. Furthermore, it seems sensible to constrain the DHR and for both the maximum and minimum kernel values, to lie between 0 and 1 i.e.

$$0 \leq f_0 + f_1 \bar{k}_1(0) + f_2 \bar{k}_2(0) \leq 1 \qquad \text{A 1.7}$$

$$0 \leq f_0 + f_1 \bar{k}_1\left(\frac{\pi}{2}\right) + f_2 \bar{k}_2\left(\frac{\pi}{2}\right) \leq 1 \qquad \text{A 1.8}$$

In which case it should also be reasonable to constrain the BHR to lie within the same limits i.e. $0 \leq f_0 + f_1 \bar{\bar{k}}_1 + f_2 \bar{\bar{k}}_2 \leq 1$. Constraint requires the calculation of the unconstrained parameters followed by a test of the various products against each constraint in turn. If any constraint is not met, all constraints should be applied[1]. Following re-calculation of the constrained model parameter sets, RMSE can be used to select a single, final set of values. Although this may seem arbitrary, it requires no *a priori* assumptions to be made about which constraints the model "should" and "should not" adhere to. The requirement for speed may be what limits the application of constraints in practice, although the number of extra calculations required for each constraint is not prohibitive.

[1] Although individual constraints could be used, this is probably not physically very sound. If just one of the constraints is not met, we can must conclude that the inversion is misbehaving.

Appendix 2

Figure A2.1 Proportional contribution of sunlit and shaded scene components to total scene reflectance, for barley (four dates) and wheat (two dates).

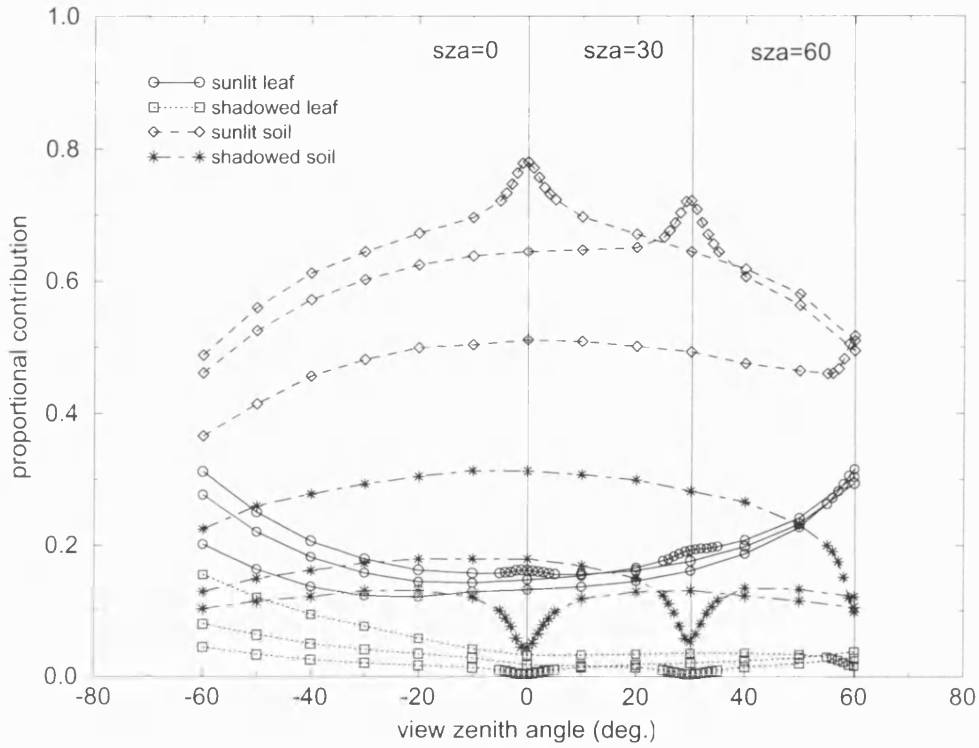

a) barley – 18th April

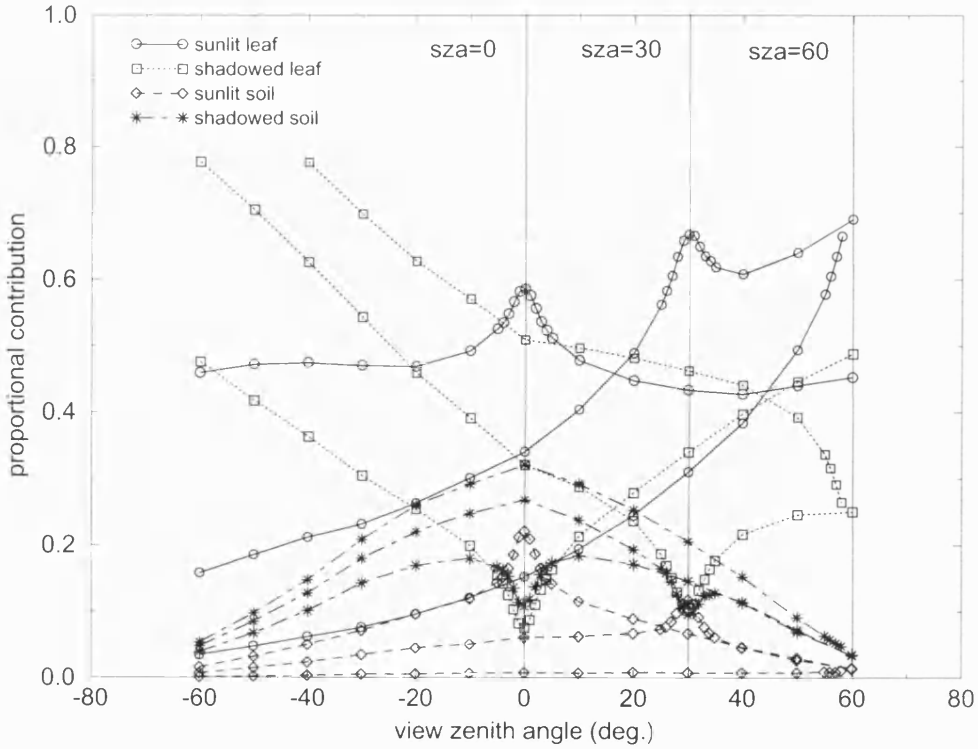

b) barley – 13th May

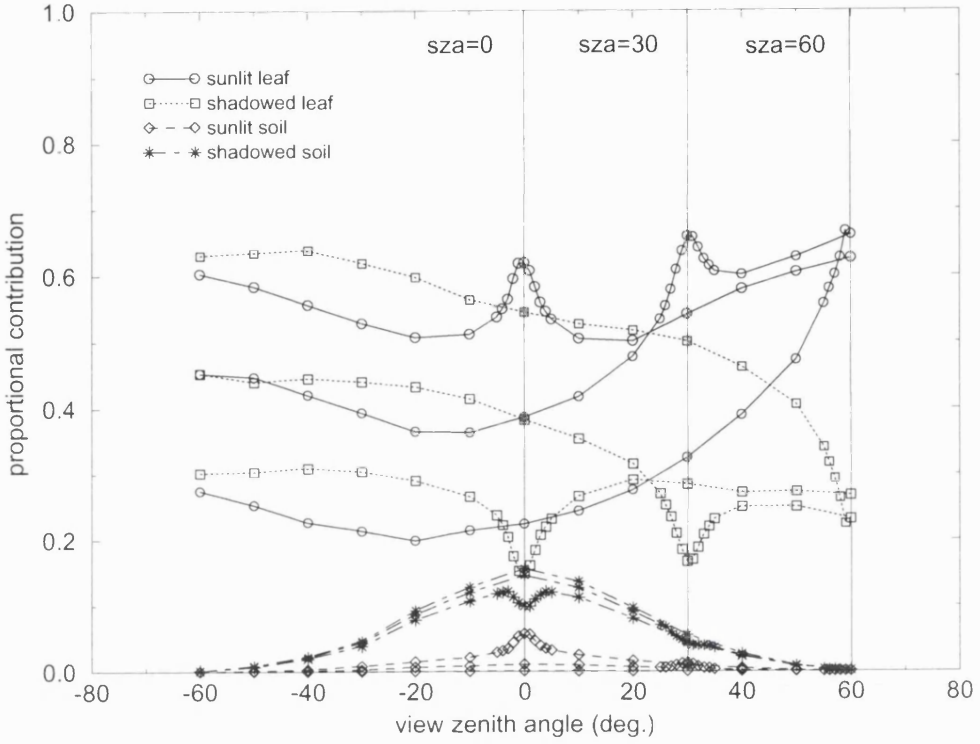

c) barley – 4th June

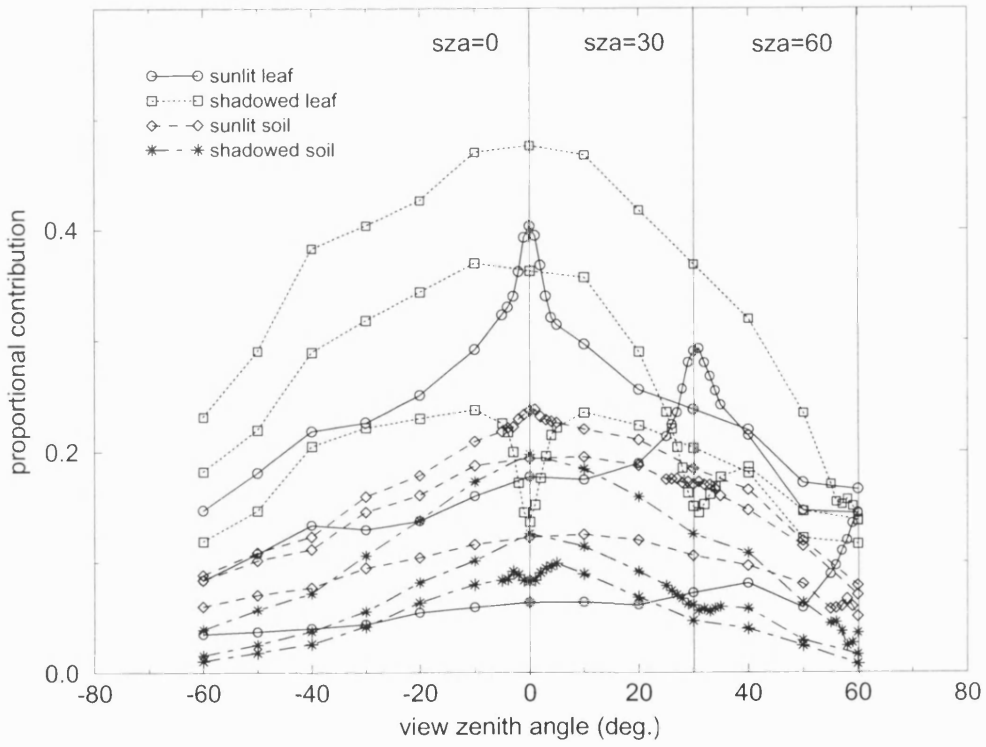

d) barley – 24th June

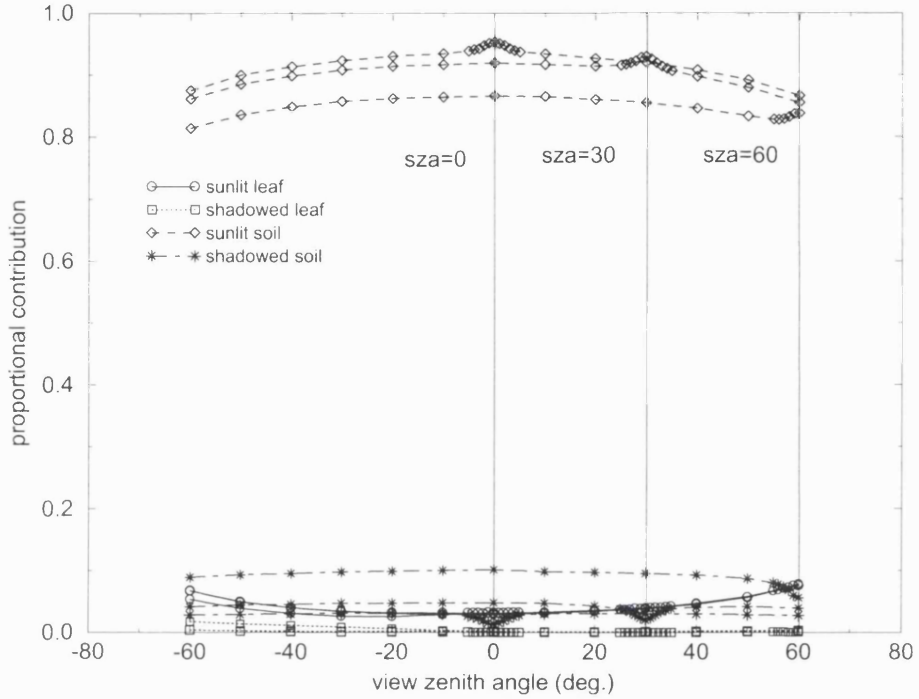

e) wheat – 23rd March

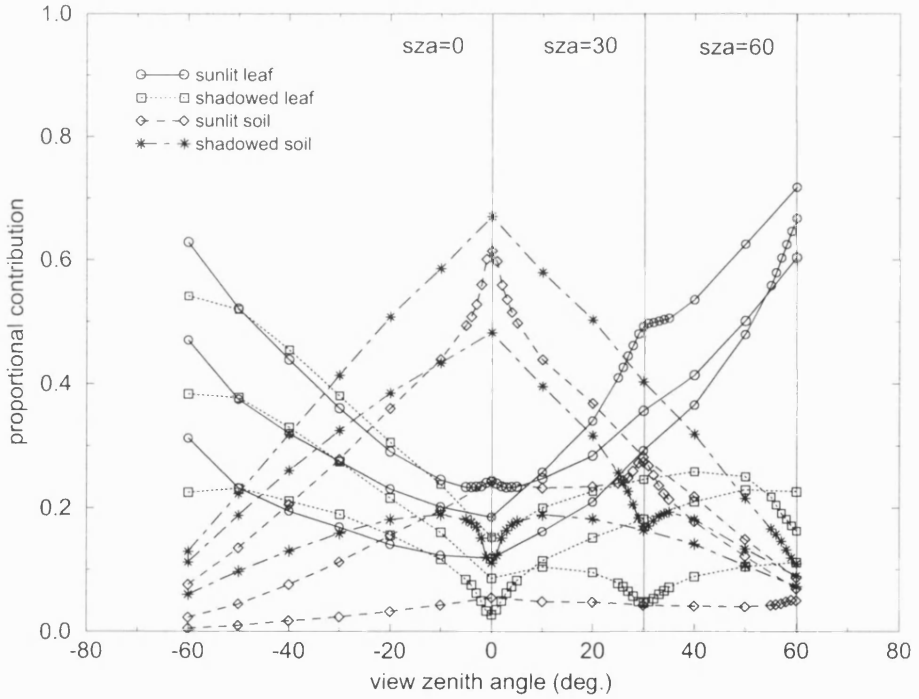

f) wheat – 23rd April

Sunlit and shaded scene components of barley and wheat

The results presented in figure **A2.1** should be compared with those in figure **4.7**, which were generated using no diffuse component of illumination, and hence have no contribution to overall scene reflectance from the shadowed canopy components. The reflectance and transmittance in each case are the same i.e. two 'synthetic' wavebands are simulated, the first in which $\rho_{leaf} = \tau_{leaf} = 0.5$ and $\rho_{soil} = 0$ i.e. in this case all signal is (by definition) scattering from vegetation only (only single scattered interactions are counted); the second waveband has $\rho_{leaf} = \tau_{leaf} = 0$ and $\rho_{soil} = 1$ i.e. in this case all signal is (by definition) single scattering from soil only. Results are presented from $\theta_i = 0°$, 30° and 60°, as well as for $\phi_{row} = 0°$, 45°, 90°. Separation of the different ϕ_{row} cases increases with LAI. It can clearly be seen in figure **A2.1a**, for example, how the sunlit leaf is at a maximum in the hotspot ($\theta_i = \theta_v = 0°$) and shadowed soil is a minimum (close to zero).

It can be seen that in these cases, the sunlit soil is the dominant scene component in both low LAI cases (figure **A2.1a** and **e**), particularly in the 23rd March wheat canopy. In this case the sunlit soil component represents greater than 80% of the total reflectance at all $\theta_{v,i}$ with all other components representing less than 10%. For barley the contribution of other components, sunlit leaf in particular, is significant.

References

Aber, J. D. (1995) Terrestrial ecosystems, (in Trenberth, 1995, p173-200).

Abuelgasim, A. A., Gopal, S., Irons, J. R. and Strahler, A. H. (1996) Classification of ASAS multiangle and multispectral measurements using artificial neural networks, *Rem. Sens. Environ.*, **57**, 79-87.

Abuelgasim, A. A., Gopal, S. and Strahler, A. H. (1998) Forward and inverse modeling of canopy bidirectional reflectance using a neural network, *Int. J. Rem. Sens.*, **19**, 453-471.

Ahmad, S. and Deering, D. W. (1992) A simple analytical function for bidirectional reflectance, *J. Geophys. Res.*, **97**, 18,867-18-886.

Akaike, H. (1974) A new look at the statistical model identification, *IEEE Trans. Auto. Control Sys.*, **19**, 716-723.

Allen, W. A., Gayle, T. V. and Richardson, A. J. (1970) Plant canopy irradiance specified by the Duntley equations, *J. Opt. Soc. Am.*, **60(3)**, 372-376.

Arking, A., Braswell, B. H., Schimel, D. S. and Wessman, C. A. (1998) Ecological research needs from multi-angle remote sensing data, *Rem. Sens. Environ.*, **63**, 155-165.

Asner, G. P. (1998) Biophysical and biochemical sources of variability in canopy reflectance, *Rem. Sens. Environ.*, **63**, 234-253.

Asner, G. P. (2000) Contributions of multi-view angle remote sensing to land-surface and biogeochemical research, *Rem. Sens. Rev.*, **18**, 137-162.

Asrar, G., Hipps, L. E. and Kanemasu, E. T. (1984) Assessing solar energy and water use efficiencies in winter wheat: a case study, *Agric. Forest Met.* **31**, 47-58.

Asrar, G., Myneni, R. B. and Kanemasu, E. T. (1989) Estimation of plant-canopy attributes from spectral reflectance measurements, in Asrar (Ed.), 1989, 252-296.

Asrar, G. Ed. (1989) *Theory and applications of optical remote sensing*, J. Wiley & Sons, New York.

Baret, F., Vanderbilt, V. C, Steve, M. D. and Jacquemoud, S. (1994) Use of spectral analogy to evaluate canopy reflectance sensitivity to leaf optical properties, *Rem. Sens. Environ.*, **48(2)**, 253-260.

Barnsley, M. J., Strahler, A. H., Morris, K. P. and Muller, J. P. (1994) Sampling the surface bidirectional reflectance distribution function (BRDF): 1. Evaluation of current and future satellite sensors, *Rem. Sens. Rev.*, **8**, 271-311.

Barnsley, M. J., Allison, D. and Lewis, P. (1997a) On the information content of multiple view-angle (MVA) images, *Int. J. Rem. Sens.*, **18(9)**, 1937-1960.

Barnsley, M. J., Lewis, P., Muller, J. -P. and Sutherland, M. (1997b) Estimating land surface albedo in the HAPEX-Sahel southern super-site: Inversion of two BRDF models against multiple angle ASAS images, *Journ. Hydrol.*, **188-189**, 749-778.

Barnsley, M. J., Lewis, P., O' Dwyer, S., Disney, M. I., Hobson, P., Cutter, M. and Lobb, D. (2000) The potential of the CHRIS-PROBA instrument for measurement of vegetation properties from space, *Rem. Sens. Rev.*, **19**,171-189.

Bateson, C. A., Asner, G. P. and Wessman, C. A. (2000) Endmember bundles: a new approach to incorporating endmember variability into spectral mixture analysis, *IEEE Trans. Geosci. Rem. Sens.*, **38(2)**, 1083-1094.

Bégué, A. (1992) Modeling hemispherical and directional radiative fluxes in regular-clumped canopies, *Rem. Sens. Environ.*, **40(3)**, 219-230.

Bengtsson, L. O. (1995) Climate system modeling prospects, in Trenberth K. (Ed.), pp.705-724.

Boas, M. L. (1983) *Mathematical methods in the physical sciences*, 2nd ed., John Wiley & Sons, New York, pp. 793.

Borel, C. C., Gerstl, S. A. W. and Powers, B. J. (1991) The radiosity method in optical remote sensing of structured 3D surfaces, *Rem. Sens. Environ.*, **36**, 13-44.

Brest, C. L. and Goward, S. N. (1987) Deriving surface albedo measurements from narrow band satellite data, *Int. J. Rem. Sens.*, **8(3)**, 351-367.

Bunnik, N. J. J. (1978) *The Multispectral Reflectance of Shortwave Radiation by Agricultural Crops in Relation with their Morphological and Optical Properties*, Pudoc, Wageningen, Netherlands.

Carlson, R. E., Yarger, D. N. and Shaw, R. H. (1971) Factors affecting the spectral properties of leaves with special emphasis on leaf water status, *Agron. J.*, **63**, 486-489.

Cess, R. D. and Potter, G. L. (1986) Narrow- and broad-band satellite measurements of shortwave radiation: conversion simulations with a general circulation model, *Journ. Clim. Appl. Meteorol.*, **25**, 1977-1984.

Chandrasekhar, S. (1960) *Radiative Transfer*, Dover, New York, USA.

Charlson, R. J., Schwartz, S., Hales, J., Cess, R., Coakley Jr., J., Hansesn, J. and Hoffmann, D. (1992) Climate forcing by anthropogenic aerosols, *Science*, **255**, 423-430.

Chelle, M. and Andrieu, B. (1999) Radiative models for architectural modeling, *Agronomie*, **19**, 225-240.

Chen, J. M. and Leblanc, S. G. (2000) A four-scale bidirectional reflectance model based on canopy architecture, *IEEE Trans. Geosci. Rem. Sens.*, **35**, 1316-1337.

Chen, J. M., Li, X., Nilson, T. and Strahler, A. H. (2000) Recent advances in geometric optical modelling and its applications, *Rem. Sens. Rev.*, **18**, 227-262.

Cierniewski, J. (1987) A model for soil surface roughness influence on the spectral response of bare soils in the visible and near-infrared range, *Rem. Sens. Environ.*, **23**:97-115.

Cierniewski, J. and Verbrugghe, M. (1997) Influence of soil surface roughness on soil bidirectional reflectance, *Int. J. Rem. Sens.*, **18(6)**, 1277-1288.

Cierniewski, J. (1999) *Geometrical modelling of soil bidirectional reflectance in the optical domain*, Bogucki Scientific, Posnan, Poland, ISBN 83-86001-87-9, pp 148.

Cihlar, J., Manak, D. and Voisin, N. (1994) AVHRR bidirectional reflectance effects and compositing, *Rem. Sens. Environ.*, **48**, 77-88.

Clarke, F. and Parry, D. (1985) Helmholz reciprocity: its validity and application to reflectometry, *Light Res. Technol.*, **17**:1-11.

Collings, L. (2001) Investigation into the use of spectral linear kernel-driven models for albedo estimation, University of London M.Sc. thesis (unpublished).

Combal, B., Baret, F., Weiss, M., Trubuil, A., Mace, D., Pragnere, A., Myneni, R.B., and Knyazikhin, Y. (2001, accepted) Retrieval of canopy biophysical variables from bi-directional reflectance using prior information to solve the ill-posed problem, *Rem. Sens. Environ.*.

Curran, P. J., Dungan, J. L., Macer, B. A., Plummer, S. E. and Peterson, D. L. (1992) Reflectance spectroscopy of fresh whole leaves for the estimation of chemical concentration, *Rem. Sens. Environ.*, 39, 153-166.

Decshamps, P.-Y., Bréon, F-M., Leroy, M., Podaire, A., Bricaud, A., Buriez, J.-C. and Sèze, G. (1994) The POLDER mission: Instrument Characteristics and scientific objectives, *IEEE Trans. Geosci. Rem. Sens.*, **32**, 598-615.

de Reffye, P., Edelin, C., Françon, J., Jaeger, M. and Puech, C. (1988) Plant models faithful to botanical structure and development, SIGGRAPH 88, **22(4)**, 151-158.

de Reffye, P. and Houllier, F. (1997) Modelling plant growth and architecture: Some recent advances and applications to agronomy and forestry, Current Science, **73(11)**, 984-992.

Dickinson, R. E. (1983) Land surface processes and climate - surface albedos and energy balance, *Adv. Geophys.*, **25**, 305-353.

Dickinson, R. E. (1984) Modelling evapotranspiration for three dimensional global climate models. In *Climate Processes and Climate Sensitivity*, J. E. Hanson and T. Takahashi (eds.), Geophysical Monograph 29, Maurice Ewing Volume 5, Amer. Geophys. Union, 58-72.

Dickinson, R. E., Pinty, B. and Verstraete, M. M. (1990) Relating surface albedos in GCMs to remotely sensed data, *Agric. For. Meteorol.*, **52(1-2)**, 109-131.

Dickinson, R. E. (1995) Changes in land use, in Trenberth K. (Ed.), pp.689-701.

Diner, D. J., Beckert, J. C., Reilly, T. H., Bruegge, C. J., Conel, J. E., Kahn, R. A., Martonchik, J. V., Ackerman, T. P., Davies, R., Gerstl, S. A. W., Gordon, H. R., Muller, J. -P., Myneni, R. B., Sellers, P. J., Pinty, B., Verstraete, M. M. (1998) Multi-angle Imaging Spectro-Radiometer (MISR) instrument description and experiment overview, *IEEE Trans. Geosci. Rem. Sens.*, **36(4),** 1072-1087.

Disney, M. I., Lewis, P., Knott, R., Hobson, P., Evans-Jones, K. and Barnsley, M. J. (1998) Validation of a manual measurement method for deriving 3D canopy structure using the BPMS, *Proc. Int. Geosc. Rem. Sens. Symp. 98*, Jul 6th-10th Seattle, USA, CD-ROM.

Disney, M. I. and Lewis, P. (1998) An investigation of how linear BRDF models deal with the complex scattering processes encountered in a real canopy, *Proc. Int. Geosc. Rem. Sens. Symp. 98*, Jul 6th-10th Seattle, USA, CD-ROM.

Disney, M. I., Lewis, P. and North, P. (2000) Monte Carlo ray tracing in optical canopy reflectance modelling, *Rem. Sens. Rev.*, **18(2-4)**, 163-197.

Dubayah, R. J., Blair, B., Bufton, J., Clark, D., JaJa, J., Knox, R., Luthcke, S., Prince, S. and Weishampel, J. (1997) The Vegetation Canopy Lidar Mission, in *Land Satellite Information in the Next Decade II: Sources and Applications*, American Society for Photogrammetry and Remote Sensing, Bethesda, MD, 100-112.

Egbert, D. D. (1972) Geometric optic modelling of vegetation, *Photog. Eng.*, **38**, 556.

Engelsen, O. (1997) *An investigation of the coupled surface-atmosphere radiative transfer problem of remote sensing in the visible and near-infrared spectral bands and its inversion*, Dissertation, University of Tromsoe.

Foley, J., van Dam, A., Feiner, S. K. and Hughes, J. F. (1992) *Computer graphics: principles and practice*, 2nd ed., Addison-Wesley, New York, pp. 1173.

Fraser, R. S., Ferrare, R. A., Kaufman, Y. J., Markham, B. L., and Mattoo, S. (1992) Algorithm for atmospheric corrections of satellite and aircraft imagery, *Int. J. Rem. Sens.*, **13**, 541-557.

Gao, F., X., Li, Strahler, A. H. and Schaaf, C. (2001) Evaluation of the LiTransit Kernel for BRDF Modeling, *Rem. Sens. Rev.*, **19**, 205-224.

GARP Joint Organizing Committee (1975) The physical basis of climate and climate modelling, *GARP Pub. Ser.* **16**, 106-118, World Meteorological Organization, Geneva.

Gastellu-Etchegorry, J. P., Demarez, V., Pinel, V. and Zagolski, F. (1996) Modelling radiation transfer in heterogeneous 3D vegetation canopies, *Rem. Sens. Environ.*, **58(2)**, 131-156.

Gerard, F. F. and North, P. R. J. (1997) Analyzing the effect of structural variability and canopy gaps on forest BRDF using a geometric-optical model, *Rem. Sens. Environ.*, **62(1)**, 46-62.

Gershenfeld, N. (1999) *The nature of mathematical modelling*, CUP, Cambridge, UK, 344pp.

Gerstl, S. A. W. and Zardecki A. A. (1985) Coupled atmosphere/canopy model for remote sensing of plant reflectance features, *Appl. Opt.*, **24**, 94-103.

Gerstl, S. A. W and Simmer, C. (1986) Radiation physics and modelling for off-nadir satellite remote sensing of non-Lambertian surfaces, *Rem. Sens. Environ.*, **20**, 1-29.

Gerstl, S. A. W. (1990) Physical concepts of optical and radar reflectance signatures, *Int. J. Rem. Sens.*, **7**, 1109-1117.

Gerstl, S. A. W. and Borel, C. C. (1992) Principles of the radiosity method versus radiative transfer for canopy reflectance modeling, *IEEE Trans. Geosci. Rem. Sens.*, **30(2)**, 271-275.

Gille, J. et al. (1996) MOPITT algorithm theoretical basis document: retrieval of CO profiles and column amounts of CO and CH4 from MOPITT radiances (level 1-2). Dept. of Physics, University of Toronto, Ontario, Canada. ftp://eospso.gsfc.nasa.gov/ATBD/REVIEW/MOPITT/ATBD-MOP-02/atbd-mop-02.pdf.

Gobron, N., Pinty, B., Verstraete, M. M. and Govaerts, Y. (1997) A semidiscrete model for the scattering of light by vegetation, *J. Geophys. Res.*, **102(D8),** 9431-9446.

Goel, N. S. and Strebel, D. E. (1983) Inversion of vegetation canopy reflectance models for estimating agronomic variables. 1. Problem definition and initial results using the Suits model, *Rem. Sens. Environ.*, **13**, 487-507.

Goel, N. S. and Strebel, D. E. (1984) Simple beta distribution representation of leaf orientation in vegetation canopies, *Agron. Journ.*, **76**, 800-803.

Goel, N. S. (1988) Models of vegetation canopy reflectance and their use in the estimation of biophysical parameters from reflectance data, *Rem. Sens. Rev.*, **4,** 1-222.

Goel, N. S. and Grier, T. (1988) Estimation of canopy parameters from inhomogeneous vegetation canopies from reflectance data, III: TRIM: a model for radiative transfer in heterogeneous three-dimensional canopies, *Rem. Sens. Environ.*, **25**, 255-293.

Goel, N. S. and Reynolds, N. (1989), Bidirectional canopy reflectance and its relationship to vegetation characteristics, *Int. J. Rem. Sens.*, **10**, 107-132.

Goel, N. S. Rozenhal, and Thompson, R. L. (1991) A computer graphics based model for scattering of objects of arbitrary shapes in the optical region, *Rem. Sens. Environ.*, **36(2)**, 73-104.

Goel, N. S. (1992) Inversion of canopy reflectance models for estimation of biophysical parameters from reflectance data, *Rem. Sens. Rev.*, (in Asrar, 1989) pp. 205-251.

Goel, N. S. and Thompson, R. L. (2000) A snapshot of canopy reflectance models, and a universal model for the radiation regime, *Rem. Sens. Rev.*, **18**, 197-225.

Goral, C.M., Torrance, K. E., Greenberg, D. P. and Battaile, B. (1984) Modeling the interaction of light between diffuse surfaces, *SIGGRAPH* **84**, 213-222.

Govaerts, Y. M., Jacquemoud, S., Verstraete, M. M. and Ustin, S. L. (1995) Modelling plant leaf bidirectional reflectance and transmittance with a 3D ray tracing approach, *Proc. Int. Geosc. Rem. Sens. Symp. IGARSS 95*, Firenze, Italy, 1460-1462.

Govaerts, Y. M. (1996) A model of light scattering in three-dimensional plant canopies: a Monte Carlo ray tracing approach, *Ph.D. thesis, JRC catalogue no. CL-NA-16394-EN-C*, Office for Official Publications of the European Communities, Luxembourg, pp. 186.

Graetz, R. D. (1991) The nature and significance of the feedback of changes in terrestrial vegetation on global atmospheric and climatic-change, *Climate Change*, **18**, 147-173.

Grant, I. F. (2000) Investigation of the variability of the directional reflectance of Australian land cover types, *Rem. Sens. Rev.*, **19**, 243-258.

Groisman, P., Ya, T. R. Karl and Knight, R. W. (1994) Observed impact of snow cover on the heat balance and the rise of continental spring temperatures, *Science*, **263**, 198-200.

Gutman, G. (1994) Normalization of multi-annual global AVHRR reflectance data over land surfaces to common sun-target-sensor geometry, *Adv. Space Res.*, **14(1)**, 121-124, 1994.

Hack, J. J. (1995) Climate system simulation: basic numerical and computational concepts, in Trenberth (1995), p. 283-318.

Hall, F. G., Townshend, J. R. G. and Engman, E. T. (1995) Status of remote sensing algorithms for estimation of land surface state parameters, *Rem. Sens. Environ.*, **51**, 138-156.

Hapke, B. (1963) A theoretical photometric function for the lunar surface, *J. Geophys. Res.* , **68**, 4545-4570.

Hapke, B. (1981) Bidirectional Reflectance Spectroscopy 1. Theory, *J. Geophys. Res.*, **86(B4)**, 3039-3054.

Hapke, B. and Wells, E. (1981) Bidirectional reflectance spectroscopy 2. Experiments and observations, *J. Geophys. Res.*, **86(B4)**, 3055-3060.

Hapke, B. (1984) Bidirectional reflectance spectroscopy 3. Correction for macroscopic roughness, *Icarus*, **59**, 41-59.

Hapke, B. (1986) Bidirectional reflectance spectroscopy 4. The extinction coefficient and the hot-spot effect, *Icarus*, **67**, 264-280.

Hapke, B. (1993) *Theory of reflectance and emittance spectroscopy*, Cambridge University Press.

Henderson-Sellers, A. and Wilson, M. F. (1983) Surface albedo data for climate modelling, *Rev. Geophys. Sp. Phys.* **21(8)**, 1743-1778.

Henderson-Sellers, A., Yang, Z.-L. and Dickinson, R. E. (1993) The Project for Intercomparison of Land Surface Parameterization Schemes (PILPS), *Bull. Amer. Meteor. Soc.*, **76**, 489-503.

Holben, B.N. (1986) Characteristics of maximum-value composite images from temporal AVHRR data, *Int. Journ. Rem. Sens.*, **7(11)**, 1417-1434.

Hosgood, B., Jacquemoud, S., Andreoli, G., Verdebout, J., Pedrini, A. and G. Schmuck (1994) The JRC Leaf Optical Properties Experiment (LOPEX'93), Rep. EUR-16095-EN, European Commission document CL-NA-16095-EN-C.

Hsiung, J. (1985) Estimates of global oceanic meridional heat transport, *J. Phys. Oceanog.*, **15**, 1405-1413.

Hu. B., Lucht, W., Li, X. and Strahler, A. H. (1997) Validation of kernel-driven semiempirical models for the surface bidirectional reflectance distribution function of land surfaces, *Rem. Sens. Environ.*, **52**, 201-214.

Hu, B., Lucht, W. and Strahler, A. H. (1999) The interrelationship of atmospheric correction of reflectances and surface BRDF retrieval: a sensitivity study, *IEEE Trans. Geosci. Rem. Sens.*, **37(2)**, 724-738.

Huete, A. (1986) Separation of soil plant spectral mixtures by factor-analysis, *Rem. Sens. Environ.*, **35**, 237-251.

Huete, A. (1989) Soil influences in remotely sensed vegetation-canopy spectra, (in Asrar, 1989), pp107-141.

Hurcom, S. J., Harrison, A. R. and Taberner, M. (1996) Assessment of biophysical vegetation properties through spectral decomposition techniques, *Rem. Sens. Environ.*, **56**, 203-214.

Hurcom, S. J. and Harrison, A. R. (1998) The NDVI and spectral decomposition for semi-arid vegetation abundance estimation, *Int. J. Rem. Sens.*, **19(16)**, 3109-3125.

Iaquinta, J. and Pinty, B. (1994) Adaptation of a bidirectional reflectance model including the hot-spot to an optically thin canopy, *Proc. VIth ISPRS Int. Symp. on Phys. Meas. and Sig. in Rem. Sens. Val d'Isere, France, 17-21 Jan.*, 683-690.

IPCC (1995a) *Climate Change 1995*, Report of the Intergovernmental Panel on Climate Change, Cambridge University Press, 64pp.

IPCC (1995b) *Impacts, Adaptations, and Mitigations of Climatic Change - Technical Analyses*, Cambridge University Press, 878pp.

IPCC (2001a) *Climate Change, 2001: The Scientific Basis*, Technical summary of Working Group I of the Intergovernmental Panel on Climate Change, available from www.ipcc.ch.

IPCC (2001b) *Climate Change, 2001: Impacts, Adaptation and Vulnerability*, Technical summary of Working Group II of the Intergovernmental Panel on Climate Change, available from www.ipcc.ch.

IGBP (1998) Carbon Cycle Working Group, The terrestrial carbon cycle: Implications for the Kyoto Protocol, *Science*, **280**, 1393-1397.

Irons, J. R., Ranson, K. J., Williams, D. L., Irish, R. R. and Huegel, F. G. (1991) An off-nadir pointing imaging spectroradiometer for terrestrial ecosystem studies, *IEEE Trans. Geosci. Rem. Sens.*, **29(1)**, 66-74.

Jackson, R. D. (1984) Remote sensing of vegetation characteristics for farm management, *SPIE Rem. Sens.*, **475**, 81-96.

Jacquemoud, S. and Baret, F. (1990) PROSPECT - A model of leaf optical properties spectra, *Rem. Sens. Environ.*, 34(2), 75-91.

Jacquemoud, S., Ustin, S. L., Verdebout, J., Schmuck, G., Andreoli, G. and Hosgood B. (1996) Estimating leaf biochemistry using the PROSPECT leaf optical properties model, *Rem. Sens. Environ.*, **56(3)**, 194-202.

Jensen, J. R. (2000) *Remote Sensing of the Environment, An Earth Resources Perspective*, Prentice Hall, London, 544pp.

Jolliffe, I. T. (1986) *Principal Component Analysis*, Springer-Verlag, Amsterdam.

Jupp, D. L. B. and Strahler, A. H. (1991) A hot-spot model for leaf canopies, *Rem. Sens. Environ.*, **38**, 193-210.

Justice, C. O., Vermote, E., Townshend, J. R.G., Defries, R., Roy, D., Hall, D. K., Salomonson, V. V., Privette, J. L., Riggs, G., Strahler, A., Lucht, W., Myneni, R. B., Knyazikhin, Y., Running, S. W., Nemani, R. R., Wan, Z., Huete, A. R., van Leeuwen, W., Wolfe, R. E., Giglio, L., Muller, J. -P., Lewis, P., and Barnsley, M. J. (1998) The Moderate Resolution Imaging Spectrometer (MODIS): land remote sensing for global change research, *IEEE Trans. Geosci. Rem. Sens.*, **36(4)**, 1228-1249.

Justice, C. O., Belward, A., Morisette, J., Lewis, P., Privette, J. and Baret, F. (2000) Developments in the validation of satellite products for the study of the land surface, *Int. J. Rem. Sens.*, **21(17)**, 3383-3390.

Kaufmann, Y. J. (1989) The atmospheric effect on remote sensing and its correction, in *Theory and Applications of Optical Remote Sensing*, ed. G. Asrar, pp. 336-428, J. Wiley & Sons, New York.

Kauth, R. J. and Thomas, G. S. (1976) The Tasseled-cap: a graphic description of the spectral-temporal development of agricultural crops as seen by Landsat, *Proc. Symp. Mach. Processing of Rem. Sens. Data*, p. 41-51.

Kimes, D. S. and Kirchner J. A. (1982) Radiative transfer model for heterogeneous 3-D scenes, *Appl. Opt.*, **21**, 4119-4129.

Kimes, D. S. (1984) Modeling the directional reflectance from complete homogenous vegetation canopies with various leaf-orientation distributions, *J. Opt. Soc. Am.*, **1**, 725-737.

Kimes, D. S. and Sellers, P. (1985) Inferring hemispherical reflectance of the Earth's surface for global energy budgets from remotely sensed nadir or directional radiance values, *Rem. Sens. Environ.*, **18**, 205-223.

Kimes, D. S., Ranson, K. J. and Sun, G. (1997) Inversion of a forest backscatter model using neural networks, *Int. J. Rem. Sens.*, **18**, 2181-2199.

Kimes, D. S., Knyazikhin, Y., Privette, J. L., Abuelgasim, A. A. and Gao, F. (2000) Inversion methods for physically-based models, *Rem. Sens. Rev.*, **18**, 381-439.

Knyazikhin, Y. V., Marshak, A. L. and Myneni, R. B. (1992) Interaction of photons in a canopy of finite dimensional leaves, *Rem. Sens. Environ.*, **39**, 61-74.

Knyazikhin, Y. V., Martonchik, J. V., Diner, D. J., Myneni, R. B., Verstraete, M. M., Pinty, B. and Gobron, N. (1998a) Estimation of vegetation canopy leaf area index and fraction of absorbed photosynthetically active radiation from atmosphere-corrected MISR data, *J. Geophys. Res.*, **103**, 32,239-32,256.

Knyazikhin, Y. V., Martonchik, J. V., Myneni, R. B., Diner, D. J. and Running, S. W. (1998b) Synergistic algorithm for estimating vegetation canopy leaf area index and fraction of absorbed photosynthetically active radiation from MODIS and MISR data, *J. Geophys. Res.*, **103**, 32,257-32,275.

Knyazikhin Y. V., Kranigk, J., Myneni, R. B., Panfyorov, O. and Gravenhorst, G. (1998c) Influence of small-scale structure on radiative transfer and photosynthesis in vegetation canopies, *J. Geophys. Res.*, **103**, 6133-6144.

Knyazikhin, Y. V. and Marshak, A. (2000) Mathematical aspects of BRDF modeling: adjoint problem and Green's function, *Rem. Sens. Rev.*, **18**, 263-280.

Kopeke, P. and Kriebel, K. T. (1987) Improvement of the shortwave cloud-free radiation budget accuracy, part 1: Numerical achievement including surface reflectance anisotropy, *Journ. Clim. Appl. Meteorol.*, **26**, 374-395.

Kubelka, P. and Munk, F. (1931) Ein Beitrag zur Optik der Farbanstriche, *Zeits. F. techn. Physik*, **12**, 593-601.

Kuusk, A. (1985) The hot-spot effect of a uniform vegetative cover, *Sov. J. Rem. Sens.*, **3**, 645-658.

Kuusk, A., Andrieu, B., Chelle, M. and Aries, F. (1997) Validation of a Markov chain canopy reflectance model, *Int. J. Rem. Sens.*, **18(10)**, 2125-2146.

Lee, T. Y. and Kaufman, Y. J. (1986) Non-Lambertian effects on remote sensing of surface reflectance and vegetation index, *IEEE Trans. Geosci. Rem. Sens.*, **24**, 699-708.

Leroy, M. and Roujean, J.-L. (1994) Sun and view-angle corrections on reflectances derived from NOAA/AVHRR data, *IEEE Trans. Geosc. Rem. Sens.*, **32**, 684-697.

Leroy, M., Deuze, J. L., Breon, F. M., Hautecoeur, O., Herman, J. C., Buriez, D., Tanre, D., Bouffies, S., Chazette, P. and Roujean, J.-L. (1996) Retrieval of atmospheric properties and surface bidirectional reflectances over land from POLDER/ADEOS, *J. Geophys. Res.* **102**, 17,023-17,037.

Leroy, M. (2001) Deviation from reciprocity in bidirectional reflectance, *J. Geophys. Res.*, **106(D11)**, 11,917-11,923.

Lewis, P. and Muller, J.-P. (1990), Botanical plant modelling for remote sensing simulation studies, *Proc. IGARSS'90*, Washington D.C., USA, 1739-1782.

Lewis, P. (1995) The utility of kernel-driven BRDF models in global BRDF and albedo studies, *Proc. IGARSS '95*, Firenze, Italy, 1186-1188.

Lewis, P. (1996) A botanical plant modelling system for remote sensing simulation studies, *Ph.D. thesis, University of London*, available from the author via http://www.geog.ucl.ac.uk/~plewis/.

Lewis, P. and Disney, M. I. (1997) Examining BRDF model operation with the Botanical Plant Modelling System, *Proc. 23rd Annual Rem. Sens. Soc. Meeting, Reading, UK, 2-4 Sept., 1997*, 298-303.

Lewis, P. and Disney, M. I. (1998) The Botanical Plant Modelling System (BPMS): a case study of multiple scattering in a barley canopy, *Proc. IGARSS'98*, Seattle, USA, CD-ROM.

Lewis, P. (1999) Three-dimensional plant modelling for remote sensing simulation studies using the Botanical Plant Modelling System (BPMS), *Agronomie, Agriculture and Environment*, **19(3-4)**, 185-210.

Lewis, P., Disney, M. I., Barnsley, M. J., and Muller, J.-P. (1999a) Deriving albedo maps for HAPEX-Sahel from ASAS data using kernel-driven BRDF models, *Hydrol. and Earth Sys. Sci.*, **3(1)**, 1-13.

Lewis, P., Disney, M. I. and Riedmann, M. (1999b) Application of the Botanical Plant Modelling System (BPMS) to the analysis of spatial information in remotely sensed imagery, in proc. 25th Annual Remote Sensing Society Conference, 7-10th September 1999, Cardiff, 507-514.

Li, X. and Strahler, A. H. (1985) Geometrical-optical modelling of a conifer forest canopy, *IEEE Trans. Geosc. Rem. Sens.*, **23**, 705-721.

Li, X. and Strahler, A. H. (1986) Geometrical-optical reflectance modelling of a conifer forest canopy, *IEEE Trans. Geosc. Rem. Sens.*, **24**, 906-919.

Li, X. and Strahler, A. H. (1988) Modelling the gap probability of a discontinuous vegetation canopy, *IEEE Trans. Geosc. Rem. Sens.*, **26**, 161-170.

Li, X. and Wan, Z. (1988) Comments on the reciprocity of in the BRDF modeling, *Progress of Nat. Sci.*, **8(3)**, 354-358.

Li, X. and Strahler, A. H. (1992) Geometrical-optical bidirectional reflectance modelling of the discrete crown vegetation canopy: effect of crown shape and mutual shadowing, *IEEE Trans. Geosc. Rem. Sens.*, **30**, 276-292.

Li, X., Woodcock, C. E. and Davis, R. (1994) A hybrid geometric optical and radiative transfer approach for modeling pyranometer measurements under a Jack Pine forest, Geog. Info. Sci., **1(1)**, 34-41.

Li, X., Strahler, A. H. and Woodcock, C. E. (1995) A hybrid geometric optical-radiative transfer approach for modeling albedo and directional reflectance of discontinuous canopies, *IEEE Trans. Geosci. Rem. Sens.*, **33**, 466-480.

Liang, S. and Strahler, A. H. (1993a) Calculation of the angular radiance distribution for a coupled atmosphere and canopy, *IEEE Trans. Geosci. Rem. Sens.*, **31**, 491-502.

Liang, S. and Strahler, A. H. (1993b) An analytic BRDF model of canopy radiative transfer and its inversion, *IEEE Trans. Geosci. Rem. Sens.*, **31**, 1081-1092.

Liang, S. and Strahler, A. H. (1994) Retrieval of surface BRDF from multiangle remotely sensed data, *Rem. Sens. Environ.*, **50**, 18-30.

Liang, S., Strahler, A. H. and Walthall, C. (1999) Retrieval of land surface albedo from satellite observations: a simulation study, *J. Appl. Meterol.*, **38**, 712-725.

Liang, S. (2000) Narrowband to broadband conversions of land surface albedo: I Algorithms, *Rem. Sens. Environ.*, **76**, 213-238.

Liang, S., Strahler, A. H., Barnsley, M. J., Borel, C. C., Gerstl, S. A. W., Diner, D. J., Prata, A. J. and Walthall, C. L. (2000a) Multiangle remote sensing: Past, Present and Future, *Rem. Sens. Rev.*, **18**, 83-103.

Liang, S., Stroeve, J. C., Grant, I. F., Strahler, A. H. and Duvel, J. P. (2000b) Angular corrections to satellite data for estimating earth radiation budget, *Rem. Sens. Rev.*, **18**, 103-137.

Liang, S., Shuey, S., Fang, H, Walthall, C., Daughtry, C. and Hunt, R. (2000c, *submitted*) Narrowband to broadband conversions of land surface albedo: II. Validation, *submitted to Rem. Sens. Environ.*

LI-COR Technical Report #102 LAI-2000 Plant canopy analyzer: theory of operation and verification studies, PCA 102-291, LI-COR inc.

Lucht (1998) Expected retrieval accuracies of bidirectional reflectance and albedo from EOS-MODIS and MISR angular sampling, *J. Geophys. Res.*, **103(D8)**, 8763-8778.

Lucht, W., Schaaf, C. B. and Strahler, A. H. (1999) An algorithm for the retrieval of albedo from space using semiempirical BRDF models, IEEE *Trans. Geosci. Rem. Sens.*, **38(2)**, 977-998.

Lucht, W., Hyman, A. H., Strahler, A. H., Barnsley, M. J., Hobson, P. and Muller, J-P. (2000) A comparison of satellite-derived spectral albedos to ground-based broadband albedo measurements modeled to satellite spatial scale for a semidesert landscape, *Rem. Sens. Environ.*, **74**, 85-98.

Lucht, W. and Lewis, P. (2000) Theoretical noise sensitivity of BRDF and albedo retrieval from the EOS-MODIS and MISR sensors with respect to angular sampling, *Int. J. Rem. Sens.*, **21(1)**, 81-98.

Lucht, W. and Roujean, J. -L. (2000) Considerations in the parametric modeling of BRDF and albedo from multiangle satellite sensor observations, *Rem. Sens. Rev.*, **18**, 343-380.

Marshak, A. L. (1989) The effect of the hot-spot on the transport equation in plant canopies, *J. Quant. Spectrosc. Radiat. Transf.*, **42(4)**, 615-630.

Martonchik, J. V., Diner, D. J., Kahn, R. A., Ackerman, T. P., Verstraete, M. M., Pinty, B. and Gordon, H. R. (1998a) Techniques for the retrieval of aerosol properties over land and ocean using multiangle imaging, IEEE *Trans. Geosci. Rem. Sens.*, **36**, 1212-1227.

Martonchik, J. V., Diner, D. J., Pinty, B., Verstraete, M. M., Myneni, R. B., Knyazikhin, Y. and Gordon, H. R. (1998b) Determination of land and ocean reflective, radiative and biophysical properties using multiangle imaging, IEEE *Trans. Geosci. Rem. Sens.*, **36**, 1266-1281.

Martonchik, J. V., Bruegge, C. J. and Strahler, A. H. (2000) A review of reflectance nomenclature used in remote sensing, *Rem. Sens. Rev.*, **19**, 9-10.

Miller, J. B. (1967) A formula for average foliage density, *Aust. J. Bot.*, **15**, 141-144.

Minnaert, M. (1941) The reciprocity principle in lunar photometry, *Astrophys. Journ.*, **93**, 403-410.

Mintz, Y. (1984) The sensitivity of numerically simulated climates to land-surface conditions, in *The Global Climate* (J. Houghton, Ed.), Cambridge University Press, Cambridge.

Monsi, M. and Saeki, T. (1953) Uber den Lichtfaktor in den Pflanzengesellscahften und seine Bedeutung fur die Stoffproduktion, *Jpn. J. Bot.*, **14**, 22-52.

Musser, G. (2001) Climate of Uncertainty, *Sci. Am.*, Oct. 2001, 14-15.

Myneni, R. B., Asrar, G. and Kanemasu, E. T. (1987a) Light scattering in plant canopies: the Successive Orders of Scattering Approximation (SOSA), *Agric. For. Meteorol.*, **39,** 1-12.

Myneni, R. B., Asrar, G. and Kanemasu, E. T. (1987b) Light scattering in plant canopies: the Successive Orders of Scattering Approximation (SOSA), *Agric. For. Meteorol.*, **40**, 71-87.

Myneni, R. B., Gutshick, V. P., Asrar, G. and Kanemasu, E. T. (1988a) Photon transport in vegetation canopies with anisotropic scattering, Parts II and IV, *Agric. For. Meteorol.*, **42**, 17-40 and 101-120.

Myneni, R. B., Asrar, G. and Kanemasu, E. T. (1988b) Solution of an integral equation encountered in studies on radiative transfer in completely absorbing leaf canopies, *J. Quant. Spectroscop. Radiat. Trans.*, **40(2)**, 157-164.

Myneni, R. B., Ross, J. and Asrar, G. (1989) A review on the theory of photon transport in leaf canopies, *Agric. For. Meteorol.*, **45**, 1-153.

Myneni, R. and Ross, J. (eds.) (1990) *Photon-vegetation interactions: applications in optical remote sensing and plant ecology*, Springer-Verlag, Heidelberg, Germany.

Myneni, R. B., Asrar, G. and Gerstl, S. A. W. (1990) Radiative transfer in three-dimensional leaf canopies, *Transp. Theory Stat. Phys.*, **19**, 205-250.

Myneni, R. B., and Ganapol, B. D. (1991) A simplified formulation for photon transport in leaf canopies with finite dimensional scatterers, *J. Quant. Spectrosc. Radiat. Transf.*, **45**, 135-140.

Myneni, R. B., Marshak and A. L, Knyazikhin, Y. (1991) Transport theory for a leaf canopy of finite-dimensional scatterering centers, *J. Quant. Spectrosc. Radiat. Transf.*, **46(4)**, 259-280.

Myneni, R. B., Asrar, G. and Hall, F. G. (1992) A three-dimensional radiative transfer model for optical remote sensing of vegetated land surfaces, *Rem. Sens. Environ.*, **45**, 85-103.

Myneni, R. B. and Asrar, G. (1993) Radiative transfer in three dimensional atmosphere vegetative media, *J. Quant. Spectrosc. Radiat. Transf.*, **49**, 585-598.

Myneni, R. B. and Williams, D. L. (1994) On the relationship between FAPAR and NDVI, *Rem. Sens. Environ.*, **49**, 200-211.

Myneni, R. B., Hall, F. G., Sellers, P. J. and Marshak, A. L. (1995a) The interpretation of spectral vegetation indexes, *IEEE Trans. Geosci. Rem. Sens.*, **33**, 481-486.

Myneni, R. B., Maggion, S., Iaquinta, J., Privette, J. L., Gobron, N., Pinty, B., Kimes, D. S., Verstraete, M. M. and Williams, D. L. (1995b) Optical remote sensing of vegetation: modelling, caveats and algorithms, *Rem. Sens. Environ.*, **51**, 169-188.

Myneni, R. B., Keeling, C. D., Tucker, C. J., Asrar, G. and Nemani, R. R. (1997) Increased plant growth in the northern high latitudes from 1981 to 1991, *Nature*, **386 (6626)**, 698-702.

Nicodemus, F. E. (1970) Reflectance nomenclature and directional reflectance and emissivity, *Appl. Opt.* **9**, pp. 1474-1575.

Nicodemus, F. E., Richmond, J. C., Hsia, J. J., Ginsburg, I. W. and Limperis, T. (1977) Geometrical consideration and nomenclature for reflectance, *Nat. Beaureau of Stand. Report, NBS MN-160*, 52 pp., Washington, D.C (in Wolff *et al.*, 1992).

Nilson, T. and Kuusk, A. (1989) A reflectance model for the homogenous plant canopy and its inversion, *Rem. Sens. Environ.*, **27**, 157-167.

Nolin, A. W. and Stroeve, J. (1997) The changing albedo of the Greenland Ice Sheet: Implications for Climate Change, *Ann. Glaciol.*, **25**, 51-57.

Nolin, A. W. and Liang, S. (2000) Progress in bidirectional reflectance modelling and applications for surface particulate media: snow and soils, *Rem. Sens. Rev.*, **18**, 307-342.

Norman, J. M., Welles, J. M. and Walter, E. A. (1985) Contrasts among bidirectional reflectance of leaves, canopies and soils, *IEEE Trans. Geosci. Rem. Sens.*, **GE-23**, 659-668.

North, P. R. J. (1996) Three-dimensional forest light interaction model using a Monte Carlo method, *IEEE Trans. Geosci. Rem. Sens.*, **34(4)**, 946-956.

North, P. R. J., Briggs S. A., Plummer S. E. and Settle, J. J. (1999) Retrieval of land surface bidirectional reflectance and aerosol opacity from ATSR-2 multiangle imagery, *IEEE Trans. Geosci. Rem. Sens.*, **37(1)**, 526-537.

O'Dwyer, S. (1999) Establishment of an operational inversion technique for multi-directional data from CHRIS (Compact High Resolution Imaging Spectrometer), M.Sc. thesis, University of London (unpublished).

Oreskes, N., Shrader-Frechette, K. and Belitz, K. (1994) Verification, Validation and Confirmation of Numerical Models in the Earth Sciences, *Science* **263**, 641-646.

Otterman, J. and Weiss, G. H. (1984) Reflections from a field of randomly located vertical protrusions, *App. Opt.*, **23**, 1931-1936.

Pinty, B., Verstraete, M. M. and Dickinson, R. E. (1989) A physical model for predicting bidirectional reflectances over bare soil, *Rem. Sens. Environ.*, **27**, 273-288.

Pinty, B., Verstraete, M. M. and Dickinson, R. E. (1990) A physical model of the bidirectional reflectance of vegetation canopies 2. Inversion and validation, *J. Geophys. Res.*, **95,** 11,767-11,775.

Pinty, B. and Verstraete, M. M. (1991) Extracting information on surface properties from bidirectional reflectance measurements, *J. Geophys. Res.*, **96,** 2865-2874.

Pinty, B., Verstraete, M. M. (1992) On the design and validation of bidirectional reflectance and albedo models, *Rem. Sens. Environ.*, **41**, 155-167.

Pinty, B. and Verstraete, M. M. (1998) Modeling the scattering of light by homogeneous vegetation in optical remote sensing, *Journ. Atmos. Sci.*, **55 (2)**, 137-150.

Pinty, B., Roveda, F., Verstraete, M. M., Gobron, N., Govaerts, Y., Martonchik, J. V., Diner, D. J., Kahn, R. A. (2000) Surface albedo retrieval from Meteosat - 1. Theory, *J. Geophys. Res. (Atmospheres)*, **105(D14)**, 18,099-18,112.

Pinty, B., Gobron, N., Widlowski, J. L., Gerstl, S. A. W., Verstraete, M. M., Antunes, M., Bacour, C., Gascon, F., Gastellu, J. P., Goel, N., Jacquemoud, S., North, P., Qin, W. H. and Thompson, R. (2001) Radiation transfer model intercomparison (RAMI) exercise, *J. Geophys. Res. (Atmospheres)*, **106(D11)**, 11,937-11,956.

Press, W. H., Teukolsky, S. A., Vetterling, W. T. and Flannery, B. P. (1994) *Numerical Recipes in C: The Art of Scientific Computing*, Cambridge University Press, Cambridge, UK, pp. 994.

Price, J. C. (1990) On the information-content of soil reflectance spectra, *Rem. Sens. Environ.*, **33(2)**, 113-121.

Price, J. C. (1992) Variability of high-resolution crop reflectance spectra, *Int. J. Rem. Sens.*, **13(14)**, 2593-2610.

Price, J. C. (1998) An approach for analysis of reflectance spectra, *Rem. Sens. Environ.*, **64(3)**, 316-330.

Price, J. C. (1994) Band selection procedure for multispectral scanners, *Appl. Opt.*, **33(15)**, 3281-3828.

Privette, J. L. and Vermote, E. F. (1995) Fitting remote sensing data with linear bidirectional reflectance models, *Proc. SPIE Symp. Sat. Rem. Sens.*, **2586**, 172-189.

Privette, J. L., Deering, D. W. and Wickland, D. E. (1997) Report on the workshop on multiangular remote sensing for environmental applications, NASA Technical Document.

Prusinkiewicz, P. and Lindenmayer, A. (1990) *The Algorithmic Beauty of Plants*, Springer-Verlag New York.

Prusinkiewicz, P. (1999) A look at the visual modelling of plants using L-systems, *Agronomie*, **19**, 211-224.

Qin, W. and Gerstl. S. A. W. (2000) 3-D scene modelling of semi-desert vegetation cover and its radiation regime, *Rem. Sens. Environ.*, **74**, 145-162.

Qin, W. and Liang. S. (2000) Plane-parallel canopy radiative transfer modelling: recent advances and future directions, *Rem. Sens. Rev.*, **18**, 281-305.

Rahman, H., Verstraete, M. M. and Pinty, B. (1993a) Coupled surface-atmospheric reflectance (CSAR) model 1. Model description and inversion on synthetic data, *J. Geophys. Res.*, **98(D11)**, 20,779-20,790.

Rahman, H., Pinty, B. and Verstraete, M. M. (1993b) Coupled surface-atmospheric reflectance (CSAR) model 2. Semiempirical surface model usable with NOAA AVHRR data, *J. Geophys. Res.*, **98(D11)**, 20,791-20,802.

Randall, D. A. *et al.* (1992) Intercomparison and interpretation of surface energy fluxes in atmospheric general circulation models, *J. Geophys. Res.*, **97**, 3711-3725.

Ranson, K. J. and Daughtry, C. S. T. (1987) Scene shadow effects on multispectral response, *IEEE Trans. Geosci. Rem. Sens.*, **25(4)**, 502-509.

Ross, J. K. (1975) Radiative transfer in plant communities. In *Vegetation and the Atmosphere* (J. L. Monteith, Ed.), Vol. 1., Academic Press, London, pp. 13-52.

Ross, J. K. (1981) *The radiation regime and architecture of plant stands*, W. Junk, The Hague, Netherlands.

Ross, J. K. and Marshak, A. L. (1988) Calculation of canopy bidirectional reflectance using the Monte Carlo method, *Rem. Sens. Environ.*, **24(2)**, 213-225.

Ross, J. K. and Marshak, A. L. (1989) The influence of leaf orientation and the specular component of leaf reflectance on the canopy bidirectional reflectance, *Rem. Sens. Environ.*, **27(3)**, 251-260.

Roujean, J.-L., Leroy, M. and Deschamps, P.-Y. (1992) A bidirectional reflectance model of the Earth's surface for the correction of remote sensing data, *J.. Res.*, **97(D18)**, 20,455-20,468.

Rouse, J. W., Haas, R. H., Schell, J. A. and Deering, D. W. (1974) Monitoring vegetation systems in the Great Plains with ERTS, *Proc. 3rd Earth Resources Technology Satellite-1 Symposium*, Greenbelt MD, NASA SP-351, 3010-3017.

Roy, D. P., Lewis, P. and Justice, C. O. (2001, accepted) Burned area mapping using multi-temporal moderate resolution spatial resolution data - a bi-directional reflectance model-based expectation approach, *Rem. Sens. Environ.*

Running, S. W., Justice, C. O., Salomonson, V., Hall, D., Barker, J., Kaufman, Y. J., Strahler, A. H., Huete, A, R, Muller, J. -P., Vanderbilt, V., Wan, Z. M., Teillet, P. and Carneggie, D. (1994) Terrestrial remote sensing science and algorithms planned for EOS/MODIS, *Int. J. Rem. Sens.*, **15**, 3587-3620.

Running, S.W., Nemani, R. and Glassy, J.M. (1996) MOD17 PSN/NPP Algorithm Theoretical Basis Document, NASA.

Saich, P., Lewis, P., Disney, M. I. and Thackrah, G. (2001) Comparison of Hymap/E-SAR data with models for optical reflectance and microwave scattering from vegetation canopies, *Proc. 3rd Int. Workshop on Retrieval of Bio- and Geo-Physical Parameters from SAR data for Land Applications*, Sheffield, Sept. 2001.

Salby, M. L. (1995) The atmosphere, in Trenberth, K. (Ed.), pp 53-115.

Sandmeier, St. and Itten, K. I. (1999) A field goniometer system (FIGOS) for acquisition of hyperspectral BRDF data, *IEEE Trans. Geosci. Rem. Sens.*, **37**, 978-986.

Schaaf, C. B., Lucht, W., Tsang, T., Gao, F., Strugnell, N., Chen, L., Liu, Y. and Strahler, A. H. (1999) Prototyping the moderate resolution imaging spectroradiometer (MODIS) BRDF and albedo product, *Proc. Int. Geosc. Rem. Sens. Symp. IGARSS* '99, Hamburg.

Schaaf, C., Strahler, A., Lucht, W., Tsang, T., Gao, F., Li, X., Strugnell, N., Chen, L., Muller, J.-P., Lewis, P., Barnsley, M. J., Hobson, P., Disney, M. I., Dunderdale, M., D'Entremont, R. P., Hu, B. and Liang, S. (2000a, in press) The At-launch MODIS BRDF and Albedo Science Data Product, *accepted Rem. Sens. Environ.*

Schaaf, C.B., Gao, F., Strahler, A.H., Tsang, T., Lucht, W., Strugnell, N., Li, X., Muller, J.-P., Lewis, P., Barnsley, M. J., Hobson, P., Disney, M. I., Dunderdale, M., Roberts, G. (2000b) The Moderate Resolution Imaging Spectroradiometer (MODIS) BRDF and albedo product: preliminary results, *Proc. Int. Geosc. Rem. Sens. Symp.*, **7**, 2000, 3048 -3050.

Schaaf, C. B., Gao, F., Strahler, A. H., Lucht, W., Li, X., Zhang, X., Jin, Y., Tsvetsinskaya, E., Muller, J.-P., Lewis, P., Barnsley, M., Roberts, G., Disney, M., Doll, C., Liang, S., Roy, D. and Privette, J. (2001a) Land Surface Albedo, Nadir BRDF-Adjusted Reflectance, and BRDF Product from the MODerate Resolution Imaging Spectroradiometer (MODIS), *Proc. 11th Conference on Satellite Meteorology and Oceanography*, AMS, Madison, WI, 15-18 October, 2001.

Schaaf, C. B., Gao, F., Strahler, A. H., Lucht, W., Li, J.-P. Muller, Lewis, P., Barnsley, M., Hobson, P., Disney, M., Roberts, G., Dunderdale, M. and Doll, C. (2001b) Land Surface Spectral Bidirectional Reflectance and Albedo from the MODerate Resolution Imaging Spectroradiometer (MODIS), American Geophysical Union Spring Meeting, Boston, MA, 29 May - 2 June, 2001.

Schimel, D. S. (1995) Terrestrial ecosystems and the carbon cycle, *Glob. Change Biol.*, **1**, 77-91.

Schulz, K., Jarvis, A., Beven, K. and Soegaard, H. (2001) The predictive uncertainty of land surface fluxes in response to increasing ambient carbon dioxide, *Journ. Climate*, **14(12)**, 2551-2562.

Sellers, P. J., Mintz, Y., Sud, Y. C. and Dalcher, A. (1986) A simple biosphere model (SiB) with point micrometeorological and biophysical data, *J. Atmos. Sci.*, **43**, 505-531.

Sellers, P. J. (1992) Remote Sensing of the land surface for studies of global change, NASA/GSFC, *Int. Sat. Land Surf. Clim. Proj. Report.*

Sellers, P. J. (1995) Biophysical models of land surface processes, (in Trenberth, 1995, p451-490).

Sellers, P. J., Dickinson, R. E., Randall, D. A., Betts, A. K., Hall, F. G., Berry, J. A., Collatz, G. J., Denning, A. S., Mooney, H. A., Nobre, C. A., Sato, N, Field, C. B., Henderson-Sellers, A. (1995b) Modelling the exchanges of energy, water and carbon between continents and the atmosphere, *Science*, **275**, 502-509.

Sellers P. J., Dickinson, R. E., Randall, D. A., Betts, A. K., Hall, F. G., Berry, J. A., Collatz, G. J., Denning, A. S., Mooney, H. A., Nobre, C. A., Sato, N., Field, C. B. and Henderson-Sellers, A. (1997) Modeling the exchanges of energy, water, and carbon between continents and the atmosphere, *Science*, **5299**, 502-509.

Settle, J. J and Drake, N. A. (1993) Linear mixing and the estimation of ground cover proportions, *Int. Journ. Rem. Sens.*, **14**, 1159-1177.

Shneider, D. (1998) The rising seas, *Sci. Am. Presents The Oceans*, **9(3)**, 28-35.

Shibayama, M., and Wiegand, C. L. (1985) View azimuth and zenith, and solar angle effects on wheat canopy reflectance, *Rem Sens. Environ.*, **18**, 91-103.

Shukla, J. and Mintz, Y. (1982) Influence of land-surface evapotranspiration on the earth's climate, *Science,* **215**, 1498-1501.

Shultis, J. K. and Myneni, R. B. (1988) Radiative transfer in vegetation canopies with anisotropic scattering, *J. Quant. Spectrosc. Radiat. Trans.*, **39**, 115-129.

Slater, P. N. (1980) *Remote Sensing: Optics and Optical Systems*, Reading, Pennsylvania: Addison Wesley, 575pp.

Smith, W.L. (1985) *Satellites*, In *Handbook of Applied Meteorology*, edited by D. D. Houghton, John Wiley and Sons, New York, pp380-472.

Snyder, W. C. (1998) Reciprocity of the bidirectional reflectance distribution function (BRDF) in measurements and models of structured surfaces, *IEEE Trans. Geosci. Rem. Sens.*, **36**, 685-691.

Stephens, G. L., Campbell, G. G. and Vonder Haar, T. H. (1981) Earth radiation budget, *Journ. Geophys. Res.*, **86**, 9739-9760.

Steven, M. D., Biscoe, P. V. and Jaggard, K. W. (1983) Estimation of sugar beet productivity from reflection in the red and infrared spectral bands, *Int. J. Rem. Sens.*, **4(2)**, 325-334.

Strahler, A. H. and Jupp, D. L. B. (1991) Modeling bidirectional reflectance of forests and woodlands using Boolean models and geometric optics, *Rem. Sens. Environ.*, **34**, 153-166.

Strahler, A. H. (1996) Vegetation canopy reflectance modeling: Recent developments and remote sensing perspectives, *Rem. Sens. Rev.*, **15**, 179-194.

Strugnell, N. C. and Lucht W. (2000) An algorithm to infer continental-scale albedo from AVHRR data, land cover class, and field observations of typical BRDFs, *Journ. Climate*, **14(7)**, 1360-1376.

Strugnell, N. C., Lucht W. and Schaaf, C. (2001) A global albedo data set derived from AVHRR data for use in climate simulations, *Geophys. Res. Lett.*, **28(1)**, 191-194.

Stum, B., Pinty, B. and Ramond, R. (1985) A parameterization of broadband conversion factors for Meteosat visible radiances, *Journ. Clim. Appl. Meteorol.*, **24**, 1377-1382.

Suits, G. H. (1972) The calculation of the directional reflectance of a vegetative canopy, *Rem. Sens. Environ.*, **2**, 117-125.

Sun, G. Q. and Ranson, K. J. (1995) A 3D RADAR backscatter model of forest canopies, *IEEE Trans. Geosci. Rem. Sens.*, **33(2)**, 372-382.

Tanre, D., Deroo, C., Duhaut, P., Herman, M., Morcrette, J. J., Perbos, J. and Deschamps, P. Y. (1986) Simulation of the satellite signal in the solar spectrum (5S), LOA University des Sciences et Techniques de Lille, 59655, Villeneuve d'Ascq Cedex, France.

Tanre, D., Herman, M. and Deschamps, P. Y. (1981) Influence of the background contribution on space measurements of ground reflectance, *Appl. Opt.*, **20**, 3673-3684.

Tarantola, A. (1987) Inverse Problem theory: methods for data fitting and model parameter estimation, Elsevier, Amsterdam, pp. 601.

Torrance, K. E. and Sparrow, E. M. (1966) Theory of off-specular reflection from roughened surfaces, in Wolff *et al.*, (eds.) pp 32-42.

Trenberth, K. E. (ed.) (1992) *Climate system modelling*, Cambridge University Press, Cambridge, UK, pp. 788.

Tucker, C. J. (1979) Red and photographic infrared linear combinations for monitoring vegetation, *Rem. Sens. Environ.*, **8**, 127-150.

Twomey, S. (1977) *Introduction to the mathematics of inversion in remote sensing and indirect measurements*, Elsevier, Amsterdam, ISBN 0-486-69451-8, pp. 243.

Vanderbilt, V. C., Grant, L. and Daughtry, C. S. T. (1985) Polarization of light scattered by vegetation, *Proc. IEEE*, **73(6)**, 1012-1024.

Van Leeuwen, W. J. D., Huete, A. R., Walthall, C. L., Prince, S. D., Bégué, A. and Roujean, J. -L. (1997) Deconvolution of remotely sensed spectral mixtures for the retrieval of LAI, fAPAR and soil brightness, *Journ. Hydrol.*, **188-189**, 697-724.

Veach, E. (1997) Robust Monte Carlo methods for light transport simulation, Ph.D. dissertation, Stanford University.

Verhoef, W. (1984) Light scattering by leaf layers with applications to canopy reflectance modelling: the SAIL model, *Rem. Sens. Environ.*, **16**, 125-141.

Vermote, El Saleous, N. Z., Justice, C. O. Kaufman, Y. J., Privette, J. L., Remer, L., Roger, J. C., Tanré, D. (1997a) Atmospheric correction of visible to middle infrared EOS-MODIS data over land surface, background, operational algorithm and validation, *J. Geophys. Res.*, **D14**, 17,131 - 17, 141.

Vermote E. F., Tanré, D., Deuzé, J. L., Herman, M. and Morcrette, J. J (1997b) Second simulation of the satellite signal in the solar spectrum (6S): an overview, *IEEE Trans. Geosc. Rem. Sens.*, **35**, 675-686.

Verstraete, M. M. (1987) Radiation transfer in plant canopies: transmission of direct solar radiation and the role of leaf normal orientation, *J. Geophys. Res.*, **92,** 10,985-10,995.

Verstraete, M. M., Pinty, B. and Dickinson, R. E. (1990) A physical model of the bidirectional reflectance of vegetation canopies 1. Theory, *J. Geophys. Res.*, **95,** 11,755-11,765.

Visser, H., Folkert, R. J. M., Hoekstra, J. and De Wolff, J. J. (2000) identifying key sources of uncertainty in climate change projections, *Climatic Change*, **45(3-4)**, 421-457.

Walthall, C. L., Norman, J. M., Welles, J. M., Campbell, G. and Blad, B. (1985) Simple equation to approximate the bidirectional reflectance from vegetated canopies and bare soil surfaces, *Appl. Opt.*, **24(3)**, 383-387.

Walthall, C. L., Roujean, J. -L. and Morisette, J. (2000) Field and landscape BRDF optical wavelength measurements: experience, techniques and the future, *Rem. Sens. Rev.*, **18(2-4)**, 503-531.

Wanner, W., Li, X. and Strahler, A. H. (1995) On the derivation of kernels for kernel-driven models of bidirectional reflectance, *J. Geophys. Res.*, **100(D10)**, 21,077-21,089.

Wanner, W., Strahler, A. H., Hu, B. Lewis, P., Muller, J.-P., Li, X., Barker Schaaf, C. L. and Barnsley, M. J. (1997) Global retrieval of bidirectional reflectance and albedo over land from EOS MODIS and MISR data: theory and algorithm, *J. Geophys. Res.*, **102**, 17,143-17,161.

Webster, P. J. and Curry, A. (1998) The oceans and weather, *Sci. Am. Presents The Oceans*, **9(3)**, 38-43.

Weiss, M., Baret, F., Myneni, R. B., Pragnere, A. and Knyazikhin, Y. (2000) Investigation of a model inversion technique to estimate canopy biophysical variables from spectral and directional reflectance data, *Agronomie*, **20(1)**, 3-22.

Wernand, M. R., Shimwell, S. J. and De Munck, J. C. (1997) A simple method of full spectrum reconstruction by a five-band approach for ocean colour applications, *Int. J. Rem. Sens.*, **18(9)**, 1977-1986.

Wessman, C. A., and Asner, G. P. (1998) Ecosystems and the problems of large-scale measurements, in *Successes, Limitations and Frontiers in Ecosystem Ecology*, P. Groffmand and M. Pace eds., Springer-Verlag, New York, 346-371.

Wielicki, B. A., Barkstrom, B. R., Baum, B. A., Charlock, T. P., Green, R. N., Kratz, D. P., Lee III, R. B., Minnis, P., Smith, G. L., Wong, T., Young, D. F., Cess, R. D., Coakley Jr., J. A., Crommelynck, D. A. H., Donner, L., Kandel, R., King, M. D., Miller, A. J., Ramanathan, V., Randall, D. A., Stowe, L. L. and Welch, R. M. (1998) Clouds and the Earth's Radiant Energy System (CERES): algorithm overview, *IEEE Trans. Geosci. Rem. Sens.*, **36(4)**, 1127-1141.

Wigley, T. M. L. and Raper, S. C. B. (2001) Interpretation of high projections for global-mean warming, *Science*, **293**, 451-454.

Wolff, L. B., Shafer, S. A. and Healey, G. E. (1992) *Physics-Based Vision: Principles and Practice: Radiometry*, Jones and Bartlett, Boston, 408 pp.

Woodcock, C. E., Strahler, A. H. and Jupp, D. L. B. (1988) The use of variograms in remote sensing 1. Scene models and simulated images, *Rem. Sens. Environ.*, **25(3)**, 323-348.

Yamaguchi, Y., Kahle, A. B., Tsu, H., Kawakami, T. and Pniel, M. (1998) Overview of Advanced Spaceborne Thermal Emission and Reflection Radiometer (ASTER), *IEEE Trans. Geosci. Rem. Sens.*, **36(4)**, 1062-1071.

Zhan X., and Kustas W. P. (2001) A coupled model of land surface CO_2 and energy fluxes using remote sensing data, *Agric. For. Meteorol.*,**107(2),**131-152.

WWW links (and date of most recent visit)

Chapter 1

www[1.1] http://www.ipcc.ch (2001)

www[1.2] http://www.oecd.org/subject/climatechange/kyoto.htm (2000)

www[1.3] http://www.unfccc.de/resource/convkp.html (2001)

www[1.4] http://www.unep.org/ (2001)

www[1.5] http://www.ipo.noaa.gov (2001)

www[1.6] http://terra.nasa.gov/ (2001)

www[1.7] http://www.eoc.nasda.go.jp/guide/satellite/satdata/adeos_e.html (2001)

www[1.8] http://envisat.esa.int (2001)

www[1.9] http://earth.esa.int/eeo4.12 (2001)

www[1.10] http://radar.metr.ou.edu/OK1/ (2001)

www[1.11] www.chris-proba.org.uk/ (2001)

Chapter 2

www[2.1] http://www.geog.umd.edu/vcl/vcltext.html (2001)

www[2.2] http://www.enamors.org/RAMI/rami.htm (2001)

Chapter3

www[3.1] http://www.asdi.com/asdi_t2_pr_sp_fsp.html (2001)

Chapter 7

www[7.1] http://www.esa.int/msg/pag0.html (2000)

www[7.2] http://www-projet.cst.cnes.fr:8060/POLDER/index.html (2001)

Chapter 8

www[8.1] http://modarch.gsfc.nasa.gov/MODIS/LAND/VAL/ (2001)

www[8.2] http://www.cimel.fr/photo/sunph_us.htm (2001)